PHOTOGRAMMETRIC EVALUATION OF SPACE LINEAR ARRAY IMAGERY FOR MEDIUM SCALE TOPOGRAPHIC MAPPING

BY

MOHAMMAD JAVAD VALADAN ZOEJ

VOLUME I

A Thesis Submitted for the Degree of Doctor of Philosophy (Ph.D.)
in Photogrammetry and Remote Sensing
in the Faculty of Science at the University of Glasgow

Topographic Science, January 1997

IN THE NAME OF ALLAH

TO MY PARENTS

ABSTRACT

This thesis is concerned with the 2D and 3D mathematical modelling of satellite-based linear array stereo images and the implementation of this modelling in a general adjustment program for use in sophisticated analytically-based photogrammetric systems. The programs have also been used to evaluate the geometric potential of linear array images in different configurations for medium scale topographic mapping. In addition, an analysis of the information content that can be extracted for topographic mapping purposes has been undertaken.

The main aspects covered within this thesis are:

- 2D mathematical modelling of space linear array images;
- 3D mathematical modelling of the geometry of cross-track and along-track stereo linear array images taken from spaceborne platforms;
- the algorithms developed for use in the general adjustment program which implements the 2D and 3D modelling;
- geometric accuracy tests of space linear array images conducted over high-accuracy test fields in different environments;
- evaluation of the geometric capability and information content of space linear array images for medium scale topographic mapping;

This thesis concludes that the mathematical modelling of the geometry and the adjustment program developed during the research has the capability to handle the images acquired from all available types of space linear array imaging systems. Furthermore it has been developed to handle the image data from the forthcoming very high-resolution space imaging systems utilizing flexible pointing of their linear array sensors. It also concludes that cross-track and along-track stereo images such as those acquired by the SPOT and MOMS-02 linear array sensors have the capability for map compilation in 1:50,000 scales and smaller, but only in conjunction with a comprehensive field completion survey to supplement the data acquired from the satellite imagery.

ACKNOWLEDGEMENTS

The author wishes to express his sincere gratitude to his supervisor, Professor G. Petrie, for suggesting this topic, for his continuous advice and supervision and for supplying the materials relevant to this research. Also, his assistance in the writing up of this thesis is greatly appreciated. Without all this help, this research would never have come to its present form.

The author's sincere thanks also go to Dr. J. Drummond, his second supervisor from September 1995, for her help, advice and encouragement. Special thanks also go to Mr. D. A. Tait for his advice and encouragement. The assistance received from the other Topographic Science staff members, who are always ready to help, is also gratefully acknowledged, in particular, that given by Mr. J. Shearer, Mr. I. Gordon, Mrs. A. Dunlop, and Mr. T. Ibbs.

Thanks are also due to the Department's Chief Technician, Mr. I. Gerrard and his assistant, Mr. L. Hill, for preparing the photographs included in this dissertation, and to the Senior Cartographer, Mr. M. Shand, for his technical support and the immediate assistance which he gave for scanning some of the graphs used in this thesis.

The author also wishes to extend his gratitude to Professor J. Briggs (Head of the Department) for granting the freedom to use the facilities available in the Department.

The author wishes to thank his research colleague, Mr. N. Al-Rousan, for providing the image coordinate and ground coordinate data of the SPOT stereo-pairs used over the Jordanian test area.

The author also wishes to thank Dr. W. Kornus and Mr. M. Lehner from DLR, Germany for their help and assistance in providing information about the MOMS-02 system and its image header data.

Thanks and gratitude are also due to Dr. C. S. Fraser from the Department of Geomatics of the University of Melbourne, Australia and Dr. E. Baltsavias of ETH Zurich for kindly providing the MOMS-02 image data and ground measurements of the Australian test area.

The author also wishes to thank Dr. B. J. Deveraux and Mr. G. S. Amable from the Department of Geography of the University of Cambridge, for providing SPOT image data measurements and ground measurements over the Crete test area.

The help of Mr. R. Fox of Ordnance Survey International, who arranged for the supply of the map sheets covering the Sudanese test area, is gratefully acknowledged.

Sincere thanks are also due to his research colleagues in Topographic Science, in particular, Mr. A. R. Alias, Mr. G. Buyuksalih, Mr. M. Duckham, Dr. Y. J. Kuo, Mr. H. Rammali, and Mr. Z. Zamlupe; and his friend, Dr. K. Solaimani for their support and friendship throughout the period of this study in the Department of Geography and Topographic Science.

The author wishes to express thanks to his sponsor, the Ministry of Culture and Higher Education of Iran, for providing the Scholarship which supported him during the period of his study.

I wish to express my gratitude to my family in Iran for their support and encouragement in completing my study. They have borne a long separation and the author owes his every achievement to them.

Finally, the author is extremely grateful to his wife, Mrs. Farzaneh Almotahari, and his daughter Faezeh who share life's joys and sorrows with him and who have been a source of constant inspiration even in moments of utter despondency. His wife's patience and continuous encouragement and support, which had a great impact on the progress of the work, never stopped.

TABLE OF CONTENTS

VOLUME I

CHAPTER 4 : TWO-DIMENSIONAL MATHEMATICAL MODELS FOR THE GEOMETRIC CORRECTIONS OF LINEAR ARRAY IMAGERIES

CHAPTER 5 : THREE-DIMENSIONAL MATHEMATICAL MODELLING OF LINEAR ARRAY STEREO IMAGES (CROSS-TRACK CASE)

CHAPTER 7 : GENERALIZED ADJUSTMENT PROGRAM

CHAPTER 8 : GEOMETRIC ACCURACY TESTS OF CROSS-TRACK LINEAR ARRAY IMAGES

CHAPTER 10 : COMPARATIVE STUDY AND ANALYSIS OF THE GEOMETRIC POTENTIAL OF LINEAR ARRAY IMAGES FOR TOPOGRAPHIC MAPPING

CHAPTER 11 : PHOTOGRAMMETRIC INTERPRETATION OF SATELLITE LINEAR ARRAY IMAGERY FOR MEDIUM SCALE TOPOGRAPHIC MAPS

VOLUME II

CHAPTER 1 : INTRODUCTION

1.1 The Importance of Photogrammetric Mapping from Space

The importance of topographic mapping in the scales 1:25,000, 1:50,000 and 1:100,000 for the efficient administration, economic development and defence requirements of all countries is beyond question. These maps also form the basis of the provision of geographic information on the environment and act as a tool for sustainable development. Indeed the demands for accurate maps within this range of scales are increasing daily. This need occurs particularly in certain developing countries where adequate mapping has not yet been completed. The most unfortunate aspect of mapping in these developing countries is that the coverage of the topographic mapping at these scales increases very slowly; and where the coverage has been completed, the pace of change taking place in many parts of these countries occurs at a higher speed than the increase in topographic map coverage or the rate of map revision. Indeed, for many countries, the revision of existing maps is now the major task confronting national mapping organisations.

Nowadays, in the photogrammetric world, the use of space imagery as a tool for the solution of the topographic mapping problem at medium to small scales, is under active investigation. From the geometric point of view, the available space imagery may conveniently be sub-divided into three categories: (i) frame-type optical imagers; (ii) line-type optical imagers; and (iii) SAR (radar) imagers.

(i) Frame-Type Optical Imagers: With this type of device, the image is acquired over the whole frame simultaneously via a projection lens to produce a perspective view of the terrain. The first widely available high resolution images of the Earth taken from space were acquired from this type of imager in the form of a photographic camera by the NASA Gemini 4 mission in 1965. The S190B Earth Terrain Camera (ETC) flown on three Skylab missions in 1973 gave a large number of near vertical stereoscopic photographs of the Earth. Basically it was a high performance reconnaissance camera and produced very high resolution photographs equivalent to a 5-10m ground pixel size (Colwell, 1983). The

success of the ETC experiment prompted the development of two further metric camera systems - The European Space Agency Metric Camera (MC) and the NASA Large Format Camera (LFC) which were flown in Space Shuttle missions in 1983 and 1984 respectively.

Currently the main sources of imagery available in this category (frame-type imagers) are those acquired by Russian cameras. Since 1960, Russia has launched several different series of manned and unmanned platforms for the collection of remotely sensed data, based on the use of photographic systems. The Russian photographic images which are now available on the market are those acquired by the KFA-1000, KFA-3000, KWR-1000, KATE-200, MK-4 and TK-350 cameras mounted in the Russian Cosmos, Soyuz, Salyut, RESURS and MIR platforms.

(ii) Line-Type Optical Imagers: This type of imager, which includes optical-mechanical scanners and pushbroom scanners, exposes a single continuous strip image sequentially through the forward motion of the platform. These systems are well known, with those from the Landsat series (flown first in 1972) such as the MSS and TM scanners having been used on a world-wide basis. The other available line-type optical imagers are SPOT-HRV (flown first in 1986); LISS-I, II and III mounted in the Indian IRS-1A (flown in 1988), IRS-1B (flown in 1991) and IRS-1C (flown in 1995) satellites; OPS mounted in the Japanese JERS-1 satellite (flown in 1992); and the German MOMS-01 (flown in 1983) and MOMS-02 (flown in 1993) devices operated from the Space Shuttle.

(iii) SAR (Radar) Imagers: In this type of imager, a narrow beam of microwave radio energy is sent out from the platform by a transmitter equipped with a directional antenna and a receiver captures the reflected radio waves and measures the elapsed time between the emitted and reflected signals. These are converted to range values and result in the production of an appropriate and distinctive image. Following on from the experimental SAR images of the Seasat and SIR-A and -B missions of the late 1970s and early 1980s, a more production oriented mission has been ESA's ERS-1 SAR launched in 1991. The Japanese JERS-1 SAR was launched in 1992. In 1994, the SIR-C/X-SAR was flown onboard the Space Shuttle in a ten day mission. In 1995, ESA launched its second satellite

in the ERS series as ERS-2 which carries a similar SAR imaging device to that of the ERS-1.

Although there are different types of space imagery available on the market, still there are deficiencies or problems associated with all the existing imaging devices when they are being used or assessed for topographic mapping. Thus they have only been used to a quite limited extent for this purpose; indeed many of these images are still under investigation by different researchers and have still not been employed routinely for mapping by national agencies or private companies.

1.2 The Problems of Using Satellite Imagery for Photogrammetric Mapping

Many researchers have investigated the images derived from various types of satellite imaging devices for topographic mapping at the basic scales of 1:25,000, 1:50,000 and 1:100,000 used for national coverage. These researches have shown up various problems and deficiencies with regard to these systems. The suitability of an imaging device for topographic mapping depends on various different factors:

- it has to be capable of acquiring overlapping image data having a sufficiently stable geometry and a ground resolution that allows it to be used for topographic mapping;
- the resulting images have to be modelled mathematically in such a way as to generate three-dimensional information about the Earth's surface from the image data;
- the images must have the capability to fulfill the requirements for producing a topographic map in terms of its content, and this data must satisfy quite stringent requirements concerning the accuracy of its position and elevation;
- its imagery needs to have compatibility with the available photogrammetric instrumentation, especially with the newer analytical and digital systems;
- it has to be operated on a continuing basis, i.e. there has to be continuity regarding image data acquisition and good access to and availability of this data;
- the overall cost of constructing and operating the device from space and of the

associated ground facilities and the pricing of the image products made available to users.

In the following sections, the various problems arising with these different space imaging systems are reviewed from the topographic mapping and photogrammetric points of view.

1.2.1 Problems of Using Frame-Type Imagers for Photogrammetric Mapping

The two main metric photographic camera systems (MC and LFC) placed in orbit by Western countries for experimental purposes could produce photographs of the Earth with resolutions of 30 lp/mm and 45 lp/mm respectively. Both of these camera systems employed a focal length of 30cm which, when operated from the Space Shuttle, provided imagery with ground resolutions between 10 to 14m (LFC) and 25m (MC). However the photographic coverage taken with these cameras (at 1:800,000 to 1:950,000 scale), although much experimented with for topographic mapping in the mid-1980s, has not been extended since the Space Shuttle disaster in 1986. Thus the MC and LFC coverage is both fragmented and rather old (Petrie, 1994).

By contrast, Russian efforts in this area have been much more extensive and indeed the Russians have concentrated heavily on the use of film cameras both for reconnaissance and mapping - in contrast to Western imaging from space which has mainly used electro-optical systems. The KFA-1000 camera has been flown extensively on short duration Cosmos satellites and on the MIR orbital platform between 1987-1993. With a narrow-angle lens with 1m focal length, a format size of 30×30cm and a film/lens resolution of 30 lp/mm, it gives a ground resolution of between 5 and 10m. However this geometry gives rise to a poor base-to-height ratio (0.12) in terms of its stereo coverage. Still, its comparatively large scale (1:270,000) and high resolution (5 to 10m) are favourable characteristics in terms of topographic map compilation and revision, although its poor geometry is further compounded by the very large geometric distortions which are inherent in the lenses and must not be neglected (Jacobsen, 1993). The KFA-3000 is the same camera, but equipped with a lens of still greater focal length (f = 3m). This means that the photographic scale is

3 times greater, as is the ground resolution. However the ultra narrow angle of coverage gives a very poor base-to-height ratio making it useless for stereo measurements, stereo compilation and DEM extraction. In purely resolution terms, the KFA-1000 has been surpassed by the KWR-1000 cameras mounted on Cosmos satellites and producing system resolutions of 70 lp/mm and ground resolutions between 1 to 3m. These advances were made possible by the use of image motion compensation permitting the use of longer exposures with fine grain, low sensitive, high resolution films (Konecny, 1995). However, KWR-1000 is a panoramic camera and is more suitable for reconnaissance applications than topographic map production. As with all panoramic cameras, the scale falls off greatly from the centre to the edge of the format in the cross-track direction. Thus only the central high-resolution part of the image is sold to non-Russian users. TK-350 is a large format camera (like the American LFC) with a focal length of 350mm and a 30×45cm format size with 7 to 10 metres ground resolution, and a base-to-height ratio equal to 0.52 would appear to have much more favourable photogrammetric characteristics (Petrie, 1995). However, its large format size makes it difficult to accommodate in Western photogrammetric instruments and it has been little used to date.

In general terms, the geometry of all space photographic imaging devices is the same as that of conventional aerial photographs, but the effect of Earth curvature has to be considered in the mathematical solution and in the measurements of height and position.

It is also worth mentioning that, regarding the current development of photogrammetric instrumentation which is moving from analytical to digital, these film-based systems have the deficiency of not providing direct digital data to users. However, in this respect, the need to use a scanner to convert the film data to digital form is the same as for aerial photography. Thus there are large numbers of high-precision scanners available to undertake this conversion, so this is not a problem.

1.2.2 Problems of Using Line-Type Imagers for Photogrammetric Mapping

In the first place, many of the older types of scanner have a dynamic imaging operation

utilising mechanical scanning of the ground using a rotating mirror or prism. This is very difficult to model from the geometric point of view. In addition, none of these systems were designed to require overlapping stereoscopic coverage of the terrain.

Landsat TM with its 30m ground pixel size can give a planimetric accuracy of the quality required for 1:100,000 scale topographic mapping but with great problems in providing the ground resolution required to detect, identify and measure the required terrain features. Doyle (1984) reported the possibility of producing of 1:300,000 scale topographic maps from TM imagery which probably could be pushed to 1:250,000 scale. However this does not address or satisfy the need to provide topographic mapping at the 1:50,000 and 1:100,000 scales which are needed to provide the basic national coverage required in most countries. Height cannot be extracted from this type of image because no stereo image is available. Another current problem with Landsat images are the doubts regarding their future availability. Since the loss of Landsat 6 and the retirement from service of the older Landsats 4 and 5, this source of imagery has effectively dried up, though the existing imagery forms an important archive for global monitoring activities.

During the early 1980s, the German MOMS and MEOSS imaging systems pioneered a quite different scanner technology - that employing linear arrays of CCDs. From the point of view of the topographic mapping community, this was a notable advance in that it eliminated the rotating mirrors and prisms which were an integral feature of the Landsat MSS and TM systems. This offered a much more stable geometry and, from the photogrammetric point of view, it could therefore be modelled in a more realistic way than the oscillating mirror scanning employed with the MSS and TM imagers. The much higher ground resolution offered by linear array systems as a result of longer dwell times was another attraction to the topographic mapping community, for whom sensors with high resolving powers are a necessity for the extraction of the many features of small dimensions that are required to be shown on medium scale topographic maps. The negative aspects of CCD linear array sensors - namely their limited range of spectral sensitivity, which is confined to the visible and near infra-red parts of the electro-magnetic spectrum - are of course a shortcoming in the eyes of many field and environmental scientists, who require and can utilize multi-

spectral imagery acquired over a wide spectral range, especially in the short and medium wave infra-red bands. However this is not an essential requirement for topographic scientists.

Another favourable aspect of linear array sensors is that it is much easier with these devices to arrange for them to be used to acquire overlapping stereo coverage of the Earth, either by use of tilting mirrors in front of nadir pointing lenses or through the oblique pointing of the lenses in a convergent configuration. The latter was first proposed for the American Mapsat and Stereosat projects conceived in the period around 1979-80. However, these projects were not funded and simply remained as proposals. Similar proposals were made by Hofmann in Germany and, in fact, were first realised in the form of an airborne sensor. The same group based in Germany also built MOMS, a simple non-stereoscopic linear array pushbroom scanner which acquired the first civilian spaceborne imagery employing this technology from the Space Shuttle in 1983 and 1984. Further development then led to the design and construction of the MOMS and MEOSS along-track stereo scanners. Unfortunately these never reached operational status due to difficulties with their orbital platforms. In the first place, the Space Shuttle diaster of 1986 resulted in a four year gap before its flights resumed. Then attempts to find an alternative satellite platform, e.g. placing the MEOSS systems on Indian launchers in the late 1980s, proved abortive when they failed to go into orbit and the systems were lost.

This then gave the opportunity for the French - led SPOT system to take the lead in the operational use of linear array imaging technology from satellites. The first SPOT satellite was launched in 1986 and has been followed by two other satellites in the series. Although, until the early 1990s, the system was unique in using this technology, its successful operation has allowed it to become well established and has proven the technology beyond doubt. Indeed so much so that it is now apparent that it will become the dominant optical imaging scanner technology for the foreseeable future.

The SPOT imagery with its 10m pixel size in panchromatic mode has been tested for the production of maps at 1:50,000 and smaller scales by various researchers. However,

although its planimetric and height accuracy seems to be sufficient for mapping at 1:50,000 and 1:100,000 scales, extracting the information necessary for these scales has proven to be difficult because of its lack of ground resolution. Furthermore, severe difficulties in feature extraction and height determination from SPOT stereo imagery have also been encountered, arising from the images having been taken in different seasons.

Besides SPOT, other pushbroom scanners employing CCD linear array sensors have been placed in orbit during the early 1990s - notably the JERS-1 OPS in 1992, MOMS-02 in 1993 and IRS-1C in 1995. These have not achieved the production status of SPOT but they have allowed photogrammetrists to investigate alternative configurations of satellite-based linear array technology.

There has only been a small amount of photogrammetric research into the mapping possibilities of the Japanese JERS-1 OPS system, but, on the basis of this limited work, and given its poor base-to-height ratio (0.3) and its poor object detectability (near 50m), it seems unlikely that this system can really meet the requirements for medium scale map compilation.

MOMS-02 with its along-track stereo geometry overcomes many of the difficulties experienced with the SPOT cross-track stereo imagery (e.g. those arising from the images having been taken in different seasons, etc.). MOMS-02 was operated from the Space Shuttle on an experimental test basis for just 10 days and its coverage is limited to the area between latitudes 28.5 degrees North and South. However, its geometric capabilities and its potential for mapping including its feature detectability are matters that are still under very active investigation. MOMS-2P is the continuation of the MOMS-02 program, the imager having been refurbished and installed into the PRIRODA module of the Russian MIR space platform in the summer of 1996. However, at the time of writing, it is still not operational.

The imagery from the Indian IRS-1C satellite is new on the market and has not yet been tested. Indeed it is only just becoming fully operational. With its similar geometry and somewhat improved ground resolution to that of SPOT imagery, it is expected to provide

more or less the same mapping capability as SPOT, but this is a matter which has still to be proven.

In general terms, since the geometry of this type of imaging device is quite different to that of conventional photogrammetry based on the use of photographic frame cameras, a quite different mathematical model has to be established in such a way to cope both with the dynamic nature of this type of image as well as the quite different ways that can be used to capture the stereo images required for full topographic mapping.

1.2.3 Problems of Using SAR (Radar) Imagers for Photogrammetric Mapping

In general terms, apart from its use in the preliminary mapping at very small scales of tropical forest areas in South America, Nigeria and Indonesia during the late 1960s and 1970s from airborne platforms, little use has been made of SAR imagery for topographic mapping in spite of the apparent advantages of its all-weather and day and night imaging capabilities. This is due to the shortcomings of the imagery in terms of :

(i) its background clutter or speckle;

(ii) the foreshortening, layover and shadowing experienced in areas of high relief;

(iii) the extreme variability in the detection of ground features, which is so highly dependent in the orientation of the object with respect to the look direction of the sensor.

Currently a great deal of attention is being paid by the remote sensing community to the revival of an old technique - radar interferometry - originally developed for use from airborne platforms in the early 1970s. This is based on the combination of two SAR data sets to provide information, via interferometric techniques, on the height differences existing on the ground. In spite of a huge research effort, till now, no results have been published to confirm that the heights and contours produced by satellite radar-interferometric methods do indeed meet the accuracy standards and specifications for 1:50,000 and 1:100,000 scale topographic maps (Petrie, 1994).

1.2.4 Comparison of the Different Satellite Imaging Systems in the Context of Topographic Mapping

Comparing these different types of sensors (i.e. frame-type imagers, line-type imagers, and SAR imagers) from a photogrammetric point of view within the specific context of topographic mapping results in the significant advantages of pushbroom scanners equipped with CCD linear arrays becoming apparent. These advantages are:

(i) the digital nature of their output in comparison with that derived from photographic systems;

(ii) their better geometry and resolution in comparison with the imagery derived from mirror scanning systems; and

(iii) their superior cost and performance in comparison with digital area sensors.

These advantages have caused photogrammetrists to investigate closely this type of imager. All future satellite imaging programs based on the use of optical scanners, such as the forthcoming American commercial Earth observation systems, are planned to use pushbroom imaging devices to produce stereo satellite imagery in both along-track and cross-track configurations with 1 to 2m ground resolution. Till now, although considerable research has been carried out (both in terms of mathematical modelling and in tests of accuracy for medium scale topographic mapping) using the cross-track stereo images produced by SPOT, research into the corresponding aspects of along-track stereo imagers has only got under way recently with the availability of the MOMS-02 stereo imagery. However, it is imperative that a suitable mathematical model be devised which will fit properly to cross-track as well as along-track stereo images prior to its implementation and use in a computer program for the geometric evaluation of these types of imagery and their operational use in photogrammetric systems.

1.3 Research Objectives

Having described the importance, problems and possibilities of photogrammetrically based mapping from space images, this thesis identifies the main objectives of this research into

the realisation of such a possibility. The purpose of this research is to devise a mathematical model for the geometry of both along-track and cross-track linear array images and for the new class of imaging sensors with flexible pointing which will become available shortly via the forthcoming American commercial Earth observation systems. This generic model then needs to be implemented in a program which will allow tests to be carried out on the geometric accuracy of along-track as well as cross-track linear array imagers in two and three dimensions for medium scale topographic mapping. In this context, the main research objectives can be defined as follows:

1. Three-dimensional mathematical modelling of different types of satellite stereo linear array imagery;

2. Implementation of these models, as well as a simpler mathematical model for two-dimensional mathematical modelling, in a general adjustment program;

3. The testing of different kinds of mono and stereo linear array images taken from space using the adjustment program to evaluate the capability of mathematical model, the applicability of the adjustment program, and the geometric accuracy attainable with these images; and

4. Evaluation of the geometric potential of stereo linear array images to produce medium scale topographic maps.

The first two objectives form the major part of this research and, if they can be satisfied, then they will allow different types of satellite linear array imagery to be tested and evaluated regarding both their geometric accuracy and their potential for producing medium scale topographic maps. The mathematical model must be established in such a way as to be able to handle along-track, cross-track and flexibly pointed stereo linear array images in a satisfactory way. Thus it must provide a very good mathematical relationship between the image space and the object space (in this case, the ground). To satisfy these requirements, certain exterior orientation parameters need to be provided for the modelling. Till now, several types of mathematical model have been developed for use with this type of imagery, but inevitably most of them have been devised by various investigators for use only with SPOT stereo images as a case of cross-track linear array imagery. These mathematical

models can be classified into four groups:

(1) Orbital parameter models: in which a mathematical model is developed based on the motion of the satellite within a defined orbit and uses the Keplerian elements to model the geometry of the image taken by the linear array imaging system.

(2) Multiple projection centre model: in which a mathematical model is developed based on the change of the position of the projection centre of the imaging system in space continuously as the spacecraft moves. It is usual to try to model these changes with a suitable polynomial transformation.

(3) Additional parameter model: in which the mathematical model is based on the conventional photogrammetric model employed with frame-type imagers using just a single projection centre for each scene. Then the distortions existing on the image arising from its pushbroom geometry are modelled through the use of additional correction parameters.

(4) Direct linear transformation model: in which the direct linear transformation model that is used extensively in close-range photogrammetry - which tries to relate the pixel coordinate system in image space directly to the ground coordinate system on the ground - is used with linear array scanner imagery.

All of these models, except the fourth one, use the well known collinearity equations of analytical photogrammetry in their solution. The direct linear transformation model is in fact an extension of these collinearity equations. These will all be investigated and analyzed regarding their suitability for use with satellite linear array imagery.

Since it is intended that the adjustment program can be handled easily by users, so it was decided the program should be written for use on a PC utilising the Windows operating system. The C++ programming language has been chosen for this purpose because it can be implemented easily within the Windows environment.

1.4 Outline of the Thesis

This thesis has been structured as follows. Chapter 2 outlines the essential characteristics that a satellite image should have if it is to be used for photogrammetrically-based topographic mapping. It also reviews the standard specifications regarding the accuracy and content of medium scale topographic maps. Chapter 3 presents an overview of the development of linear array imaging systems. It also conducts a discussion on the more important devices from the photogrammetric point of view. Chapter 4 describes the available mathematical models for the two-dimensional correction of linear array images. Chapter 5 first reviews some well-known mathematical models which have been developed by different researchers. A critical discussion of these different models then follows. The chapter then presents the three-dimensional mathematical modelling and solution for the geometric correction of cross-track linear array stereo images devised by the present author. Chapter 6 deals with the mathematical modelling of along-track linear array images in three-dimensions developed by the present author. It also reviews and discusses the different methods which have been developed by other researchers. Chapter 7 presents the general adjustment program developed by the present author for both the two and three dimensional modelling of linear array imagery. Chapters 8 and 9 deal with the extensive series of experimental tests of geometric accuracy which have been carried out on different linear array images using the adjustment program written by the present author. It also compares and discusses the results of this research with those published recently by other researchers. The capabilities of the mathematical model and the associated adjustment program and the geometric accuracy of linear array images have also been discussed in these chapters. In Chapter 10, a much wider analysis is carried out which evaluates the geometric potential of linear array images for producing topographic maps at medium scales. In Chapter 11, the extraction of the features using linear array satellite images for medium scale topographic mapping is reviewed and MOMS-02 imagery is evaluated and discussed with regard to its capability to provide the specific features and the information content which are required for mapping at these scales. Finally Chapter 12 summarises the overall results of this research work and gives recommendations for future work.

CHAPTER 2 : PHOTOGRAMMETRIC MAPPING FROM SPACE

2.1 Introduction

The space era began three to four decades ago with the launch of Sputnik I, the first artificial Earth satellite, by the Soviet Union in 1957. Within a short time span, numerous exciting events unfolded including the first orbital flight over the Earth by man. Then, in July 1969, under the insightful eye of the TV camera, the world viewed man landing on the surface of another planetary body - the Moon. By 1996, the international space community had launched more than 3,000 satellites from different sites around the globe. In the field of communications and broadcasting and in meteorology, satellites have become operational tools. Starting with Landsat in 1972, remote sensing satellite systems have promoted the discipline itself and satellite remote sensing images have found applications in many disciplines. One of these application areas is the field of topographic mapping. Compared with most other remote sensing applications (e.g. in agriculture, forestry, geology, hydrology), which need low or intermediate spatial resolution, cartographic applications require high spatial resolution in order to discern the transportation network and the finer features present on the terrain which need to be presented on topographic maps. Also a stereo-viewing capability is required in order to measure the third dimension and to generate accurate information on terrain relief and land forms. Having regard to these requirements, only a few satellite imaging systems can be qualified as cartographic satellite systems.

In the first section of this chapter, the advantages of carrying out photogrammetric operations from space as compared with traditional methods are discussed. In the second section, the characteristics of space image systems for mapping are described. These include the geometric quality of a topographic map; photogrammetric considerations when carrying out mapping from space; the image resolution required for mapping, and the determination of sensor position and attitude in space.

2.2 Justification for Photogrammetry from Space

For a long time, terrestrial field survey and conventional photogrammetry using aerial photographs have been the main methods used to generate the data required for topographic mapping. In view of their relatively slow speed of production and high costs, the classical field surveying methods are limited to small areas, which eliminates this method for serious consideration in the context of national or world-wide production and revision of maps. For the task of producing and revising maps at large and medium scales, conventional photogrammetry based on the use of aerial photographs is the only acceptable method of obtaining the data required for maps within a reasonable time frame and cost. However, it is most important to realize that, even when based on such a method, no topographic mapping with any claim to usefulness and reliability can be carried out without a certain amount of field survey work to establish ground control; to collect the names and information on boundaries (which form an integral part of a topographic map); to classify features that cannot be identified on the photograph; and to complete the mapping of those features which are obscured by vegetation, buildings or shadows. This field survey component may only amount to 5% of the total effort involved in a mapping project but the information which it provides is the vital ingredient which makes the map a reliable and acceptable product to the user (Petrie 1985).

Even then, the global demand for topographic maps at smaller scales such as 1:50,000 and 1:100,000 scale, which are those necessary for the efficient planning of resources on a regional or national scale, cannot be fulfilled easily using traditional aerial photogrammetric methods. Indeed, the progress of map production and revision by this method is still too slow, having regard to the demands of users for up-to-date topographic information. According to the statistics which have been presented at the UN Cartographic Conference in Beijing in May 1994 (Table 2.1), 65% of the land area in the world is covered by topographic maps in the scale range of 1:50,000, while this survey also showed a coverage of only 33.5% for 1:25,000 topographic maps. The world map updating progress for areas already mapped amounts to 4.9% for the 1:25,000 scale and 2.3% for the 1:50,000 scale (Konecny 1995). However, it should be noted that Table 2.1 is simply a statistical report of

the existing topographic map coverage at medium and small scales compiled by the United Nations.

Table 2.1 Status of World Topographic Mapping 1993

Area	% in 1:25,000	% in 1:50,000	% in 1:100,000	% in 1:250,000
Africa	2.9	41.1	21.7	89.1
Asia	15.2	84.0	66.4	100
Australia and Oceania	18.3	24.3	54.4	100
Europe	86.9	96.2	87.5	90.9
North America	45.1	77.7	37.3	99.2
South America	7.0	33.0	57.9	84.4
Former USSR	100	100	100	100
World 1993	33.5	65.6	55.7	95.1
World 1987	17	59	56	90
Annual Progress 1987-1993	2.8	1.1	0	0.9
Map Updating Progress 1987	4.9	2.3	0.7	3.4

A more detailed analysis of the topographic maps at these scales for Africa is given by Petrie (1996). Based on this evaluation, it is highly doubtful that comprehensive mapping at 1:50,000 scale is required, since so many of the countries in Africa have enormous areas of desert or semi-arid land with little or no population and few cultural (i.e. man-made) features. In which case, comprehensive mapping at 1:50,000 scale is either unnecessary or, if implemented, is overkill. According to Petrie (1996), the result is that many African countries have adopted a dual scale strategy for their topographic mapping. For example, many of former British ruled territories, e.g. in Kenya, Zambia and Botswana, have adopted 1:50,000 as the basic scale for mapping in their more populous and developed regions and either 1:100,000 or 1:125,000 scale for the more remote and arid or mountainous regions. Similarly, in the former French-ruled territories, 1:200,000 is the standard scale for the mapping of their large sparsely populated areas and 1:50,000 scale mapping is confined to the smaller areas of developed land. Thus the UN figures have to be treated with some caution and understanding. However, notwithstanding these remarks, still there are some countries (e.g. Sudan) which suffer both from a lack of topographic maps for most of their area even at their standard 1:100,000 scale and from a lack of revision of those maps that are available.

What is the solution in order to meet the world-wide demand for maps? Can the use of

satellite imagery provide at least part of this solution?

For nearly three decades, researchers have considered satellite imagery as a solution for these problems. Even prior to the launch of Landsat, Petrie (1970) had pointed out some obvious economic advantages of space imagery for mapping. These are the reductions in cost and the saving in time for mapping a large area at small scales by these images through replacing numerous aerial photographs by a single space photograph. Light et al., (1980) has shown that a spacecraft orbiting at 200km altitude and carrying a metric camera equipped with an f = 300mm lens camera could photograph an area of 10,800 km^2 in a single exposure. Only one stereo model and 3 control points would be needed to carry out small scale mapping from such photographs. The point is that photography from orbital altitudes covers more ground per photograph and therefore requires fewer ground control points. Leatherdale (1978) also described the reduction of the density of geodetic control points needed to achieve reasonable map accuracies. However the negative side of this discussion about space images is that the increase in the terrain area covered by an individual image leads to a decrease both in the photographic scale and in the ground resolution of the image and therefore to difficulties in the interpretation and extraction of features from the images.

Another significant advantage of space image systems is that they are moving along a well defined orbit. Sophisticated orbital models derived from the satellite ephemeris are a possible source for the determination of the exterior orientation parameters. Their use could reduce the number of control points required or, in the case of them not being accurate enough, they can provide a good approximation or starting values for these parameters in a bundle adjustment program. These potential advantages of space imageries for mapping have made photogrammetrists investigate and test the different types of satellite images available for topographic mapping.

2.3 The Essential Characteristics of Space Imagery for Mapping

Basically a topographic map contains three kinds of topographic information concerning:

(i) content, (ii) position, and (iii) elevation. The content comprises the features represented on the map either by points, lines and areas using symbols or colours or by the actual image itself. Position, the second type of information, relates the locations of the features shown on the map to a national or global geodetic reference system. For most mapping systems, positional information is provided by referencing images or stereo-models to known ground control points. Elevation, the third type of information, is shown principally on topographic maps by means of contours which are derived primarily from stereoscopic coverage acquired by the sensor. The datum for the topographic elevation values is usually established by reference to mean sea level.

The remainder of this section outlines the essential characteristics that a space system should exhibit in order to serve both topographic mapping and those other applications that rely on photogrammetry. It also aims to cover the requirements and factors involved in producing topographic maps. In this context, depending on the information (content, location, and elevation) that has to be included in a topographic map, different factors, such as ground resolution, planimetric accuracy, contour interval, and spot height accuracy, must be considered. With respect to the special importance of ground resolution in mapping from space, this factor is investigated in detail in Section 2.3.3.

2.3.1 Geometric Quality of a Topographic Map

The planimetric accuracy of a topographic map is best evaluated by finding the errors at a number of individual well-defined points on the map whose positional coordinates are known accurately, and then judging the result against a standard specification set by the mapping authorities of the country for which the map is being produced. The required accuracy for planimetric position specified by the U.S. National Map Accuracy Standards (NMAS) is defined by 90% errors, e.g. 90% of the well-defined features on the map shall be within ± 0.5mm of their correct position at 1:50 000 scale. These can be expressed in terms of standard errors as: *Positional data* σ_p = *0.3 mm* × *map scale number*. For elevation accuracy, U.S. NMAS states that "when tested, not more than 10% of the elevations shown by contours shall be in error by more than one-half the contour interval" (Marsden 1960).

This is equivalent to a standard error of: "Elevation $\sigma_e = 0.3 \times C.I.$ (contour interval)".

The required accuracy of the spot-heights included in a topographic map, is usually about one-fifth to one-eighth of the required contour interval (Tham, 1968). The contour interval that is actually used on a specific map depends on the standards set in each country for a specific map scale and on the character of the land forms and relief present on the terrain. According to Ghosh (1987), the most used contour intervals at each of the commonly used map scales for topographic mapping are as given in Table 2.2.

Table 2.2 Contour Intervals and Map Scales

Map Scale	Contour Interval (m)
1:5,000	2, 5
1:10,000	2, 5, 10
1:20,000	5,10
1:50,000	10, 20, 40
1:100,000	20, 50

2.3.2 Geometric Considerations in Mapping from Space

The photogrammetric methods used in mapping from space imagery can be divided into two sub-categories. These are planimetric (two-dimensional) mapping, in which only the horizontal geometry of the object is rectified for applications such as topographic map revision and image map production; and topographic (three-dimensional) mapping, in which data in all three dimensions are generated, as required in the production of fully contoured topographic maps.

Due to the great distance from which the Earth is viewed from space, if an imaging device is equipped with a lens of a suitable focal length giving a limited overall field of view and is directed vertically at the Earth, it produces an image with a nearly orthographic projection which can be recorded and used directly for mapping if the ground has little relief. The resulting displacements from tilt which are present in the image can be corrected adequately with simple polynomial functions. Such a space image records the Earth's surface in an

approximately correct planimetric form and can be used successfully to produce a purely planimetric map or image map for areas of flat ground or those having a small range of elevations. The major considerations in purely planimetric mapping relate to the scale (f/H) and the ground resolution of the imagery.

However, if heights and contours have to be determined in areas having significant relief, then stereoscopic images are necessary. While scale and ground resolution are still very important, considerations regarding the use of stereoscopic images from space in topographic mapping are significantly different to those involved in purely planimetric mapping. In particular, they are related to the stereoscopic geometry of the imagery and especially to its base-to-height ratio. The scale and the base-to-height ratio are taken into account in the following standard formula for the determination of height differences from measured parallaxes using stereo images:

$$dh = (H/f).(H/B).dp$$

where

f : is the focal length of the space camera,

H : is the orbital altitude,

B : is the base,

dp : is the stereoscopic parallax,

dh : is the difference in height.

It is evident from the above equation that, for a given image scale, large base-to-height ratios are desirable to achieve good heighting accuracy. Consideration of the base-to-height ratio for different types of imaging systems depends on the geometry of the system which is used to acquire stereoscopic images of the terrain.

In the case of stereo SPOT pushbroom scanner imagery (which will be described in more detail in Section 3.5 and Chapter 5), the off-nadir viewing capability of SPOT makes it possible to obtain stereopairs of a given scene by acquiring cross-track images at different angles during different satellite passes on neighbouring orbital tracks. In which case, the base-to-height ratio depends largely on the viewing angles used. This relationship can be

shown as:

$$\frac{B}{H} = \tan\alpha_1 - \tan\alpha_2 \quad , \quad \alpha_i = \arcsin(\frac{r}{R_e}\sin\beta_i) \quad , \quad i = 1,2$$

where

α_1, α_2 : are the angles of incidence for the first and second scenes,

β : is the viewing angle,

r : is the distance of the SPOT satellite from the Earth's centre,

R_e : is the Earth's radius.

The use of the maximum viewing angles of ±27° for the two images of a SPOT stereo pair can result in images with a very good base-to-height ratio. If $\beta_1 = 27°$, $\beta_2 = -27°$, r = 7,205km , R_e = 6,370km, then: B/H = 1.19.

In the case of stereo MOMS-02, which is another type of pushbroom scanner capable of producing stereo imagery (that will be discussed later in Section 3.6 and Chapter 6), the B/H value is constant and equal to 0.8.

2.3.3 Resolution Required for Mapping

Resolution (or resolving power) is a measure of the ability of an optical system to distinguish between signals that are spatially near or spectrally similar. Sensor performance to support both topographic mapping and those other applications that utilize multispectral information should be concerned with three kinds of resolutions; namely, spectral, spatial, and radiometric. Spectral resolution refers to the dimension of and the number of specific wavelength intervals in the electromagnetic spectrum to which a sensor is sensitive. Spatial resolution is a measure of the smallest angular or linear separation between two objects that can be resolved by the sensor. The smaller the object detected, the higher the spatial resolution. Radiometric resolution defines the sensitivity of a detector to differences in signal strength as it records the radiant flux reflected or emitted from the terrain. It defines the number of just-discriminable signal levels; consequently, it may be a significant element in

the identification of scene objects. Of the above mentioned resolutions, spatial resolution is especially important to the topographic mapping community.

In photogrammetry, much of the terminology regarding resolution that is in widespread use has been developed around the use of photographic images. In this context, image resolution is a measure of the minimum distance between two close objects that can be distinctly discerned as two objects on the image. This definition of resolution is best represented in terms of the Modulation Transfer Function (MTF), but the use of MTF is somewhat impractical in production topographic mapping operations. Therefore a photogrammetrist generally relies on the resolution of an image in terms of line-pairs per millimetre ($R_{lp/mm}$) that it can resolve. In these terms, a resolution of n lp/mm means that a maximum of n pairs of alternating black and white lines can be imaged distinctly within a 1mm distance on a low contrast image. It is possible theoretically to obtain an image from space with any desired resolution, in ground terms, by selecting a lens with an appropriate focal length and resolution to produce the appropriate scale photography in conjunction with an appropriate photographic film. It is therefore desirable sometimes to express the ground resolution of a space photograph in terms of metres per line-pair ($R_{m/lp}$). The two resolutions are related together as:

$$R_{m/lp} = (\text{photo scale}/1000) / R_{lp/mm}.$$

In the case of an electro-optical system, spatial resolution refers to the pixel dimension, which is equivalent to pixel size for scanning sensors, and is denoted as ($R_{m/pix}$) in terms of ground pixel size. The pixel size is determined by the angular dimension of the Instantaneous Field Of View (IFOV) and the rate at which the detectors are sampled. IFOV is defined as the angle which corresponds to the sampling unit. The information contained within the area covered by the IFOV is represented by a single pixel in the image plane. The maximum angle of view over which a sensor can effectively detect the electromagnetic energy is called the Field Of View (FOV). In the context of the scanners, which are the class of imaging devices being dealt with in this dissertation, the coverage of the ground corresponding to the FOV is called the swath width.

A direct relationship exists between ground resolution of the sensor and the useful scale to which its images can be enlarged. For example, for electro-optical sensors, a sensible enlargement factor (M) can be approximated by the number of pixels per millimetre in the image plane divided by a number between 6 and 12 depending on the quality and contrast of the imagery (Light, 1989).

There is also a direct relationship between ground resolution and image scale number. This relationship has been described in Doyle (1984) and Light (1986a, 1986b and 1989). Doyle defined the following two formulas for photographic and electro-optical systems respectively:

$$S_m = 4{,}000\ R_{m/lp}$$

$$S_m = 10{,}000\ R_{m/pix}$$

where

S_m : is image scale number,

$R_{m/lp}$: is the ground resolution in m/lp,

$R_{m/pix}$: is the ground resolution in m/pixel.

The terms $R_{m/lp}$ and $R_{m/pix}$ are related through the Kell-factor of $2\sqrt{2}$ or $R_{m/lp} \approx 2.5\ R_{m/pix}$ (Naithani, 1990).

Light applied two different methods using different criteria to determine the appropriate pixel size of the sensor for mapping applications:

(i) The first method is based on printing criteria and the relationship between ground pixel dimension (m/pixel) and image scale, and is given by the relationship:

$$image\ scale = 11{,}806\ pixel\ size$$

(ii) In the second method, he utilizes the parallax equation from photogrammetry and other standard assumptions to determine the pixel size needed for topographic mapping as follows: *pixel size=0.3 (1/0.36) (base/height) CI*, where CI is the contour interval.

It can be seen from Table 2.3 that Doyle's method and the two methods devised by Light support each other and verify the concepts for estimating the pixel size or spatial resolution

required in a sensor system. It should be noted that in this Table in the second method of light, it is assumed base/height to be 0.6.

Table 2.3 Requirements for image map series

S_m	Doyle's method		Light's method (1)		Light's method (2)		C.I. (m)	σ_P (m)	σ_E (m)
	$R_{m/pix}$	$R_{m/lp}$	$R_{m/pix}$	$R_{m/lp}$	$R_{m/pix}$	$R_{m/lp}$			
100,000	10.0	25.0	8.5	21.25	10.0	25.0	20	30.0	6.0
50,000	5.0	12.5	4.2	10.50	5.0	12.5	10	15.0	3.0
25,000	2.5	6.3	2.1	5.25	2.5	6.3	5	7.5	1.5

In the above table, σ_P and σ_E are the standard errors for position and elevation respectively and are defined as follows:

$$\sigma_P = 0.3 \text{ mm} \times \text{map scale}$$

$$\sigma_E = 0.3 \text{ m} \times \text{C.I. (contour interval)}$$

where

S_m : is the scale number,

$R_{m/pix}$: represents resolution in m/pixel, and

$R_{m/lp}$: is resolution in m/line pair.

It must be noted that the reliable identification of the cultural features such as roads, railroads and buildings, that are normally shown on line maps at any scale, requires a ground resolution of 2 to 3 m/lp or better than 1 to 2 m/pixel. If the sensor used for image mapping does not provide this level of resolution, cultural features will not be adequately represented unless they are derived from field completion using ground survey methods or other source material.

2.3.4 Sensor Position and Attitude

The vehicle or carrier in which remote sensor devices are borne is usually called the platform. Typical platforms are satellites, the Space Shuttle and aircraft, but they can also include radio controlled airplanes, balloons, kites for low altitude remote sensing, as well as the use of ladder trucks or "cherry pickers" for close-range investigations.

In the case of either the Space Shuttle or a satellite, after its separation from the carrier rocket, the space platform begins its passage over the Earth, in a defined orbit inwhich the orbital plane must pass through the Earth's centre. While the platform moves rapidly over the Earth at 6 to 8 km/sec, its surface is being imaged continuously or at intervals by the imaging system. The coordinates of the projection centres of the images and the attitude of the imaging system depend on the position, velocity and altitude of the platform in its orbit. Consequently, if the orbit can be defined precisely, then the exterior orientation parameters of the images taken by the sensors will be known and the need for ground control points can be largely reduced or even eliminated. Although such a precise ephemeris is not available at the present time, the recovered values can be still used as starting values for the exterior orientation parameters to be used in a bundle adjustment program.

2.3.4.1 Determination of the Sensor Position, Altitude and Attitude

The positioning and the determination of the altitude and attitude of a spacecraft form substantial parts of the navigation of the spacecraft. Navigation may be described as a feedback loop whose aim it is to direct the movement of a craft, expeditiously and safely, from one point to other (Vanicek and Krakiwsky 1986). The most important contribution of navigation to space photogrammetry is to support the orientation and triangulation of the overlapping stereo imagery. At the present time, the possible navigation techniques that are useful for space photogrammetry are:

- the measurement of the position and height of the spacecraft by the Tracking and Data Relay Satellite System (TDRSS).
- onboard measurement of position and attitude during the image acquisition phase using an Inertial Navigation System (INS).
- onboard measurement of position and attitude during the image acquisition phase using the Global Positioning System (GPS).
- the integration of GPS with INS.

Sophisticated orbital models derived from the ephemerides may also give useful information to photogrammetrists.

At the present time, the GPS and INS systems can now be contemplated for use on board spacecraft. Thus, when it is carrying the MOMS-2P scanner, it is planned to use both the GPS and INS on board the Russian MIR space station. The position and attitude of the future SPOT 4 and 5 programmes will also have navigation data provided by GPS and INS. The future American space imaging systems will also use the position and the attitude data coming from INS and GPS which is provided onboard their platforms.

In the next Chapter (3), the development of linear array imaging systems as an appropriate space imaging system for photogrammetric applications is discussed.

CHAPTER 3 : DEVELOPMENTS OF LINEAR ARRAY TECHNOLOGY FOR PHOTOGRAMMETRIC MAPPING FROM SPACE

3.1 Introduction

From the geometric or photogrammetric point of view, the imaging systems used in the different space and aerial missions can be classified into three main groups:

(i) frame-type optical imagers, (such as photographic frame type cameras, television cameras, CCD areal array cameras and video frame scanners) where the image is acquired simultaneously over the whole of the imaging frame via a projection lens to produce a perspective view of the object from a single exposure station;

(ii) line-type optical imagers (such as optical-mechanical scanners and pushbroom scanners) which produce a single continuous strip image sequentially through the forward motion of the platform; and

(iii) side-looking radar, in which a narrow beam of microwave radio energy is sent out from the platform by a transmitter equipped with a directional antenna and a receiver captures the reflected radio waves and measures the elapsed time between the emitted and reflected signals. These are converted to ranges and result in the production of an appropriate and distinctive image.

Among all these different types of sensors, pushbroom scanners equipped with linear array sensors have been used and investigated widely by photogrammetrists. This arises from the various favourable characteristics of this type of sensor such as their digital nature, their good geometry and resolution, and their cost and performance.

3.2 Linear Array or Pushbroom Scanner Systems

In its simplest configuration (Figure 3.1), the linear array imager consists of a linear array of detectors located in its focal plane.

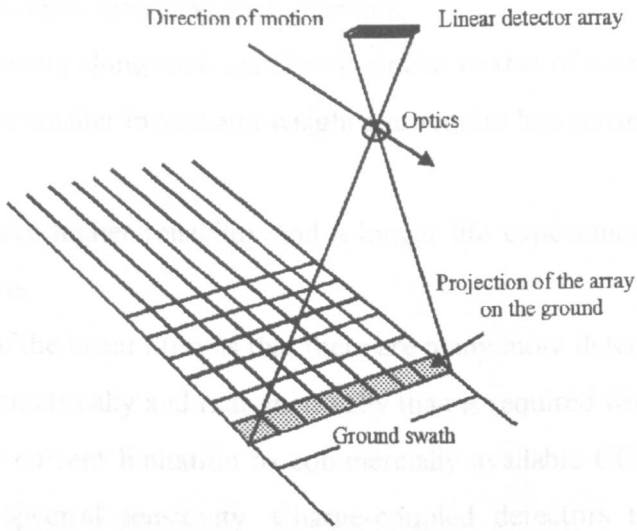

Figure 3.1 Pushbroom scanner or linear array system

The projection of the linear array onto the ground forms a very narrow rectangle with its long side oriented perpendicular to the projected line of flight. The linear array is read out such that one complete line of data is generated each time this projected field of view advances by one line. Thus the motion of the platform or satellite provides the along-track scan of the imaging sensor (hence the designation pushbroom scanner) while the cross-track scan is accomplished by the readout of the linear array. This linear array of detectors normally consists of numerous Charge-Coupled Devices (CCDs) positioned end to end. As illustrated in Figure 3.1, each detector element (pixel) is dedicated to sensing the energy in a single ground resolution cell along any given scan line. The data for each scan line are generated electronically by sampling each element along the array (thus eliminating the need for a scanning mirror). The size of the individual detectors comprising a linear array, together with the focal length of the imaging lens, determines the size of each ground element corresponding to a single pixel. With multi-spectral pushbroom scanners, each spectral band, or channel, of the sensor requires its own linear array and its own optical filter.

The use of linear arrays has obvious advantages over mirror scanning systems:

(i) in that they can provide a better spatial and radiometric resolution;

(ii) their geometric integrity is greater because of the fixed relationship between the

detector elements recording each scan line;

(iii) the geometry along each scan line is similar to that of a aerial mapping camera;

(iv) they are smaller in size and weight and require less power for their operation; and

(v) they have higher reliability and a longer life expectancy since they have no moving parts.

One disadvantage of the linear array is that there are many more detectors to be accurately calibrated both geometrically and radiometrically than is required with optical mechanical scanners. Another current limitation to commercially available CCDs is their relatively limited range of spectral sensitivity. Charge-coupled detectors that are sensitive to wavelengths longer than the near infrared are not readily available.

3.3 Historical Development of Pushbroom Technology

The first pushbroom imaging system was the continuous-strip camera known as the "Sonne Camera", which was first used in 1932. The idea of using this type of camera in aircraft came from General Goddard of the U.S. Air Force. It was further developed prior to World War II and used operationally for low-altitude, high-speed reconnaissance both during and after the War. An example is the U.S. Air Force's KA-18A strip camera, developed during the 1960s and manufactured by Chicago Aerial Industries. The use of continuous strip photography for reconnaissance purposes has been published by Goddard (1951); Katz (1951); and Ockert (1960).

At first sight, the appearance of a strip camera resembles that of a frame camera; however, its focal plane frame is limited to a narrow slit, oriented normal to the direction of flight. Consequently, as the platform moves over the area of interest, only a small portion of the film, corresponding to the area of the slit opening, is exposed at any instant. Then a long continuous strip image is formed by integration of the successively exposed narrow strips of terrain on to the photographic film (Figure 3.2).

Stereo coverage may be achieved by using a camera equipped with two lenses with their

optical axes decentred with respect to the slit, the one slightly ahead, the other to the rear. Consequently, one of the lenses photographs an object before the aircraft passes over it, while the other exposes its image after the passage of the aircraft (Figure 3.3).

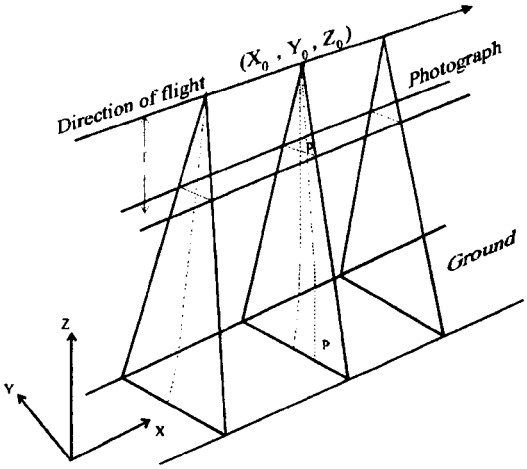

Figure 3.2 Geometry of strip photography

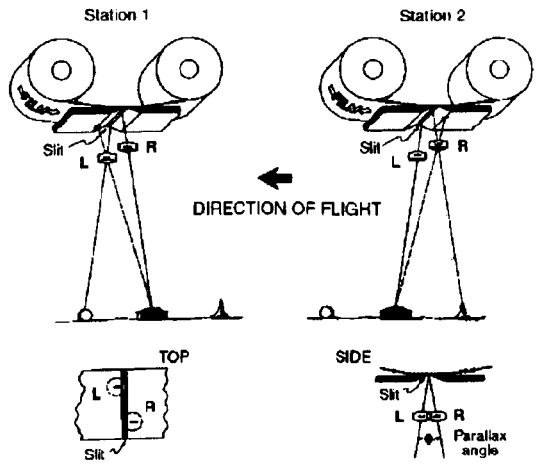

Figure 3.3 Plan and side views of the Sonne camera. The stereo coverage is achieved in the direction of flight by off-setting the lenses, with one forward-looking and one backward-looking.

However, very little has been published in the 1950s and 1960s, regarding the possibilities of carrying out mapping using strip camera images. The first investigation into measuring the terrain height with a stereoscopic continuous strip camera was done by Katz (1952). Elms (1962), also published a paper about the strip camera concept and mapping from strip photography. According to Masry (1969), this lack of interest was due to the dynamic mode of the strip camera which resulted in a strip photograph with exterior orientation parameters continuously varying along the strip. This made photography of this type much more complicated and difficult to use for mapping than conventional photography. It could be said too that there were no photogrammetric instruments available at that time which could be used for the continuous determination of these parameters with a sufficient degree of accuracy and which could handle the imagery with a view to map production.

However, developments and improvements in photogrammetric equipment made investigators think seriously of the possibilities of utilising strip photography for mapping.

For example, computer-based analytical plotters made the calculation of image and model coordinates and plotting from continuously variable parameters possible. Also, instruments such as the laser gyro, gave the possibilities of determining the attitude of the camera at short intervals. These developments renewed interest in this type of photography and a detailed analysis of the geometry of strip photographs in comparison with those of other imaging systems was published by Konecny (1971,1972). The analytical treatment of stereo strip photographs has also been investigated by Case (1966), Masry (1969) and Derenyi (1973).

With the development of solid state linear arrays, which involve no moving parts, strip cameras began to be replaced by this new type of sensor. The rapid development of these solid state sensors and the digital images that resulted from them for military reconnaissance purposes also made scientists think seriously of using these imagers in space. Linear arrays also brought to mind the possibility of automated mapping of the Earth from space in three as well as two dimensions, since the image data could be transmitted directly back to the Earth from a satellite.

In the 1970s, experiments using linear array systems were conducted by Messerschmitt-Bolkow-Blohm (MBB), now Deutsche Aerospace AG (DASA), and resulted in the first images being taken from the air by the single-line pushbroom scanner EOS in 1978. Almost certainly these had been preceded by American developments carried out for military reconnaissance purposes. Indeed a number of American reconnaissance satellites pioneered this technology, though few details are known.

In 1977, a serious effort to define a civilian stereo-imaging satellite was undertaken by the American space agency NASA and by the US Geological Survey (USGS) (Colvocoresses, 1979). By combining the technology of linear arrays, the concept of epipolar plane scanning, and the experience gained from Landsat and other space imaging systems, MAPSAT was defined by the Itek Corporation for the USGS in 1981 on the basis of along-track stereo-imaging. It was to be equipped with three linear array systems - a vertical (nadir) sensor and two inclined (forward and backward looking) sensors, each of which would be set at ±23

degrees from the vertical (Figure 3.4). The use of the forward and backward images would provide stereo images with a base-to-height ratio of approximately 1.0, while the use of the vertical with either the forward or backward images would still provide a base-to-height ratio of about 0.5.

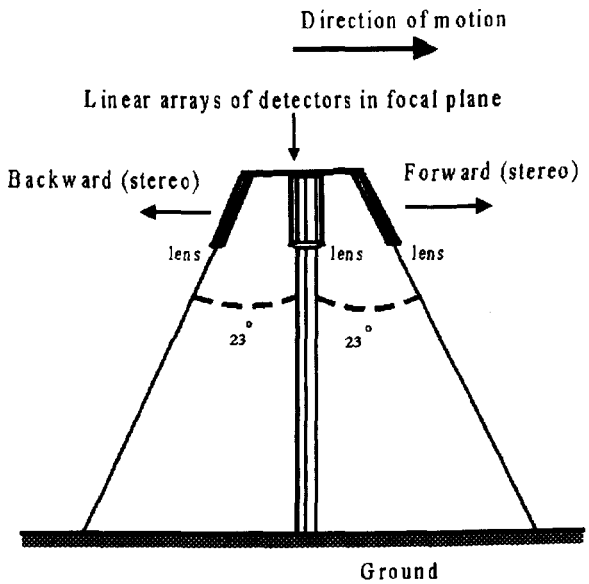

Figure 3.4 MAPSAT sensor configuration

At the same time as MAPSAT, another similar project named Stereosat was initiated by the Jet Propulsion Lab (JPL) and funded by NASA (Welch, 1981). This also proposed a satellite mission capable of producing stereoscopic coverage of the Earth's surface with three linear array imaging systems. However, the MAPSAT and Stereosat projects could not find financial backing and were not implemented.

In Germany, after the successful demonstration of EOS as an airborne imaging system in 1978, the German Federal Ministry of Research and Technology (BMFT), ordered the development of a pushbroom scanner, the Modular Optoelectronic Multispectral Scanner (MOMS), for the purpose of producing images from the Space Shuttle. MOMS-01 was orbited twice in 1983 and 1984 (Bodechtel et al., 1986). In both of its experimental missions, it was used to acquire monoscopic images only. Therefore this system did not allow a 3D photogrammetric object reconstruction. To extend the system's capability, German scientists took up the idea of the three-line array. Two ideas for using three line

scanners have been developed in Germany:

(1) With the first of these, the forward, nadir, and backward pointing images are acquired using three separate optical systems with three different focal planes much as with the MAPSAT proposal (Figure 3.4).

(2) The second approach has involved the use of three parallel linear arrays located at the focal plane of a single optical system such that light rays having an angle of incidence α come to focus onto array lines A and C, while those coming from the nadir direction are focused on array line B (Figure 3.5).

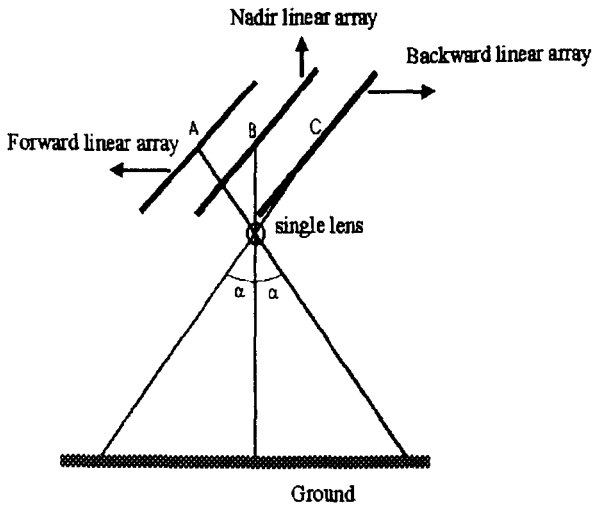

Figure 3.5 Configuration of three line scanners utilizing a single lens

The former arrangement has been used for MOMS-02, while the latter has been applied in other systems named MEOSS (Monocular Electro-Optical Stereo System) and the airborne Digital Photogrammetric Assembly (DPA) scanner. In all of these systems, the stereo images are taken along-track. MEOSS was launched on an Indian rocket in 1988. However, the launch was unsuccessful. After that, an airborne version of MEOSS was put into operation. Again, in 1993, MEOSS was launched by another Indian satellite, but again it was lost (Heipke et al. 1994). The DPA is currently operating from an airborne platform (Muller et al. 1994).

In 1980, France also began serious research into developing a satellite program using linear array technology. The French Centre National d'Etudes Spatiales (CNES) developed the

Systeme Probatoire d'Observation de la Terre (SPOT) which has been designed not only to produce monoscopic images but also cross-track stereoscopic images. These use pointable linear array systems referred to as the High Resolution Visible (HRV) sensors. In 1986, SPOT-1 was launched and became the first operational civilian Earth observation satellite system using pushbroom scanners. Since then, two further satellites in the SPOT series have been placed in orbit. In its optimal stereo-mode, it can produce stereo images with a good base-to-height ratio of 1.0.

In 1988 and 1991 respectively, India launched its first two operational remote sensing satellites, IRS-1A and IRS-1B. Both of these satellites carry three pushbroom scanners based on CCDs, designated Linear Imaging Self Scanners (LISS) which produce monoscopic images only. In 1995, India launched its third operational remote sensing satellite, IRS-1C, also employing pushbroom scanners and allowing the acquisition of cross-track stereoscopic images.

In 1992, Japan launched its OPS pushbroom scanner on the JERS-1 satellite. This comprises 8 linear array sensors, each pixel having a rectangular 18.3m × 24.2m format in terms of ground coverage. This system is able to acquire along-track stereo images, but with a rather poor base-to-height ratio (0.3).

In 1993, MOMS-02 was operated from the Space Shuttle for just 10 days in an experimental test project and was able to acquire stereo images of certain parts of the Earth with a fixed base-to-height ratio of 0.8 (considering its forward and backward images). An operational MOMS-02 mission is planned as part of the Russian PRIRODA satellite programme starting in the summer of 1996.

In the USA, several commercial companies are planning to launch their high resolution pushbroom imaging systems into orbit. Six of them: EarthWatch Inc., the Orbital Science Corporation, Space Imaging Inc, GDE, Resource 21 and GER Corp. have announced that they intend to launch their systems from 1997 onwards (Fritz, 1996a, b, c).

3.4 MOMS-01

MOMS-01 was flown on an experimental basis on two of the Space Shuttle missions. The MOMS-01 imagery from the first of these missions was obtained during the seventh Shuttle flight in June 1983; during the eleventh flight in February 1984, further images were acquired. The missions were intended to verify the technical concept under space conditions and to prove the applicability of high resolution CCD data for geoscientific thematic mapping (Bodechtel et al. 1986).

The MOMS-01 optical system utilized the pushbroom principle with four linear solid state sensor arrays. The detector elements in each of these arrays were Reticon CCDs with 1,728 pixels per array (see Figure 3.6).

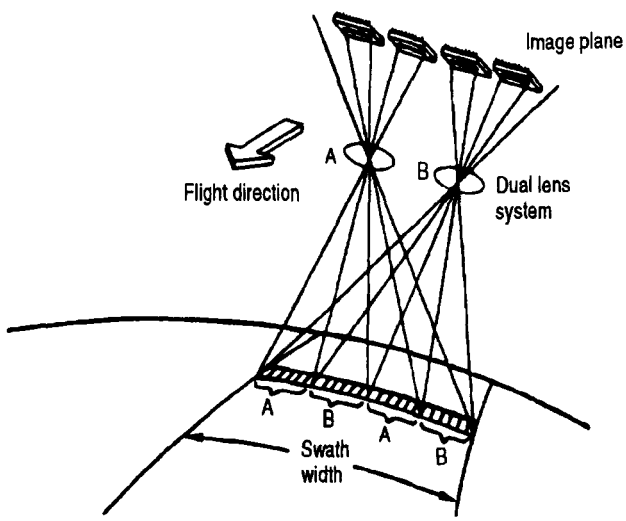

Figure 3.6 Geometric arrangement of the MOMS-01 optical system

The scan line extension beyond a single CCD array was achieved through the use of a dual lens system which allowed a line of 6,912 pixels, each 0.016mm wide, to be imaged simultaneously. The exposure time was identical to or smaller than the interval between imaged lines. The MOMS-01 data represented a 20×20m pixel size on the ground from an orbital height of 300km. Only monoscopic imagery could be acquired with the sensor and the image strip had a width of approximately 140km over the terrain.

During the two MOMS-01 space missions with a duration of 14 days, a total number of 26 image sequences were recorded, covering areas between latitudes 28.5° N and 28.5° S. The two missions fully proved the performance capabilities of the MOMS-01 concept. Thus the conditions for the development of an even more advanced system were met.

3.5 SPOT

SPOT-1 was launched on board an Ariane launch vehicle on 21st February 1986. SPOT-1 has a circular, near-polar, Sun-synchronous orbit with a nominal altitude of 832km and an orbital inclination of 98.7°. The payload for SPOT consists of two identical High Resolution Visible (HRV) imaging systems and their associated tape recorders. Each HRV sensor is designed to operate as a pushbroom scanner in one of two modes of sensing: either a 10m pixel size panchromatic (black and white) P-mode with a 6,000 element sub-array or a 20m pixel size multispectral (colour IR) XS-mode with 3,000 element sub-arrays. The optical system of the HRV sensor is a folded catadioptric telescope (Figure 3.7) with an equivalent focal length (f) of 1,082mm and an aperture of f/3.5. The reflected solar radiation coming from the Earth's surface is turned through 90° at the telescope entrance by a plane elliptical mirror, named the Strip-Selection Mirror (SSM). This mirror can be rotated to either side by ground command to provide a viewing angle up to 27° from the vertical in 0.6° steps (see Figure 3.7).

An HRV instrument is said to carry out oblique viewing when the absolute value of the viewing angle is greater than 7.5°. Using this off-nadir capability, both systems can be tilted to image areas up to 475km from the sub-satellite track. The swath width will then increase from 60km to 80km and the minimal revisiting time frame will be 5 days instead of the nominal 26 days (Figure 3.8).

Stereoscopic imaging is also possible arising from the off-nadir viewing capability of the HRV, which of course has great interest for the photogrammetrist (Figure 3.9). Over two consecutive days, the stereo-base-length is half the flight altitude. A base-to-height ratio of about 1.0 results from the use of the maximum tilt angles of ±27°.

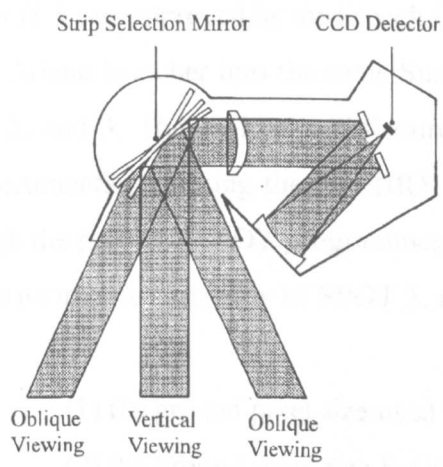

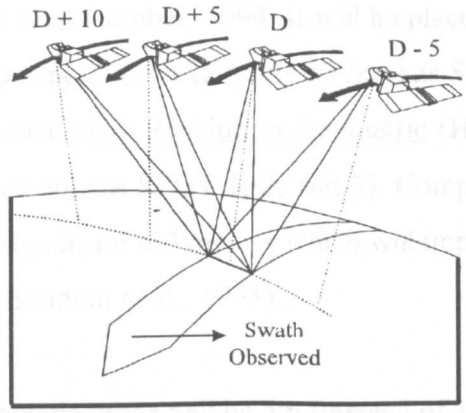

Figure 3.7 Oblique and vertical viewing of SPOT **Figure 3.8 Revisiting time frame of SPOT imagery**

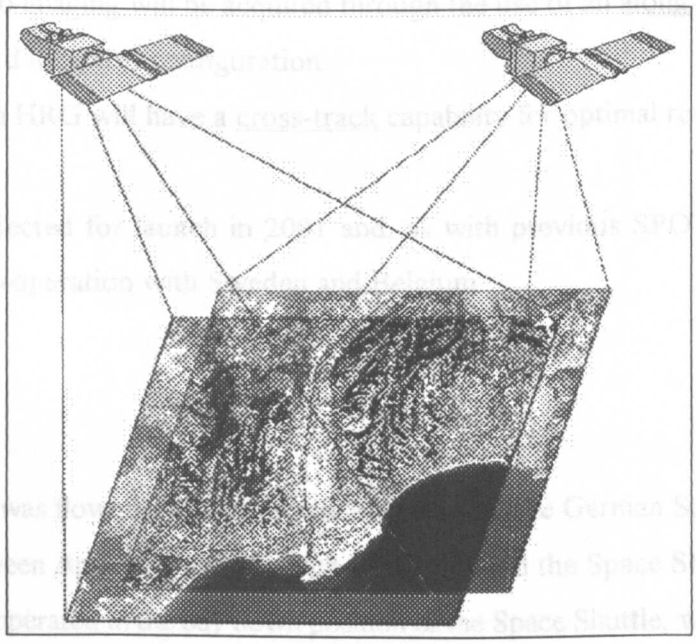

Figure 3.9 Cross-track stereo capability of SPOT imagery

3.5.1 SPOT, Future Prospects

SPOT 2 and 3, with the same characteristics as SPOT 1, were launched in January 1990 and September 1993 respectively. SPOT 3 continues its mission, although its on-board recorders have failed. SPOT 2 still acquires and transmits scenes in real time as a backup. SPOT 4, projected for launch in 1998, will have more or less the same imaging capabilities and geometric characteristics as the previous SPOT satellites.

SPOT 5 was approved by the French Government on 4 October, 1994. It will be placed by an Ariane launcher into the same Sun-synchronous polar orbit (altitude 830km) as SPOT 1, 2, and 3. The payload will feature three identical High Resolution Geometric (HRG) instruments (replacing the two HRV sensors used aboard SPOT 1, 2, and 3). Compared with the previous SPOT programmes, there are significant differences which will improve the geometric capability of SPOT 5, as follows (Baudoin et al., 1993):

(1) the ground pixel size used for panchromatic mode will be 5m (instead of 10m);
(2) the ground pixel size for its multispectral mode will include both 20m and 10m (instead of 20m for all three channels);
(3) stereo imaging will be acquired through the use of an along-track (forward and backward imagery) configuration.
(4) Each HRG will have a cross-track capability for optimal revisits.

SPOT 5 is projected for launch in 2001 and, as with previous SPOT satellites, will be developed in co-operation with Sweden and Belgium.

3.6 MOMS-02

The MOMS-02 was flown for experimental purposes on the German Spacelab D2-mission for 10 days between April 26th and May 6th, 1993 onboard the Space Shuttle mission STS-55. The system operated in the bay down position of the Space Shuttle, which had a nominal altitude of 296km and an orbital inclination of 28.5° resulting in the main test areas being located in Equatorial regions. During the 10 day period, 48 data takes were recorded.

The technical features of the MOMS-02 pushbroom scanners are oriented toward the requirements of the photogrammetric and thematic sciences. In order to be able to fulfil the different user requirements, a modular concept, which was already successfully proven by MOMS-01, was selected. The optical system consists of five lenses. Three of them are designed to provide along-track stereoscopic imagery using one nadir and two forward and backward looking lenses. The remaining two acquire the multispectral images in the VIS

and NIR range (providing four channels numbered Bands 1, 2, 3, 4). Figure 3.10 illustrates the MOMS-02 optical arrangement. The nadir-pointing central lens (Band 5), with a focal length of 660mm, acquires the highest resolution imagery with a ground pixel size of 4.5×4.5m from an orbital altitude of 296km and forms the core of the system. In order to obtain a sufficient swath width with such a high resolution, two linear detector arrays are joined optically to each other in the focal plane.

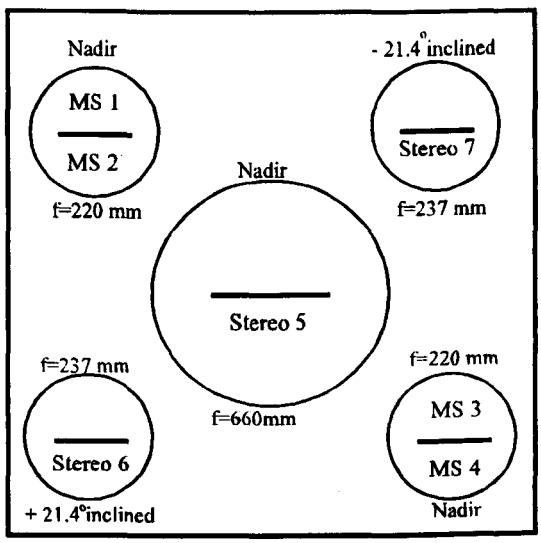

Figure 3.10 MOMS-02 optical arrangement

The two other stereo lenses (Bands 6 and 7), each with a focal length of 237.2mm, are inclined +21.4° and -21.4° respectively relative to the direction of the flight, which in combination with the central high resolution lens make it possible to get three-fold stereoscopic images. MOMS-02 provides a fixed base-to-height ratio of 0.8 when using the two forward and backward pointing lenses. The focal length of these lenses was selected as a way to obtain a 1:3 ratio for the ground pixel size of the high resolution (4.5m×4.5m ground pixel size) and the two tilted stereo channels (13.5m×13.5m ground pixel size).

The swath width for the high resolution channel is 37km, with 78km for each of the other channels. These values are relative to the nominal orbit altitude of 296km. Because of the viewing angle of 21.4° of each of the two stereo channels, the image swath on the Earth's surface for these channels is separated from the swath of the nadir channels by about 120km. Thus MOMS-02 takes corresponding stereo images at an interval of 40 seconds (see Figure

3.11) instead of waiting days, weeks or even months to obtain the second overlapping image as in the case of SPOT. So MOMS-02 can guarantee that no major changes will occur between the two recordings as a result of its exposure at another Sun elevation, during another time of day or even another season.

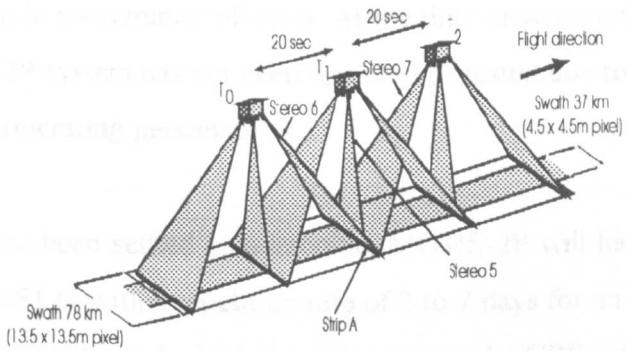

Figure 3.11 Stereo imaging principle of MOMS-02 Strip A is covered by stereo 6 from station T_o; stereo 5 from T_1; and stereo 7 from T_2

Figure 3.12 shows the total MOMS-02 imaging geometry, and the resulting ground track.

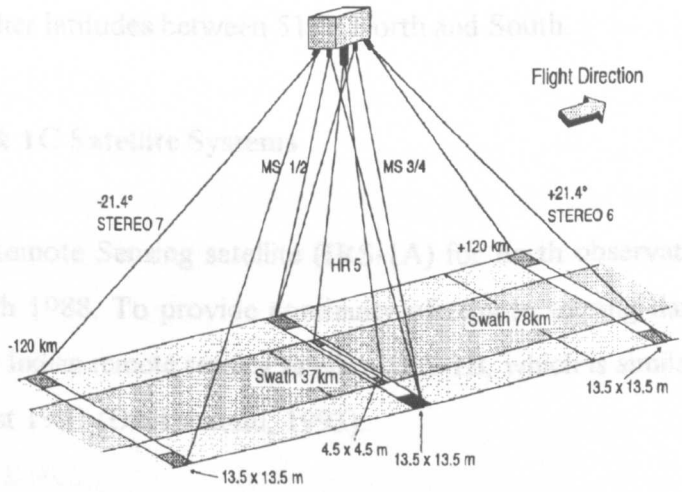

Figure 3.12 MOMS-02 imaging geometry from a single position in space

The remaining two other lenses, each with a focal length of 220mm, enable the multispectral imaging of a total of four channels. There are two sensors in the focal plane of each multispectral scanner, together with their corresponding filters. The focal length of each multispectral scanner was selected to satisfy the requirement that they should generate identical pixel sizes to those of the tilted stereo channels.

3.6.1 MOMS-2P

After the successful experimental mission on Spacelab D2, MOMS-02 has been refurbished and returned to space where it has been installed into the PRIRODA module of the Russian MIR space platform in the summer of 1996. At the time of writing this chapter (October 1996), the MOMS-2P system has not been operated or tested due to an industrial dispute among the Russian operating personnel.

Once this dispute has been settled or overcome, MOMS-2P will be able to acquire data within the latitudes ±51.6° with a repetition rate of 2 to 7 days for an 18 months period. A navigation package consisting of a high precision gyro and a GPS set has been included in order to provide the necessary position and attitude data for supporting high precision image data to be used mainly for extracting digital terrain models. The major advantages of the MOMS-02 PRIRODA mission compared with the D2 mission are (Seige, 1993):

- long term observation capability,
- coverage of higher latitudes between 51.6° North and South.

3.7 IRS-1A, 1B & 1C Satellite Systems

The first Indian Remote Sensing satellite (IRS-1A) for Earth observation purposes was launched in March 1988. To provide continuity of remote sensing data over India, the second operational Indian remote sensing satellite, IRS-1B, which is similar to IRS-1A, was launched in August 1991 (Deckshatulu, 1993).

IRS-1A and IRS-1B are three axes stabilised satellites, orbiting in a polar Sun-synchronous orbit at an altitude of 904km and an orbital inclination of 99.5 degrees. The orbital period for these systems is 103.2 minutes and the repeat cycle is 2 days. To take images of the ground, both of these satellites use three multispectral pushbroom imagers equipped with CCD detector arrays and defined as Linear Imaging Self Scanners - LISS-I, LISS-IIA, and LISS-IIB. LISS-I provides data at a ground pixel size of 72.5m and a swath width of 148km, while LISS-IIA and LISS-IIB each provide a swath of 74km and a ground pixel size

of 36.25m.

Following the successful operation of the first generation satellites IRS-1A and IRS-1B, India launched IRS-1C in December 1995. This satellite has enhanced capabilities in the form of higher resolution scanners operating from an 817km polar Sun-synchronous circular orbit and an orbital inclination of 98.69 degrees with a repetitivity of 20 days. Three scanners - one operating in the panchromatic band and the other two in multispectral bands - have been included in the system configuration. The panchromatic sensor provides imagery with a ground pixel size of 6m covering a swath of 70km. It also has an off-nadir viewing capability which gives the opportunity to have cross-track stereo images of the ground within about 5 days, weather permitting. The off-nadir viewing angle can be controlled from the ground to provide angles up to maximum of ±26 degrees. LISS-III is the first of the multispectral sensors which incorporates a middle infrared band in addition to its coverage of the visible and near infrared bands. LISS-III provides imagery having a ground pixel size of 23.5m covering a swath of 148km. The third sensor is the Wide Field Sensor (WIFS) which operates in two visible bands and provides imagery with a ground pixel size of 188m covering a swath of 770km.

An on board tape recorder provides the IRS-1C satellite with the capability of recording data over parts of the globe other than India for transmission to both Indian and other receiving stations. IRS-1D, scheduled to be launched in 1997, is identical to IRS-1C and will be an in-orbit replacement of IRS-1C to ensure data continuity beyond the mid 1990s.

3.8 JERS-1 OPS System

The Japanese Earth Resource Satellite, JERS-1, is a joint project between the National Space Development Agency (NASDA) and the Ministry of International Trade and Industry (MITI). NASDA is in charge of the satellite, while MITI is responsible for the provision of the observation equipment. JERS-1 was launched into an orbit with an altitude of 570km by an H-I launch vehicle in February 1992. It carries both a synthetic aperture radar (SAR) and an optical sensor named OPS as its Earth observation system. JERS-1 has a data

recorder installed so that it can record images for a region over which it would be difficult to acquire data otherwise because of the absence of a ground station.

OPS consists of eight linear array sensors to observe the Earth surface (Honda, 1993). The characteristics of the JERS-1 satellite and the OPS system are listed in Tables 3.1 and 3.2.

Table 3.1 JERS-1 Satellite Characteristics

Altitude	570 km
Inclination	98°
Period	96 min.
Dimension	93×183×316 cm^3
Weight	1400 kg

Table 3.2 OPS Characteristics

Bands	1	2	3	4
(μm)	0.52-0.6	0.63-0.69	0.76-0.86	0.76-0.86
Bands	5	6	7	8
(μm)	1.60-1.71	2.01-2.12	2.13-2.25	2.27-2.40
IFOV	18 m			
Swath width	75 km			
Stereo angle	15.33°			
B/H	0.3			
Ground pixel size	18.3 m × 24.2 m			

All of the OPS sensors are nadir pointing, except band 4, which looks forward at a 15.33 degrees viewing angle. Sensors 3 and 4 both operate in the near infrared band of 0.76μm to 0.86μm wavelength and their combination provides along-track stereoscopic imagery. As noted with MOMS-02, this type of stereo imagery has the advantage of increasing the possibility of obtaining good stereo pairs. However OPS uses a combination of a nadir pointing and a forward looking lens. Therefore the base-to-height ratio (0.3) of a stereo pair given by this system is not as good as those of MOMS-02 (0.8) or SPOT (1.0) when using the images acquired by their maximum oblique viewing angles of ±21.4 and ±27 degrees respectively.

3.9 American Commercial Earth Observation Pushbroom Imaging Satellites

At the present time, six commercial companies in the USA - EarthWatch Inc., Space Imaging Inc., Orbital Science Corporation, GDE, Resource 21, and GER Corporation - are developing high resolution imaging satellites utilizing pushbroom sensors (Fritz, 1996a,b,c).

EarthWatch, is planning to launch its pushbroom imaging system - QuickBird - into a non-Sun-synchronous orbit with an inclination of 52° and an altitude of 600km in late 1997. QuickBird is intended to have four multispectral bands with a ground pixel size of 3.28m, and a single panchromatic sensor with a ground pixel size of 0.82m. QuickBird will have the ability to provide along-track stereo images of the Earth with a viewing-angle of ±30° which results in a base-to-height ratio of 1.0. The system will use an in-orbit Global Positioning System (GPS) for the precise positioning of the satellite.

EarthWatch is also going to launch its staring array imaging system - EarlyBird - into a Sun-synchronous orbit with an altitude of 470km early in 1997. It is intended to have three multispectral bands with a ground pixel size of 15m and a panchromatic sensor with a ground pixel size of 3m. EarlyBird's multispectral frames cover an area of 30 by 30km^2 over which it can image simultaneously a series of 6 by 6km^2 panchromatic scenes. The entire multispectral frame can be covered in stereo by 36 panchromatic scenes.

Space Imaging Inc. is planning to place its pushbroom imaging system - CRSS - into a polar Sun-synchronous orbit with an altitude of 680km by December 1997. The system will use GPS in conjunction with three digital star trackers to maintain precise sensor position and attitude. Thus it is intended to provide absolute positioning without ground control in the 12 to 15 metres range (Fritz, 1996a). Space Imaging's system is a flexible pointing system and has the capability to provide both along-track and cross-track stereo images with an optimal base-to-height ratio. In its multispectral mode, the system will have four bands with a ground pixel size of 4m, while its panchromatic mode is intended to provide the images with 0.82m pixel size. Uplinks to the satellite will contain user requested latitude/longitude bounds, desired band widths, and imaging priorities.

The Orbital Science Corporation, is going to launch OrbView-1 by December 1997. Again this is a high resolution pushbroom imaging system, which will be placed in a polar Sun-synchronous orbit with a 460 km orbital altitude. The initial satellite will include a panchromatic sensor giving 1 and 2 metres ground pixel size and a multispectral sensor providing an 4 metres ground pixel size. OrbView-1 will feature a linear array sensor that

can image scenes up to 45 degrees off axis in all directions. This will enable the system to provide along-track and cross-track stereo images with optimal base-to-height ratios. The system uses in-orbit GPS positioning of the satellite to achieve precision-pointing to customer areas of interest.

GDE Systems Inc. is planning to launch its imaging system by late 1999 in a Sun-synchronous orbit with an altitude of 743km. This high resolution system is being designed to acquire monoscopic imagery with 0.8m ground pixel size in 15km by 1,700km strips or in 120km by 120km patches. It is again a flexible pointing stereo system and its operators are planning to acquire along-track and cross-track stereo imagery in 15km by 700km strips or in 70km by 70km patches.

Resource 21 is a commercial remote sensing information systems and services company which is planning to place four satellites in exactly the same orbital plane, but with tightly controlled phasing by early 1999. This phasing will result in two satellites in each of two ground tracks that repeat every seven days. Each of the two satellites within a particular ground track revisits, the same ground sites every third or fourth day using the same access geometry. This strategy results in twice weekly revisits of all sites. The Resource 21 imaging system is called M10 and is a multispectral pushbroom sensor which is mainly designed for the collection of 205km swaths with 10m ground pixel size using nadir pointing of the sensors. It has also the capability to provide off-nadir image collection. This system is designed primarily for the monitoring of agricultural sites which use farm equipment instrumented with GPS for precision farming.

The Geophysical & Environmental Research Corporation (GER) is planning to launch its GER Earth Resource Observation System - GEROS - which will include a constellation of six satellites each carrying a 10m multispectral sensor and a panchromatic pushbroom sensor having a ground pixel size of less than 10m. GEROS is also being developed with an initial emphasis on precision farming applications.

Besides these six American commercial companies, the Israeli Aircraft Industries (IAI) has

formed a joint venture with Core Software Technology (CST) of Pasadena, California to develop EROS, a constellation of high resolution remote sensing satellites. This consists of a first generation EROS-A satellite and seven second generation EROS-B satellites. EROS-A is a pushbroom imaging system and is planned for a mid-1997 launch into a Sun-synchronous orbit with 480km altitude. It is a panchromatic imaging system with a 1.3m ground pixel size designed to provide 11km by 11km scenes. Launch plans for EROS-B are to have the initial launch in late 1998, with the seventh launch taking place in January 2003. The EROS-B sensors will provide a 4.5m pixel size in multispectral mode and a 1m ground pixel size in panchromatic imaging mode.

Table 3.3 summarizes the technical and operational aspects of these seven future commercial systems.

Table 3.3 Characteristics of forthcoming American commercial Earth observation satellites equipped with pushbroom imaging systems

Corporation	EarthWatch		Orbital Sciences		Space Imaging		GDE	Resource 21		GER		IAI/CST
System	QuickBird		OrbView-1		CRSS		------	Resource 21		GEROS		EROS-A
Mode	Pan	XS	Pan	XS	Pan	XS	Pan	XS	XS	Pan	XS	Pan
Pixels [bit]	11	11 x 4	8	8	11	11	11	12	12	TBA	TBA	11
Data Size [Mb]	1,000	4,000	128	128	TBA	TBA	TBA	TBA	TBA	180	2,000	50
Altitude [km]	600		460		680		743	743		650		480
Inclination	52°		97.2°		98.1°		98.8°	98.1°		TBA		97.3°
Sun-synchronous	no		yes		yes		yes	yes		TBA		yes
Period(days/revisit)	15.3		15.5		14.6		14.4	-------		16		15.3
Pixel Size (m)	0.82	4	1 & 2	4	0.82	4	0.8	10	20	TBA	10	1.3
Swath Width [km]	22	22	4 & 8	8	11	11	≥15	205	205	TBA	TBA	11
Scene Size [km²]	22×22	22×22	64 to 7,200		121 to 11,000		4,900	1 to 820,000		TBA		500
Stereo	along-track		flexible		flexible		flexible	flexible		flexible		along-track
Field of View	TBA		1°		0.93°		≥1.2°	15.9°		TBA		1.3°
Pointing Along-track	±30°		±45°		±45°		±45°	±30°		N/A		±30°
Pointing Cross-track	±30°		±45°		±45°		±45°	±40°		N/A		±30°

TBA= To Be Announced.

3.10 Accuracy and Detectability Requirements of Space Imagery Required for Mapping

To evaluate the suitability of space imagery for photogrammetric mapping, three criteria must be considered: (i) the planimetric accuracy achievable; (ii) the elevation accuracy achievable; (iii) the detectability of objects from the imagery.

(i) Considering the planimetric accuracy requirements of an RMSE = ±0.3mm at the publishing scale of the maps, results in ±7.5m for 1:25,000; ±15m for 1:50,000; and ±30m for 1:100,000.

(ii) According to map accuracy standards, the point measurement accuracy in elevation should be 1/5 of the contour interval, which depends on the terrain. It means ±2m point accuracy (RMSE) in height for flat areas (using a 10m contour interval); ±4m in the case of intermediate areas (with a 20m contour interval); and ±10m for mountainous regions (using a 50m contour interval).

(iii) Detectability requirements depend on the nature of the objects to be shown in the map. Considering the Kell factor equal to 2 or $2\sqrt{2}$ results in requirements of a 2m pixel size for urban buildings; a 5m pixel size for the minor road network and fine hydrological features; and a 10m pixel size for major roads and building blocks, though of course much will depend on the contrast of features with their surroundings when detecting individual map elements.

In summary, to accomplish 1:25,000 and 1:50,000 scale mapping to a standard specification using the images taken by spaceborne linear array sensors, they should provide ±7.5m to ±15m positional accuracy, ±3 to ±5m in elevation accuracy, and 2 to 5m for object detectability.

3.10.1 Analysis of the Potential of Satellite Linear Array Sensors for Topographic Mapping

Although the French SPOT system can provide enough positional geometric accuracy for the compilation of 1:50,000 scale maps, its elevation accuracy is marginal and, in general, it cannot provide good enough detectability of the features required for inclusion in 1:50,000 and 1:25,000 scale maps.

The Japanese JERS-1 OPS system cannot really meet the requirements for medium scale map compilation. That is because it cannot provide a good elevation accuracy (due to its poor base-to-height ratio (0.3)) and its poor object detectability of 35 to 50m.

The images acquired by the Indian IRS-1C satellite have almost the same geometry as SPOT images but with better (i.e. a smaller) ground pixel size (6m). In the same manner as SPOT, they can provide enough planimetric accuracy for 1:50,000 scale maps, but the altimetric accuracy is marginal. Again the main problems lie in the detectability of the objects on the ground.

The German MOMS-02 linear array system may be able to provide the required planimetric and altimetric accuracy for the 1:50,000 map scale. Considering the three linear arrays (forward, nadir, backward) together, this should give a detectability of 10m to 12m, because of the 4.5m ground pixel size obtained with the nadir pointing image. This gives enough accuracy for 1:50,000 scale maps in areas where smaller features such as buildings, tracks and footpaths are not present. But, in this case, the swath width of the area covered by the MOMS-02 stereo image will decrease from 78km (considering forward and backward images only) to only 37km (considering all three images, i.e. forward, nadir and backward) to give the stereo coverage.

Although, for the compilation of medium scale line maps, most of the available pushbroom scanners do not provide sufficient resolution, it is worth mentioning that their powerful capability for the generation of digital photogrammetric products such as DTMs and

orthoimages over large areas must not be forgotten. Indeed this is an attractive feature for many geoscience users who may not be concerned with the detail required for a fully specified topographic map at these scales.

The forthcoming American systems should provide the required geometric accuracy as well as enough detectability for maps at 1:50,000 and 1:25,000 scales. Because of their flexibility, they should also able to provide stereo images of the area requested by the users at any time, provided of course that it is cloud free.

In the following Chapters, the geometries of the images taken by linear array imaging systems are investigated in detail. Chapter 4 outlines the mathematical modelling of these images in two dimensions. The three dimensional mathematical modelling of stereo linear array images is discussed in Chapters 5 and 6.

CHAPTER 4 : TWO-DIMENSIONAL MATHEMATICAL MODELS FOR THE GEOMETRIC CORRECTIONS OF LINEAR ARRAY IMAGERIES

4.1 Introduction

There are essentially two different approaches that can be used to correct the geometric distortions that are present in a remotely sensed image in general and a linear array image in particular: *(i) a deterministic approach, and (ii) a transformation approach.*

The deterministic approach can be used where the type and magnitude of the distortions are modelled and these models are then used to correct the data. These techniques work well when the types of distortion such as Earth rotation and Earth curvature or the sensor characteristics such as lens distortion are well-known. Thus this approach works very well with aerial or space photography where pre-flight calibration can determine many of these parameters. However it works less well with the dynamic imaging characteristics of the scanners which are widely used in remote sensing.

By contrast, the transformation approach depends on the assumption of a mathematical relationship existing between the pixel locations of points in the remotely sensed images and the corresponding locations in terms of the ground coordinates of those points. This approach does not depend on any well defined physical relationship as in the deterministic approach but in a purely mathematical relationship. Thus the parameters of the mathematical functions are derived through the application of a transformation procedure.

4.2 Functional Relationship

In order to reconstruct the position and shape of objects from linear array images, it is necessary to define the functional relationship between the image coordinates (x,y) of a point and the coordinates of the same point in a specified ground coordinate system (X,Y,Z). In general terms, this relation can be expressed in three dimensions, as:

$$\begin{aligned} x &= f(X, Y, Z) \\ y &= g(X, Y, Z) \end{aligned} \tag{4.1}$$

or in two dimensions as:

$$\begin{aligned} x &= f(X, Y) \\ y &= g(X, Y) \end{aligned} \tag{4.2}$$

Such functional relationships can be realised through the use of a suitable mathematical model which describes, in the best possible way, the physical phenomena that are involved during the imaging. The choice of the model depends on a number of factors such as the assumption that the variations in the parameters or discrepancies occur either in a deterministic or a stochastic manner; the magnitude of such variations that are to be expected; the computational effort involved; and the accuracy of representation desired.

The geometry of imageries based on the use of linear arrays and the pushbroom principle of operation differs significantly from that of photographic imageries. These differences include the different nature of the imagery itself and the very different perspective relations that are involved. In turn, these lead to a quite different geometry for the imaging rays. The image produced by a pushbroom scanner is a continuous strip image made up of a large number of individual scan lines occurring at a frequency corresponding to the scanning resolution within the lines (see Figure 4.1).

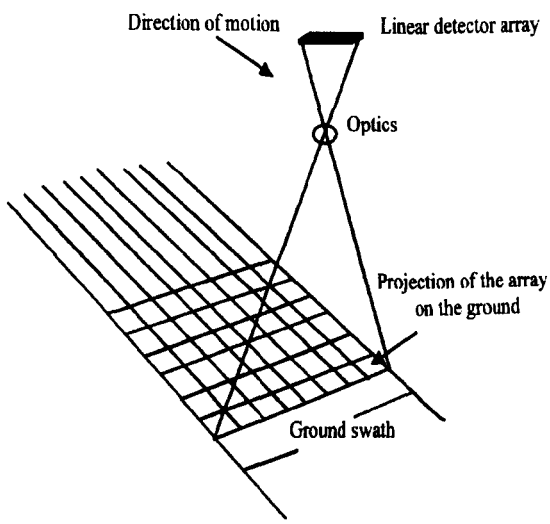

Figure 4.1 Along-track pushbroom linear array system

Therefore the two-dimensional image is constructed as an indefinitely long strip covering the ground swath lying under the flight line. The constant frequency of the scanning imaging action allows the image coordinate axis, measured along the strip, to be regarded as a function of time. Since the positions and orientation of the linear array sensor in space or in the air are continually changing along the orbit or flight path, the imaging geometry becomes dynamic and time dependent.

4.3 Mathematical Modelling of Linear Array Imageries

Many researches have been carried out into the geometry of linear array imagery and a number of different mathematical models for the photogrammetric orientation, rectification and reconstruction of these imageries have been devised and published. Taking a broad view, these various mathematical models can be divided into three main groups:

(i) those following a two-dimensional interpolative approach using polynomials of various degrees;

(ii) those following a two-dimensional projective transformation; and

(iii) those of a three-dimensional type developed from a rigorous geometrical analysis of the linear array imagery.

In this chapter, only the two-dimensional approaches, i.e. cases (i) and (ii), will be discussed and analysed. Flat ground with no relief displacements will be assumed throughout.

The principal aim of utilizing a two-dimensional image transformation in photogrammetry is to carry out image rectification. With these methods, no effort is made to estimate the orientation parameters. Instead, the common approach is to use a mathematical formula whose parameters relate the image space to the object space as well as possible. Using the known coordinates of ground control points (GCPs) in the object space, and the measured coordinates of the corresponding points in the image space as observations, the parameters of the transformation model are computed. Next the computed parameters are substituted back into the transformation model which is then used to compute the planimetric ground coordinates of any other points whose image coordinates have been measured. In practice,

polynomial transformations are used widely for this purpose, especially where high positional accuracies are not required, e.g. in thematic mapping and in projects where the interpretation of the ground features is the main matter of interest.

4.4 Two-Dimensional Interpolative Approach

The interpolative approach can be applied using polynomials of different types or the multiquadric method. Each of these will be inspected in the following sections of this Chapter.

4.4.1 Polynomial Approach

The polynomial transformation that is commonly used takes the form:

$$
\begin{aligned}
X = {} & a_0 && \text{(a constant term)} \\
& + a_1x + a_2y && \text{(linear (1st order) terms)} \\
& + a_3xy + a_4x^2 + a_5y^2 && \text{(quadratic (2nd order) terms)} \\
& + a_6x^2y + a_7xy^2 + a_8x^3 + a_9y^3 && \text{(cubic (3rd order) terms)} \\
& + a_{10}x^3y + a_{11}xy^3 + a_{12}x^4 + a_{13}y^4 + a_{14}x^2y^2 && \text{(quartic (4th order) terms)} \\
& + a_{15}x^3y^2 + a_{16}x^2y^3 + a_{17}x^5 + a_{18}y^5 + a_{19}x^4y + a_{20}xy^4 && \text{(quintic (5th order) terms)} \\
& + \ldots \\
Y = {} & b_0 \\
& + b_1x + b_2y \\
& + b_3xy + b_4x^2 + b_5y^2 \\
& + \ldots \qquad \text{as above} \qquad (4.3) \\
& + \ldots \\
& + b_{15}x^3y^2 + b_{16}x^2y^3 + b_{17}x^5 + b_{18}y^5 + b_{19}x^4y + b_{20}xy^4 \\
& + \ldots
\end{aligned}
$$

where

X and Y are the ground coordinates of the point;

x and y are the image coordinates of the point; and

a_i and b_i (i = 1 to n) are the transformation parameters.

As can be seen from equation (4.3), each of the individual equations generating either the X or the Y coordinates include a variety of different terms. The number of terms of a specific order in these equations will always be one greater (n+1) than the order of the terms (n), e.g. there are five fourth order terms, four third order terms, etc.

As mentioned above, the coefficients of the polynomial transformation are conveniently determined using the measured image and known ground control point coordinates. Normally a least squares procedure will be employed with the solution - since there will often be more ground control points available than the minimum number necessary to solve the unknown coefficients. The choice of the number and order of the polynomial terms used in an image transformation is determined by the degree of accuracy required for the particular application, the number of control points required to achieve this accuracy, and the computational facilities available. It is most helpful when deciding which of these terms should actually be used in the transformation of measured image coordinates to terrain coordinates to understand the effects of each term on the transformation and the pattern of distortion or displacement that is modelled or corrected by each term. These are shown graphically in Figures 4.2a and 4.2b (Petrie and Kennie, 1990).

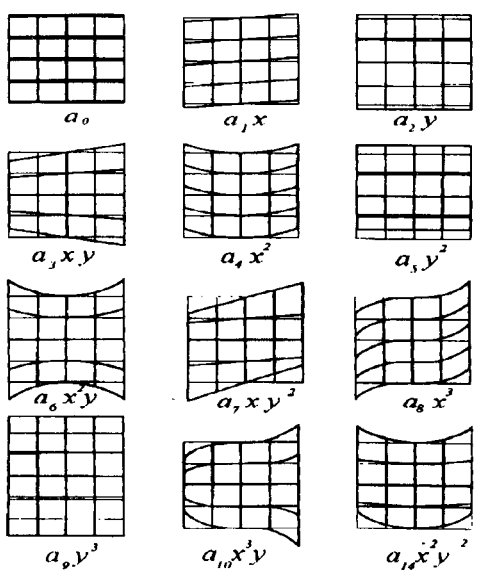

Figure 4.2a The effects of the polynomial terms in X

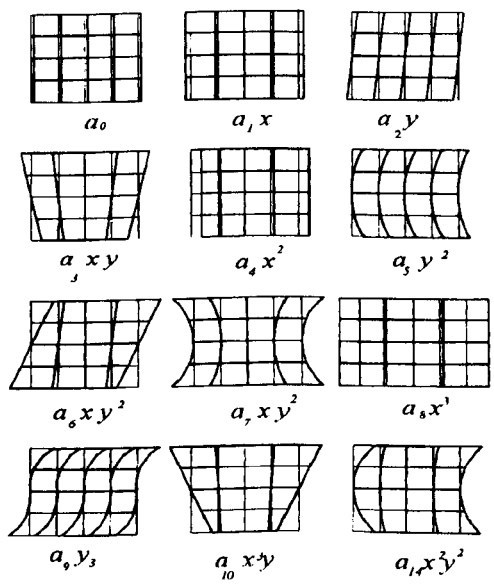

Figure 4.2b The effects of the polynomial terms in Y

Thus, for example, a first order polynomial or affine transformation will only include the first

3 terms of each equation in (4.3), i.e.

$$X = a_0 + a_1 x + a_2 y$$
$$Y = b_0 + b_1 x + b_2 y \qquad (4.4)$$

This can accomplish scaling, rotation, and shearing, but not warping. A second order or higher order polynomial can be used to model these more complex distortions (Mather, 1987). The polynomial method is well explained by Wong (1975), Konecny (1976), El-Niweiri (1988), Ganguly (1991), and Petrie and El-Niweiri (1994). Whatever its defects, it is worth noting that the use of the general polynomial transformation with up to 20 to 25 terms has been widespread in remote sensing practice to date.

Polynomials do have the disadvantage that the model from which the coefficients have been determined may fit well at the control points, but may deviate strongly elsewhere in the image due to the unpredictable effects of the higher order terms. An alternative method to the use of the general polynomial which attempts to overcome this disadvantage, is to use spline functions or a piecewise polynomial procedure.

4.4.2 Piecewise Polynomial Procedure

This uses low order polynomials within bounded regions, thus avoiding the tendency toward ill conditioning which results from the use of higher order polynomial coefficient matrices (Konecny, 1976). The types of spline function which may be used for the transformation and rectification of an individual small patch or piece of an image are shown in the box at the top of the next page.

It will be seen that a certain minimum number of ground control points need to be available in each patch or piece - 4 in the case of bilinear; 9 in the case of biquadratic; and 16 in the case of the bicubic function. This means that a dense network of ground control points needs to be available across the whole image in order to implement this method.

A problem that can arise with the use of the piecewise (or patchwise) approach occurs along the boundaries of the sub-images into which the overall image is split. Some method may have to be devised and applied to allow a smooth transition and continuity between one part

of the image and the next, i.e. between the different sub-images. For example, constraints can be introduced by forcing the individual functions in the patches to coincide along boundary lines, so that joint functions will result.

a) Piecewise bilinear functions (first order splines)

$$\begin{aligned} X &= a_0 + a_1 x + a_2 y + a_3 xy \\ Y &= b_0 + b_1 x + b_2 y + b_3 xy \end{aligned} \tag{4.5}$$

It can be seen that these simply comprise both the first order terms of the general polynomial given above in equation (4.3), and the product (xy) of these two terms - hence the use of the term bilinear.

b) Biquadratic polynomials (second order splines)

$$\begin{aligned} X &= a_0 + a_1 x + a_2 y + a_3 xy + a_4 x^2 + a_5 y^2 + a_6 x^2 y + a_7 xy^2 + a_8 x^2 y^2 \\ Y &= b_0 + b_1 x + b_2 y + b_3 xy + b_4 x^2 + b_5 y^2 + b_6 x^2 y + b_7 xy^2 + b_8 x^2 y^2 \end{aligned} \tag{4.6}$$

Again the individual terms included in this comprise all of those up to second order which were included in the general polynomial equation (4.3), including their products (xy^2, x^2y, x^2y^2) - hence the use of the term biquadratic.

c) Bicubic polynomials (third order splines)

$$\begin{aligned} X &= a_0 + a_1 x + a_2 y + a_3 xy + a_4 x^2 + a_5 y^2 + a_6 x^2 y + a_7 xy^2 + a_8 x^2 y^2 + \\ &\quad a_9 x^3 + a_{10} y^3 + a_{11} x^3 y + a_{12} xy^3 + a_{13} x^3 y^3 + a_{14} x^3 y^2 + a_{15} x^2 y^3 \\ Y &= b_0 + b_1 x + b_2 y + b_3 xy + b_4 x^2 + b_5 y^2 + b_6 x^2 y + b_7 xy^2 + b_8 x^2 y^2 + \\ &\quad b_9 x^3 + b_{10} y^3 + b_{11} x^3 y + b_{12} xy^3 + b_{13} x^3 y^3 + b_{14} x^3 y^2 + b_{15} x^2 y^3 \end{aligned} \tag{4.7}$$

Once again, these comprise all the terms up to those of the third order occurring in the general polynomials, and will include the fourth order (eg. x^3y) and fifth order (eg. x^3y^2) terms formed by the products containing third-order terms - hence the name bicubic.

A basic critique of this method is that a general mathematical model which relates the (slave)

image to the (master) ground control coordinates data set no longer exists. Instead, there are a number of mathematical relations that are being employed independently in different parts of the image data set. These different parts are also being chosen on a random or non-specific basis.

It is evident, however, when higher order polynomial interpolation functions do not work with sufficient accuracy globally across the whole image, piecewise polynomial procedures can yield a significantly improved accuracy in terms of geometric registration and fit. Yet, even these discontinuous interpolation functions cannot cope with image data sets exhibiting locally varying geometric distortions of a considerable magnitude. In these cases, the pointwise polynomial procedure and the multiquadric interpolation method are possible and promising alternatives, albeit with a large increase in the computational effort that is required.

4.4.3 Pointwise Procedure

In the so-called pointwise procedure, a global polynomial is first used in a preliminary stage to match the image and ground coordinates of the control points. Residual vectors will then result at each of the GCPs. Then a new transformation procedure is defined for each new point in the image, using only the surrounding subset of ground control points (GCPs). Essentially this comprises an individual transformation for each point (or pixel) in the image using only the closest GCPs. In this case, for each new point, the technique assembles a set of neighbouring GCPs according to some criterion. This may be the n closest GCPs (Figure 4.3a) or it may be the m GCPs lying in each of the four quadrants centered on the position of the new point (Figure 4.3b). A typical pointwise procedure utilizes either a weighted distance average method or a moving average method as the secondary transformation for new points.

In the case of the weighted distance average method, the corrections for the coordinates of a new point are computed using the residual vector error values at each of the surrounding GCPs (based on Figure 4.3a or 4.3b) whereby the value at each GCP is given a weight as

a function of its distance from the new point:

$$\Delta X_P = \frac{\sum_{i=1}^{n} w_i \Delta X_i}{\sum_{i=1}^{n} w_i} \quad ; \quad \Delta Y_P = \frac{\sum_{i=1}^{n} w_i \Delta Y_i}{\sum_{i=1}^{n} w_i} \tag{4.8}$$

where

ΔX_P , ΔY_P : are the corrections for the new points;

ΔX_i , Δy_i : are the known residual errors for each of the surronding GCPs coming from the preliminary polynomial transformation; and

w_i : are the weights of the errors at each of the GCPs and are a function of the distance (d) between the new point and each of the GCPs.

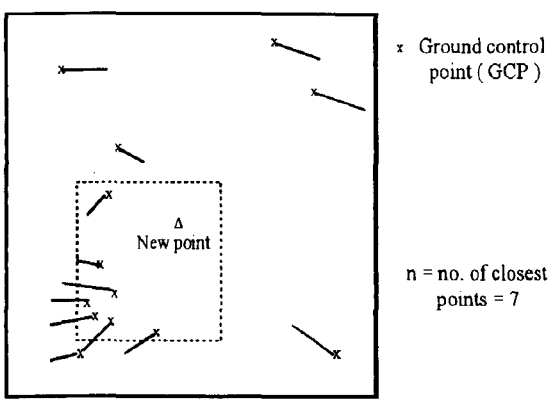

Figure 4.3a Search routine for the closest points using a square window to collect nGCPs.

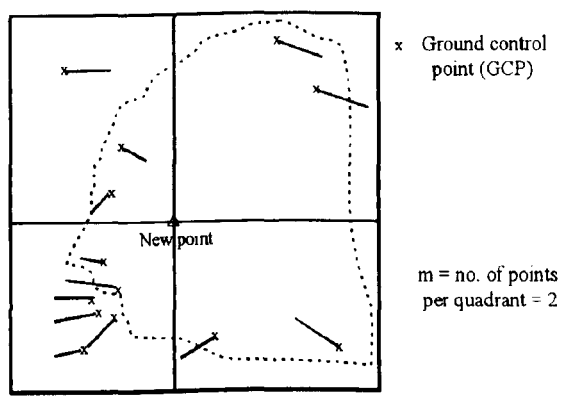

Figure 4.3b Quadrant search routine for m=2 GCPs.

A typical weight function can be considered as: $w_i = 1/d_i^k$

Obviously, a large value of k increases the effect of the closest GCP while reducing the influence of all the other points.

In the case of the moving average method, using the error values at the selected neighbouring GCPs, a local polynomial of a low order (first or second order) is then computed. The coefficients in the transformation (polynomial) formulae are derived using a least squares procedure. The coefficients of the interpolation function will vary from point to point. This increases the flexibility of the correction method although much more

computation is involved (Leberl 1975 and 1990).

If all coordinate values have been reduced with respect to an origin in the new point, then only the absolute term of the polynomial has to be computed. Each required coordinate correction at a control point leads to one correction equation; normal equations are then formed from the correction equations and are solved for the coefficients.

Thus, in this moving average procedure, the contribution of a correction equation to the normal equation is always given a weight that is a function of the distance between the new point that will be adjusted and the ground control point. This makes the coefficients in the transformation formula different for each point that is being transformed. The name "moving average" is based on the fact that the functional value of a polynomial can always be expressed as a linear combination ("average") of the values of the errors in the GCPs.

These pointwise methods make it possible to obtain a good fit at any number of points by attaching a larger weight to the contributions from nearby control points. A good overall result of the adjustment can be obtained by careful selection of the weight function and the polynomial that are used in the procedure.

4.4.4 Multiquadric Interpolation

This method was devised by R. L. Hardy in 1968 and was first described in Hardy (1971) for the interpolation of irregular surfaces. This method was later renamed as the multiquadric-biharmonic method - since the method was actually a numerical type of biharmonic analysis (Hardy, 1990). Later Gopfert (1982) and Ehlers (1987) modified this method to make it suitable for the correction of remotely sensed image data. In this form, it is particularly suited for the rectification of remote sensing images of large scale and locally varying geometric distortions.

In practice, the first step before the application of the multiquadric algorithm to an image is to use a standard polynomial routine. Polynomials of first or second degree should be used

to carry out a preliminary transformation to keep the distortions that can be introduced by polynomials of a higher order to a minimum. This process keeps the remaining residuals small enough to be handled more easily in a computer.

The residuals at the ground control points (GCPs) within the pre-rectified image can be calculated from the differences between the known coordinates of these points and the transformed values of the image coordinates of the same points generated using the polynomial coefficients into a reference system such as UTM, as follows:

$$\begin{aligned} dX_K &= X_K - X'_K \\ dY_K &= Y_K - Y'_K \end{aligned} \tag{4.9}$$

where (k=1, ..., n) and,

dX_K , dY_K : are the residuals;

X_K , Y_K : are the known GCP planimetric coordinates; and

X'_K , Y'_K : are the interpolated planimetric coordinates of the GCPs.

Next, the multiquadric method is used to interpolate vectors (dx , dy) for every pixel (x' , y') based on the GCP residuals obtained in the pre-rectified image. This is done in such a way that the residual vectors (dX_K , dY_K) are modelled exactly for each GCP. The positions of all the other pixels in the image are then interpolated using a weighted distance factor in relation to all employed GCPs. With this, a perfect fit will result at all the GCPs. However, this also means that the quality of the rectification at the GCPs themselves cannot be checked. According to Ehlers (1996), the actual multiquadric procedure can be summarized as follows:

(i) Calculate the distance $f_j(x', y')$ between a point (x', y') in the image and the GCP (X_j, Y_j):

$$f_j(x',y') = [(x' - X_j)^2 + (y' - Y_j)^2]^{\frac{1}{2}} \tag{4.10}$$

(ii) Calculate the distance f_{ij} between two ground control points i and j with planimetric coordinates (X_i, Y_i) and (X_j, Y_j):

$$f_{ij} = [(X_i - X_j)^2 + (Y_i - Y_j)^2]^{\frac{1}{2}} \tag{4.11}$$

Note: $f_{ij} = f_{ji} = f_j(X_i, Y_i) = f_i(X_j, Y_j)$.

(iii) Set up the interpolation matrix $F = (f_{ij})_{(n,n)}$, where (n,n) means that F is an n by n matrix.

(iv) According to (4.9), the residual vectors $[dX]$ and $[dY]$ should be modelled so that they can be calculated from F, where $[dX] = F\,A$ and $[dY] = F\,B$. For the $[dX]$ values the relationship is:

$$\begin{pmatrix} dX_1 \\ dX_2 \\ \vdots \\ dX_n \end{pmatrix} = \begin{pmatrix} f_{11} & f_{12} & \cdots & f_{1n} \\ f_{21} & f_{22} & \cdots & f_{2n} \\ \vdots & & & \vdots \\ f_{n1} & f_{n2} & \cdots & f_{nn} \end{pmatrix} \begin{pmatrix} a_1 \\ a_2 \\ \vdots \\ a_n \end{pmatrix} \tag{4.12}$$

This results in n equations for n unknowns in each set and these can be solved to gain values for A. The matrix F is symmetric and has zero values along its diagonal (i.e. $f_{11}=f_{22}= \ldots f_{nn} =0$). Now the above equations can be solved to produce A and the residual improvements dX_K (where $K=1, \ldots, n$) can be modelled as follows:

$$f_{K1}\,a_1 + f_{K2}\,a_2 + \ldots + f_{Kn}\,a_n = dX_K \tag{4.13}$$

(v) The same must be done with the Y coordinates and vector B to give the $[dY]$ values:

$$\begin{pmatrix} dY_1 \\ dY_2 \\ \vdots \\ dY_n \end{pmatrix} = \begin{pmatrix} f_{11} & f_{12} & \cdots & f_{1n} \\ f_{21} & f_{22} & \cdots & f_{2n} \\ \vdots & & & \vdots \\ f_{n1} & f_{n2} & \cdots & f_{nn} \end{pmatrix} \begin{pmatrix} b_1 \\ b_2 \\ \vdots \\ b_n \end{pmatrix} \tag{4.14}$$

Again the residual improvements dY_K for $K = 1, \ldots, n$ can be modelled as follows:

$$f_{K1}\,b_1 + f_{K2}\,b_2 + \ldots + f_{Kn}\,b_n = dY_K \tag{4.15}$$

(vi) Now a geometric interpolation according to equations (4.13) and (4.15) can be

performed for every pixel (x', y') in the image using the interpolation function $f_j(x', y')$ from equation (4.10). Let f_j now stand for $f_j(x', y')$ with $j = 1, \ldots, n$. Equations (4.12) and (4.14) will now become:

$$\begin{aligned} f_1 a_1 + f_2 a_2 + \ldots + f_n a_n &= dx \\ f_1 b_1 + f_2 b_2 + \ldots + f_n b_n &= dy \end{aligned} \tag{4.16}$$

Now the true location of each point (x', y') can be calculated using the improvement vectors (dx, dy) as follows:

$$(X, Y) = (x', y') + (dx, dy) \tag{4.17}$$

If point (X, Y) is a GCP with coordinates (X_K, Y_K), a perfect fit results. For all other points in the image, an interpolation is carried out according to the multiquadric interpolation model given above. The interpolation coefficients f_j provide a distance weighting function. The great advantages of the multiquadric algorithm are that:

(i) it describes a continuous interpolation function;
(ii) all GCPs contribute to the geometric transformation; and
(iii) the image geometry can be wrapped in any given constraint.

However, it is not possible to check the accuracy of this procedure at the control points as one is used to doing with polynomial mapping functions. Instead there is a perfect fit at the control points. Consequently, independent test points have to be employed for accuracy checking. Figure 4.4, taken from Ehlers (1993), gives a comparison of the results of carrying out a rectification of an image using a global polynomial and the multiquadric method with the same ground control point (GCP) pattern.

The differences between the pointwise procedure and the multiquadric method arise from the selection of the GCPs. In the case of the pointwise procedure, only the closest GCPs are considered in the computation of the correction for each image point while, in the case of multiquadric interpolation, all of the GCPs are considered in the computation at the same time.

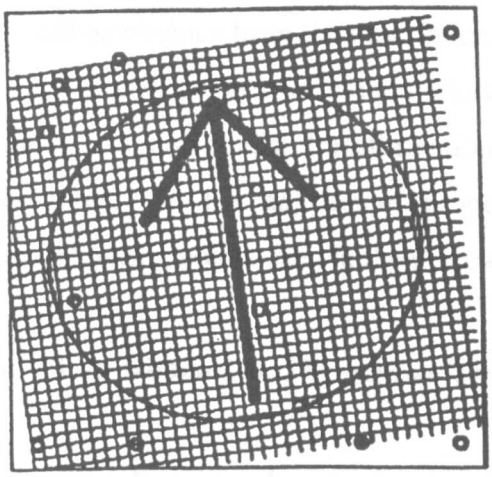

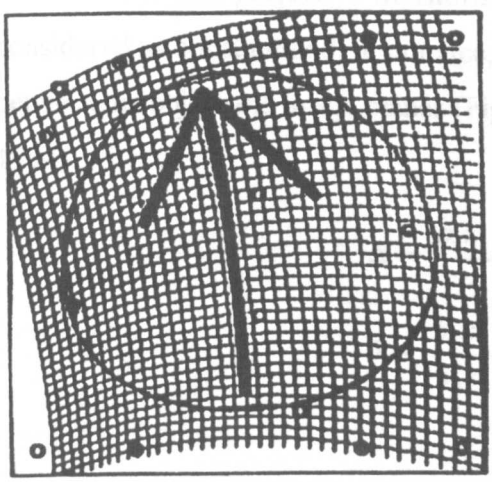

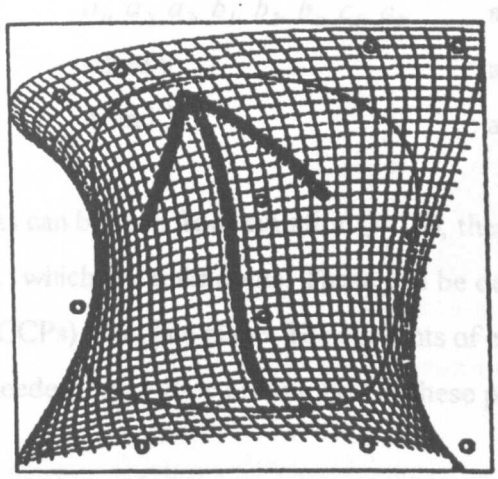

Figure 4.4(a) Results of <u>polynomial interpolation</u> of degrees 1 through 3 (top to bottom). Even with a third degree polynomial interpolation no exact registration is possible.

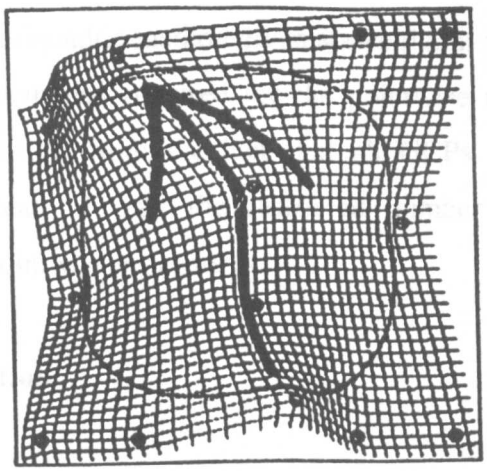

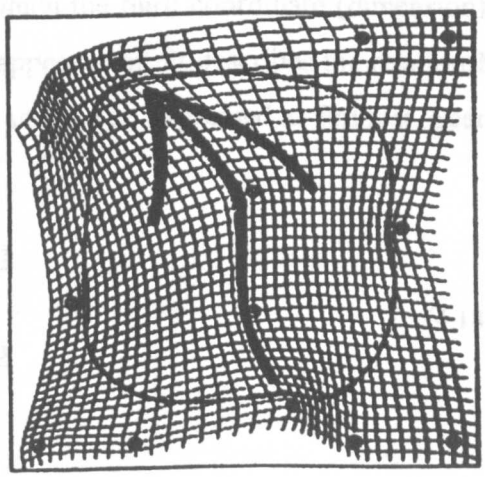

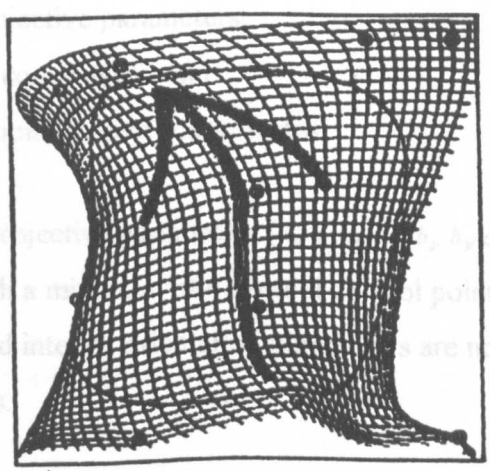

Figure 4.4(b) <u>Multiquadric interpolation</u> with polynomial preregistration of degrees 1 through 3 (top to bottom). All GCPs are exactly registered to their position in the reference image (Ehlers, 1993).

It will be obvious from the description of the multiquadric method given above that it will require a much greater computational effort than that required for the pointwise and piecewise polynomial transformations. This results from the fact that all GCPs are considered in the adjustment procedure instead of only the restricted number of neighbouring points used in the piecewise and pointwise procedures.

4.5 Two-Dimensional Projective Transformation

The two-dimensional projective transformation is a simplified version of the well known three-dimensional projective transformation in which the third coordinate (dimension) is considered as constant and, in practice, may not appear at all. It describes the relationship between the object and image planes (Figure 4.5), and can be expressed as follows (Searle, 1984):

$$X = \frac{a_1 x + a_2 y + a_3}{c_1 x + c_2 y + 1}$$
$$Y = \frac{b_1 x + b_2 y + b_3}{c_1 x + c_2 y + 1} \qquad (4.18)$$

where

$a_1, a_2, a_3, b_1, b_2, b_3, c_1, c_2$	: are the projective parameters;
x and y	: are image coordinates; and
X and Y	: are the ground (object) coordinates.

As can be seen from equation (4.18), there are 8 projective parameters ($a_1, a_2, a_3, b_1, b_2, b_3, c_1, c_2$) which are unknowns. These can be defined with a minimum of 4 ground control points (GCPs) lying in a plane. The elements of exterior and interior orientation parameters are not needed, since they are implicit in these parameters.

In the case of linear array imagery, the projection of the linear array on to the ground forms a very narrow rectangle with its long side oriented perpendicular to the projected line of motion. The linear array is read out such that one complete line of data is generated each time this projected field of view advances by one line. Therefore the projective

transformation described above is modified to give a line-perspective relationship between the ground and the image (Figure 4.6).

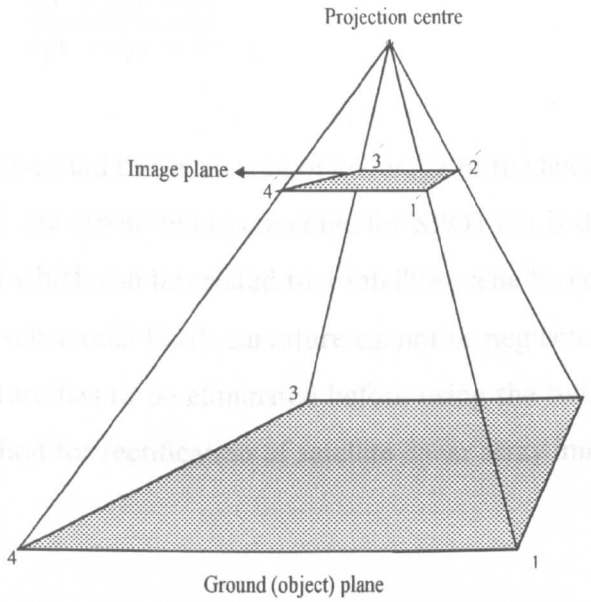

Figure 4.5 The projective relationship between the ground (object) and image plane (minimum requirement is four control points)

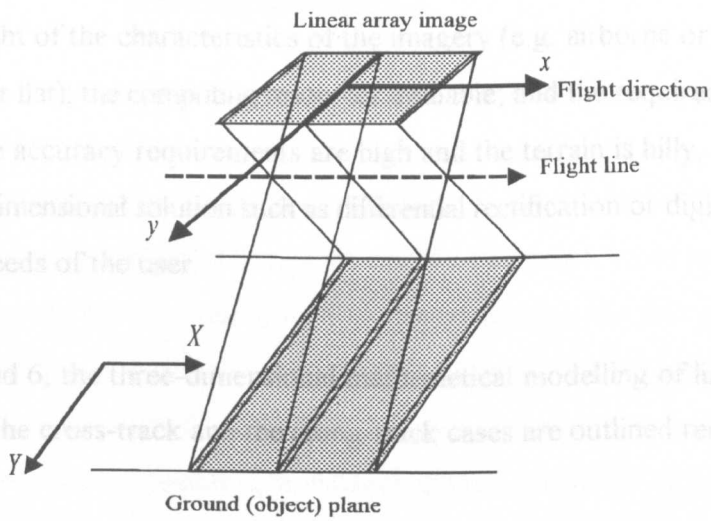

Figure 4.6 Line-perspective relationship between ground and linear array imagery

Each scan line has a different perspective (or projective) centre, and it can be assumed that all are tied to a straight line approximating to the orbit or flight line. If x is the axis in the direction of the platform motion and y represents the pixel in a scan line, the projective transformation can be modified to the following equations (Novak, 1992):

$$X = \frac{a_1 x + a_2 y + a_3}{1}$$

$$Y = \frac{b_1 x + b_2 y + b_3}{c_1 x + c_2 y + 1} \tag{4.19}$$

Due to Earth curvature, and the large area of coverage of the linear array image produced from a satellite (e.g. the 60km×60km coverage for SPOT), it is difficult to define a plane area on the ground which can be related to a satellite scene by equation (4.18). Even for very flat terrain, the substantial Earth curvature cannot be neglected. As a result, the effect of the Earth curvature has to be eliminated before using the two-dimensional projective transformation method for rectification of satellite linear array imageries.

4.6 Conclusion

It will be apparent that a wide variety of techniques exist for the two-dimensional digital rectification of linear array imagery. The selection of one of these for a specific task can only be made in the light of the characteristics of the imagery (e.g. airborne or spaceborne) and the terrain (hilly or flat); the computing resources available; and the required accuracy of the final result. If the accuracy requirements are high and the terrain is hilly, it is obvious that only a full three-dimensional solution such as differential rectification or digital monoplotting will satisfy the needs of the user.

In Chapters 5 and 6, the three-dimensional mathemetical modelling of linear array stereo images for both the cross-track and the along-track cases are outlined respectively.

CHAPTER 5 : THREE-DIMENSIONAL MATHEMATICAL MODELLING OF LINEAR ARRAY STEREO IMAGES (CROSS-TRACK CASE)

5.1 Introduction

Linear array cross-track stereo imagers acquire their stereo images of the ground from adjacent orbits (see Figure 5.1) arising from their off-nadir viewing capabilities. They can provide these images with a base-to-height ratio which can range from good (0.5) to excellent (1.0).

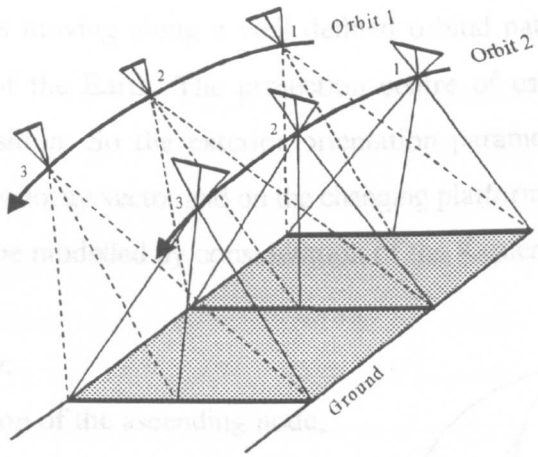

Figure 5.1 Formation of linear array stereo model from cross-track images

However, the difference in time (sometimes three or four months) between the two recordings of the same area by this type of sensor, can cause some problems with the formation of the model of the ground; with the stereo viewing and interpretation of these models; and with the use of automatic image matching procedures to create DEMs. This is due to the changing reflectance from the ground arising from seasonal climatic differences (dry/wet or summer/winter) resulting in changes in the appearance of the vegetation and hydrology of the imaged area (Petrie and Liwa, 1995; Petrie 1996).

The first example of this type of sensor is SPOT. As mentioned previously, the initial satellite in the series was launched in 1986; since then, two more have been launched and put into service. The second example of this type of imager which produces images that are available on the market is that mounted in the Indian IRS-1C satellite, launched in 1995.

Quite a number of researchers have investigated the geometry and mathematical modelling of cross-track stereo imagers. Although almost all of these mathematical models have been applied to SPOT images, they can be used for any other system such as IRS-1C with the same geometry. All of these mathematical models are based on the use of collinearity equations, but each investigator has taken a different approach and used different parameters in his formula. These methods are discussed briefly in the following sections.

5.2 Orbital Parameter Model

The SPOT satellite is moving along a well defined orbital path and is always pointing towards the centre of the Earth. The projection centre of each image line equals the satellite's current position. So the exterior orientation parameters then depend on the satellite's position and velocity vector and on the changing platform attitude. In other words, these parameters can be modelled by consideration of the Keplerian elements which are as follows (Figure 5.2):

f : true anomaly;

Ω : right ascension of the ascending node;

i : orbital inclination;

b : semi-minor axis of the elliptical orbit;

a : semi-major axis of the elliptical orbit;

ω_p : argument of perigee.

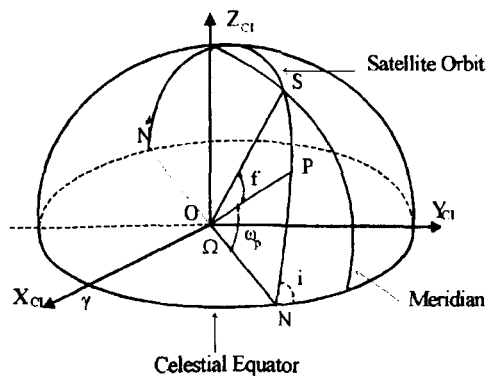

Figure 5.2 CI system (Keplerian parameters)

In Figure 5.2:

N and N′ : are ascending and descending node respectively,

P : is perigee;

γ : is First Point of Aries;

O : is the centre of the Earth;

S : is the position of the satellite on its orbit; and

$(X, Y, Z)_{CI}$: is the Conventional Inertial (CI) Coordinate system.

Some of the Keplerian elements can be replaced by other parameters such as:

r	: geocentric distance to the satellite;	e_x: e cos ω_p;
e	: orbit eccentricity;	e_y: e sin ω_p;
M	: mean anomaly;	E: eccentric anomaly;

Various approaches using orbital parameters have been investigated by different researchers. Some of them are reviewed briefly below.

5.2.1 Orbital Parameter Model Developed by Toutin and Guichard

Guichard (1983) and Toutin (1986) applied the laws of celestial mechanics to develop a mathematical model for object reconstruction using SPOT images. The satellite trajectory is modelled considering the disturbing forces, such as the flattening of the Earth, the irregularity in the Earth's form, etc. Because these forces are small in relation to the main force of terrestrial gravitation (resulting from the Earth's approximation to a spherical body with concentric homogeneous layers), the solution of a system affected by the disturbing forces consists of small variations compared to a system which is not affected by disturbing forces. Thus the same Keplerian parameters are used as in the undisturbed system, except that they are no longer constant in time. The resulting parameters: a(t), i(t), e(t), M(t), $\omega_p(t)$, and $\Omega(t)$ are known as oscillatory orbital parameters.

The different spaces with their reference systems that are considered in the mathematical representation for connecting the two-dimensional image coordinates to three-dimensional object coordinates are as follows (Figure 5.3):

(a) Image coordinate system (x,y), (Figure 5.3a); where:
- the origin is centred on the central point of image m_0;
- coordinate y is the position corresponding to the detector element number in a scan line;
- coordinate x is the line corresponding to the scan line number and is proportional to time.

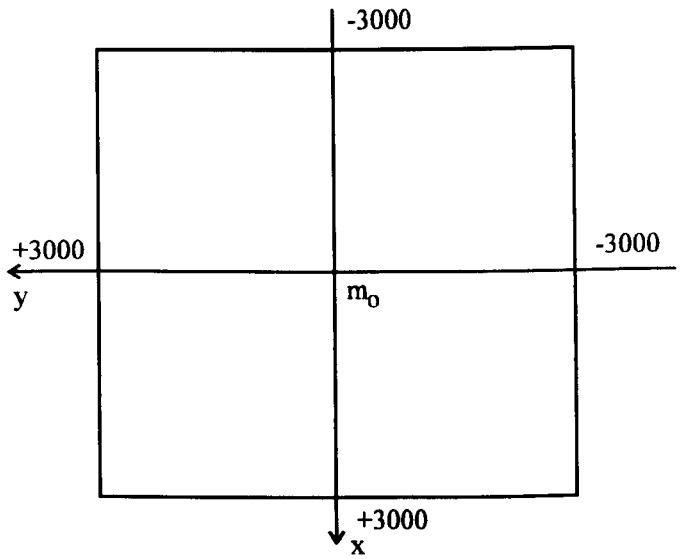

Figure 5.3a Image coordinate system

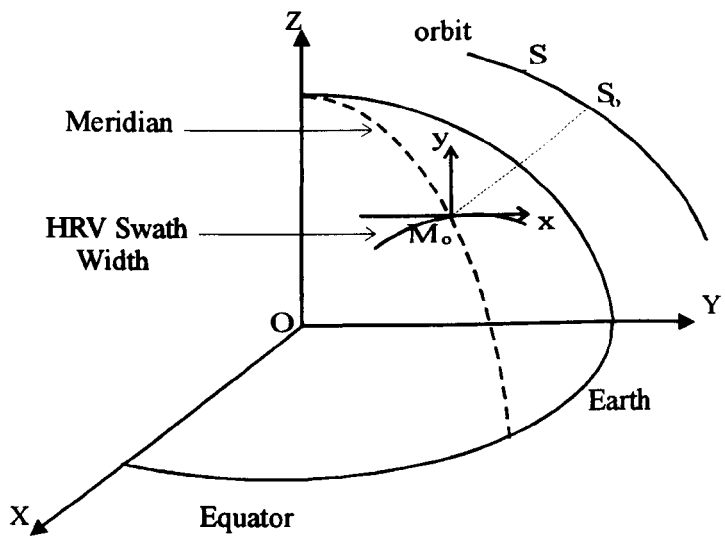

Figure 5.3b Local terrain coordinate system

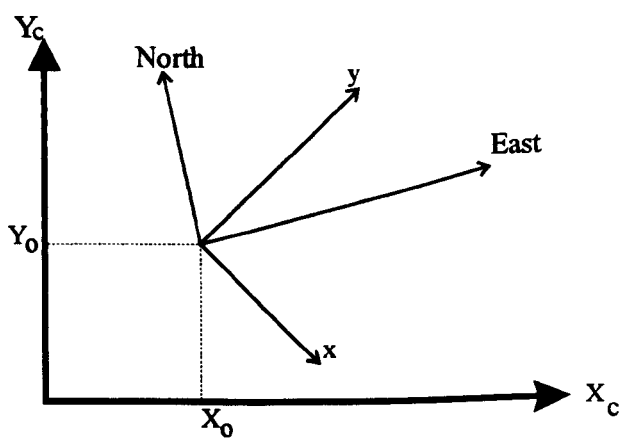

Figure 5.3c Cartographic coordinate system

(b) A local terrain coordinate system, with its terrain coordinates (X_L , Y_L , h), (Figure 5.3b); where:

- the origin is centred on M_0, the intersection of the centre line of the scene with the ellipsoid;
- coordinate X_L is the coordinate of the axis tangential to the ellipsoid in the central scan line plane; and
- coordinate Y_L is the coordinate of the perpendicular axis in the same plane tangential to the ellipsoid and in the direction of the ascending orbit;
-coordinate h is the altitude of the ground point.

(c) Cartographic coordinates (X_C, Y_C, Z_C) are defined in a global coordinate system (Figure 5.3c) in which the rectification or reconstruction of the terrain operates. A projection system such as the Universal Transverse Mercator (UTM) would typically form this particular reference system.

In this overall system, the viewing instrument is considered as a combination of sensor and satellite. The various distortions and geometric deformations related to the "vector + sensor" combination and the Earth's surface are integrated into a series of transformations (rotations and translations) to pass from the image coordinate system to the intermediate (or local terrain) system (Toutin 1986). Finally the resulting *collinearity equations* which allow the imaging ray to pass from ground (or cartographic) coordinates to image coordinates can be stated as follows (Toutin 1985, 1986 and 1990):

$$\begin{aligned} & Px + Y_L(1 + \delta\gamma X_L) - \tau H - H_0 \Delta T^* = 0 \\ & X + \theta H(\cos\chi)^{-1} + \alpha y(Q + \theta X - H(\cos\chi)^{-1}) - Q\Delta R = 0 \end{aligned} \qquad (5.1)$$

where:

$X = (X_L - a_1 Y_L)(1 + h/N_0) + a_2 Y_L^2 + a_3 X_L Y_L$; $\quad H = h - X_L^2/(2N_0)$;

P and Q : are scale factors along the y and x axes respectively;

θ and τ : are functions of the levelling angles in x and y respectively;

a_1 : is a function of the rotation of the Earth;

H_0 : is the satellite elevation at the centre line;

N_0 : is the normal to the ellipsoid;

χ, $\delta\gamma$, a_2, a_3 : are the known second order parameters, which are a function of satellite, scene centre and Earth centre geometry;

ΔT^*, ΔR : are the non-linear variations in attitude;

x, y : are the image coordinates;

X_L, Y_L, h : are the ground coordinates in a local terrain coordinate system.

In the above equations, x and y are the observations and the ground coordinates X_L, Y_L, h are the known parameters. The terms $\delta\gamma$, b, c as well as N_0, H_0 and χ are determined from the latitude of the scene centre and the orbital oscillatory parameters (Toutin 1985, 1986). Therefore the basis of this approach amounts to the determination by a least squares solution of the five unknowns P, Q, θ, τ, and a_1 using collinearity equations, plus three unknowns of translation and rotation between the local terrain system and the cartographic system (Toutin 1990). So a total of eight parameters have to be determined.

5.2.2 Orbital Parameter Model Developed by Gugan

Gugan (1987) developed a mathematical model for the orientation of SPOT imagery using the orbital parameters as defined in Section 5.2. This method is essentially similar to the method which was developed by Salmanowicz (1986) for the geometric corrections of linear array images.

In this approach, the x axis of the image coordinate system is considered to lie along the flight direction and the y axis lies in the direction of the image lines. The mathematical formulae used relate this image coordinate system directly to a geocentric coordinate system, with the X axis pointing towards the Greenwich meridian, the Z axis passing through the North Pole and Y axis being defined in such a way as to make the system right-handed.

According to this approach, the exterior orientation parameters of the SPOT image can be

modelled by consideration of the Keplerian elliptical orbital parameters (see Figure 5.2). Among these orbital parameters, two have very little effect on the image geometry. These are the semi-minor axis of the orbital ellipse (b), and the argument of perigee (ω_p) due to the very low eccentricity (e) of the SPOT orbit. The argument of the satellite with respect to perigee (f) and the right ascension of the ascending node (Ω) are both modelled by linear angular changes with time (since they are affected by the movements of the satellite along its orbital path and by the Earth's rotation) as follows:

$$\begin{aligned} f &= f_0 + f_1 x \\ \Omega &= \Omega_0 + \Omega_1 x \end{aligned} \tag{5.2}$$

where x corresponds to the line number and to the measure of time.

The sensor attitude, defined by the orthogonal rotation matrix R_0, and by its position in space (X_s) with respect to the geocentric coordinate system, can be found from the following orbital parameters:

$\Omega' = 180° - \Omega$; $\quad i' = i - 90°$; $\quad f' = 90° - (f + \omega_p)$; $\quad D = (0, 0, r)^t$

where

i : is the orbital inclination; $\quad a$: is the orbit semi-major axis; and

r : is the radius of the orbit and can be computed by : $r = a\,(1 - e^2)(1 + e\cos f)^{-1}$.

Due to the orbit perturbations, the sensor is unlikely to be pointing precisely towards the centre of the Earth. Therefore an additional attitude rotation must be considered. Finally the *collinearity equations* are expressed as follows:

$$(0, y, -c)^t = s\,R_A\,R_O\,([X_A] - [X_s]) \tag{5.3}$$

where

$[X_A]$: is the vector of object coordinates;

R_A : is rotation matrix ($R_A = R_\kappa R_\varphi R_\omega$);

$[X_s]$: is the vector of the satellite position coordinates;

R_O : is additional attitude rotation ($R_O = R_\Omega R_i R_f$);

c and s : are the focal length and scale factor respectively;

ω, φ, and κ : are roll, pitch, and swing or yaw respectively.

In this method, 7 parameters (f, Ω, i, a, ω, φ, κ) are assumed to be unknowns and are derived using the least squares method.

5.2.3 Orbital Parameter Model Developed by Westin

Westin (1990 and 1991) developed a mathematical model for the modelling of cross-track stereo images using orbital parameters. To define the position of the sensor in its orbit, he used six independent Keplerian parameters - a (semi-major axis of the elliptical orbit); e (eccentricity); i (orbital inclination); Ω (right ascension of the ascending node); ω_p (argument of perigee); and M (mean anomaly). To simplify the orbital modelling, he assumed that, during the timespan of one scene, the orbit is circular. Then to take into account the actual elliptical form of the orbit, he allowed the orbital radius to vary with time by fitting a third order polynomial in time. As a result, in his method, the set of orbital elements to be determined or estimated is reduced to four - i, Ω, t_0 (time at the ascending node), and r_0 (orbital radius at $t = t_0$). The attitude of the imaging system is described using a first order polynomial in time for the three rotation angles ω, φ, and κ as follows:

$$\omega = \omega_0 + \Delta\omega(t)$$

$$\varphi = \varphi_0 + \Delta\varphi(t)$$

$$\kappa = \kappa_0 + \Delta\kappa(t)$$

Thus 7 parameters (i, Ω, t_0, r_0, ω_0, φ_0, κ_0) need to be computed in his orbital parameter model.

To relate the image to the ground, Westin defined different coordinate systems as follows:

(i) Conventional Inertial System (CI): The orbital parameters are referred to this system. It has its origin at the Earth's centre with the X axis pointing to the Vernal Equinox, the Z axis pointing to the North Celestial Pole, and the Y axis completing a right-handed system.

(ii) Local Orbital Reference System: This is a moving coordinate system with its origin defined at the satellite's centre of mass. The Z axis is pointing in the same direction as the satellite position vector given in the CI system. The X axis is perpendicular to the Z axis and is located in the orbital plane, pointing in the

direction of satellite motion. The Y axis completes a right-handed system.

(iii) Attitude Measurement Reference System: This is a system which is fixed in relation to the satellite body. It coincides with the local orbital refrence system when the attitude angles are all zero.

(iv) Sensor Coordinate System: The coordinates of the detectors are referred to this system. The origin is positioned at the perspective centre of the optical sensor. The y axis is parallel to the array of detectors, pointing eastward in a descending pass. The z axis is perpendicular to the y axis, directed from the array towards the perspective centre. The x axis completes a right-handed system pointing in the direction of satellite motion.

(v) SPOT Ephemeris Reference System: The ephemeris from the SPOT header is given in a geocentric, Earth-fixed system (i.e. GRS80).

(vi) Ground Control Point Reference System: This is the local geodetic system in which the ground control points have been measured. Its origin is approximately at the scene centre, with its Y axis pointing North, its X axis pointing East and its Z axis in the direction of gravity.

Westin also used collinearity equations to relate the image space to the ground space. To establish this relationship, he used different orthogonal rotation matrices as can be seen in the following equation:

$$\begin{pmatrix} x \\ y \\ -f \end{pmatrix} = S\, R_{BS}^{t}\, R_{FB}^{t}\, R_{IF}^{t} \begin{pmatrix} X - X_0 \\ Y - Y_0 \\ Z - Z_0 \end{pmatrix} \tag{5.4}$$

where

x, y : are the image ccordinates of the image points;

f : is the focal length of the sensor;

S : is the scale factor;

R_{BS} : is the sensor-body transformation which relates the sensor coordinate system to the attitude measurement reference system. It accounts for the mirror angle, as well as for a constant alignment offset between the

individual sensors;

R_{FB} : is body-flight transformation which relates the attitude reference system to the local orbital reference system. It accounts for the attitude deviations;

R_{IF} : is the flight-inertial transformation which relates the local orbital reference system to the CI system. It is a function of the orbital parameters.

Using the mathematical model described above and a least squares adjustment procedure, he solved the equations for the exterior orientation parameters. In practice, it seems that he has used his method to test the SPOT images only in two dimensions (Westin, 1991). In other words, he has simply rectified a single image, although obviously it could be employed as the basis of a full 3D solution.

5.2.4 Orbital Parameter Method Developed by De Haan

De Haan (1991, 1992) developed a mathematical model again using orbital parameters for the orientation of SPOT imagery and based on the use of *collinearity equations*. Four coordinate systems have been considered in his modelling:

(i) Image coordinate system (x,y), with the y axis along the flight direction and a measure of time, and the x axis chosen to lie in the cross-track direction.

(ii) Attitude reference system with (at_1, at_2, at_3) coordinate axes. The attitude of the satellite's platform is measured with respect to these axes. It is a satellite fixed triad; the directions of the respective axes are shown in Figure 5.4.

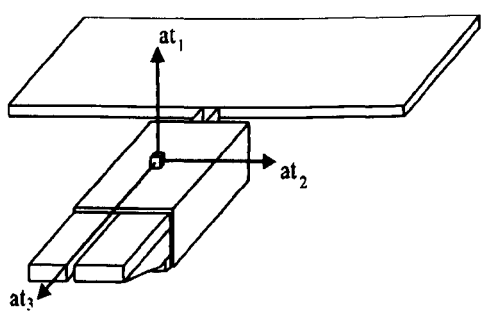

Figure 5.4 Attitude Reference System

(iii) Orbital reference system (p, r, w), which is a predefined target attitude with pitch (p), roll (r), and yaw (w) axes. The directions of these axes depend on the

satellite's position and velocity vector (Figure 5.5).

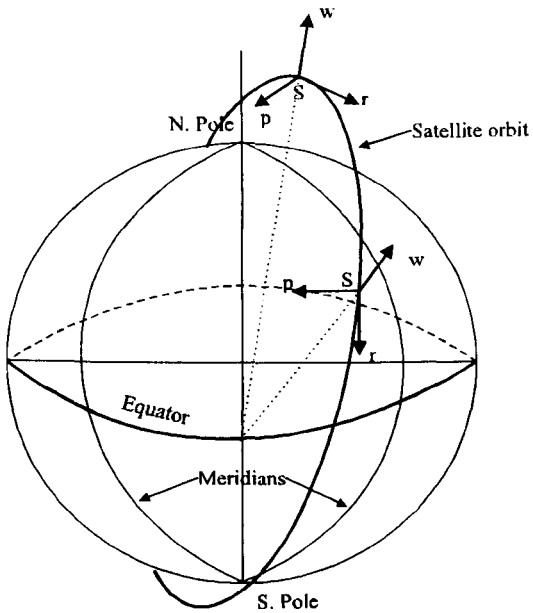

Figure 5.5 Orbital reference System

(iv) Ground coordinate system (X, Y, Z), which is a geocentric reference system.

In this method, arising from the dynamic nature of the SPOT imagery and the dependency of the exterior orientation parameters on the satellite's position and velocity vector and on the changing platform attitude, the satellite's orbit, the attitude of its platform and the characteristics of the optical instrument have been modelled.

The orbital arc provides the projection centre of each image row and defines the target attitude of the satellite's platform. The orbital arc is represented with the following equations of motion, where:

$$\begin{aligned} \frac{dX(t)}{dt} &= \dot{X}(t) & \frac{d\dot{X}(t)}{dt} &= \frac{dU}{dX} \\ \frac{dY(t)}{dt} &= \dot{Y}(t) & \frac{d\dot{Y}(t)}{dt} &= \frac{dU}{dY} \\ \frac{dZ(t)}{dt} &= \dot{Z}(t) & \frac{d\dot{Z}(t)}{dt} &= \frac{dU}{dZ} \end{aligned} \tag{5.5}$$

$X(t)$, $Y(t)$, $Z(t)$, $\dot{X}(t)$, $\dot{Y}(t)$, $\dot{Z}(t)$: are the satellite's position and velocity vector; and

U : is the gravitational potential of the Earth.

The satellite's attitude control system constantly tries to align the platform with the target attitude by applying torques. It continuously receives information on the current platform attitude from gyros, which provide the rate of change of the attitude taking place about the pitch, roll and yaw axes. Using this information, the satellite is only able to determine the target platform orientation with a certain precision. The orientation to which it tries to align the platform is not identical to the correct (nominal) target attitude. Besides, the differences between the two orientations slowly change with time due to gyro drift. Therefore, besides the high frequency variations, which are described by the velocity data, a slow trend remains, which has to be determined by image measurements and the use of ground control points (GCPs). In this approach, cubic splines have been introduced to model this slow trend.

The third and last aspect of the geometric procedure in De Haan's approach is to attempt to model the characteristics of the orbital instruments. This is carried out with the four look angles, which define the look directions of the two end positions of the detectors. These angles are provided as auxiliary data and can define the central projection geometry with respect to the attitude reference system (at_1, at_2, at_3). They describe the exact orientation of the scan line with respect to the actual platform attitude.

Finally, in the mathematical model that has been described by De Haan (1991), the collinearity equations have been written as follows:

$$(x \; y \; -f) = k R_{ia} R_{ao} R_{og} \; (X_P - X_s(t)) \tag{5.6}$$

where

x, y : image coordinates;

f : focal length;

k : a scale factor;

X_p : the ground coordinate vector of the image point;

X_s : the ground coordinate vector of the projection centre;

R_{og} : rotation matrix to transform the ground coordinate system into the orbital reference system (p,r,w) defined by the satellite's position and velocity vector at time t;

R_{ao} : rotation matrix to transform the orbital reference system to the attitude reference system (at_1,at_2,at_3) defined by the functions of the coefficients of the spline functions for pitch, roll, and yaw;

R_{ia} : rotation matrix to transform the attitude reference system to the instrumental system defined by the detector look angles.

Three groups of image geometry parameters, describing respectively the orbit, attitude and optical instrument as well as the ground coordinates of the measured image points are determined simultaneously with the following types of data:

(i) auxiliary data (satellite ephemeris, pitch, roll and yaw velocities, and the end detector look angles);

(ii) measured image coordinates;

(iii) terrain coordinates of the ground control points.

Altogether 13 independent unknowns (3 satellite's position, 3 satellite's velocity, 3 rotation angles (p, r, w), and 4 detector look angles) have to be determined with de Haan's method.

5.2.5 Orbital Parameter Model Described by Priebbenow

Priebbenow (1991) has also described a mathematical model for the geometric correction of SPOT imagery based on *collinearity equations* and using orbital equations to model the satellite trajectory. In this method, the variations of the satellite attitude with time are modelled using low order polynomials and the on-board attitude velocity measurements. Different coordinate systems are considered in this mathematical representation (see Figure 5.6):

(i) GRS 80 geocentric coordinate system (X_e, Y_e, Z_e): Its origin is the centre of the Earth with the Z_e axis pointing towards the North Pole and the Xe axis passing through the Greenwich Meridian. The Y_e axis completes the right ha nded system.

(ii) Model coordinate system (X_m, Y_m, Z_m): Its origin lies on the surface of the GRS

80 ellipsoid at the mean of the nominal scene centres, as determined from the auxiliary image data. The Z_m axis lies in the direction of the normal and the Y_m axis is the mean flight direction of the satellite, as determined from the scene orientation angles provided with the image auxiliary data. Finally the X_m axis completes the right handed system.

(iii) Ideal platform coordinate system (X_p, Y_p, Z_p): This coordinate system approximates the mean actual platform coordinate system whose axes are parallel to the roll, pitch and yaw axes of the platform. The origin of the ideal coordinate system coincides with the centre of the satellite. The Z_p axis lies in the direction of the normal to the satellite's position on the orbit; the X_p axis is tangential to the orbit trajectory and the Y_p axis completes the right handed system.

(iv) Image coordinate system (x', y'): Its origin is located at the centre of the central line of the image; the x' axis is in the flight direction; and the y' axis lies in the direction of the image lines.

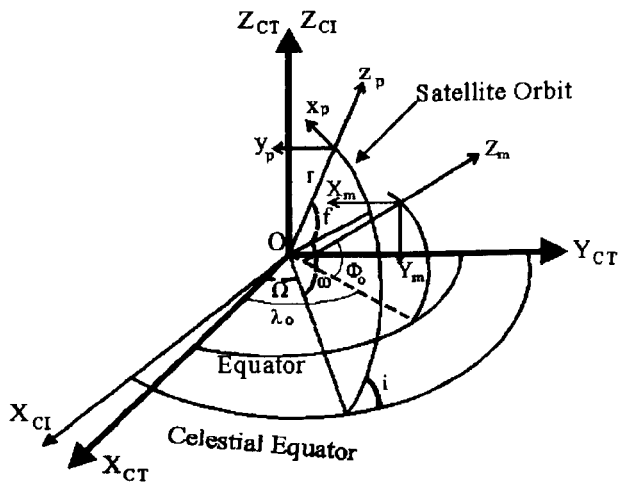

Figure 5.6 Model coordinate system (X_m, Y_m, Z_m); Ideal platform coordinate system (x_p, y_p, z_p); and satellite orbital parameters (r, i, Ω, ω, f), showing their relationship to the CT and CI coordinate systems.

In this method, the relationship between the image coordinate system and the object coordinate system has been described as follows:

$$\begin{pmatrix} 0 \\ y' \\ -f' \end{pmatrix} = \lambda M \begin{pmatrix} X_m - X_s \\ Y_m - Y_s \\ Z_m - Z_s \end{pmatrix} \quad , \quad x' = kt \tag{5.7}$$

where:

- x', y' are the observed image coordinates;

- f' is the focal length of the SPOT HRV instrument;

- k is a factor which defines the relationship between the image coordinate x' and the time t;

- t is the imaging time of each line relative to the imaging time of the centre of the image;

- λ is a scale factor;

- X_m, Y_m, Z_m are the coordinates of the ground point in the model coordinate system;

- X_s, Y_s, Z_s are the coordinates of the projection centre of SPOT in the model coordinate system. These coordinates will vary with time and are expressed in terms of the oscillating orbital parameters (r, i, Ω, ω, e_x, e_y), each of which varies with time;

- M is an orthogonal matrix which rotates the model coordinates into a system parallel to the HRV instrument's coordinate system. It can be expressed as follows:

$$M' = R_Z(\pi/2 - H)\, R_Y(\Phi_0)\, R_X(\lambda_0 - \Omega)\, R_Z(\pi/2 - i)\, R_Y(-\omega)$$
$$R_Z(\kappa_p)\, R(\varphi_p)\, R(\omega_p)\, R_Y(\varphi_m)\, R_X(\omega_m)\, R_Z(\kappa_m)$$

where

- the term, $R_Z(\pi/2 - H)\, R_Y(\Phi_0)\, R_X(\lambda_0 - \Omega)\, R_Z(\pi/2 - i)\, R_Y(-\omega)$ defines the angular relationship between the model coordinate system and the ideal platform coordinate system;

- Φ_0, λ_0, and H are angles used to define the model coordinate system,and are treated as fixed parameters;

- Ω, i, and ω are the oscillating parameters, defined above;

- ω_p, φ_p, and κ_p are the angular relationships between the ideal and the actual platform coordinate systems. These angles are small and vary with time. They consist of two components: polynomials expressed as a function of time, using the parameters (ω_0, ω_1, ω_2, φ_0, φ_1, φ_2, κ_0, κ_1, κ_2), and estimates of the yaw(t), pitch(t), and roll(t):

$$\begin{aligned} \omega_p &= \omega_0 + \omega_1 t + \omega_2 t^2 + \text{roll}(t) \\ \varphi_p &= \varphi_0 + \varphi_1 t + \varphi_2 t^2 - \text{pitch}(t) \\ \kappa_p &= \kappa_0 + \kappa_1 t + \kappa_2 t^2 + \text{yaw}(t) \end{aligned} \qquad (5.8)$$

- ω_m, φ_m and κ_m define the angular relationship between the HRV instrument and the actual platform coordinate system and are derived from the detector look angles provided with the satellite auxiliary data. They are treated as fixed parameters.

The following parameters are considered unknowns in this model:

(i) the four satellite orbital parameters r, i, Ω, and ω (N.B. e_x, e_y are not treated as unknowns and their values are derived from the satellite ephemeris records provided with the auxiliary image data);

(ii) the nine attitude angles ω_0, ω_1, ω_2, φ_0, φ_1, φ_2, κ_0, κ_1, and κ_2;

This makes a total of 13 unknown parameters. The values of these parameters are determined using the observed image coordinates and the ground coordinates of a set of ground control points in a least squares adjustment.

5.2.6 Orbital Parameter Model Described by Radhadevi and Ramachandran

To reduce the control point requirements to a minimum, Radhadevi and Ramachandran (1994) have developed a method for modelling the geometry of the SPOT satellite's imagery, again based on the *collinearity equations* and using orbital parameters. The approach is similar to the approach described by Westin (1990) (see Section 5.2.3) and used for extracting ground planimetric information (only 2D).

The initial orbit is estimated from the ephemeris data such as the values of i (inclination), Ω (right ascension of the ascending node), r (radius of the orbit at $t = t_0$) and v (central travel angle derived by: $v = 2\pi\ (t - t_0)\ /\ p$ where p is the period). Among these parameters, i, Ω, and v have been determined by a first order polynomial and r has been determined by a third order polynomial as follows:

$$\Omega = \Omega_0 + \Omega_1 t$$
$$v = v_0 + v_1 t \qquad (5.9)$$
$$i = i_0 + i_1 t$$

$$r = r_0 + r_1 t + r_2 t^2 + r_3 t^3 \qquad (5.10)$$

The attitude angles ω (roll), φ (pitch), and κ (yaw) have been taken into account as a function of time and are described by third order polynomials:

$$\begin{aligned} \omega(t) &= \omega_0 + \omega_1 t + \omega_2 t^2 + \omega_3 t^3 \\ \varphi(t) &= \varphi_0 + \varphi_1 t + \varphi_2 t^2 + \varphi_3 t^3 \\ \kappa(t) &= \kappa_0 + \kappa_1 t + \kappa_2 t^2 + \kappa_3 t^3 \end{aligned} \tag{5.11}$$

A number of coordinate systems are defined for use in the mathematical formulation of these equations:

(i) Image coordinate system (sensor coordinate system), with the x axis in the flight direction and y axis the cross-track direction.

(ii) Earth Central Inertial (CI) coordinate system, is the system to which the orbital parameters are referred. It has its origin at the Earth centre of mass and its X axis points to the Vernal Equinox. The Z axis points to the North Celestial Pole, while the Y axis completes a right-handed system. The control points transfer to this system before being employed in the collinearity equations.

(iii) Local Orbital reference system, ia a moving coordinate system with its origin defined at the satellite's centre of mass. The Z axis is pointing in the same direction as the satellite position vector given in the CI system. The X axis is perpendicular to the Z axis and lies in the orbital plane, pointing in the direction of the satellite motion. The Y axis completes a right-handed system.

(iv) Attitude measurement reference system, which is a fixed system in relation to the satellite body. It coincides with the local orbital reference system when the attitude angles are all zero.

The relation between image coordinate system and the geocentric coordinate system can then be expressed as:

$$[X] = [X_P] + d\,R_{GF}\,R_{FB}\,R_{BS}\,[x_s] \tag{5.12}$$

where:

$[x_s]$: the image points vector in the sensor system;

R_{GF} : transformation matrix which relates the orbital reference system to the CI

system. It is a function of time within one scene;

R_{FB} : transformation matrix which relates the attitude reference system to the orbital reference system. It accounts for the attitude deviations and thus it is a function of time within an individual scene;

R_{BS} : transformation matrix which relates the sensor coordinate system to the attitude reference system. It accounts for the mirror angle, as well as for the constant alignment offsets between the individual sensors. It is thus constant within one scene for one particular sensor;

$[X_P]$: satellite position vector;

$[X]$: ground control point position vector in the CI system;

d : scale factor.

Then the collinearity equations can be expressed as follows:

$$[x_s] = \frac{1}{d} M([X] - [X_P]) \tag{5.13}$$

or

$$\begin{pmatrix} 0 \\ y \\ -f \end{pmatrix} = \frac{1}{d} \begin{pmatrix} m_{11} & m_{12} & m_{13} \\ m_{21} & m_{22} & m_{23} \\ m_{31} & m_{32} & m_{33} \end{pmatrix} \begin{pmatrix} X - X_p \\ Y - Y_p \\ Z - Z_p \end{pmatrix} \tag{5.14}$$

where

$M = (R_{GF} R_{FB} R_{BS})^t$: is the rotation matrix used to transform the points from the geocentric coordinate system to the sensor coordinate system; and

f : is the principal distance of the SPOT HRV imager.

The twenty two unknown parameters (Ω_0, Ω_1, v_0, v_1, i_0, i_1, r_0, r_1, r_2, r_3, ω_0, ω_1, ω_2, ω_3, φ_0, φ_1, φ_2, φ_3, κ_0, κ_1, κ_2, and κ_3) will be determined by a least squares adjustment, based on the collinearity equations.

5.3 Multiple Projection Centre Model

Since the images acquired by linear array across-track stereo imagers are collected line by line during the same orbit, the individual images do not overlap, so the stereo model cannot be set up using data acquired in the same orbit based on the conventional mathematical model of photogrammetry. Instead it must use data acquired from an adjacent orbit with a tilting mirror being used to ensure that the same area is covered. Also, since the centre of the projection of each scanning line, even in the same image, is different from every other line, the collinearity equations of analytical photogrammetry are only valid for a single scan line (see Figure 5.7). In other words, there are multiple lines, each with its own projection centre (henece multiple projection centres) whose coordinate values have to be determined.

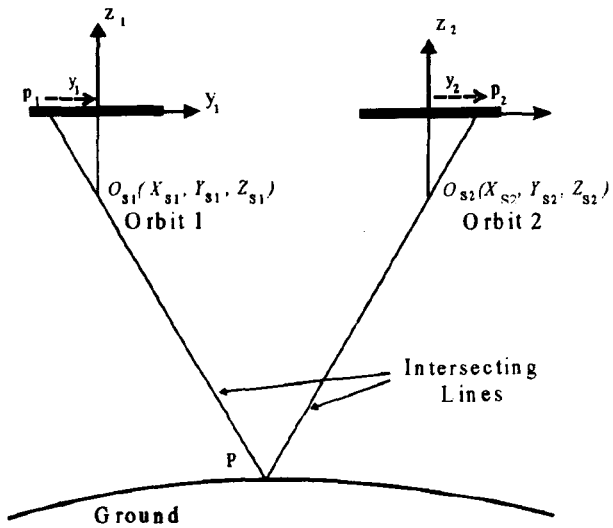

Figure 5.7 Section containing the y/z plane through the two projection centres for a single scan line on each of the two images

The exterior orientation of each single line is given by six parameters (three positional values and three rotations), which are highly correlated with the corresponding parameters of neighbouring lines. If the satellite's position and the attitude of the sensor with respect to the projection centre are determined for one reference line, then the small changes of the satellite's position and attitude for adjacent lines become functions of time during the period over which the whole scene is being imaged. These changes can be approximated well enough using polynomials based either on time or the line number. The appropriate order of polynomials to be adopted depends on the length of an orbit; the stability and rate of

change in the satellite and sensor attitude; the degree of accuracy required; the number of control points; and the computational facilities available. Various researchers, e.g. Shibasaki et al. (1988), Deren and Jiayu (1988), Ganguly (1991), Kratky (1987, 1988a, 1988b) have used the multiple projection centre model for geometric corrections of SPOT images. However the basic approach is the same with all of these; the differences lie mainly in the degree of polynomial used and in the incorporation of some additional information or parameters and the way in which this is done. Thus, in general terms, in all of the methods employing the multiple projection centre model, the exterior orientation parameters (X_s, Y_s, Z_s, ω_s, φ_s, κ_s) have been approximated by polynomials of the time or line number, for example as follows:

$$\begin{aligned} X_s &= X_0 + X_1 x_i + X_2 x_i^2 & Y_s &= Y_0 + Y_1 x_i + Y_2 x_i^2 \\ Z_s &= Z_0 + Z_1 x_i + Z_2 x_i^2 & \omega_s &= \omega_0 + \omega_1 x_i + \omega_2 x_i^2 \\ \varphi_s &= \varphi_0 + \varphi_1 x_i + \varphi_2 x_i^2 & \kappa_s &= \kappa_0 + \kappa_1 x_i + \kappa_2 x_i^2 \end{aligned} \qquad (5.15)$$

where

x_i : the image coordinate in the flight direction (time dependent);

$X_0, Y_0, Z_0, X_1, Y_1, Z_1, X_2, Y_2, Z_2$: are coefficients of the constant, linear, and quadratic terms of the image coordinates in the flight direction to define the projection centre's position;

$\omega_0, \varphi_0, \kappa_0, \omega_1, \varphi_1, \kappa_1, \omega_2, \varphi_2, \kappa_2$: are coefficients of the constant, linear, and quadratic terms of the image coordinates in the flight direction to define the orientation angles related to the reference line.

According to the collinearity conditions (Figure 5.7) and the above considerations, the following equations can be derived:

$$\begin{pmatrix} x_i \\ y_i \\ -c \end{pmatrix} = K R_t \begin{pmatrix} X_i - X_s \\ Y_i - Y_s \\ Z_i - Z_s \end{pmatrix} \qquad (5.16)$$

where

K : scale factor;

c : principal distance;

x_i , y_i : the image coordinates of the image point i;

X_i , Y_i , Z_i : the ground coordinates of the image point i;

X_s , Y_s , Z_s : the ground coordinates of the projection centre; and

R_t : the rotation matrix of the attitude parameters, including constant, linear, and quadratic terms.

The collinearity equations will be linearized by Taylor series and, after measuring the corresponding points in the image, the values of the unknown parameters will be derived from a least squares solution using ground control points.

5.4 Additional Parameter Model

This mathematical model has been described by Konecny (1987), Konecny et al. (1987), and Kruck (1987) and has been implemented in IPI-Hannover's BINGO program for the block adjustment of SPOT images. It follows the traditional method of removing systematic errors in photogrammetric block adjustment through the use of additional parameters, only in this case, it is combined with the collinearity equations for a linear array sensor. According to this method, a regular determinable geometry is assumed and the irregularities detected by the ground control point (GCP) discrepancies are formulated as additional parameters (Konecny 1987).

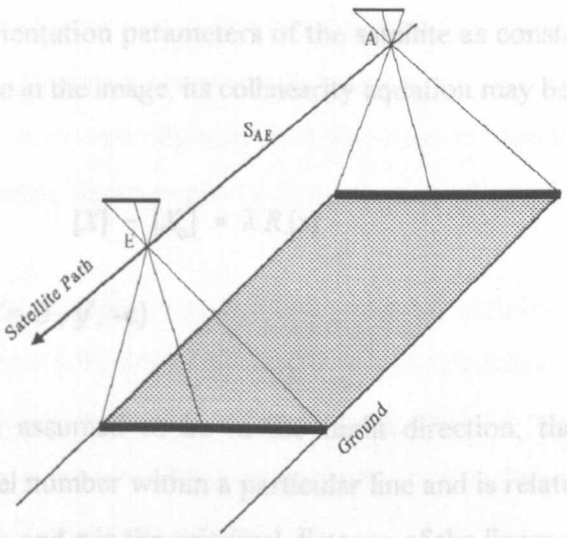

Figure 5.8 CCD linear array with non-accelerated uniform movement

Figure 5.8 illustrates the assumption for a regular linear movement of a CCD linear array scanner. The sensor is moving uniformly without acceleration during the period of acquisition of the image from A to E. The flight path from A to E may be considered to be straight. The centre of the projection moves linearly from A to E, which means:

$$[X_{0,i}] = [X_{0,A}] + (\frac{S_i}{S_{AE}})([X_{0,E}] - [X_{0,A}]) \tag{5.17}$$

where

$[X_{o,i}]$: the positional vector of the projection centre at time t_i;

$[X_{o,A}]$: the positional vector of the projection centre for the first line;

$[X_{o,E}]$: the positional vector of the projection centre for the last line;

S_i : distance from $X_{o,A}$ to $X_{o,i}$; and

S_{AE} : distance from $X_{o,A}$ to $X_{o,E}$.

The ratio of the distances in the above equation may be replaced by:

$$\frac{i}{n} = \frac{S_i}{S_{AE}} \tag{5.18}$$

where i is the number of the actual line (or time of exposure); and n is the total number of lines.

Assuming the angle orientation parameters of the satellite as constant, then for a discrete point located on one line in the image, its collinearity equation may be formulated according to:

$$[X] - [X_0] = \lambda R[x] \tag{5.19}$$

where: $[x] = (x' = 0 , y', -c)$

The x' axis has been assumed to be in the flight direction; the y' coordinate value corresponds to the pixel number within a particular line and is related to an origin located at the centre of the line; and c is the principal distance of the linear array sensor.

In reality, the angles ω, φ, and κ are not constant, because the accelerations due to the non-uniform gravity field of the Earth and the non-circularity of the orbit (i.e. its elliptical form) cause the platform not to move in its defined or nominal orbit. In this case, the six parameters of orientation (X_0, Y_0, Z_0, ω, φ, κ) are functions of time. On the other hand, they are highly intercorrelated within a line, specifically φ with X_0 and ω with Y_0 (assuming that the flight is taking place in the x' direction) and Z_0 with the variation in the satellite altitude which leads to a change in scale. This results from the fact that the angular coverage of a single line is small, for example, in the case of SPOT, it is only 4.1 degrees. Therefore changes of X_0, Y_0, and Z_0 do not need to be modelled if φ, ω and the affinity parameters are included in the modelling.

In terms of the actual mathematics adopted in this solution, the changes in ω, φ, and κ may be expressed as additional parameters which change the image geometry. Therefore, the orientation angles are treated as time invariant. Within this approach, for each image, the coordinates of the image centre point and the orientation angles, as well as the additional parameters, are considered to be unknowns in a bundle adjustment. By using the satellite orbital data (ephemerides), approximations of the unknowns can be computed. In addition, the ground control points and tie points will be included in the adjustment.

5.5 Direct Linear Transformation Model

Recently El-Manadili and Novak (1996) developed a mathematical model for the geometric corrections of stereo SPOT imagery based on the well-known Direct Linear Transformation (DLT) model. This was developed originally by Abdel-Aziz and Karara (1971) and has been much used with non-metric photography in close-range applications of photogrammetry.

In this approach, a pixel coordinate system is considered with its origin at the left upper corner of the image (Figure 5.9), where the U axis is in the direction of the image lines, and the V axis is in the direction of the flight. The image coordinate system is considered with the same origin as the pixel coordinate system and its x and y directions, in the same directions as the U and V axes respectively.

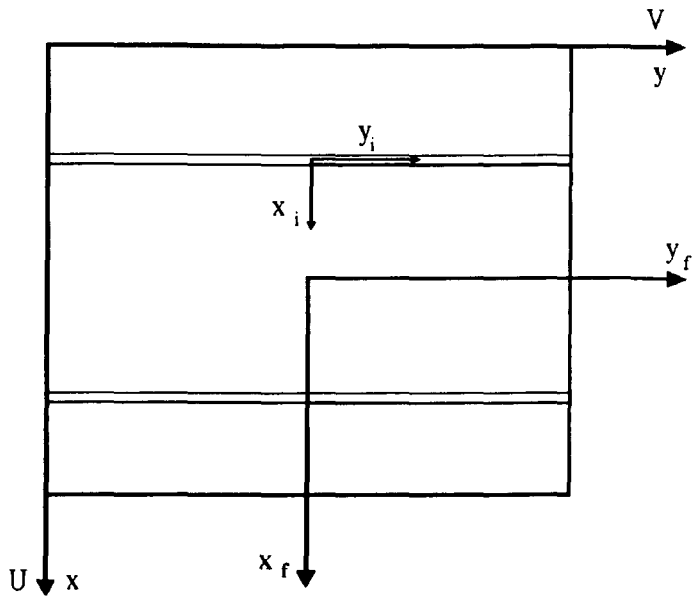

Figure 5.9 Pixel (U,V), Image (x,y), Frame (x_f,y_f), and Scan line (x_i,y_i)coordinate systems as defined in the DLT method of Manadili and Novak (1996)

A frame coordinate system is considered with its origin at the centre of the scene, its x_f axis in the direction of flight and its y_f axis perpendicular to the x_f axis in the scene plane. Regarding the dynamic nature of SPOT imagery, for each scan line, another coordinate system, termed the scan line coordinate system is considered with its origin at the centre of the line, its x_i axis in the direction of the flight and its y_i axis perpendicular to the x_i axis along the pixels on the scan line.

The ground coordinate system is considered to be a Shifted GeoCentric Ground Coordinate System (SGCGCS). The origin of the GeoCentric Ground Coordinate System (GCGCS) is the centre of gravity of the Earth; its X_G axis is directed towards the Greenwich meridian; the Z_G axis points towards the North Pole, and the Y_G axis makes the system right-handed. The SGCGCS has its origin in the centre of the ground area while its three axes remain parallel to GCGCS (Figure 5.10).

The mathematical relationship between these two systems as depicted in Figure 5.10, can be shown to be as follows:

$$[X_{GS}] = [X_G] - [D_f] \tag{5.20}$$

where

$[X_{GS}]$ and $[X_G]$: are the vectors of the point coordinates in the SGCSCS and GCGCS systems respectively; and

$[D_f]$:is the vector of the position of the centre of the ground area in the GCGCS system.

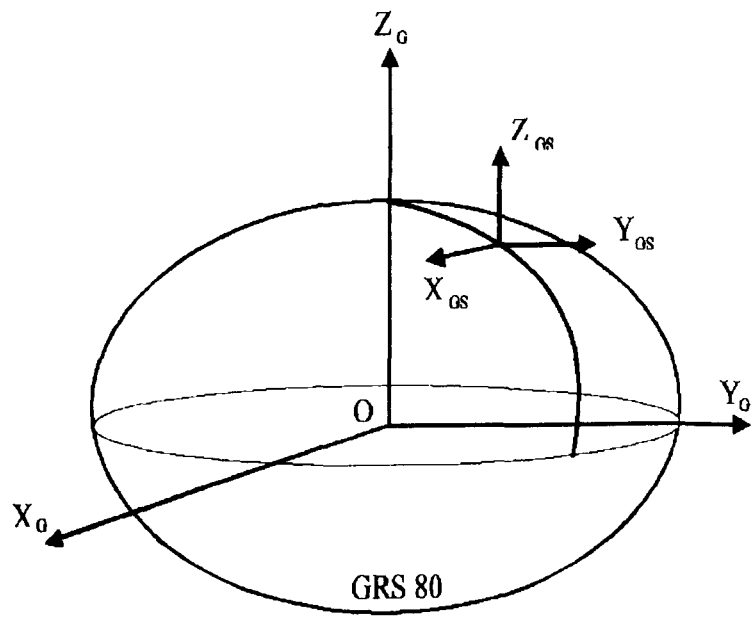

Figure 5.10 SGCGCS and GCGCS coordinate systems

According to this approach, the pixel coordinates (U,V) are first corrected for the systematic errors caused by the rotation of the Earth and the off-nadir viewing. Then, to implement the regular collinearity equations for the image coordinates of a point, the points are transformed to the frame coordinate system. First, the coordinates of the points in the scan line coordinate system must be corrected for the satellite's deviations from their nominal positions, the perturbations in the satellite velocity vectors, and the rates of change of the sensor attitude angles. Applying these corrections, and carrying out the substitution of scan line coordinates with pixel coordinates and finally the image coordinate system, and then expanding the consequent collinearity equations will result in the conventional DLT model with 11 linear orientation parameters as follows:

$$x = \frac{L_1 X_{GS} + L_2 Y_{GS} + L_3 Z_{GS} + L_4}{L_9 X_{GS} + L_{10} Y_{GS} + L_{11} Z_{GS} + 1}$$
$$y = \frac{L_5 X_{GS} + L_6 Y_{GS} + L_7 Z_{GS} + L_8}{L_9 X_{GS} + L_{10} Y_{GS} + L_{11} Z_{GS} + 1} \qquad (5.21)$$

where

X_{GS}, Y_{GS}, Z_{GS} : are the coordinates of the projection centre in the SGCGCS coordinate system; and

L_1, L_2, ..., L_{11} : are the eleven linear orientation parameters defining the relationship between two-dimensional image space and three-dimensional object space.

These parameters can be computed through the use of a suitable bundle adjustment program and an appropriate number of ground control points.

5.6 A Brief Comparison and Discussion of the Different Methods

As can be seen from the above Sections, in the orbital parameter method (Section 5.2), the researchers concentrate on the motion of the satellite and consequently on the behaviour of the imaging instrument along a defined orbit, which can be viewed as being a significant advantage for space imaging systems. The exterior orientation parameters of the sensors can be defined by a sophisticated orbital model derived from the orbital parameters which has the effect of reducing the number of ground control points required to implement the method. In fact, the accuracy of the satellite ephemeris is not yet good enough to provide the precise exterior orientation parameters that are required. However, using all the available information in the mathematical modelling of the terrain reconstruction will reduce the number of ground control points that are required. The other advantage of utilizing the orbital parameter method is that the object coordinates of the image points can be computed directly in a geocentric coordinate system. This will avoid the effects of Earth curvature. Also since the position of the projection centre of the sensor (the origin of the image coordinate system) lies on the orbit itself, it becomes a function of orbital elements and does

not inherently include Earth rotation.

Conceptually, all of the orbital parameter methods are basically the same; the differences arise from the different orbital elements that are being considered and the different intermediate spaces that are utilized and how they are filled. This results in the different number of unknowns which have to be solved in the various SPOT bundle adjustment programs that have been developed based on this method. For example, in the mathematical model described by Toutin and Guichard, 8 independent unknowns need to be computed; whereas in Gugan's method, there are 7; in Westin's method, 7; in De Haan's method, 17; in Priebbenow's method, 13; and in Radhadevi and Ramachandran's method, 22.

By contrast to the orbital parameter method, those investigators using the multiple projection centre method (Section 5.3), look at the images acquired by linear array imaging systems in much the same way as aerial photographs taken with a camera. They consider two spaces for the reconstruction and modelling of the terrain - the image space and the object or ground space. Then, regarding the dynamic nature of the image, each single line is considered as a photograph. It is evident that, since the orbital information of the imaging system is not used in this method, more ground control points have to be used to replace this lack of information by comparison with the orbital parameter method. In general, the number of unknowns, which has to be solved in this method, depends on the type of polynomial that has been used to model the changes in the position and attitude of the imaging system. For example, in the case of equation (5.15), 18 unknown parameters should be solved in the bundle adjustment program.

In the additional parameter method (Section 5.4), not only one single line but the whole image comprising many lines acquired by a linear array system is considered in exactly the same way as a photograph. Then the distortions present in the image, arising from the dynamic nature of the linear array imaging systems, are considered as systematic errors that can be modelled by a set of additional parameters. This means that, in the collinearity equations, a single set of common ω, φ, and κ values is adopted and the changes in these parameters are then modelled as the additional parameters. Altogether 9 orientation

parameters and 7 additional parameters have to be determined for each of the images with this method. Again the number of ground control points required to reach a specific accuracy with this method is more than that required for the orbital parameter method for the reasons that have already been explained above.

In the DLT method (Section 5.5), as with the additional parameter method, the whole linear array system is considered in exactly the same way as a photograph. The difference lies in the image coordinate system used in the collinearity equations. In the additional parameter method, the frame coordinate system has been used as the image coordinate system in the collinearity equations. However, in the DLT method, the image coordinate system is coinciding with the pixel coordinate system and is used directly in the collinearity equation. This is the reason why the collinearity equations become the DLT equations. Consequently 11 linear orientation parameters must be determined for each image in this method. Since the parameters are linear, linearization of the DLT equations is very simple and this will save in the time and power required for the bundle adjustment program. Again, the number of ground control points required to reach a specific accuracy with this method is greater than that required for the orbital parameter method.

In this research, the orbital parameter model has been selected for reconstruction of the terrain using both cross-track and along-track stereo imagery. One reason for this is that, in the opinion of the present author, this model is more precise and allows a very good mathematical relationship to be established between the geometry of the image and the object coordinate system. Furthermore, if the model used for cross-track imagery is similar to that which has been used for the along-track stereo imagery, this could help greatly in the programming of both these solutions as well as in the comparison of the results obtained with these two different types of pushbroom scanner imagery.

In the following Section, the mathematical modelling of cross-track stereo imagery, based on the orbital parameter model, which has been developed by the present author is explained.

5.7 The Mathematical Modelling of the Cross-Track Stereo Images Used in the Present Project

As already discussed in Section 5.2, the orbital parameter model can be applied to cross-track stereo images in order to determine their exterior orientation parameters. The model adopted here is in principle similar to that developed by Gugan and Dowman (1988) and outlined in Section 5.2.2, but it has been devised quite independently by the present author and, as will be seen, differs substantially from it. The satellite is moving in a defined elliptical orbit. The position and the attitude of the sensor are changing in a systematic way so as to keep it pointing towards the centre of the Earth. An orbital resection method has been developed to model these changes by finding the orbital parameters of the satellite. A bundle adjustment program has been developed to determine these parameters using ground control points. Within this program, different coordinate systems need to be considered for the transformation between the image and object coordinate systems.

5.7.1 Image Coordinate System

The coordinates of the linear array of detectors are referred to this system. The origin is positioned at the centre of the scan line which moves along the orbit of the satellite. The y axis is parallel to the array of detectors, pointing Eastward in a descending pass. The z axis is perpendicular to the y axis, directed from the scan line along the optical axis in the direction opposite to that of the ground. The x axis completes a right-handed system pointing in the direction of satellite motion (see Figure 5.11).

As mentioned before, the pushbroom scanners have a linear array of thousands of detectors. This array images a strip of the Earth's surface beneath the satellite. Consequently, an image is built up by combining thousands of these linear strips, as the satellite moves along its orbit. However, the linear array itself passes through the principal point in the focal plane where the x coordinate is zero and the z coordinate is always constant. The x coordinate of the resulting image is therefore a measure of the time at which a point was imaged relative to the origin. It should be noted that, since stereo data is acquired by altering the cross-track

mirror pointing, the stereo base is in the y direction and the normal sense of the x and the y parallaxes will be reversed.

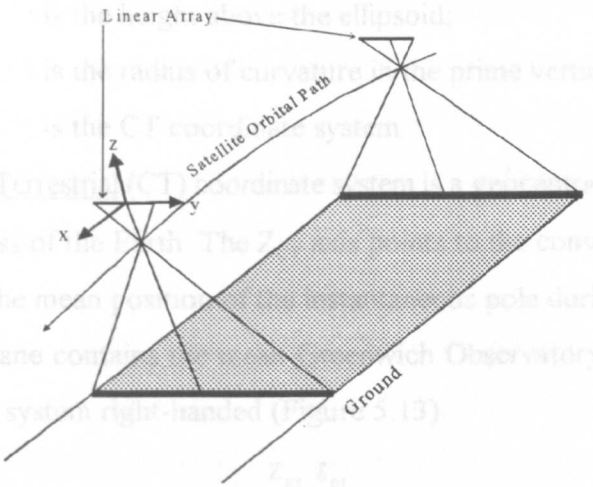

Figure 5.11 Image coordinate system for a linear array sensor

5.7.2 Object Coordinate Systems

The relevant object coordinate systems are as follows:

a) The Universal Transverse Mercator (UTM) coordinate system (X_{UTM} , Y_{UTM}) and normal (geoidal) height (H) above mean sea level.

b) The Ellipsoidal Geodetic (EG) coordinate system is selected so as to approximate the figure of the Earth as a biaxial ellipsoid. Each point is defined in this system by its geodetic longitude (λ_{EG}), geodetic latitude (ϕ_{EG}), and geodetic height (h_{EG}), i.e. its height above the ellipsoid (see Figure 5.12).

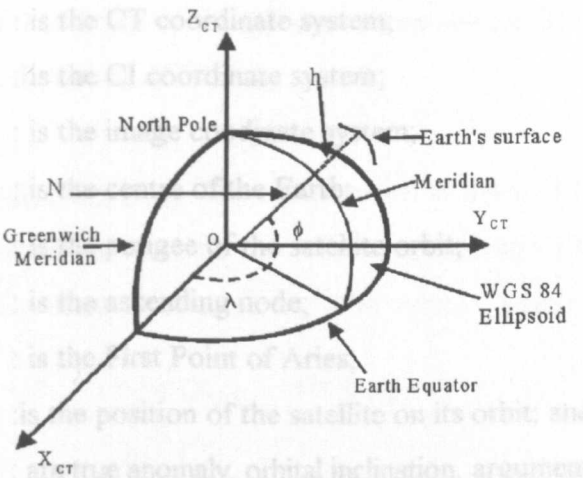

Figure 5.12 CT and EG coordinate system

where

ϕ, λ : are the geodetic latitude and longitude;

h : is the height above the ellipsoid;

N : is the radius of curvature in the prime vertical; and

$(X, Y, Z)_{CT}$: is the CT coordinate system.

c) The Conventional Terrestrial (CT) coordinate system is a geocentric system, i.e. its origin is at the centre of mass of the Earth. The Z_{CT} axis points to the conventional origin (CIO), which is defined as the mean position of the instantaneous pole during the period 1900 to 1905; the $(XZ)_{CT}$ plane contains the mean Greenwich Observatory; and the Y_{CT} axis is selected to make the system right-handed (Figure 5.13).

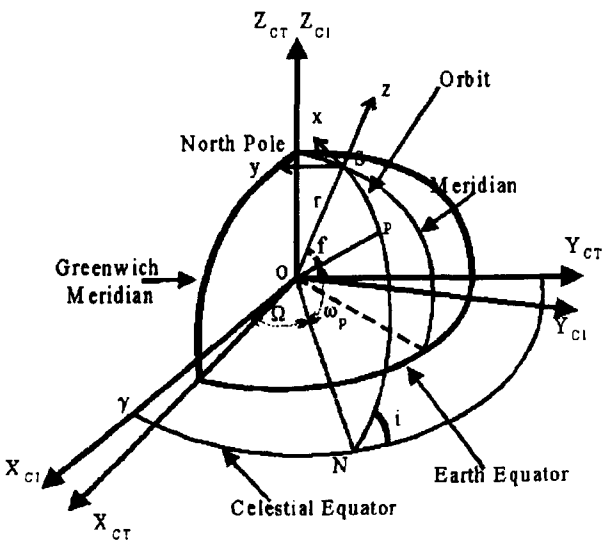

Figure 5.13 CI, CT, and Image coordinate systems

where

$(X, Y, Z)_{CT}$: is the CT coordinate system;

$(X, Y, Z)_{CI}$: is the CI coordinate system;

x, y, z : is the image coodinate system;

O : is the centre of the Earth;

P : is the perigee of the satellite orbit;

N : is the ascending node;

γ : is the First Point of Aries;

S :is the position of the satellite on its orbit; and

f, i, ω_p, Ω : are true anomaly, orbital inclination, argument of perigee, and right ascension of the ascending mode, respectively.

d) The Conventional Inertial (CI) coordinate system, is a space fixed coordinate system, i.e. a coordinate system which is at rest or in a uniform rectilinear motion without any acceleration. The basic theory of motion for artificial satellites has been developed with respect to such a system, which is why this system is used for the description of satellite motion. The origin of the system is supposed to coincide with the Earth's centre. The Z-axis is oriented towards the North Pole and the X axis to the *First Point of Aries* (γ). The Y axis completes a right handed system (see Figure 5.13).

In the method developed by the present author, the bundle adjustment is normally carried out in the CT system, while the plotting carried out for map making is expressed in UTM coordinates and normal (geoidal) height. So, before and after the bundle adjustment, both a transformation and the inverse transformation of coordinates will be necessary between these various object coordinate systems defined above.

5.7.2.1 Transformations Between the Object Coordinate Systems

I) Direct Coordinate Transformation from UTM Map Projection System to Conventional Terrestrial Coordinate System

Based on the available mathematical formula, if there is a requirement to transform Universal Transverse Mercator (UTM) coordinates into the Conventional Terrestrial (CT) coordinate system, all of the points must be first transformed into the Ellipsoidal Geodetic coordinate system (EG) and then to the CT coordinate system. The procedures for these two operations can be described as follows:

(a) UTM to EG coordinate system: The computation in the UTM system is carried out using the established general equations for the Transverse Mercator (TM) projection, taking into account the specific characteristics of the UTM version, where:

$$X_{TM} = \left(\frac{1}{k_0}\right)(X_{UTM} - 500{,}000)$$

$$Y_{TM} = \frac{Y_{UTM}}{k_0} \qquad (5.22)$$

where:

X_{TM} : Easting in TM X_{UTM} : Easting in UTM

Y_{TM} : Northing in TM Y_{UTM} : Northing in UTM

k_0 : central meridian projection scale factor in UTM

Then the computation of the EG coordinates from the UTM values can be summarised as follows:

$$\phi = \phi' - (VI)\, X_{TM}^2 + (VII)\, X_{TM}^4 - \bar{C} \tag{5.23}$$

$$\lambda = (VIII)\, X_{TM} - (IX)\, X_{TM}^3 + \bar{D} \tag{5.24}$$

where ϕ is the latitude of the point; and λ is the longitude of the point.

Note: The full expressions of the terms ϕ', *VI, VII, VIII, IX,* $\bar{C}$, $\bar{D}$ can be found in Appendix A.

(b) Ellipsoidal Geodetic coordinate system (EG) to the Conventional Terrestrial (CT) coordinate system: The transformation equations between the EG and CT systems with respect to Figure 5.13 can be shown to be as follows:

$$\begin{pmatrix} X_i \\ Y_i \\ Z_i \end{pmatrix}_{CT} = \begin{pmatrix} (N_i + h_i)\cos\phi_i \cos\lambda_i \\ (N_i + h_i)\cos\phi_i \sin\lambda_i \\ (N_i \frac{b^2}{a^2} + h_i)\sin\phi_i \end{pmatrix} + \begin{pmatrix} X_e \\ Y_e \\ Z_e \end{pmatrix}_{CT} \tag{5.25}$$

where:

$$N_i = \frac{a^2}{\sqrt{a^2 \cos^2\phi_i + b^2 \sin^2\phi_i}} \text{ ; and}$$

a is the semi-major axis of the ellipsoid; b is the semi-minor axis of the ellipsoid; and X_e, Y_e, Z_e are the CT coordinates of the ellipsoid's centre.

Note that in equation (5.25), it is considered that there is only a shift between the centre of the datum in which the EG coordinate system is defined and the centre of the ellipsoid datum in which CT coordinate system is defined (WGS 84). But usually the UTM projection

system is defined based on a local geodetic datum such as European Datum, 1950, or Clarke 1880, and so on. Therefore rotations between the two datums should be considered too.

II) Inverse Coordinate Transformation, from CT to UTM Coordinate System

The procedures for these operations can be described as follows:

(a) Conventional Terrestrial (CT) to the Ellipsoidal Geodetic (EG) system: According to equation (5.25), the following formula can be derived:

$$\begin{pmatrix} X \\ Y \\ Z \end{pmatrix} = \begin{pmatrix} X_i - X_e \\ Y_i - Y_e \\ Z_i - Z_e \end{pmatrix}_{CT} = \begin{pmatrix} (N_i + h_i)\cos\phi_i \cos\lambda_i \\ (N_i + h_i)\cos\phi_i \sin\lambda_i \\ (N_i \frac{b^2}{a^2} + h_i)\sin\phi_i \end{pmatrix} \tag{5.26}$$

The computation of the EG coordinates from the CT coordinates is done by a series of iterations. From equation (5.26):

$$Z = (N + h - e^2 N)\sin\phi \tag{5.27}$$

where, $e^2=(a^2 - b^2)/a^2$.

If $p=(X^2 + Y^2)^{1/2}$ then, from equation (5.24): $p = (N+h)\cos\phi$ and finally:

$$\frac{Z}{p} = \tan\phi\,(1 - \frac{e^2 N}{N + h}) \tag{5.28}$$

The iterations are initiated by first solving ϕ from the above equation. Putting $h=0$,

$$\phi^{(0)} = \arctan(\frac{Z}{p}(1 - e^2)^{-1}) \tag{5.29}$$

The kth iteration then consists of evaluating successively $N^{(k)} = N(\phi^{(k-1)})$ from equation (5.26); $h^{(k)} = h(\phi^{(k-1)}, N^{(k)})$ from $p = (N+h)\cos\phi$; and $\phi^{(k)} = \phi(N^{(k)}, h^{(k)})$ from equation (5.27).

These iterations are repeated until the following inequalities are satisfied for some a priori chosen value of ϵ:

$$\left\| h^{(k)} - h^{(k-1)} \right\| < \alpha\,\epsilon \qquad \text{and} \qquad \left\| \phi^{(k)} - \phi^{(k-1)} \right\| < \epsilon$$

Once ϕ and h have been found, λ is evaluated from the first two equations (5.26):

$$\lambda = \arctan(Y/X).$$

(b) Ellipsoidal Geodetic (EG) to UTM system: According to the definitions already described in the direct transformation from UTM to the EG coordinate system given in I(a), the following formulae can be derived:

$$X_{TM} = (IV)\,\lambda + (V)\,\lambda^3 + \bar{B} \tag{5.30}$$

$$Y_{TM} = (I) + (II)\,\lambda^2 + (III)\,\lambda^4 + \bar{A} \tag{5.31}$$

$$X_{UTM} = 500{,}000 + k_0 X_{TM} \tag{5.32}$$

$$Y_{UTM} = k_0 Y_{TM} \tag{5.33}$$

The final results are the required UTM coordinates. The full expressions of the terms *I, II, III, IV, V,* $\bar{A}$ and $\bar{B}$ can be found in Appendix A.

5.7.3 Derivation of the Collinearity Equations

The collinearity equations are used to relate the image coordinates and the object (CT) coordinates. The instantaneous position of the satellite is defined normally with respect to the CI system using the six Keplerian parameters described in Section 5.1 and shown in Figure 5.2 and can be computed using these elements as follows:

$$\begin{pmatrix} X_0 \\ Y_0 \\ Z_0 \end{pmatrix}_{CI} = R_3(\pi-\Omega)\; R_1(i-\frac{\pi}{2})\; R_2(\frac{\pi}{2}-(f+\omega_p)) \begin{pmatrix} 0 \\ 0 \\ r \end{pmatrix} \tag{5.34}$$

where, $r = a\,(1 - e^2) / (1 + e \cos f)$; and

X_0, Y_0, Z_0 : are the coordinates of the satellite in the CI coordinate system;

f : is an element describing the position of the satellite in the orbital

plane - essentially it is the argument or angular distance of the satellite after passing perigee, as measured at the Earth's centre; in the literature, it is often called (rather confusingly) the true anomaly though it has nothing to do with gravity anomalies.

Ω : is the right ascension of the ascending node;

i : is the orbital inclination;

e : is the orbit eccentricity;

a : is the semi-major axis of the elliptical orbit; and

ω_p : is the argument of perigee.

Expanding the above equation will result in the following:

$$\begin{pmatrix} X_0 \\ Y_0 \\ Z_0 \end{pmatrix}_{CI} = r \begin{pmatrix} \cos\Omega \cos(f+\omega_p) - \sin\Omega \sin(f+\omega_p) \cos i \\ \sin\Omega \cos(f+\omega_p) + \cos\Omega \sin(f+\omega_p) \cos i \\ \sin(f+\omega_p) \sin i \end{pmatrix} \tag{5.35}$$

The collinearity equation relates the points in the object coordinate system to the corresponding points in the image coordinate system. As mentioned before, in the case of linear array imagery, this type of equation can be generated for each line. The relationship between these two coordinate systems is based on the three rotations using Keplerian parameters mentioned above, plus three rotations ω, φ, κ for the undefined rotations of the satellite at the time of imaging. In the case of cross-track imagers, because of mirror inclination, this angle must be considered too. Then the following equations will result:

$$\begin{pmatrix} x_i - x_0 \\ y_i - y_0 \\ -c \end{pmatrix} = S R_1(\beta)\, R_3(\kappa) R_2(\varphi) R_1(\omega)\, R_2((f+\omega_p) - \frac{\pi}{2}) R_1(\frac{\pi}{2} - i) R_3(\Omega - \pi) \begin{pmatrix} X_i^g - X_0 \\ Y_i^g - Y_0 \\ Z_i^g - Z_0 \end{pmatrix}_{CI} \tag{5.36}$$

where

S : is the scale factor;

β : is the viewing angle;

x_i, y_i : are the image coordinates of the object point i;

x_0, y_0 : are the image coordinates of the principal point;

X_i^g, Y_i^g, Z_i^g : are the object coordinates of the image point i;

X_0, Y_0, Z_0 : are the coordinates of the position of the perspective centre of the satellite sensor in the CI system,

c : is the principal distance ≈ focal length of the SPOT imaging system,

R_j : means the rotation around the j axis.

As can be seen from the equation (5.36), it is expected that the position of the satellite and the ground control points will be given in the CI coordinate system. In practical terms, the ground coordinates will be given in a CT coordinate system such as the coordinates produced by GPS observations. Also the position and velocity of the satellite (given as ephemeris data in the SPOT header) which are used to compute the approximations for the Keplerian elements (see Appendix B) are given in a coordinate system such as the World Geodetic System (WGS84) which is also a CT system. In which case, it is also necessary to transform these coordinates into the CI coordinate system. In practice, since all of the output coordinates have to be computed in the CT coordinate system, then the Keplerian elements used in the formula (5.36) are computed with respect to this type of system. Therefore the equation (5.36) can be rewritten as follows:

$$\begin{pmatrix} x_i - x_0 \\ y_i - y_0 \\ -c \end{pmatrix} = S R_1(\beta)\, R_3(\kappa) R_2(\varphi) R_1(\omega)\, R_2((f+\omega_p)-\frac{\pi}{2}) R_1(\frac{\pi}{2}-i) R_3(\Omega-\pi) \begin{pmatrix} X_i^g - X_0 \\ Y_i^g - Y_0 \\ Z_i^g - Z_0 \end{pmatrix}_{CT} \quad (5.37)$$

where (X_0, Y_0, Z_0) and (X_i^g, Y_i^g, Z_i^g) are the coordinates of the perspective centre of the satellite sensor and the ground control points respectively in the Conventional Terrestrial (CT) coordinate system.

As mentioned before, because of the dynamic geometry of linear array systems, the positional and attitude parameters of a linear array sensor are treated as being time dependent. The only available measure of time is the satellite's along-track (x) coordinates. Therefore the major components of the dynamic motion, the movement of the satellite in orbit and the Earth rotation are modelled as linear angular changes of f and Ω with respect

to time - defined as f_1 and Ω_1. Thus:

$$f_i = f_0 + f_1 x$$
$$\Omega_i = \Omega_0 + \Omega_1 x \tag{5.38}$$

where

f_i and Ω_i are the true anomaly and the right ascension of the ascending node of each line i,

f_0 and Ω_0 are the true anomaly and the right ascension of the ascending node with respect to a reference line, e.g. the centre line of the scene,

f_1 and Ω_1 are the first values for the rates of change of f_i and Ω_i.

The orbital eccentricity (e) remains very stable for orbiting satellites, so this is kept as a constant. The argument of perigee (ω_p) moves in the orbit plane relatively slowly (about 3° per day), and since it is highly correlated to f, it should also be kept as a constant, its value being calculated from the ephemeris data provided with the header of the linear array images. The orbit semi-major axis (a) will not vary much, but since the argument of perigee is being held constant, the inclusion of a in the solution will correct for both of these unknowns.

Considering the attitude of a scan line as a reference, the attitude parameters ω, φ, and κ of the other lines can therefore be modelled by a polynomial transformation of the along-track image coordinates as follows:

$$\begin{aligned} \omega &= \omega_0 + \omega_1 x + \omega_2 x^2 \\ \varphi &= \varphi_0 + \varphi_1 x + \varphi_2 x^2 \\ \kappa &= \kappa_0 + \kappa_1 x + \kappa_2 x^2 \end{aligned} \tag{5.39}$$

The coordinates (X_0, Y_0, Z_0) of the satellite position in space are determined using the equation (5.35).

To expand the collinearity equation (5.37) given above and simplify the result, the rotations related to Keplerian elements are defined as :

$$R_S = R_2((f+\omega)-\pi/2)\, R_1(\pi/2-i)\, R_3(\Omega-\pi)$$

or:

$$R_S = \begin{pmatrix} -\sin((f+\omega_p)\cos\Omega - \cos((f+\omega_p)\cos i\sin\Omega & -\sin\Omega\sin((f+\omega_p)+\cos i\cos\Omega\cos((f+\omega_p) & \cos((f+\omega_p)\sin i \\ \sin i\sin\Omega & -\sin i\cos\Omega & \cos i \\ \cos((f+\omega_p)\cos\Omega - \sin((f+\omega_p)\sin\Omega\cos i & \cos((f+\omega_p)\sin\Omega+\cos i\cos\Omega\sin((f+\omega_p) & \sin((f+\omega_p)\sin i \end{pmatrix} \quad (5.40)$$

The rotations related to the ω, φ, and κ values are defined as, $R_A = R_3(\kappa)\, R_2(\varphi)\, R_1(\omega)$ or:

$$R_A = \begin{pmatrix} \cos\varphi\cos\kappa & \cos\omega\sin\kappa+\sin\omega\sin\varphi\cos\kappa & \sin\omega\sin\kappa-\cos\omega\sin\varphi\cos\kappa \\ -\cos\varphi\sin\kappa & \cos\omega\cos\kappa-\sin\omega\sin\varphi\sin\kappa & \sin\omega\cos\kappa+\cos\omega\sin\varphi\sin\kappa \\ \sin\varphi & -\sin\omega\cos\varphi & \cos\omega\cos\varphi \end{pmatrix} \quad (5.41)$$

Combining the rotation matrices R_A and R_S will result in R_{AS} with the following elements:

$$R_{AS} = \begin{pmatrix} R_{11}^{AS} & R_{12}^{AS} & R_{13}^{AS} \\ R_{21}^{AS} & R_{22}^{AS} & R_{23}^{AS} \\ R_{31}^{AS} & R_{32}^{AS} & R_{33}^{AS} \end{pmatrix} \quad (5.42)$$

The elements of the matrix R_{AS} can be expanded as follows:

$$\begin{aligned}
R_{11}^{AS} &= R_{11}^{A}R_{11}^{S}+R_{12}^{A}R_{21}^{S}+R_{13}^{A}R_{31}^{S} \\
R_{12}^{AS} &= R_{11}^{A}R_{12}^{S}+R_{12}^{A}R_{22}^{S}+R_{13}^{A}R_{32}^{S} \\
R_{13}^{AS} &= R_{11}^{A}R_{13}^{S}+R_{12}^{A}R_{23}^{S}+R_{13}^{A}R_{33}^{S} \\
R_{21}^{AS} &= R_{21}^{A}R_{11}^{S}+R_{22}^{A}R_{21}^{S}+R_{23}^{A}R_{31}^{S} \\
R_{22}^{AS} &= R_{21}^{A}R_{12}^{S}+R_{22}^{A}R_{22}^{S}+R_{23}^{A}R_{32}^{S} \\
R_{23}^{AS} &= R_{21}^{A}R_{13}^{S}+R_{22}^{A}R_{23}^{S}+R_{23}^{A}R_{33}^{S} \\
R_{31}^{AS} &= R_{31}^{A}R_{11}^{S}+R_{32}^{A}R_{21}^{S}+R_{33}^{A}R_{31}^{S} \\
R_{32}^{AS} &= R_{31}^{A}R_{12}^{S}+R_{32}^{A}R_{22}^{S}+R_{33}^{A}R_{32}^{S} \\
R_{33}^{AS} &= R_{31}^{A}R_{13}^{S}+R_{32}^{A}R_{23}^{S}+R_{33}^{A}R_{33}^{S}
\end{aligned} \quad (5.43)$$

Considering the rotation related to the mirror angle β:

$$R_\beta = \begin{pmatrix} 1 & 0 & 0 \\ 0 & \cos\beta & \sin\beta \\ 0 & -\sin\beta & \cos\beta \end{pmatrix} \quad (5.44)$$

If $R = R_\beta R_{AS}$, then the rotations in equation (5.37) can be defined in general terms as:

$$R = \begin{pmatrix} R_{11}{}^{AS} & R_{12}{}^{AS} & R_{13}{}^{AS} \\ R_{21}{}^{AS}\cos\beta + R_{31}{}^{AS}\sin\beta & R_{22}{}^{AS}\cos\beta + R_{32}{}^{AS}\sin\beta & R_{23}{}^{AS}\cos\beta + R_{33}{}^{AS}\sin\beta \\ -R_{21}{}^{AS}\sin\beta + R_{31}{}^{AS}\cos\beta & -R_{22}{}^{AS}\sin\beta + R_{32}{}^{AS}\cos\beta & -R_{23}{}^{AS}\sin\beta + R_{33}{}^{AS}\cos\beta \end{pmatrix} \quad (5.45)$$

Now the equation (5.37) can be simplified as follows:

$$\begin{pmatrix} x_i - x_0 \\ y_i - y_0 \\ -c \end{pmatrix} = SR \begin{pmatrix} X_i^g - X_0 \\ Y_i^g - Y_0 \\ Z_i^g - Z_0 \end{pmatrix} \quad (5.46)$$

Dividing the first and the second elements of the above matrix by the third one will result in the following equations:

$$\begin{aligned} x_i - x_0 &= -c \frac{R_{11}D_1 + R_{12}D_2 + R_{13}D_3}{R_{31}D_1 + R_{32}D_2 + R_{33}D_3} \\ y_i - y_0 &= -c \frac{R_{21}D_1 + R_{22}D_2 + R_{23}D_3}{R_{31}D_1 + R_{32}D_2 + R_{33}D_3} \end{aligned} \quad (5.47)$$

where:

$$D_1 = X_i^g - X_0 \quad , \quad D_2 = Y_i^g - Y_0 \quad , \quad D_3 = Z_i^g - Z_0$$

Note: In the case of SPOT, $x_i = x_0 = y_0 = 0$ can be put in equation (5.47).

In the above equations, there are 18 unknowns which are:

- the unknown Keplerian parameters: f_0, f_1, Ω_0, Ω_1, a, i;
- the unknown attitude parameters of exterior orientation: ω_0, φ_0, κ_0, ω_1, φ_1, κ_1, ω_2, φ_2, κ_2;
- the ground coordinates of the image points : X_i^g, Y_i^g, Z_i^g.

5.8 Geometric Corrections of the SPOT Stereo Imagery

SPOT Image produces several levels of processed imagery as standard products, Levels 1A and 1B being those most commonly supplied to users. Level 1A is raw data that have been corrected radiometrically, while Level 1B data has been corrected additionally for certain

known geometric distortions (Earth rotation and curvature, mirror look angles and orbit characteristics). As a result of these geometric corrections which ensure that the resulting image has a greater correspondence to topographic maps, Level 1B images are in widespread use among the geoscience community.

From the photogrammetric point of view, while the geometry of the SPOT Level 1A images is relatively straightforward to understand, in the case of SPOT Level 1B images, the basic geometry of the SPOT images has been altered during processing and is a little more difficult to comprehend. However it should be realised that the Level 1B processing does not remove the effects of topographic relief. Thus the relief displacements inherent in the image when it was acquired by the SPOT linear array sensor are still retained in the Level 1B image. So it is possible to measure heights and to extract digital elevation data from Level 1B data as well as from the raw Level 1A data.

5.8.1 Geometry of SPOT Level 1A

In the SPOT Level 1A image, only the detector normalization is performed using a linear model which equalizes the difference in sensitivity between individual CCD detectors. Hence no geometric corrections are applied. The image is not resampled and the image area is constant, comprising either 6,000 lines, each of which contains 6,000 pixels in panchromatic mode; or 3,000 lines, each containing 3,000 pixels in each band of a multispectral image, irrespective of the viewing angle. This means that the image appears as a square, irrespective of the mirror inclination which produces the tilt required to give the cross-track coverage of a SPOT stereo-pair. This results in a panoramic effect for oblique (off-nadir) viewing, since the number of pixels remains constant while the area covered by a single pixel in the East-West direction varies according to the viewing angle. Thus for a SPOT pan image, the area covered by each pixel on the ground could be 10m or more depending on the viewing angle of the sensor (see Figure 5.14). The basic image coordinate system, mentioned above in Section 5.7.1, can be applied to this type of image without any change.

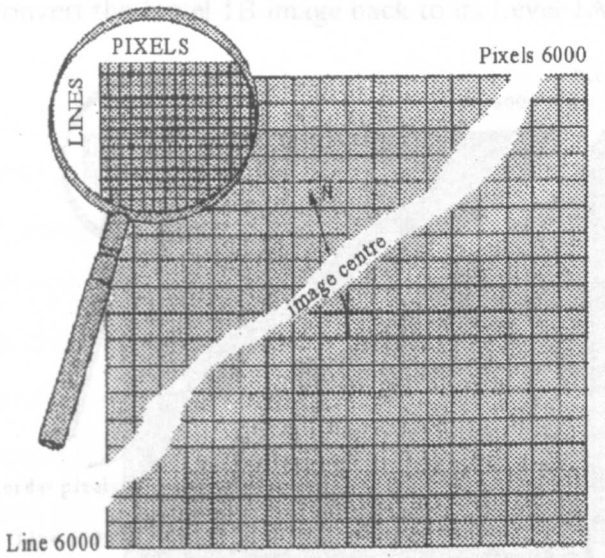

Figure 5.14 A view of a SPOT Level 1A image

5.8.2 Geometry of SPOT Level 1B

A SPOT Level 1B image also incorporates the radiometric corrections mentioned above for Level 1A but, in addition, geometric corrections are applied to it during processing which take into account the systematic distortions due to Earth rotation and curvature, sensor viewing angle and desmearing. Thus this level of image is partially rectified and approximates to an orthographic view of the Earth, but with the displacements due to relief remaining in the image. Furthermore, in this level, after these geometric corrections have been applied, the image is resampled at regular intervals of 10 or 20 metres according to the spectral mode used. The number of pixels contained in the image is therefore altered; it varies from 6,400 to 8,500 in panchromatic mode and from 3,200 to 4,250 in multispectral mode according to the viewing angle, giving an image size of 60km in the North-South direction and 60 to 80km in the East-West direction. The non-imaged parts of the overall image area are generated by adding zero value pixels (Figure 5.15).

The scene centre is placed either on the 3,000th or the 1,500th line, depending on the spectral mode. In this case, to apply the same image coordinate system as that defined above in Section 5.7.1, the image has to be changed in a certain way in order to have the same geometry as that existing at the time of imaging the ground. If this approach is adopted, it

is then necessary to convert the Level 1B image back to its Level 1A equivalent.

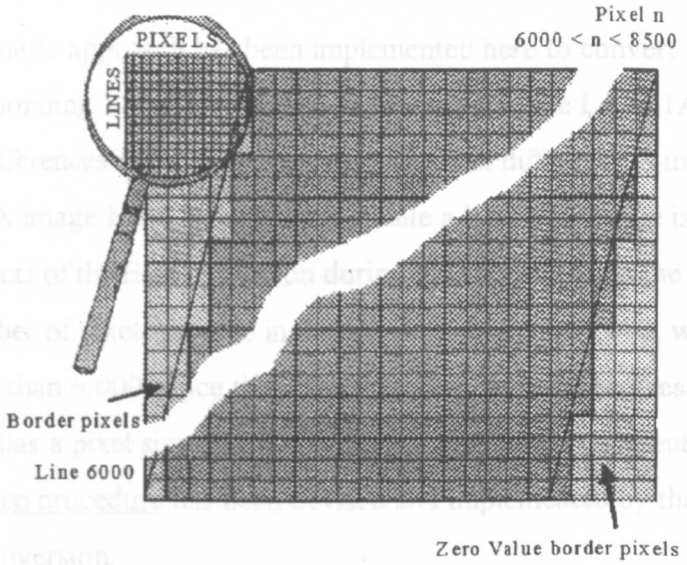

Figure 5.15 A view of a SPOT Level 1B image

In order to do this, first a rotation is necessary to change the parallelogram shape of the image back into a square. Then the scale in each line and the pixel direction must be changed in such a way as to ensure that it has the same scale and format as that of a Level 1A image (i.e. 6,000 lines and 6,000 pixels in the case of panchromatic image).

In the case of the SPOT Level 1B images produced in the USA, the geometry of the image at the time of imaging the ground during the flight can be reconstructed in a relatively straightforward way using an inverse parametric solution.

For the French produced SPOT Level 1B imagery, the problem of utilizing this type of image in the bundle adjustment can be solved in one of two ways: either (i) using the Level 1B image directly in the solution, which needs a complicated and time consuming approach to establish the exact geometry of this type of image, or (ii) converting the Level 1B image back to its Level 1A geometry. In the case of converting the Level 1B image back to its 1A form, it is necessary to know the polynomial coefficients that have been used to transform the Level 1A to this level and then to implement them in a reverse transformation. How to obtain these parameters is another problem.

5.8.3 Correction of Level 1B Images

A simple and pragmatic approach has been implemented here to convert Level 1B images back to the corresponding Level 1A form. A comparison of the Level 1A and 1B images shows two major differences in terms of geometry. The first difference is in the shape of the images. A Level 1A image has a square shape, while a Level 1B image is a parallelogram arising from the effects of the Earth's rotation during the acquisition of the image. As noted previously, the number of pixels per line in the Level 1A image is 6,000, while in the Level 1B image it is more than 6,000, since the image has been rectified and resampled in such a way that each pixel has a pixel size of 10m on the ground. With due attention to these two differences, a two step procedure has been devised and implemented by the author to carry out the required conversion.

In the first step, each point i with the pixel coordinates (p_i^0, l_i^0) in the Level 1B image has to be transformed in such a way as to produce a rectangular shaped image. This is achieved as follows (see Figure 5.16):

$$\begin{aligned} \tan \alpha &= \textit{offset} / \textit{number of lines} \\ p_i^1 &= \tan \alpha \,(\textit{total number of lines} - l_i^0) \\ l_i^1 &= l_i^0 \end{aligned} \tag{5.48}$$

where the superscript 1 refers to the result after the first transformation.

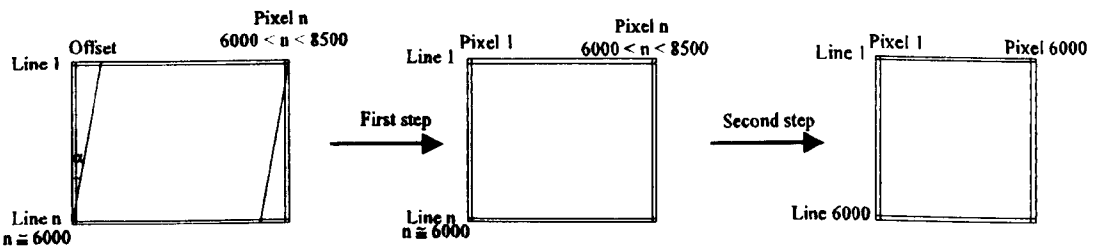

Figure 5.16 Two step transformation from SPOT Level 1B image to its corresponding Level 1A form

But still the size of this rectangle is different to that of the corresponding Level 1A image. In the second step, two coefficients have been computed to let the final image have the same size (6,000 × 6,000 pixels) in two directions as a Level 1A image (see Figure 5.16). These coefficients are used to produce the pixel and line coordinates of each point respectively.

$$\textit{coefficient for the p coordinate} = 6{,}000 / \textit{total number of pixels in each line}$$
$$\textit{coefficient for the l coordinate} = 6{,}000 / \textit{total number of pixels in each line} \qquad (5.49)$$

However, additional displacements have been introduced into the Level 1B imagery by the original corrections for Earth curvature/panoramic distortion. These displacements occur predominantly in the cross-track (y) direction, and, since they are approximately symmetrical about the image centre line, parameters adjusting the attitude as a function of the cross-track image coordinates should give a good correction for these displacements (Gugan 1987). Consequently these attitude parameters can be introduced by replacing the x^2 terms in equation (5.39) by a y^2 term for this purpose, which leads to the following equations:

$$\begin{aligned} \omega &= \omega_0 + \omega_1 x + \omega_2 y^2 \\ \varphi &= \varphi_0 + \varphi_1 x + \varphi_2 y^2 \\ \kappa &= \kappa_0 + \kappa_1 x + \kappa_2 y^2 \end{aligned} \qquad (5.50)$$

where x and y are the image coordinates. They have been incorporated in the procedure to transform the Level 1B image coordinates to their Level 1A form.

The geometric correction of cross-track imagery in general and of SPOT Level 1A and 1B images in particular has been implemented as a part of the author's bundle adjustment program. This program is explained in more detail in Chapter 7.

In the next Chapter (6), the mathematical modelling of linear array along-track stereo images in three dimensions is discussed.

CHAPTER 6: THREE-DIMENSIONAL MATHEMATICAL MODELLING OF LINEAR ARRAY STEREO IMAGES (ALONG-TRACK CASE)

6.1 Introduction

Linear array along-track stereo imagers have at least two optical systems scanning the Earth's surface simultaneously from the same orbit, each having a different along-track pointing angle (see Figure 6.1). A stereo pair is obtained using a combination of any two of the backward, nadir and forward-looking images acquired by the system.

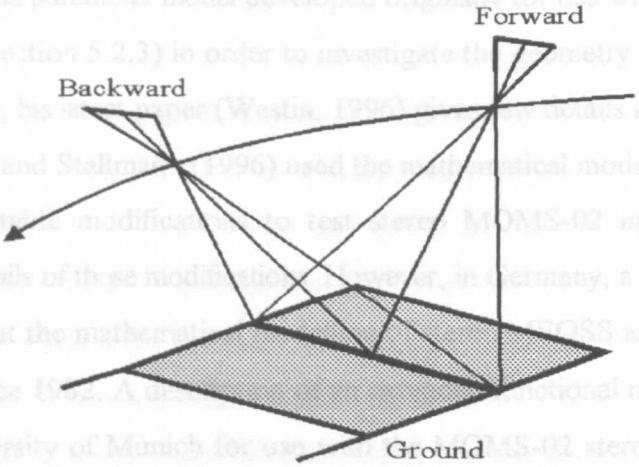

Figure 6.1 Formation of linear array stereo model from along-track images

This arrangement offers the advantage of near-simultaneous acquisition of the images of the same area compared with those acquired by cross-track stereo imagers. This feature makes stereo interpretation and mensuration much easier since it eliminates entirely the difficulties with cross-track stereo scanners arising from the images being taken months apart, resulting in considerable changes in the appearance of terrain features due to seasonal changes. For this reason, most satellite-based optical sensors planned for the future will employ this mode of stereo imaging. In some cases, this will be in addition to a cross-track pointing capability for more frequent revisiting of the same area. The along-track stereo system is implemented using either two or three linear arrays, usually with each having its own specific lens system for acquisition of the image data.

The first operational civilian along-track stereo imager is the Japanese JERS-1 OPS which was launched in 1992. Its main features have been described in Section 3.8. The latest along-track linear array stereo imager available to civilian users is the MOMS-02 (Modular Opto-electronic Multispectral Scanner). This system was operated from the Space Shuttle for a limited period in 1993 and its principal characteristics have been described in Section 3.6.

Compared to cross-track stereo imagers (e.g. SPOT), few researchers have worked on the mathematical modelling and geometric evaluation of this type of imager. Westin (1996) has modified his orbital parameter model developed originally for use with SPOT data (Westin, 1990, see also Section 5.2.3) in order to investigate the geometry of JERS-1 OPS stereo images. However, his latest paper (Westin, 1996) gives few details as to how this has been done. Baltsavias and Stallmann (1996) used the mathematical model developed by Kratky (1989) with suitable modifications to test stereo MOMS-02 imagery, again without revealing any details of these modifications. However, in Germany, a serious effort has been made to carry out the mathematical modelling of stereo MEOSS and MOMS-02 imagery from scratch since 1982. A description of an extended functional model developed at the Technical University of Munich for use with the MOMS-02 stereo-imagery is given by Ebner et al. (1992), with a test of his method reported in Ebner et al. (1996). Fraser and Shao (1996a) have developed their mathematical modelling of stereo MOMS-02 imagery based on the same concepts as Ebner et al. (1992). From the dates of these references, it will be seen that most of this development is very recent and has been carried out over the same time period as the present author has been developing his modelling.

However, the basis of the mathematical modelling of stereo MOMS-02 as a case of along-track stereo imagers that has been developed in Germany by Hofmann and Ebner is quite different to any of those described in the previous chapter on the modelling of cross-track images. Furthermore the modelling developed by the present author is very different to that of Hofmann and Ebner.

In the next Section of this Chapter, the characteristics of MOMS-02 will be discussed as a

preliminary to Section 6.3 which discusses the mathemetical modelling of MOMS-02 carried out in Germany. Section 6.4 outlines briefly the modelling of JERS-1 OPS carried out by Westin (1996). The mathematical modelling of along-track stereo images developed by the present author is discussed in detail in Section 6.5.

6.2 Characteristics of MOMS-02 Stereo Images

As mentioned before, the MOMS-02 imager consists of a stereo module and a multispectral module. Certain combinations of the panchromatic stereo and the multispectral channels can be selected using any one of seven different imaging modes. The main difference between MOMS-02 and the other available along-track stereo imagers such as JERS-1 OPS lies in its capability to provide three-fold (forward, nadir, and backward) along-track stereo imaging using the three lenses of the stereo module each equipped with a single CCD sensor array. The nadir looking CCD sensor comprises two arrays, each with 6,000 sensor elements, which are combined optically to give one single array with 9,000 sensor elements. In conjuction with a lens of f = 660mm, they produce a ground pixel size of 4.5m. The other two CCD arrays of the stereo module used for the acquisition of the forward and backward images each consist of 6,000 sensor elements. Using a lens of focal length f = 237mm, these result in a ground pixel size of 13.5m. Among the several different modes of operation which are possible with MOMS-02, two of them are especially important in the context of topographic mapping applications. They are stereo mode 1 and stereo mode 3.

In stereo imaging mode 1, 8,304 pixels of the High Resolution (HR) nadir channel (Channel 5) and 2,976 pixels of the forward and backward stereo Channels 6 and 7, with a look angle of 21.5 degrees with respect to the vertical in the direction of motion, are active. This results in the imaging of a strip of the Earth's surface which is 38km wide and 4.5m in breadth by the HR channel and the same width and 13.5m in breadth by the stereo Channels 6 and 7. This ensures a nadir image that covers the same area as the forward and backward channels and actually consists of three sub-images named a, b, and c (see Figure 6.2). These slightly overlap (by 120 pixels) in the flight direction. Consequently, the images cover an area of 40 × 140 km^2 and 37 × 109 km^2 for the fore/aft and nadir cases respectively.

To increase the capability of the MOMS-02 mode 1 imaging system for acquiring imagery of the Earth, this system is also equipped with a tiltable mirror to allow an image of the ground to be taken with 30 degrees inclination in the cross-track direction.

In stereo imaging mode 3, 5,800 pixels of each of the stereo Channels 6 and 7 are active. Considering a look angle of 21.5 degrees with respect to the vertical for the forward and backward lenses, this array images a strip of the Earth's surface around 78km wide and 13.5m in breadth. A MOMS-02 mode 3 image is built up by combining 8,120 of these linear strips, which results in a ground coverage of 78 × 109 km^2 for both the forward and backward images.

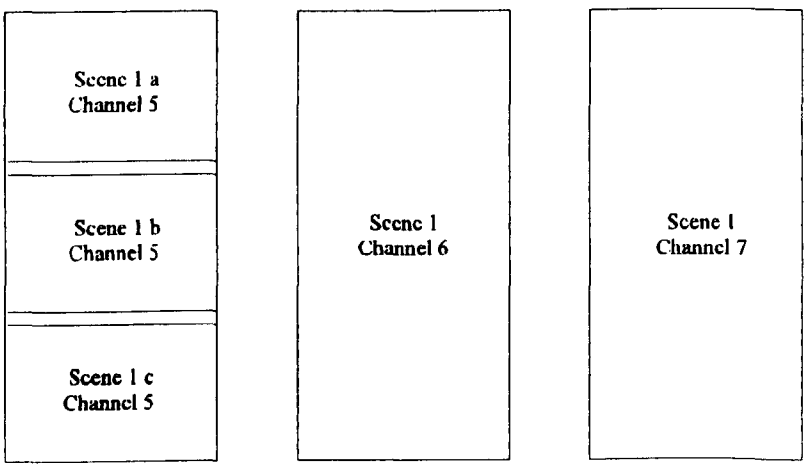

Figure 6.2 Formation of Channel 5 with respect to Channels 6 and 7

With regard to header information, each scene acquired by the MOMS-02 imager has 139 frame header lines which give a description of the following image in text form. All lines of the images begin with a 200 column line header followed by the image pixels and then a 100 column line trailer. This results in a total size of 6,100 × 8,260 pixels in the case of a mode 3 scene and 3,276 × 8,260 pixels in the case of a mode 1 scene. Tables 6.1, 6.2 and 6.3 show the structure of the lines present in the high resolution image of Channel 5 in mode 1, and the structure of the lines produced by stereo Channels 6 and 7 in modes 1 and 3 respectively.

The information comprising the approximate values of position, velocity and the attitude of the satellite at the time of imaging the ground, which are important in the solution that has

been devised by the author both for the modelling of the stereo pair and for the bundle adjustment program, are defined as GN&C data inside the frame header information of each line. The structure of this data is shown in Table 6.4.

Table 6.1 Structure of Lines for High Resolution Channel 5 in Mode 1

Field	Byte	Type	Description
1	0 - 1	1 * 2	line index : 2 (dec)
2	2 - 3	1 * 2	length of line : 8604
3	4 - 5	1 * 2	index of spectrum band x : 1 (dec)
4	6 - 7	1 * 2	byte address of the first pixel : 200
5	8 - 9	1 * 2	byte address of the last pixel : 8603
6	10 - 11	1 * 2	line number
7	12 -13	1 * 2	record number
8	14 - 15	1 * 2	byte address of the first synthetic pixel : 8504
9	16 - 23		spares
10	24 - 199		information of frame and line header
11	200 - 8503	byte	picture data channel x
12	8504 - 8513	byte	grey value of white : 0xff
13	8514 - 8603	byte	grey value of grey key

Table 6.2 Structure of Lines for Stereo Channels 6 and 7 in Mode 1

Field	Byte	Type	Description
1	0 - 1	1 * 2	line index : 2 (dec)
2	2 - 3	1 * 2	length of line : 3276
3	4 - 5	1 * 2	index of spectrum band x : 1 (dec)
4	6 - 7	1 * 2	byte address of the first pixel : 200
5	8 - 9	1 * 2	byte address of the last pixel : 3275
6	10 - 11	1 * 2	line number
7	12 -13	1 * 2	record number
8	14 - 15	1 * 2	byte address of the first synthetic pixel : 3176
9	16 - 23		spares
10	24 - 199		information of frame and line header
11	200 - 3175	byte	picture data channel x
12	3176 - 3185	byte	grey value of white : 0xff
13	3186 - 3275	byte	grey value of grey key

Table 6.3 Structure of Lines for Stereo Channels 6 and 7 in Mode 3

Field	Byte	Type	Description
1	0 - 1	1 * 2	line index : 2 (dec)
2	2 - 3	1 * 2	length of line : 6100
3	4 - 5	1 * 2	index of spectrum band x : 1 (dec)
4	6 - 7	1 * 2	byte address of the first pixel : 200
5	8 - 9	1 * 2	byte address of the last pixel : 6099
6	10 - 11	1 * 2	line number
7	12 -13	1 * 2	record number
8	14 - 15	1 * 2	byte address of the first synthetic pixel : 6000
9	16 - 23		spares
10	24 - 199		information of frame and line header
11	200 - 5099	byte	picture data channel x
12	6010 - 6009	byte	grey value of white : 0xff
13	6010 - 6099	byte	grey value of grey key

Table 6.4 Structure of GN&C Data

Field	Bits	Description
1	16	days of year, GMT, right justified
2	32	GMT time of day in multiple of 10ms; binary right justified
3	16	GMT delta for attitude/rate in multiples of 10 ms, when added to GMT yields valid time for attitude readings, binary right justified
4	3 * 32	position: in ft., floating point scalars
5	3 * 32	velocity: in ft/sec, floating point scalars
6	3 * 32	atttitude: Euler angles in radians, scalars
7	3 * 32	attitude rate: in radians per sec. on body axes, floating point scalars

However, regarding the orbital parameter model devised and used in this present research (which will be discussed for along-track stereo imagers in general including MOMS-02) since the size of the scene varies in different modes, the centre of the image coordinate system for each line and the reference line for computing the attitude parameters as well as the Keplerian elements f and Ω must be considered differently for each mode. In the case of MOMS-02 stereo mode 1, the origin of the image coordinate system is assumed to be pixel

1488.5 of each line, while the reference line is assumed to be line number 4,060.5. In the case of MOMS-02 stereo mode 3, the reference line will stay the same as mode 1, while the origin of the image coordinate system for each line becomes pixel number 2,900.5.

6.3 Mathematical Modelling of Stereo MOMS Imagery Used by the Technical University of Munich

The mathematical modelling of along-track stereo imagers in Germany has first been described by Hofmann et al (1982) at the time when three-line imagers such as MEOSS and MOMS-02 were first proposed. It was then developed further as a generalized combined point determination by Ebner and Muller (1986 and 1987), Hofmann and Muller (1988) and Ebner et al (1990). They formulated their model using collinearity conditions for each line of the image. Since it was impossible to compute the exterior orientation parameters for each line, they then introduced several reference lines at intervals along the image - the so-called orientation image lines - and computed the parameters for these lines. The parameters for any other line were then generated as a function of the parameters of neighbouring orientation image lines using a first-order Lagrange polynomial. Later Ebner et al. (1992) extended the equations with specific reference to the MOMS-02 geometry and characteristics.

As mentioned before, three of the channels of the MOMS-02 imager operate in panchromatic mode, in such a way that one of them, the High Resolution (HR) channel using a lens with a focal length of 660.0mm, is oriented in the vertical or nadir direction and the other two with lenses having a focal length of 237mm are tilted at 21.9 degrees from the vertical pointing in the forward and backward directions respectively. By recording the images of a ground area taken from these three different viewing angles, an along-track stereo model can be produced. Arising from the fact that the MOMS-02 system consists of five closely related lenses allied to the appropriate linear arrays and several images may be acquired in line scanning mode simultaneously, the definition of the MOMS-02 pixel and image coordinate systems and the reconstruction of the interior and exterior orientations exhibit some unusual features or aspects. The relationship between the three-fold stereo

arrangement in the form of calibration data and the definitions of the image and ground coordinate systems used in the model developed by Ebner et al. (1992) will be explained in the following sections.

6.3.1 Calibration Data

The MOMS-02 camera geometry is described by three parameters for each lens :

(i) The *mean focal length f*,

(ii) A *displacement dy* between the centres of each single CCD array and the centre of a reference sensor line (in the line direction); and

(iii) An *angle of convergence* γ with respect to a fixed camera coordinate system, normally defined as being equal to the image coordinate system of the nadir lens.

These values have been obtained through the geometric system calibration of the MOMS-02 imager that has been conducted by DASA, the manufacturer of the scanner, one year after the mission. The principle of the calibration was based on the highly precise measurement of the object side angles in two perpendicular directions (along and across the sensor line) for every 500th pixel of each CCD array. Basically the calibration equipment consisted of a Cassegrain collimator with an 650mm wide aperture, defining a common reference direction, and a nodal bench with two perpendicular rotation axes. The angles were measured with respect to the reference direction (defined by the centre pixel of the nadir looking CCD array) through the optics of the MOMS-02 nadir lens and reflected the real camera geometry, including all effects such as the irregularities of the CCD arrays, lens distortion, etc (Kornus et al. 1995). Table 6.5 shows the values of the three calibration parameters (f, dy, γ) for each of the three channels, 5, 6, and 7, of the MOMS-02 system measured using this procedure.

Table 6.5 Calibration Camera Parameters

Parameter	Stereo Channel 6	Stereo Channel 7	HR Channel 5
f (mm)	237.16	237.20	660.30
dy (pixel)	12.47	16.35	0.0
γ (deg)	-21.457	21.457	0.0

It should be noted that the displacement dx in the flight direction is zero, i.e. $dx = 0$.

6.3.2 Image Coordinate System

According to Ebner et al. (1992), a separate image coordinate system is defined for each lens as follows (see Figure 6.2):

- origin : centre of the first active pixel of the sensor line;
- y axis : (ideally) a straight line directed through all the pixel centres in the linear array;
- x axis : orthogonally completes a right-handed system (close to the flight direction).

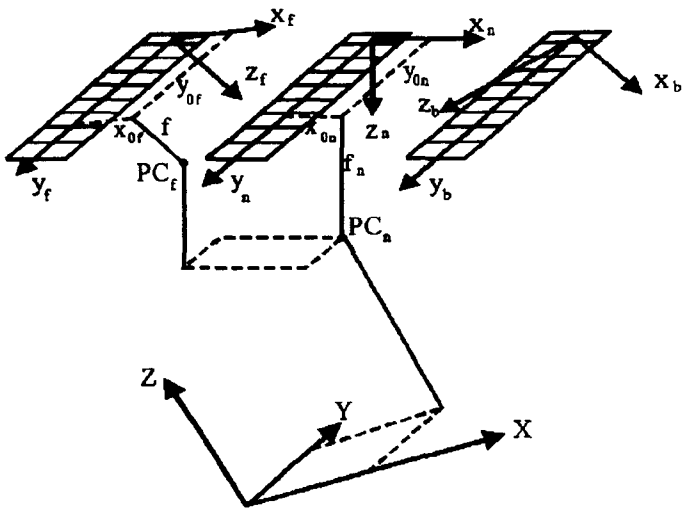

Figure 6.3. Image, and Ground coordinate systems as used by Ebner et al. (1992)

where

x_n, y_n, z_n : are the axes of the image coordinate system for the nadir looking lens;

x_f, y_f, z_f : are the axes of the image coordinate system for the forward looking lens;

x_{0n}, y_{0n} : are the image coordinates of the principal points for the nadir looking lens;

x_{0f},y_{0f} : are the image coordinates of the principal points for the forward looking lens;

PC_n, PC_f : are the perspective centres of the nadir and forward looking lenses respectively,

X, Y, Z : are the axes of the ground coordinate system.

Note that the specification of the backward looking lens is the same as that of the forward

looking lens.

Multiplying the pixel coordinates with the pixel size of 10 μm yields metric values for the image coordinates if required.

6.3.3 Object Coordinate System

The object coordinate system is defined to be a fixed geocentric system (e.g. the WGS84 coordinate system). In which case, facilities to carry out transformations between the UTM or other projection system and this geocentric coordinate system will be required. Also a transformation between the navigation data (which is used to introduce the approximations for the position and attitude of the system during the motion of the spacecraft) and the object coordinate system is necessary.

6.3.4 Navigation Data

The orbit and attitude data for MOMS-02 were derived at the GFZ Potsdam from the orbital determination carried out in-flight using external TDRSS doppler data and from onboard INS data respectively. The data are given for each second over a time period of 300 seconds, including the time interval of 51 seconds during which the imagery was acquired. They describe the position of the sensor and the orientation of the sensor axes with respect to a local horizontal cartesian coordinate sysytem. The origin of this coordinate system is defined to be approximately in the centre of the area being covered by the image scene with its X axis pointing East, the Y axis pointing North and the Z pointing upwards. The absolute accuracies of the navigation data were initially specified to be 30m for the positions and between 100" and 700" for the attitude angles (Kornus et al. 1995).

6.3.5 Derivation of Collinearity Equations

Ebner et al. (1992) used collinearity equations with the stereo MOMS-02 images to determine their exterior orientation parameters. The special features of the mathematical

modelling of three-line imaging systems devised by Ebner arise from the fact that the relative positions of all the other lenses are fixed with respect to the HR lens which he considers as the reference lens and are known from the system calibration. As a result, he proposed that only the exterior orientation parameters for the HR lens need to be computed. The exterior orientation of any other lens is then described by successive transformations from the specific lens into the reference image system and from there into the ground coordinate system. Then, for each inclined lens, an additional 6 transformation parameters are introduced to model rigorously the displacements Δx, Δy, Δz of the projection centres (PC) and the rotations $\Delta\omega$, $\Delta\varphi$, $\Delta\kappa$ of the image coordinate system with respect to the image coordinate system of the HR lens. Thus, the MOMS-02 camera geometry in Ebner's model is described by 21 parameters as follows (see also Figure 6.3):

(i) 3 interior orientation parameters for the HR lens (x_{0N}, y_{0N}, z_{0N});
(ii) 6 relative exterior orientation parameters of the forward looking lens with respect to the nadir looking HR lens ($\Delta\omega_F$, $\Delta\varphi_F$, $\Delta\kappa_F$, ΔX_F, ΔY_F, ΔZ_F); and
(iii) the 3 interior orientation parameters of the forward looking lens (x_{0F}, y_{0F}, z_{0F});
(iv) 6 relative exterior orientation parameters of the backward looking lens with respect to the nadir looking HR lens ($\Delta\omega_B$, $\Delta\varphi_B$, $\Delta\kappa_B$, ΔX_B, ΔY_B, ΔZ_B); and
(v) the 3 interior orientation parameters of the backward looking lens (x_{0B}, y_{0B}, z_{0B});

As mentioned earlier, these parameters are determined by a prior camera calibration and treated as constant values. Then the extended collinearity equations for the inclined lenses can be described as follows (Ebner et al. 1992):

$$\begin{pmatrix} x-x_{0F,0B} \\ y-y_{0F,0B} \\ -c_{F,B} \end{pmatrix} = KM(\Delta\omega_{FN,BN}, \Delta\varphi_{FN,BN}, \Delta\kappa_{FN,FB})\, D(\omega_{0N}, \varphi_{0N}, \kappa_{0N}) \begin{pmatrix} X-(X_{0N}+\Delta X_{0F,0B}) \\ Y-(Y_{0N}+\Delta Y_{0F,0B}) \\ Z-(Z_{0N}+\Delta Z_{0F,0B}) \end{pmatrix} \qquad (6.1)$$

with

$$\begin{pmatrix} \Delta X_{0F,0B} \\ \Delta Y_{0F,0B} \\ \Delta Z_{0F,0B} \end{pmatrix} = D'(\omega_{0N}, \varphi_{0N}, \kappa_{0N}) \begin{pmatrix} \Delta x_{F,B} \\ \Delta y_{F,B} \\ \Delta z_{F,B} \end{pmatrix} \quad , \quad (MD = R) \qquad (6.2)$$

Note: In the case of the nadir looking lens, $\Delta x_N = \Delta y_N = \Delta z_N = 0$, $M = I$.

Then, in general terms, the extended collinearity equations can be described as follows:

$$x = x_0 - c\frac{R_{11}(X-X_0)+R_{12}(Y-Y_0)+R_{13}(Z-Z_0)-(M_{11}\Delta x+M_{12}\Delta y+M_{13}\Delta z)}{R_{31}(X-X_0)+R_{32}(Y-Y_0)+R_{33}(Z-Z_0)-(M_{31}\Delta x+M_{32}\Delta y+M_{33}\Delta z)}$$

$$y = y_0 - c\frac{R_{21}(X-X_0)+R_{22}(Y-Y_0)+R_{23}(Z-Z_0)-(M_{21}\Delta x+M_{22}\Delta y+M_{23}\Delta z)}{R_{31}(X-X_0)+R_{32}(Y-Y_0)+R_{33}(Z-Z_0)-(M_{31}\Delta x+M_{32}\Delta y+M_{33}\Delta z)} \qquad (6.3)$$

where:

x, y	: image coordinates of the object point;
x_0, y_0	: image coordinates of the principal point;
k	: scale factor;
c	: focal length;
M, D, R	: rotation matrices ($MD=R$);
X, Y, Z	: ground coordinates of the object point;
ω_0, φ_0, κ_0	: rotation angles of the exterior orientation of the HR lens;
X_0, Y_0, Z_0	: ground coordinates of the projection centre of the HR lens;
Δx, Δy, Δz	: displacements of the projection centres of the backward and forward lenses in image space with respect to the nadir lens.

As noted previously, because the orientations of neighbouring scan lines are highly correlated, the orientation parameters will be determined only for the so-called "orientation image lines", which are introduced at certain time intervals. Between these orientation image lines, an interpolation using a Lagrange polynomial will take place. The Lagrange polynomials used are defined as:

$$P_N(t) = \sum_{i=0}^{n} P(t_i) \prod_{\substack{j=0 \\ j \neq i}}^{n} \frac{t - t_j}{t_i - t_j} \qquad (6.4)$$

In order to obtain more accurate parameters, instead of using the first order polynomial, as with the previous proposed mathematical model, the third order Lagrange polynomial has been used. As can be seen from equation (6.4), the exterior orientation parameters at time

t are expressed as a linear combination of the related parameters assigned to (n+1) neighbouring orientation images i at time t_i. The complete extended collinearity equations are derived by replacing the exterior orientation elements X_0 , Y_0 , Z_0 , ω_0 , φ_0 , κ_0 in equations (6.3) by the related expressions computed through equation (6.4).

As can be seen from equation (6.3), the relationship between the image space and ground space is based on approximations for the exterior orientation parameters and the only rotation angles available to transform the points from one space to another are the conventional rotations ω , φ , and κ. Consequently the model depends very much on the precise positional and attitude observations, especially if only a few ground control points are available. For this reason, the bundle adjustment algorithm has been supplemented more recently by a rigorous dynamic modelling of the spacecraft motion to take orbital constraints into account (Ebner et al. 1996). It is capable of handling all MOMS-02 stereo modes including mode 1/30°, i.e. the mode 1 images taken with 30° tilt angle in the cross-track direction, as mentioned in Section 6.2. The mathematical modelling and the bundle adjustment procedure of Ebner and his group have been realised in the form of the CLIC program. The group at University of Melbourne under Professor Fraser has produced a program based on the same algorithm apparently quite independently (Fraser and Shao, 1996b).

The results from this mathematical model will be compared later with the results from the mathematical model developed by the present author in Chapter 9. The following Section first explains first briefly the mathematical modelling of along-track stereo images by Westin (1996). In the Section after that, the basis of the mathematical model developed for use with along-track stereo images at the University of Glasgow is explained in detail.

6.4 Mathematical Modelling of Along-Track Stereo Images by Westin

Again, as with his solution for cross-track stereo images oultlined in Section 5.2.3, Westin (1996) has used an orbital parameter model based on the six Keplerian parameters for the geometric correction of JERS-1 OPS images in the case of along-track stereo imagers. His

three dimensional method can be divided into distinct two steps:

(i) to carry out a *space resection* and *rectify* each *single image* (in two dimensions only);

(ii) to implement a *matching technique* to extract conjugate points and to compute the *elevation data* using *space intersection* to give the third dimension.

In the other words, using a space resection, he first computes the exterior orientation parameters for one single image. Then he computes the accuracy of the control and check points only in two dimensions using these values and a constant height value. Next he carries out the same procedure for the overlapping image. To evaluate the model in the third dimension, he then uses the multi-point matching technique described by Rosenholm (1987) to combine the two images and to extract the conjugate points. Using the appropriate intersection formula, he then computes the elevation data, i.e. the DEM, for the conjugate points. The accuracy of the resulting height values is then evaluated after the generation of DEM. A comparison between this model and the model presented by Ebner et al. (1996) and with the mathematical model developed and used by the present author in his research will be given in Section 6.5.

6.5 Mathematical Modelling of Along-Track Stereo Images Used in This Research

The orbital parameter model which has been developed for use with cross-track stereo images by the present author has been adapted and modified to form the basis of his modelling of along-track stereo images in order to determine their exterior orientation parameters and the terrain coordinates of measured image points. These modifications have been presented later to the general bundle adjustment program (see Chapter 7) to implement the computation of points measured on along-track stereo images. The image and ground coordinate systems are the same as those defined in Sections 5.7.1 and 5.7.2 of Chapter 5 and need not be repeated again here.

It should be noted that, since the stereo data is acquired in the along-track direction, the stereo base is in the x direction and the true sense of the x- and the y-parallaxes will remain

the same as in conventional photogrammetry. In these respects, it is therefore quite different to the situation which exists with cross-track stereo imagery.

6.5.1 Derivation of the Collinearity Equations

As mentioned in Chapter 5, the mathematical relationship between the image and object coordinate systems is based on three rotations using Keplerian elements and three rotations for the undefined rotations of the satellite at the time of imaging. This relationship defines the collinearity equations which relate the points in the object coordinate system to the corresponding points in the image coordinate system for each line of the linear array image. This formula can be written in general form as follows:

$$\begin{pmatrix} x_i - x_0 \\ y_i - y_0 \\ -c \end{pmatrix} = S R_3(\kappa) R_2(\varphi) R_1(\omega)\ R_2((f+\omega_p)-\frac{\pi}{2}) R_1(\frac{\pi}{2}-i) R_3(\Omega-\pi) \begin{pmatrix} X_i^g - X_0 \\ Y_i^g - Y_0 \\ Z_i^g - Z_0 \end{pmatrix}_{CT} \qquad (6.5)$$

where

S	: is the scale factor;
x_i, y_i	: are the image coordinates of the object point i;
x_0, y_0	: are the image coordinates of the principal point;
X_i^g, Y_i^g, Z_i^g	: are the object coordinates of the image point i;
X_0, Y_0, Z_0	: are the coordinates of the position of the (satellite) perspective centre in the CI system;
c	: is the principal distance ≈ focal length of the imaging system; and
R_j	: means the rotation around the j axis, where j = 1, 2, or 3.

The above explanation is common for both cross-track or along-track stereo images. Geometrically the differences between these two types of linear array stereo images that have to be considered in the mathematical relationship between the image and object coordinate systems, can be picked out as follows:

(i) In the case of cross-track stereo imagers because of mirror inclination, which is the operation employed for the acquisition of stereo images, a rotation of the viewing angle (β) around the along-track axis (x), i.e. $R_3(\beta)$, has to be included in the mathematical formula (see equation 5.34).

(ii) In the case of along-track stereo imagers, the along-track viewing angle (α) is fixed and provides the capability to the system to acquire stereo images. This angle has to be included into the equation (6.5) as a rotation around the cross-track axis (y), i.e. $R_2(\alpha)$.

(iii) Cross-track stereo imagers acquire the individual images making up a stereo pair from two different orbits, while along-track stereo imagers acquire the two images of the stereo-pair during a common orbit. As a result, the values for semi-major axis *(a)*, orbital inclination *(i)*, right ascension of the ascending node (Ω) and argument of perigee (ω) are the same for the two images.

It is worth mentioning that, in the case of MOMS-02, mode 1/30°, although the stereo images are taken in the along-track direction using a fixed viewing angle (α), the imaging system can also be operated in an inclined position with a fixed viewing angle (β) in the cross-track direction (as discussed in Section 6.2). As a result, both angles should be included in equation (6.5). The consequences of these considerations give rise to the following changes to the mathematical modelling:

(a) Having regarding to these differences (i) to (iii) set out above, then, in the case of along-track stereo images, instead of the mirror angles (β) which were used in the case of cross-track stereo images, forward and backward looking angles (α) must come into the account. Consequently, in the case of along-track stereo imagers, equation (6.5) becomes:

$$\begin{pmatrix} x_i - x_0 \\ y_i - y_0 \\ -c \end{pmatrix} = S R_2(\alpha) R_3(\kappa) R_2(\varphi) R_1(\omega)\ R_2((f+\omega_p)-\frac{\pi}{2}) R_1(\frac{\pi}{2}-i) R_3(\Omega-\pi) \begin{pmatrix} X_i^g - X_0 \\ Y_i^g - Y_0 \\ Z_i^g - Z_0 \end{pmatrix}_{CT} \qquad (6.6)$$

Note: for MOMS-02, mode 1/30°, $R_1(\beta)$ should also be included in the equation (6.6).

(b) In the mathematical modelling of the cross-track imagery, again the movement of the satellite in orbit and the Earth rotation are modelled as linear angular changes of f and Ω with respect to time - which are defined as f_1 and Ω_1 (see equation 5.38). In the case of along-track stereo imagers, since the orbit is the same for a pair of stereo images, then, as mentioned above, the orbital parameters remain the same with the exception of the true anomaly (f) that indicates the position of the satellite with respect to the perigee and r which defines the radial distance of the satellite from the Earth's centre.

(c) Again, as with cross-track stereo imagers, the attitude of a particular scan line can be considered as a reference value, which allows the attitude parameters ω, φ, and κ of the other lines to be modelled by a polynomial based on the along-track image coordinates as follows:

$$\begin{aligned} \omega &= \omega_0 + \omega_1 x + \omega_2 x^2 \\ \varphi &= \varphi_0 + \varphi_1 x + \varphi_2 x^2 \\ \kappa &= \kappa_0 + \kappa_1 x + \kappa_2 x^2 \end{aligned} \tag{6.7}$$

The coordinates (X_0, Y_0, Z_0) of the satellite position in space are determined using equation (5.35). To expand the collinearity equation (6.6), the same explanations that have been given in the case of cross-track stereo imagers for equations (5.40) to (5.43) in Section 5.7.3 can be used. In fact, the main difference lies in the implemetation of R_β which has to be replaced by a rotation around the second axis as R_α. For simplification in the case of along-track stereo images and, in general, in the bundle adjustment program, the angle α can be assumed to be part of the rotation angle φ. (N.B. In the case of MOMS-02 mode 1/30°, the angle β can be assumed to be part of the rotation angle ω). Therefore the final matrix R is a combination of the rotation matrices R_A and R_S ($R = R_A \times R_S$), defined already in Section 5.7.3 as equations (5.40) and (5.41), which results in the following equation:

$$R = \begin{pmatrix} R_{11} & R_{12} & R_{13} \\ R_{21} & R_{22} & R_{23} \\ R_{31} & R_{32} & R_{33} \end{pmatrix} \tag{6.8}$$

The elements of the matrix R can be expanded as follows:

$$
\begin{aligned}
R_{11} &= R_{11}{}^{A} R_{11}{}^{S} + R_{12}{}^{A} R_{21}{}^{S} + R_{13}{}^{A} R_{31}{}^{S} \\
R_{12} &= R_{11}{}^{A} R_{12}{}^{S} + R_{12}{}^{A} R_{22}{}^{S} + R_{13}{}^{A} R_{32}{}^{S} \\
R_{13} &= R_{11}{}^{A} R_{13}{}^{S} + R_{12}{}^{A} R_{23}{}^{S} + R_{13}{}^{A} R_{33}{}^{S} \\
R_{21} &= R_{21}{}^{A} R_{11}{}^{S} + R_{22}{}^{A} R_{21}{}^{S} + R_{23}{}^{A} R_{31}{}^{S} \\
R_{22} &= R_{21}{}^{A} R_{12}{}^{S} + R_{22}{}^{A} R_{22}{}^{S} + R_{23}{}^{A} R_{32}{}^{S} \\
R_{23} &= R_{21}{}^{A} R_{13}{}^{S} + R_{22}{}^{A} R_{23}{}^{S} + R_{23}{}^{A} R_{33}{}^{S} \\
R_{31} &= R_{31}{}^{A} R_{11}{}^{S} + R_{32}{}^{A} R_{21}{}^{S} + R_{33}{}^{A} R_{31}{}^{S} \\
R_{32} &= R_{31}{}^{A} R_{12}{}^{S} + R_{32}{}^{A} R_{22}{}^{S} + R_{33}{}^{A} R_{32}{}^{S} \\
R_{33} &= R_{31}{}^{A} R_{13}{}^{S} + R_{32}{}^{A} R_{23}{}^{S} + R_{33}{}^{A} R_{33}{}^{S}
\end{aligned}
\tag{6.9}
$$

Now equation (6.6) can be simplified as follows:

$$
\begin{pmatrix} x_i - x_0 \\ y_i - y_0 \\ -c \end{pmatrix} = SR \begin{pmatrix} X_i^g - X_0 \\ Y_i^g - Y_0 \\ Z_i^g - Z_0 \end{pmatrix} \tag{6.10}
$$

Dividing the first and the second elements of the above matrix by the third one will result in the following equations:

$$
\begin{aligned}
x_i - x_0 &= -c \frac{R_{11} D_1 + R_{12} D_2 + R_{13} D_3}{R_{31} D_1 + R_{32} D_2 + R_{33} D_3} \\
y_i - y_0 &= -c \frac{R_{21} D_1 + R_{22} D_2 + R_{23} D_3}{R_{31} D_1 + R_{32} D_2 + R_{33} D_3}
\end{aligned}
\tag{6.11}
$$

where:

$$D_1 = X_i^g - X_0 \quad , \quad D_2 = Y_i^g - Y_0 \quad , \quad D_3 = Z_i^g - Z_0$$

In the above equations, the unknowns are:

- the six unknown Keplerian parameters: f_0, f_1, Ω_0, Ω_1, a, i;
- the nine unknown attitude parameters of exterior orientation: ω_0, φ_0, κ_0, ω_1, φ_1, κ_1 , ω_2, φ_2, κ_2;
- the three ground coordinates of the image points : X_i^g, Y_i^g, Z_i^g.

Note that, in the case of linear array images, $x_i = x_0 = y_0 = 0$ can be put in equation (6.11).

The solution of the collinearity equation is explained in detail in the account of the bundle adjustment program given in Chapter 7.

6.6 A Brief Comparison and Discussion of the Mathematical Models Used by Ebner, Westin and the Present Author

As can be seen, all of these methods use collinearity equations. The main difference between Westin's method and the other two methods lies in its two step solution to the problem of three dimensional modelling of the along-track stereo images. From the point of view of most photogrammetrists, it does not seem logical to evaluate the accuracy of the heights of the model only after the time consuming task of using a matching technique to generate a DEM. One would expect to see and evaluate the accuracy of the exterior orientation of the stereo model via inspection of the residuals at the GCPs in three dimensions prior to the running of the DEM. However the Westin model and the model developed by the present author do construct the mathematical relationship between the image space and object space using Keplerian elements and additional attitude parameters. Both these models have considered fully the dynamic nature of the linear array imaging systems.

The feature, indeed one might say the weakness, of the mathematical model used by Ebner et al. (1992) is really the lack of this complete mathematical model. All of the transformations between the image space and object space are restricted to conventional exterior orientation parameters (X, Y, Z, ω, φ, κ) which surely cannot construct this relationship with enough accuracy. Although the dynamic nature of the linear array imaging system is taken into account using the Lagrange polynomial, it still does not include the physical model of the spacecraft motion (i.e. its position and attitude). However, to overcome this inherent disadvantage, Ebner et al. (1996) have used a more rigourous model to describe the spacecraft motion in terms of position only and enter this to their bundle adjustment program in the form of orbital constraints. This improves the mathematical model greatly. However, due to the lack of a dynamic model describing the sensor's attitude

behaviour during an imaging sequence, the attitude constraints still cannot be introduced into the bundle adjustment and the modelling of their behaviour is restricted to the use of the Lagrange polynomial.

These various methods are compared in more detail later in Chapter 9 where the results of experimental tests on stereo MOMS-02 mode 1 and mode 3 images using the author's modelling and bundle adjustment programs are given. The next Chapter (7) discusses the general solution of collinearity equations for stereo linear array images and their implementation in a bundle adjustment program written by the author.

CHAPTER 7 : GENERALIZED ADJUSTMENT PROGRAM

7.1 Introduction

The goal of the adjustment procedure and the program that implements it is to determine accurately the unknown parameters from the measurements (observations) of the image coordinates of the object points on an individual linear array image and the known ground control point (GCP) coordinate information. The observations and the parameters that link them to the GCP coordinates are related to each other by a polynomial in the 2D case and by collinearity equations in the 3D case. In this Chapter, first the polynomial adjustment program used as a 2D solution is explained; then in the Section after that, the bundle adjustment program for the 3D case is discussed. Finally the details of the general adjustment program, which is a program based on the use of the C++ programming language and the Windows API, are described.

7.2 Polynomial Adjustment Program

As mentioned before in Chapter 3, a 2D polynomial transformation is a mathematical formula whose parameters relate the image space directly to the object space as well as possible. Using the measured image coordinates and the known coordinates of the ground control points in the object space, the transformation parameters are computed. In general, 2D polynomial transformations can be expressed in the following form:

$$\begin{aligned} X_i &= a_0 + a_1 x_i + a_2 y_i + a_3 x_i y_i + a_4 x_i^2 + a_5 y_i^2 + \ldots + a_{24} x_i^4 y_i^4 \\ Y_i &= b_0 + b_1 x_i + b_2 y_i + b_3 x_i y_i + b_4 x_i^2 + b_5 y_i^2 + \ldots + b_{24} x_i^4 y_i^4 \end{aligned} \qquad (7.1)$$

where

X_i and Y_i : the object coordinates of the point i, where i = 1 to n and n is the number of observations;

x_i and y_i : the image coordinates of the point i; and

a_j and b_j : are the parameters of the polynomials, where j = 0, 1, 2, ... , 24.

Note: In this case, a polynomial with 25 terms is being considered.

In matrix form, the equation (7.1) can be rewritten as follows:

$$L = A X \tag{7.2}$$

where:

L : is the vector of the object coordinates (observations);

A : is the matrix of coefficients comprising different expressions for the image coordinates;

X : is the vector of the polynomial parameters (unknown).

To solve these equations with good accuracy in such a way that they give acceptable results at those additional points (independent check points) that have not been used in the above equations, a least squares adjustment should be applied. The least squares process can only be applied when there are redundant measurements. In other words, the redundancy or degree of freedom must be larger than zero (i.e. number of observations > the number of parameters). However, the equation (7.2) can be rewritten using the best estimator $\hat{X}$ of X (vector of parameters) as follows:

$$\hat{V} = A \hat{X} - L \tag{7.3}$$

where $\hat{V}$ is the vector of residuals.

Considering the weight matrix P which comprises the weights associated with each of the observations L, then the equation (7.3) can be solved for $\hat{X}$ using a least squares adjustment as follows:

$$\hat{X} = (A^T P A)^{-1} A^T P L \tag{7.4}$$

The results of this solution will be the best estimation of the (previously unknown) polynomial parameters. These values can then be used later to transform the image coordinates of the check points or any other measured points on the linear array image into the ground coordinate system. The results of the polynomial adjustment program and the accuracy of the results obtained during the present project will be analyzed and discussed in more detail in Chapters 8 and 9 where a report on the results of the experimental work carried out on linear array images will be made. Before doing so, the basis of a rigorous bundle adjustment method for the solution of the 3D mathematical modelling of stereo linear

array images will be discussed in the following sections.

7.3 Bundle Adjustment Program

The collinearity equations which relate the image space to the object space are non-linear and have to be linearized by a Taylor series expansion before the condition equations of the adjustment can be formulated and solved by iteration. The condition equations developed in the mathematical model (collinearity equations (5.36) and (6.5)) are functions of several parameters (6 Keplerian parameters, 9 attitude parameters and the 3 coordinates of each ground point in each image) for which only approximate values or, in the case of ground control points, absolute values are known. In general terms, the collinearity equations for *m* image points and *n* ground points can be shown to be as follows:

$$\begin{aligned} x_j^i &= F_j^i\,(f_0^i, \Omega_0^i, i^i, a^i, f_1^i, \Omega_1^i, \omega_0^i, \varphi_0^i, \kappa_0^i, \omega_1^i, \varphi_1^i, \kappa_1^i, X_j^g, Y_j^g, Z_j^g) \\ y_j^i &= F_{j+1}^i\,(f_0^i, \Omega_0^i, i^i, a^i, f_1^i, \Omega_1^i, \omega_0^i, \varphi_0^i, \kappa_0^i, \omega_1^i, \varphi_1^i, \kappa_1^i, X_j^g, Y_j^g, Z_j^g) \end{aligned} \qquad (7.5)$$

where the superscript i and subscript j refer to the number of image and object (ground) points respectively. The above equations can be extended as follows:

$$\begin{aligned} x_1^1 &= F_1^1\,(f_0^1, \Omega_0^1, i^1, \ldots, \omega_1^1, \varphi_1^1, \kappa_1^1, X_1^g, Y_1^g, Z_1^g) \\ y_1^1 &= F_2^1\,(f_0^1, \Omega_0^1, i^1, \ldots, \omega_1^1, \varphi_1^1, \kappa_1^1, X_1^g, Y_1^g, Z_1^g) \\ &\vdots \\ x_n^1 &= F_{2n-1}^1\,(f_0^1, \Omega_0^1, i^1, \ldots, \omega_1^1, \varphi_1^1, \kappa_1^1, X_n^g, Y_n^g, Z_n^g) \\ y_n^1 &= F_{2n}^1\,(f_0^1, \Omega_0^1, i^1, \ldots, \omega_1^1, \varphi_1^1, \kappa_1^1, X_n^g, Y_n^g, Z_n^g) \\ &\vdots \\ x_1^m &= F_1^m\,(f_0^m, \Omega_0^m, i^m, \ldots, \omega_1^m, \varphi_1^m, \kappa_1^m, X_1^g, Y_1^g, Z_1^g) \\ y_1^m &= F_2^m\,(f_0^m, \Omega_0^m, i^m, \ldots, \omega_1^m, \varphi_1^m, \kappa_1^m, X_1^g, Y_1^g, Z_1^g) \\ &\vdots \\ x_n^m &= F_{2n-1}^m\,(f_0^m, \Omega_0^m, i^m, \ldots, \omega_1^m, \varphi_1^m, \kappa_1^m, X_n^g, Y_n^g, Z_n^g) \\ y_n^m &= F_{2n}^m\,(f_0^m, \Omega_0^m, i^m, \ldots, \omega_1^m, \varphi_1^m, \kappa_1^m, X_n^g, Y_n^g, Z_n^g) \end{aligned} \qquad (7.6)$$

To simplify the solution of these equations, the following assumptions have been made regarding equations (5.47) and (6.11):

$$
\begin{aligned}
m &= R_{11}D_1 + R_{12}D_2 + R_{13}D_3 \\
n &= R_{21}D_1 + R_{22}D_2 + R_{23}D_3 \\
q &= R_{31}D_1 + R_{32}D_2 + R_{33}D_3
\end{aligned} \tag{7.7}
$$

Substituting $r = m/q$ and $s = n/q$, then the equations (5.47) and (6.11) in the general case can be written in the following matrix form:

$$
F = \begin{pmatrix} F(x) \\ F(y) \end{pmatrix} = \begin{pmatrix} x \\ y \end{pmatrix} - \begin{pmatrix} x_0 \\ y_0 \end{pmatrix} + c\begin{pmatrix} r \\ s \end{pmatrix} = 0 \tag{7.8}
$$

The above equations can be rewritten in the following form:

$$
F(\hat{\bar{L}}, \hat{\bar{X}}) = 0 \quad , \quad \hat{\bar{L}} = \bar{L} + \hat{v} \tag{7.9}
$$

where:

$\hat{L}$: is the vector of observations (image coordinates);

$\hat{v}$: is the vector of the residuals of the measured image coordinates; and

$\hat{\bar{X}}$: is the vector of the exterior orientation parameters and the ground point coordinates.

Note: in this text, the symbols $^-$,$\hat{\bar{}}$, and $\hat{}$ are defined and applied as (i) observation, (ii) observation plus correction, and (iii) correction respectively.

Equation (7.9) is non-linear and can be linearized by the use of Taylor series:

$$
\bar{0} = F(\bar{L} + \bar{X}^0) + \frac{\partial F(\hat{L}, \hat{X})}{\partial \hat{L}}\Big|_{\substack{\bar{X}^0 \\ \bar{L}}} (\hat{L} - \bar{L}) + \frac{\partial F(\hat{X}, \hat{L})}{\partial \hat{X}}\Big|_{\substack{\bar{X}^0 \\ \bar{L}}} (\hat{X} - \bar{X}^0) \tag{7.10}
$$

where $\bar{X}^0$ is the vector of approximations for the exterior orientation parameters and the ground point coordinates.

In the above equation, if:

$$
A = \frac{\partial F(\hat{\bar{L}}, \hat{\bar{X}})}{\partial \hat{\bar{L}}}\Big|_{\substack{\bar{X}^0 \\ \bar{L}}} \quad , \quad \hat{X} = \hat{\bar{X}} - \bar{X}^0
$$

$$
B = \frac{\partial F(\hat{\bar{X}}, \hat{\bar{L}})}{\partial \hat{\bar{X}}}\Big|_{\substack{\bar{X}^0 \\ \bar{L}}} \quad , \quad W = F(\bar{L}, \bar{X}^0)
$$

then

$$\bar{0} = A\hat{v} + B\hat{X} + W \tag{7.11}$$

where

$\hat{X}$: is the vector of successive corrections for the unknown exterior orientation parameters and the coordinates of the object points;

B: is the coefficient matrix, in which the elements are partial differentials of the collinearity equations with respect to the unknown exterior orientation parameters and the coordinates of the object points;

A: is the coefficient matrix, in which the elements are partial differentials of the collinearity equations with respect to the image coordinates of the points; and

W: is the discrepancy vector.

7.3.1 Simplification of the Condition Equations

With respect to equation (7.8), the computation of the partial derivatives of the collinearity equations related to the object space parameters, i.e. the coordinates of the ground control points (GCPs) and the exterior orientation parameters, and those related to the interior orientation parameters, can be simplified as follows:

$$\begin{pmatrix} \dfrac{\partial F(x)}{\partial(parameters)} \\ \dfrac{\partial F(y)}{\partial(parameters)} \end{pmatrix} = - \begin{pmatrix} dx_0 \\ dy_0 \end{pmatrix} + dc \begin{pmatrix} r \\ s \end{pmatrix} + c \begin{pmatrix} dr \\ ds \end{pmatrix} \tag{7.12}$$

Then separating the interior orientation parameters from the exterior orientation parameters and GCPs, the above equations will be converted to the following form:

$$\begin{pmatrix} \dfrac{\partial F(x)}{\partial(parameters)} \\ \dfrac{\partial F(y)}{\partial(parameters)} \end{pmatrix} = \begin{pmatrix} -1 & 0 & r \\ 0 & -1 & s \end{pmatrix} \begin{pmatrix} dx_0 \\ dy_0 \\ dc \end{pmatrix} + c \begin{pmatrix} dr \\ ds \end{pmatrix} \tag{7.13}$$

Regarding the last matrix of the equation (7.13), it can be expanded as:

$$\begin{pmatrix} dr \\ ds \end{pmatrix} = d\begin{pmatrix} \frac{m}{q} \\ \frac{n}{q} \end{pmatrix} = \begin{pmatrix} \frac{q\,dm - m\,dq}{q^2} \\ \frac{q\,dn - n\,dq}{q^2} \end{pmatrix} = \frac{1}{q}\begin{pmatrix} dm - \frac{m}{q}dq \\ dn - \frac{n}{q}dq \end{pmatrix} = \frac{1}{q}\begin{pmatrix} dm - r\,dq \\ dn - s\,dq \end{pmatrix} = \frac{1}{q}\begin{pmatrix} 1 & 0 & -1 \\ 0 & 1 & -s \end{pmatrix}\begin{pmatrix} dm \\ dn \\ dq \end{pmatrix} \quad (7.14)$$

Since the parameters m, n, and q are the functions of the exterior orientation parameters and GCPs, i.e.:

$$\begin{aligned} m &= F_m\,(f_0, \Omega_0, i, \ldots, \omega_1, \varphi_1, \kappa_1, X^g, Y^g, Z^g) \\ n &= F_n\,(f_0, \Omega_0, i, \ldots, \omega_1, \varphi_1, \kappa_1, X^g, Y^g, Z^g) \\ q &= F_q\,(f_0, \Omega_0, i, \ldots, \omega_1, \varphi_1, \kappa_1, X^g, Y^g, Z^g) \end{aligned} \quad (7.15)$$

Therefore the last matricial term in equation (7.14) can be written as follows:

$$\begin{pmatrix} dm \\ dn \\ dq \end{pmatrix} = \begin{pmatrix} \frac{\partial m}{\partial f_0} & \frac{\partial m}{\partial \Omega_0} & \cdots & \frac{\partial m}{\partial \varphi_1} & \frac{\partial m}{\partial \kappa_1} \\ \frac{\partial n}{\partial f_0} & \frac{\partial n}{\partial \Omega_0} & \cdots & \frac{\partial n}{\partial \varphi_1} & \frac{\partial n}{\partial \kappa_1} \\ \frac{\partial q}{\partial f_0} & \frac{\partial q}{\partial \Omega_0} & \cdots & \frac{\partial q}{\partial \varphi_1} & \frac{\partial q}{\partial \kappa_1} \end{pmatrix}\begin{pmatrix} df_0 \\ d\Omega_0 \\ \vdots \\ d\varphi_1 \\ d\kappa_1 \end{pmatrix} + \begin{pmatrix} \frac{\partial m}{\partial X^g} & \frac{\partial m}{\partial Y^g} & \frac{\partial m}{\partial Z^g} \\ \frac{\partial n}{\partial X^g} & \frac{\partial n}{\partial Y^g} & \frac{\partial n}{\partial Z^g} \\ \frac{\partial q}{\partial X^g} & \frac{\partial q}{\partial Y^g} & \frac{\partial q}{\partial Z^g} \end{pmatrix}\begin{pmatrix} dX^g \\ dY^g \\ dZ^g \end{pmatrix} \quad (7.16)$$

Considering the following simplifications:

$$E = \begin{pmatrix} \frac{\partial m}{\partial f_0} & \frac{\partial m}{\partial \Omega_0} & \cdots & \frac{\partial m}{\partial \varphi_1} & \frac{\partial m}{\partial \kappa_1} \\ \frac{\partial n}{\partial f_0} & \frac{\partial n}{\partial \Omega_0} & \cdots & \frac{\partial n}{\partial \varphi_1} & \frac{\partial n}{\partial \kappa_1} \\ \frac{\partial q}{\partial f_0} & \frac{\partial q}{\partial \Omega_0} & \cdots & \frac{\partial q}{\partial \varphi_1} & \frac{\partial q}{\partial \kappa_1} \end{pmatrix},\ H = \begin{pmatrix} \frac{\partial m}{\partial X^g} & \frac{\partial m}{\partial Y^g} & \frac{\partial m}{\partial Z^g} \\ \frac{\partial n}{\partial X^g} & \frac{\partial n}{\partial Y^g} & \frac{\partial n}{\partial Z^g} \\ \frac{\partial q}{\partial X^g} & \frac{\partial q}{\partial Y^g} & \frac{\partial q}{\partial Z^g} \end{pmatrix},\ C = \begin{pmatrix} 1 & 0 & -1 \\ 0 & 1 & -s \end{pmatrix},\ B_i = \begin{pmatrix} -1 & 0 & r \\ 0 & -1 & s \end{pmatrix}$$

and replacing equations (7.12) to (7.16) in equation (7.11) results in:

$$\bar{0} = \begin{pmatrix} v_x \\ v_y \end{pmatrix} + B_i\begin{pmatrix} dx_0 \\ dy_0 \\ dc \end{pmatrix} + \frac{c}{q}CE\begin{pmatrix} dX_0 \\ dY_0 \\ \vdots \\ d\varphi_2 \\ d\kappa_2 \end{pmatrix} + \frac{c}{q}CH\begin{pmatrix} dX^g \\ dY^g \\ dZ^g \end{pmatrix} + W \quad (7.17)$$

Again, if the following assumptions are considered:

$B_e = (c/q)\,CE$; $B_g = (c/q)\,CH$; $V = (v_x, v_y)$;

$\Delta_i = (dx_0, dy_0, dc)$; $\Delta_e = (dX_0, DY_0, ..., d\varphi_2, d\kappa_2)$; $\Delta_g = (dX^g, dY^g, dZ^g)$.

then:

$$\bar{0} = A\,V + B_i\Delta_i + B_e\Delta_e + B_g\Delta_g + W \tag{7.18}$$

where:

i: points to the interior orientation; *e*: points to the exterior orientation; and

g: points to the ground control points; *A*:is equal to unit matrix I (see equation 7.17).

Note: In equation (7.18), the terms related to the interior orientation parameters are considered constant and will be eliminated since these parameters are well known from the previous calibration.

In equation (7.18), matrix B_e can be considered as follows:

$$B_e = \begin{pmatrix} \frac{c}{q} & 0 & -\frac{cr}{q} \\ 0 & \frac{c}{q} & -\frac{cs}{q} \end{pmatrix} \begin{pmatrix} \frac{\partial m}{\partial X_0} & \frac{\partial m}{\partial Y_0} & \cdots & \frac{\partial m}{\partial \varphi_2} & \frac{\partial m}{\partial \kappa_2} \\ \frac{\partial n}{\partial X_0} & \frac{\partial n}{\partial Y_0} & \cdots & \frac{\partial n}{\partial \varphi_2} & \frac{\partial n}{\partial \kappa_2} \\ \frac{\partial q}{\partial X_0} & \frac{\partial q}{\partial Y_0} & \cdots & \frac{\partial q}{\partial \varphi_2} & \frac{\partial q}{\partial \kappa_2} \end{pmatrix} \tag{7.19}$$

With respect to equation (7.19) and regarding the assumption of $B_g = (c/q)\,CH$, then matrix B_g can be shown to be as follows:

$$B_g = \frac{c}{q}\begin{pmatrix} 1 & 0 & -r \\ 0 & 1 & -s \end{pmatrix} \begin{pmatrix} \frac{\partial m}{\partial X^g} & \frac{\partial m}{\partial Y^g} & \frac{\partial m}{\partial Z^g} \\ \frac{\partial n}{\partial X^g} & \frac{\partial n}{\partial Y^g} & \frac{\partial n}{\partial Z^g} \\ \frac{\partial q}{\partial X^g} & \frac{\partial q}{\partial Y^g} & \frac{\partial q}{\partial Z^g} \end{pmatrix} \tag{7.20}$$

The elements of matrices B_e and B_g , which present the derivatives of the collinearity equations with respect to the exterior orientation parameters and the coordinates of the ground points respectively, are given in Appendix C.

7.3.2 A General Solution for the Condition Equations

Equation (7.11) is a simple condition equation to acquire the unknown parameters in a bundle adjustment. More complete equations will arise when some of the unknowns are entered into the bundle adjustment as quasi-observations, i.e. as parameters with a prior knowledge about them, but which may not be accurate enough to give a correct and final solution. With respect to the state of our knowledge about the different types of parameters, three general cases can be distinguished:

(i) Case 1: In this case, the goal is to determine the exterior orientation parameters where the observations are the measured image coordinates of the points with known precision. The coordinates of the ground control points and the interior orientation parameters are entered into the bundle adjustment as known parameters without error. The results of the bundle adjustment program will be the values of the exterior orientation parameters plus the covariance matrix of these parameters. This case can be considered as a simple resection.

(ii) Case 2: In this case, the goal is again to determine the exterior orientation parameters. However, an estimate of the exterior orientation parameters is known a priori. Then, in the bundle adjustment program, the observations are again the measured image coordinates of the points with known precision, plus the quasi-observations of the exterior orientation parameters got from the satellite header data. In this case, the interior orientation parameters and the coordinates of the ground control points are entered into the adjustment program as the known parameters without errors. The result of the bundle adjustment will be the exterior orientation parameters and a statement of their precision as in Case 1. This case can be considered as a resection with quasi-observations.

(iii) Case 3: This case can be considered either as a general resection and intersection for a single stereo model or as a complete space triangulation. The goal is again to determine the exterior orientation parameters and estimate their precision, plus the ground coordinates of the image points and their precision. The input observations are the measured image coordinates of the points and their precision, plus the quasi-observations of the exterior

orientation parameters and the ground coordinates of the measured points with their precision. The result of the bundle adjustment program will be the values of the exterior orientation parameters and their precision, plus the values of the ground coordinates, and their precision. In this project, Cases 2 and 3 have been considered. Where a good set of control point values is available (e.g. the coordinates of ground control points measured by GPS), Case 2 will be used, otherwise Case 3 will be implemented. In the following Sections, first the solution for Case 3, as a full case, is presented. Then a solution for Case 2 forming part of Case 3 is presented.

7.3.2.1 Resection and Intersection (Case 3)

With respect to equation (7.11) and the supplemental observations arising from the use of quasi-observations, the following equations can be considered:

$$\begin{aligned} F(x) &= 0 = x - x_0 + \frac{cm}{q} \\ F(y) &= 0 = y - y_0 + \frac{cn}{q} \\ F(X_e) &= 0 = L_e - \hat{\bar{X}}_e \\ F(X_g) &= 0 = L_g - \hat{\bar{X}}_g \end{aligned} \tag{7.21}$$

where L_e and L_g are the quasi-observations for the exterior orientation parameters and the ground coordinates of the measured points respectively.

Quasi-observation equations for the exterior orientation parameters can be linearized as:

$$\begin{cases} \hat{\bar{X}}_e = \bar{X}_e + \hat{v}_e \\ \hat{\bar{X}}_e = \bar{X}_e^0 + \hat{X}_e \end{cases} \rightarrow \quad \hat{v}_e - \hat{X}_e + W_e = 0 \quad , \quad (W_e = \bar{X}_e - \bar{X}_e^0) \tag{7.22}$$

where $\bar{X}_e$ is the vector of quasi-observations for the exterior orientation parameters; and $\bar{X}_e^0$ is the vector of approximations for the exterior orientation parameters.

The quasi-observation equations for the ground control points can be linearized as follows:

$$\begin{cases} \hat{\bar{X}}_g = \bar{X}_g + \hat{v}_g \\ \hat{\bar{X}}_g = \bar{X}_g^0 + \hat{X}_g \end{cases} \rightarrow \quad \hat{v}_g - \hat{X}_g + W_g = 0 \quad , \quad (W_e = \bar{X}_g - \bar{X}_g^0) \tag{7.23}$$

Assuming $\hat{X}_e = \Delta_e$ and $\hat{X}_g = \Delta_g$, then the global mathematical model is:

$$\begin{aligned} \hat{v} &+ B_e\Delta_e + B_g\Delta_g + W = 0 \\ \hat{v}_e &- I\Delta_e + W_e = 0 \\ \hat{v}_g &- I\Delta_g + W_g = 0 \end{aligned} \tag{7.24}$$

Equation (7.18) can be written in the following matrix form:

$$\begin{pmatrix} \hat{v} \\ \hat{v}_e \\ \hat{v}_g \end{pmatrix} + \begin{pmatrix} B_e & B_g \\ -I & 0 \\ 0 & -I \end{pmatrix} \begin{pmatrix} \Delta_e \\ \Delta_g \end{pmatrix} + \begin{pmatrix} W \\ W_e \\ W_g \end{pmatrix} = 0 \tag{7.25}$$

For a stereo pair of linear array images, the equation (7.25) will be expanded as follows:

$$\begin{pmatrix} \hat{v}^L \\ \hat{v}^R \\ \hat{v}_e{}^L \\ \hat{v}_e{}^R \\ \hat{v}_g \end{pmatrix} + \begin{pmatrix} B_e{}^L & 0 & B_g{}^L \\ 0 & B_e{}^R & B_g{}^R \\ -I & 0 & 0 \\ 0 & -I & 0 \\ 0 & 0 & -I \end{pmatrix} \begin{pmatrix} \Delta_e{}^L \\ \Delta_e{}^R \\ \Delta_g \end{pmatrix} + \begin{pmatrix} W^L \\ W^R \\ W_e{}^L \\ W_e{}^R \\ W_g \end{pmatrix} = 0 \tag{7.26}$$

where the exposants R and L represent the left and right images respectively.

In more general form, the equation (7.26) can be written as follows:

$$\bar{V} + \bar{B}\bar{\Delta} + \bar{W} = 0 \tag{7.27}$$

For one pair of linear array images with n_1 and n_2 image points for the left and right images respectively and m ground control points, the dimensions of the vectors and matrices in equation (7.26) will be as follows:

$$\begin{aligned} &\hat{v}^L_{(2n_1)} \;;\; \hat{v}^R_{(2n_2)} \;;\; \hat{v}_e{}^L_{(15)} \;;\; \hat{v}_e{}^R_{(15)} \;;\; \hat{v}_{g(3m)} \\ &B_e{}^L_{(2n_1,\,15)} \;;\; B_e{}^R_{(2n_2,\,15)} \;;\; B_g{}^L_{(2n_2,\,3m)} \\ &\Delta_e{}^L_{(15)} \;;\; \Delta_e{}^R_{(15)} \;;\; \Delta_{g(3m)} \\ &w^L_{(2n_1)} \;;\; w^R_{(2n_2)} \;;\; w_e{}^L_{(15)} \;;\; w_e{}^R_{(15)} \;;\; w_{g(3m)} \end{aligned} \tag{7.28}$$

in which case, the dimensions of the more general matrices in equation (7.27) will be:

$$V_{(2n_1 + 2n_2 + 30 + 3m)} \; ; \; B_{(2n_1 + 2n_2 + 30 + 3m \; , \; 30 + 3m)} \; ; \; \Delta_{(30 + 3m)} \; ; \; W_{(2n_1 + 2n_2 + 30 + 3m)} \quad (7.29)$$

The matrix of partial differentials of the collinearity equations with respect to the unknown exterior orientation parameters and the ground coordinates of the image, i.e. matrix B, can be shown to be as follows:

$$B = \begin{pmatrix}
\frac{\partial F(x_1)}{\partial f_0^{\,L}} & \cdots & \frac{\partial F(x_1)}{\partial \kappa_2^{\,L}} & 0 & \cdots & 0 & \frac{\partial F(x_1)}{\partial X_g^{\,1}} & \cdots & \frac{\partial F(x_1)}{\partial Z_g^{\,m}} \\
\frac{\partial F(y_1)}{\partial f_0^{\,L}} & \cdots & \frac{\partial F(y_1)}{\partial \kappa_2^{\,L}} & 0 & \cdots & 0 & \frac{\partial F(y_1)}{\partial X_g^{\,1}} & \cdots & \frac{\partial F(y_1)}{\partial Z_g^{\,m}} \\
\vdots & \cdots & & 0 & \cdots & 0 & & \cdots & \vdots \\
\frac{\partial F(x_{n_1})}{\partial f_0^{\,L}} & \cdots & \frac{\partial F(x_{n_1})}{\partial \kappa_2^{\,L}} & 0 & \cdots & 0 & \frac{\partial F(x_{n_1})}{\partial X_g^{\,1}} & \cdots & \frac{\partial F(x_{n_1})}{\partial Z_g^{\,m}} \\
\frac{\partial F(y_{n_1})}{\partial f_0^{\,L}} & \cdots & \frac{\partial F(y_{n_1})}{\partial \kappa_2^{\,L}} & 0 & \cdots & 0 & \frac{\partial F(y_{n_1})}{\partial X_g^{\,1}} & \cdots & \frac{\partial F(y_{n_1})}{\partial Z_g^{\,m}} \\
0 & \cdots & 0 & \frac{\partial F(x_1)}{\partial f_0^{\,R}} & \cdots & \frac{\partial F(x_1)}{\partial \kappa_2^{\,R}} & \frac{\partial F(x_1)}{\partial X_g^{\,1}} & \cdots & \frac{\partial F(x_1)}{\partial Z_g^{\,m}} \\
0 & \cdots & 0 & \frac{\partial F(y_1)}{\partial f_0^{\,R}} & \cdots & \frac{\partial F(y_1)}{\partial \kappa_2^{\,R}} & \frac{\partial F(y_1)}{\partial X_g^{\,1}} & \cdots & \frac{\partial F(y_1)}{\partial Z_g^{\,m}} \\
0 & \cdots & 0 & & \cdots & & & \cdots & \vdots \\
0 & \cdots & 0 & \frac{\partial F(x_{n_2})}{\partial f_0^{\,R}} & \cdots & \frac{\partial F(x_{n_2})}{\partial \kappa_2^{\,R}} & \frac{\partial F(x_{n_2})}{\partial X_g^{\,1}} & \cdots & \frac{\partial F(x_{n_2})}{\partial Z_g^{\,m}} \\
0 & \cdots & 0 & \frac{\partial F(y_{n_2})}{\partial f_0^{\,R}} & \cdots & \frac{\partial F(y_{n_2})}{\partial \kappa_2^{\,R}} & \frac{\partial F(y_{n_2})}{\partial X_g^{\,1}} & \cdots & \frac{\partial F(y_{n_2})}{\partial Z_g^{\,m}} \\
-1 & \cdots & 0 & 0 & \cdots & 0 & 0 & \cdots & 0 \\
\vdots & \cdots & 0 & 0 & \cdots & 0 & 0 & \cdots & \vdots \\
0 & \cdots & -1 & 0 & \cdots & 0 & 0 & \cdots & 0 \\
0 & \cdots & 0 & -1 & \cdots & 0 & 0 & \cdots & 0 \\
\vdots & \cdots & 0 & 0 & \cdots & 0 & 0 & \cdots & \vdots \\
0 & \cdots & 0 & 0 & \cdots & -1 & 0 & \cdots & 0 \\
0 & \cdots & 0 & 0 & \cdots & 0 & -1 & \cdots & 0 \\
\vdots & \cdots & 0 & 0 & \cdots & 0 & 0 & \cdots & \vdots \\
0 & \cdots & 0 & 0 & \cdots & 0 & 0 & \cdots & -1
\end{pmatrix} \quad (7.30)$$

The weight matrix for the image coordinates, i.e. the observations of the points; the corresponding ground coordinates of the image points; and the exterior orientation

parameters, i.e. their quasi-observations, which is necessary in any least squares adjustment, can be shown to be equation (7.31).

$$P = \begin{pmatrix} P_{xy}{}^{L} & 0 & 0 & 0 & 0 \\ 0 & P_{xy}{}^{R} & 0 & 0 & 0 \\ 0 & 0 & P_{e}{}^{L} & 0 & 0 \\ 0 & 0 & 0 & P_{e}{}^{R} & 0 \\ 0 & 0 & 0 & 0 & P_{g} \end{pmatrix} \tag{7.31}$$

Note: the dimension of the weight matrix is: P ($2n_1 + 2n_2 + 30 + 3m$).

Or in more detail, the weight matrix can be shown to be as follows:

$$P = \begin{pmatrix} \frac{1}{(\sigma^2_{x_1})^L} & \cdots & 0 & 0 & \cdots & 0 & 0 & \cdots & 0 & 0 & \cdots & 0 & 0 & \cdots & 0 \\ \vdots & & & & & & & & & & & & & & \\ 0 & \cdots & \frac{1}{(\sigma^2_{y_{n1}})^L} & 0 & \cdots & 0 & 0 & \cdots & 0 & 0 & \cdots & 0 & 0 & \cdots & 0 \\ 0 & \cdots & 0 & \frac{1}{(\sigma^2_{x_1})^R} & \cdots & 0 & 0 & \cdots & 0 & 0 & \cdots & 0 & 0 & \cdots & 0 \\ \vdots & & & & & & & & & & & & & & \\ 0 & \cdots & 0 & 0 & \cdots & \frac{1}{(\sigma^2_{y_{n2}})^R} & 0 & \cdots & 0 & 0 & \cdots & 0 & 0 & \cdots & 0 \\ 0 & \cdots & 0 & 0 & \cdots & 0 & \frac{1}{\sigma^2_{f_0{}^L}} & \cdots & 0 & 0 & \cdots & 0 & 0 & \cdots & 0 \\ 0 & \cdots & 0 & 0 & \cdots & 0 & 0 & \cdots & \frac{1}{\sigma^2_{\kappa_1{}^L}} & 0 & \cdots & 0 & 0 & \cdots & 0 \\ 0 & \cdots & 0 & 0 & \cdots & 0 & 0 & \cdots & 0 & \frac{1}{\sigma^2_{f_0{}^R}} & \cdots & 0 & 0 & \cdots & 0 \\ 0 & \cdots & 0 & 0 & \cdots & 0 & 0 & \cdots & 0 & 0 & \cdots & \frac{1}{\sigma^2_{\kappa_1{}^R}} & 0 & \cdots & 0 \\ 0 & \cdots & 0 & 0 & \cdots & 0 & 0 & \cdots & 0 & 0 & \cdots & 0 & \frac{1}{\sigma^2_{X_1{}^g}} & \cdots & 0 \\ 0 & \cdots & 0 & 0 & \cdots & 0 & 0 & \cdots & 0 & \cdots & 0 & 0 & \cdots & 0 & \frac{1}{\sigma^2_{Z_m{}^g}} \end{pmatrix} \tag{7.32}$$

The final solution for the equation (7.27) will be given as:

$$\bar{\Delta} = -(\bar{B}^t P \bar{B})\, \bar{B}^t P \bar{W} \tag{7.33}$$

The results of this bundle adjustment will be the values of the exterior orientation parameters and the ground coordinates of the measured image points, together with a statement of their accuracy. These values will be used later to transform all of the measured image points to the ground coordinate system. The results of the bundle adjustment program and their accuracy have been analyzed and discussed in more detail in Chapters 8 and 9 where the results of the experimental tests carried out on both cross-track and along-track stereo images will be presented.

The solution of the condition equations in the case of a resection with quasi-observations (Case 2) can be extracted directly from the above solution. This matter is explained in the next Section.

7.3.2.2 Resection with Quasi-Observations (Case 2)

Since in Case 2, the coordinates of the ground control points are considered to be constant with good accuracy, then all of the elements related to these parameters in different equations presented in Section 7.3.2.1 have to be eliminated. This will result in a much simpler set of matrices. Starting with equation 7.26 as a general mathematical model for a stereo pair of linear array images, this equation is simplified for Case 2 as follows:

$$\begin{pmatrix} \hat{v}^L \\ \hat{v}^R \\ \hat{v}_e{}^L \\ \hat{v}_e{}^R \end{pmatrix} + \begin{pmatrix} B_e{}^L & 0 \\ 0 & B_e{}^R \\ -I & 0 \\ 0 & -I \end{pmatrix} \begin{pmatrix} \Delta_e{}^L \\ \Delta_e{}^R \end{pmatrix} + \begin{pmatrix} W^L \\ W^R \\ W_e{}^L \\ W_e{}^R \end{pmatrix} = 0 \qquad (7.34)$$

This equation has again the same general mathematical form shown in equation (7.27) but with the following new dimensions:

$$V_{(2n_1 + 2n_2 + 30)} \;;\; B_{(2n_1 + 2n_2 + 30\,,\,30)} \;;\; \Delta_{(30)} \;;\; W_{(2n_1 + 2n_2 + 30)} \qquad (7.35)$$

The new matrix of partial differentials of the collinearity equations with respect to the unknown exterior orientation parameters, i.e. matrix B, can be shown in the following

matrix form:

$$B = \begin{pmatrix} \frac{\partial F(x_1)}{\partial f_0^L} & \cdots & \frac{\partial F(x_1)}{\partial \kappa_2^L} & 0 & \cdots & 0 \\ \frac{\partial F(y_1)}{\partial f_0^L} & \cdots & \frac{\partial F(y_1)}{\partial \kappa_2^L} & 0 & \cdots & 0 \\ \vdots & \cdots & & 0 & \cdots & 0 \\ \frac{\partial F(x_{n_1})}{\partial f_0^L} & \cdots & \frac{\partial F(x_{n_1})}{\partial \kappa_2^L} & 0 & \cdots & 0 \\ \frac{\partial F(y_{n_1})}{\partial f_0^L} & \cdots & \frac{\partial F(y_{n_1})}{\partial \kappa_2^L} & 0 & \cdots & 0 \\ 0 & \cdots & 0 & \frac{\partial F(x_1)}{\partial f_0^R} & \cdots & \frac{\partial F(x_1)}{\partial \kappa_2^R} \\ 0 & \cdots & 0 & \frac{\partial F(y_1)}{\partial f_0^R} & \cdots & \frac{\partial F(y_1)}{\partial \kappa_2^R} \\ 0 & \cdots & 0 & & \cdots & \\ 0 & \cdots & 0 & \frac{\partial F(x_{n_2})}{\partial f_0^R} & \cdots & \frac{\partial F(x_{n_2})}{\partial \kappa_2^R} \\ 0 & \cdots & 0 & \frac{\partial F(y_{n_2})}{\partial f_0^R} & \cdots & \frac{\partial F(y_{n_2})}{\partial \kappa_2^R} \\ -1 & \cdots & 0 & 0 & \cdots & 0 \\ \vdots & \cdots & 0 & 0 & \cdots & 0 \\ 0 & \cdots & -1 & 0 & \cdots & 0 \\ 0 & \cdots & 0 & -1 & \cdots & 0 \\ \vdots & \cdots & 0 & 0 & \cdots & 0 \\ 0 & \cdots & 0 & 0 & \cdots & -1 \end{pmatrix} \tag{7.36}$$

In Case 2, the weight matrix for the image coordinates of the points (observations) and the exterior orientation parameters (quasi-observations) can be shown as equation (7.37).

$$P = \begin{pmatrix} P_{xy}^{\ L} & 0 & 0 & 0 \\ 0 & P_{xy}^{\ R} & 0 & 0 \\ 0 & 0 & P_e^{\ L} & 0 \\ 0 & 0 & 0 & P_e^{\ R} \end{pmatrix} \tag{7.37}$$

Note: the dimension of the weight matrix is: P ($2n_1 + 2n_2 + 30$).

The final solution for equation (7.27) in Case 2 will be similar to that for Case 3, but with the matrices having different dimensions given as:

$$\bar{\Delta} = -(\bar{B}^t P \bar{B})\, \bar{B}^t P \bar{W} \tag{7.38}$$

The results of this bundle adjustment will be the values of the exterior orientation parameters together with a statement of their accuracy. These values will be used in the intersection formula given in the next Section to transform all of the measured image points into the ground coordinate system. This will give the residuals for the control points in general and for the check points in particular.

7.3.3 Spatial Intersection

To calculate the ground coordinates of the image points using the computed exterior orientation parameters and the available interior orientation parameters, the spatial intersection technique given in Slama (1980) has been used. The main difference in the present case with that discussed in Slama (1980) is that the collinearity equations there are given for each left or right image and the exterior orientation parameters are kept as constant values during the computation. However in the present case, these equations are valid for each line of the left or right image and so exterior orientation parameters for each line corresponding to the selected image point must be computed before implementing the intersection formula. Considering either equation (5.46) or equation (6.10) in the case of cross-track or along-track stereo images respectively, the following equation will result:

$$\begin{pmatrix} X_i^g - X_0 \\ Y_i^g - Y_0 \\ Z_i^g - Z_0 \end{pmatrix} = \frac{1}{S} R^t \begin{pmatrix} x_i - x_0 \\ y_i - y_0 \\ -c \end{pmatrix} \tag{7.39}$$

Assuming $1/S = \lambda$ and replacing matrix R with the elements shown in equations (5.45) or (6.8) depending on whether cross-track or along-track stereo images are being considered, this results in:

$$
\begin{aligned}
X_i^g - X_0^{L_j} &= \lambda_{L_j}[R_{11}^{L_j}(x_i - x_0^{L_j}) + R_{21}^{L_j}(y_i - y_0^{L_j}) + R_{31}^{L_j}(-c^{L_j})] \\
Y_i^g - Y_0^{L_j} &= \lambda_{L_j}[R_{12}^{L_j}(x_i - x_0^{L_j}) + R_{22}^{L_j}(y_i - y_0^{L_j}) + R_{32}^{L_j}(-c^{L_j})] \\
Z_i^g - Z_0^{L_j} &= \lambda_{L_j}[R_{13}^{L_j}(x_i - x_0^{L_j}) + R_{23}^{L_j}(y_i - y_0^{L_j}) + R_{33}^{L_j}(-c^{L_j})]
\end{aligned}
\tag{7.40}
$$

where superscript L refers to the left image and subscript j refers to the line number.

For the right image, the formula will be the same but superscript L becomes R. Now with the following assumption:

$$
\begin{aligned}
U_i^{L_j} &= R_{11}^{L_j}(x_i - x_0^{L_j} + R_{21}^{L_j}(y_i - y_0^{L_j} + R_{31}^{L_j}(-c^{L_j}) \\
V_i^{L_j} &= R_{12}^{L_j}(x_i - x_0^{L_j} + R_{22}^{L_j}(y_i - y_0^{L_j} + R_{32}^{L_j}(-c^{L_j}) \\
W_i^{L_j} &= R_{13}^{L_j}(x_i - x_0^{L_j} + R_{23}^{L_j}(y_i - y_0^{L_j} + R_{33}^{L_j}(-c^{L_j})
\end{aligned}
\tag{7.41}
$$

Then the following equation will result (N.B. for simplification, the subscript j has been eliminated in the following equations):

$$
\begin{aligned}
X_i^g - X_0^L &= \lambda_L U_i^L \\
Y_i^g - Y_0^L &= \lambda_L V_i^L \\
Z_i^g - Z_0^L &= \lambda_L W_i^L
\end{aligned}
\tag{7.42}
$$

Rearrangement of equation (7.42) results in equation (7.43) as follows:

$$
\begin{aligned}
X_i^g &= X_0^L + \lambda_L U_i^L \\
Y_i^g &= Y_0^L + \lambda_L V_i^L \\
Z_i^g &= Z_0^L + \lambda_L W_i^L
\end{aligned}
\tag{7.43}
$$

Using the same approach for the right image results in the following equations:

$$
\begin{aligned}
X_i^g &= X_0^R + \lambda_R U_i^R \\
Y_i^g &= Y_0^R + \lambda_R V_i^R \\
Z_i^g &= Z_0^R + \lambda_R W_i^R
\end{aligned}
\tag{7.44}
$$

Combining equations (7.43) and (7.44) gives:

$$\begin{aligned} X_0^L + \lambda_L U_i^L &= X_0^R + \lambda_R U_i^R \\ Y_0^L + \lambda_L V_i^L &= Y_0^R + \lambda_R V_i^R \\ Z_0^L + \lambda_L W_i^L &= Z_0^R + \lambda_R W_i^R \end{aligned} \tag{7.45}$$

Using equation (7.45), the parameter λ_R can be calculated as:

$$\lambda_R = \frac{(X_0^R - X_0^L) V_i^L - (Y_0^R - Y_0^L) U_i^L}{V_i^R U_i^L - V_i^L U_i^R} \tag{7.46}$$

Parameter λ_L also can be calculated using equation (7.45) as follows:

$$\lambda_L = \frac{(X_0^R - X_0^L) V_i^R - (Y_0^R - Y_0^L) U_i^R}{V_i^R U_i^L - V_i^L U_i^R} \tag{7.47}$$

Therefore, by substituting λ_R or λ_L in equation (7.44) or (7.43) respectively, the ground coordinates of each image point i, i.e. X_i^g, Y_i^g, and Z_i^g, can be calculated.

The spatial intersection formula is placed in a later part of the bundle adjustment program. As will be seen later, the 2D polynomial adjustment program and 3D bundle adjustment program have been implemented as different modules within a main program based on programming in the C++ language within the Windows 3.1 operating system used in PCs. The next Section of this Chapter will describe this Windows program in detail.

7.4 The Main Adjustment Program

The main program for the least squares adjustment has been written using the Borland C++ compiler for Windows 3.1. This version of the operating system supports over 1,000 function calls that applications can use. All the main Windows functions are declared in a header file named WINDOWS.H, which is included in the Windows Software Development Kit and the Borland C++ compiler. It contains a multitude of definitions needed by all Windows programs, including prototypes (declarations) for the hundreds of Windows functions; and the definitions of structures, constants, and derived data types. All Windows programs must include the WINDOWS.H header file.

Within the developed bundle adjustment program components, three main modules can be identified or categorized for the major types of functions that need to be implemented in the main adjustment procedure. Each of these main modules is further divided into several sub-modules. Each sub-module represents a collection of functions grouped together for a definite or specific application (see Figure 7.1). Each main module is described briefly as follows:

(i) Edit Text: This module comprises three sub-modules dealing with file manipulation, input/output manipulation and input/output printing. File manipulation contains the functions needed to open a text file (e.g. the input to or output from the bundle adjustment program); to display this on the screen; to save any changes in the file; or to save it under another name. Input/output manipulation deals with the need to cut or paste either some part of the file or the whole text file; to clear the screen or to undo a function. The printing sub-module contains a function to print an input/output text file using a printer defined by the Print Manager of the Windows 3.1 operating system.

(ii) Bundle Adjustment: This module comprises five sub-modules. The matrix manipulation sub-module is common to both the polynomial and the bundle adjustment main modules. The image coordinate transformation contains functions to tranform the raw pixel coordinates to image coordinates with respect to the centre of each line, and in the case of SPOT Level 1B images, it transforms the image coordinates in this Level back to their Level 1A equivalents. Header data manipulation deals with the computation of approximations for the exterior orientation parameters using Lagrange polynomials and the required mathematical equations. The derivations sub-module undertakes the computation of the exterior orientation parameters for each line and the derivations of the collinearity equations with respect to the exterior orientation parameters (Cases 2 and 3 of the bundle adjustment program) and ground control points (Case 3). The intersection sub-module deals with the intersection equations required to calculate the ground coordinates of any image point.

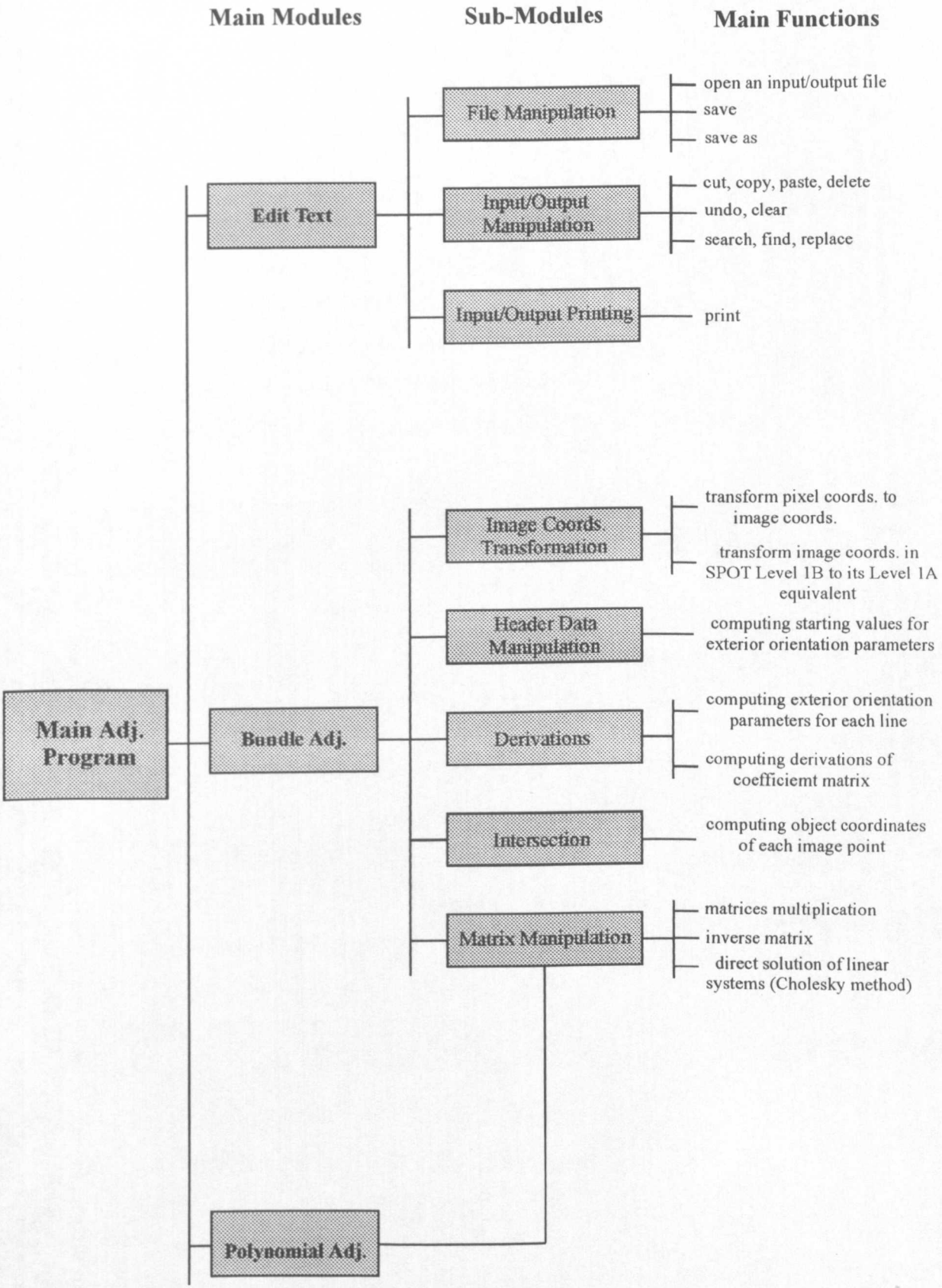

Figure 7.1 Modules and Sub-Modules in the Main Adjustment Program

(iii) Polynomial Adjustment: As mentioned before in Section 7.2, this module deals with the geometric correction of satellite linear array images in two dimensions only. It comprises only the matrix manipulation sub-module. It mainly contains the functions needed for matrix multiplication, inverse matrix operations and the Cholesky direct solution of linear equations.

To make it easy for the user to work on different modules, a menu bar that is typical of those found in Windows software packages has been designed and implemented using the Borland Resource Workshop and incorporated in the main Windows program. Each choice in the menu bar produces a pop-up (or drop-down) menu that shows another list of choices. Figure 7.2 illustrates the menu bar as well as the pop-up menu used in the present program.

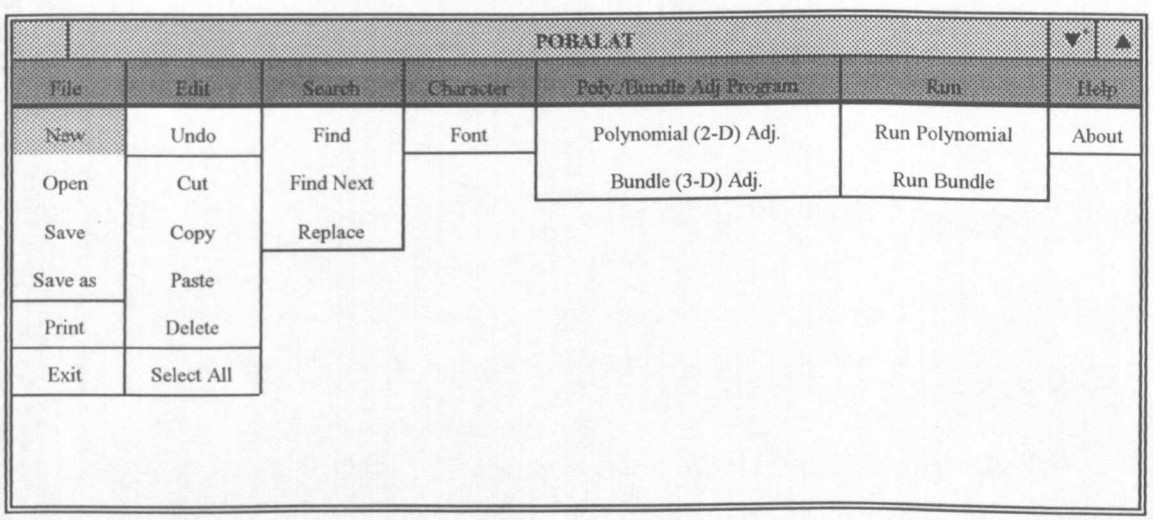

Figure 7.2 Illustration of the Menu Bar and Pop-up Menu in Main Adjustment Program

As can be seen, while the first four choices of the menu bar are related to the edit text modules, the fifth and sixth choices deal with the polynomial and bundle adjustment modules respectively. Selecting the Poly/Bundle Adj. Program choice in the menu bar results in a further choice of two pop-up menus that prepare the input data for running either the polynomial or the bundle adjustment program using the menu bar option Run.

(i) Selecting the Polynomial (2-D) Adj. Pop-up menu brings up a dialog box on the screen.

This dialog box has also been designed using Borland's Resource Workshop and implemented in the main program to help users to select the appropriate polynomial terms and to enter the number of ground control points and the pixel size of the image which will be used later in the actual polynomial adjustment program. Figure 7.3 shows the dialog box related to this polynomial adjustment selection.

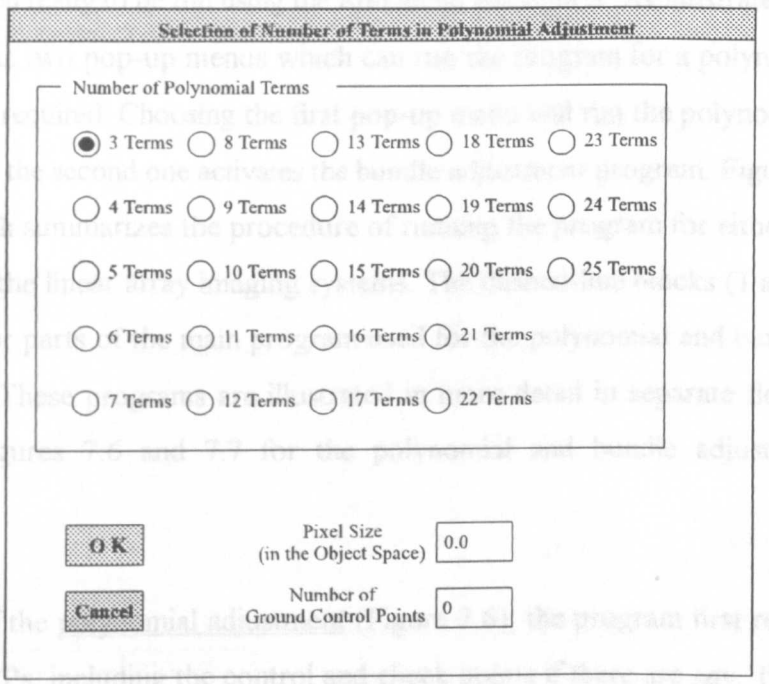

Figure 7.3 Selection of the Number of Polynomial Terms Dialog Box

(ii) Selecting the Bundle (3-D) Adj. Pop-up menu brings up another dialog box (Figure 7.4) on the screen which helps the user to select the appropriate satellite linear array imaging system.

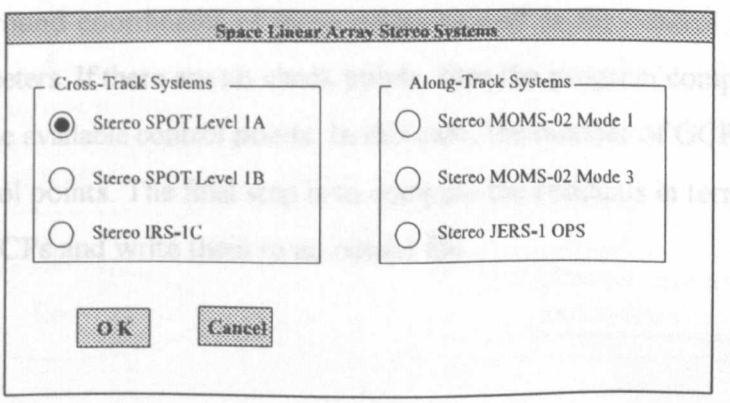

Figure 7.4 Selection of Linear Array Stereo Systems Dialog Box

This dialog box presents the appropriate case related to each type of linear array stereo image to the bundle adjustment program and ensures that the program is ready to be run in three dimensions.

After preparing the input data for either the polynomial or bundle adjustment procedure, the program is then ready to be run using the Run menu bar option. As illustrated in Figure 7.2, this option has two pop-up menus which can run the program for a polynomial or bundle adjustment as required. Choosing the first pop-up menu will run the polynomial adjustment module, while the second one activates the bundle adjustment program. Figure 7.5 is a flow diagram which summarizes the procedure of running the program for either the 2D or 3D modelling of the linear array imaging systems. The dashed-line blocks (1 and 2) represent the two major parts of the main program used for the polynomial and bundle adjustment respectively. These programs are illustrated in more detail in separate flow diagrams as shown in Figures 7.6 and 7.7 for the polynomial and bundle adjustment solutions respectively.

In the case of the polynomial adjustment (Figure 7.6), the program first reads in the total number of GCPs, including the control and check points if there are any. Then the general matrix A whose elements are the terms of the poynomial equations required for control and check points is established. Then the programs call the matrix manipulation sub-module at different times for the construction of the normal equations in the least squares adjustment and, after that, for computing the unknowns of the polynomial equations using the Cholesky direct solution for linear equations. Now if there are any check points, then the program will compute the ground coordinates of these points as well as the control points using the computed parameters. If there are no check points, then the program computes the ground coordinates of the available control points. In this case, the number of GCPs is equal to the number of control points. The final step is to compute the residuals in terms of the RMSE values for the GCPs and write them to an output file.

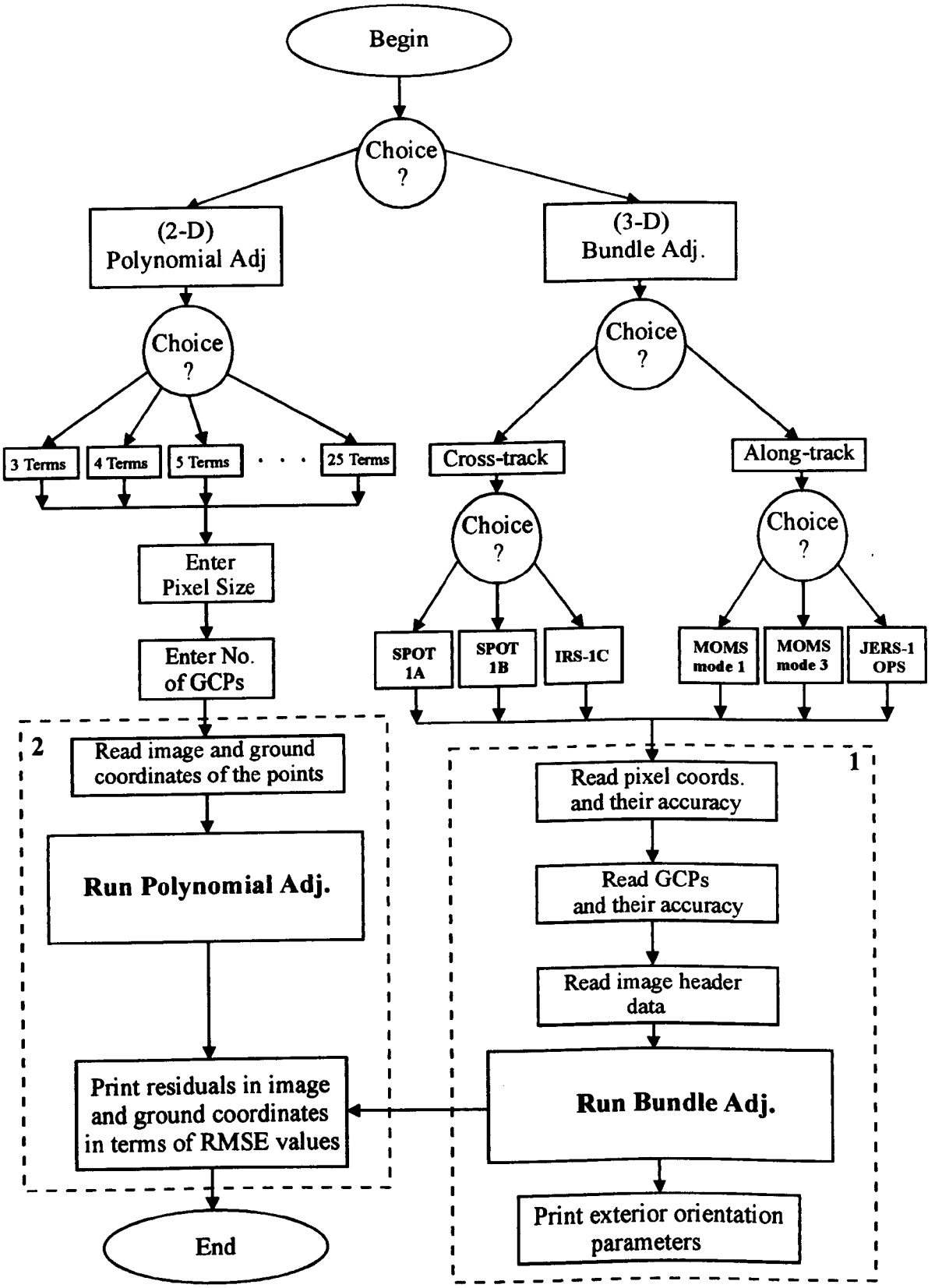

Figure 7.5 The flow diagram shows an overview of the main adjustment program

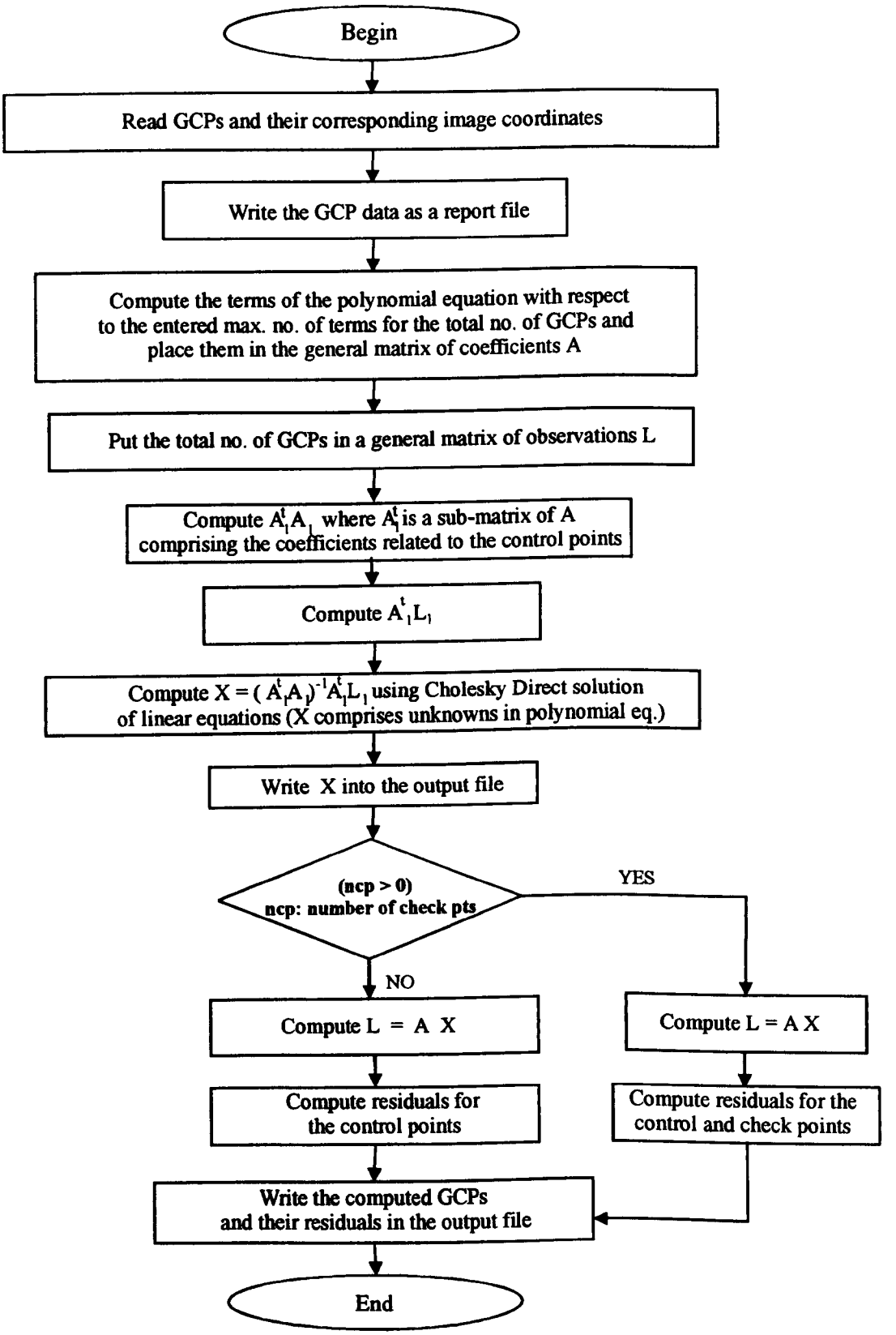

Figure 7.6 The flow diagram shows the steps that are executed in the case of the polynomial adjustment program

In the case of the bundle adjustment program, as can be seen from Figure 7.7, several steps can be considered:

Step 1: The program reads the ground coordinates of the GCPs and their corresponding pixel coordinates plus their accuracy values from the input files (for the right and left images) and then writes them into an output file.

Step 2: The program calls the image coordinates transformation sub-module to compute the image coordinates of the GCPs. In the case of SPOT Level 1B images, as mentioned before, this sub-module also converts the Level 1B values back to their equivalent Level 1A values.

Step 3: The program reads the header data and computes the Keplerian elements (for the centre line of each linear array image) using the header data manipulation sub-module which provides the starting values for the determination of the exterior orientation parameters.

Step 4: The weight matrix for the observations and quasi-observations is constructed.

Step 5: In this step, the iterations and the computation of the exterior orientation parameters for each line, for which the image coordinates have been given, are executed using polynomial equations. This is carried out within the derivation sub-module which also computes the derivation of the collinearity equations with respect to the exterior orientation parameters (Cases 2 and 3) and control points (Case 3 only).

Step 6: After computing the derivation, matrix A (i.e. the matrix of coefficients for the least squares adjustment) and discrepancy vector W are constructed.

Step 7: The program calls the matrix manipulation sub-module several times to construct the normal equations required for least squares adjustment.

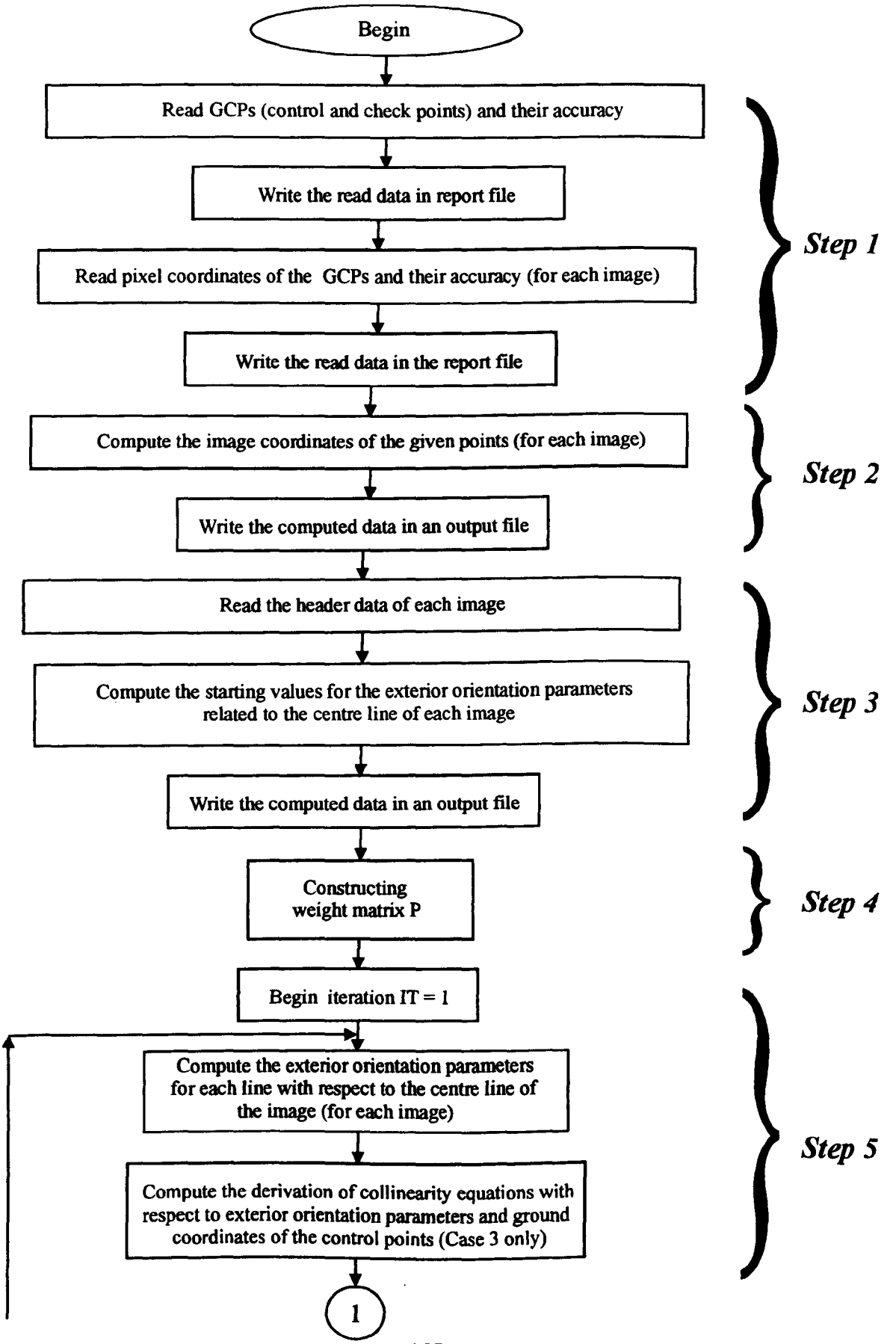
Begin
Read GCPs (control and check points) and their accuracy
Write the read data in report file
Read pixel coordinates of the GCPs and their accuracy (for each image)
Write the read data in the report file
Compute the image coordinates of the given points (for each image)
Write the computed data in an output file
Read the header data of each image
Compute the starting values for the exterior orientation parameters related to the centre line of each image
Write the computed data in an output file
Constructing weight matrix P
Begin iteration IT = 1
Compute the exterior orientation parameters for each line with respect to the centre line of the image (for each image)
Compute the derivation of collinearity equations with respect to exterior orientation parameters and ground coordinates of the control points (Case 3 only)
1
Step 1
Step 2
Step 3
Step 4
Step 5

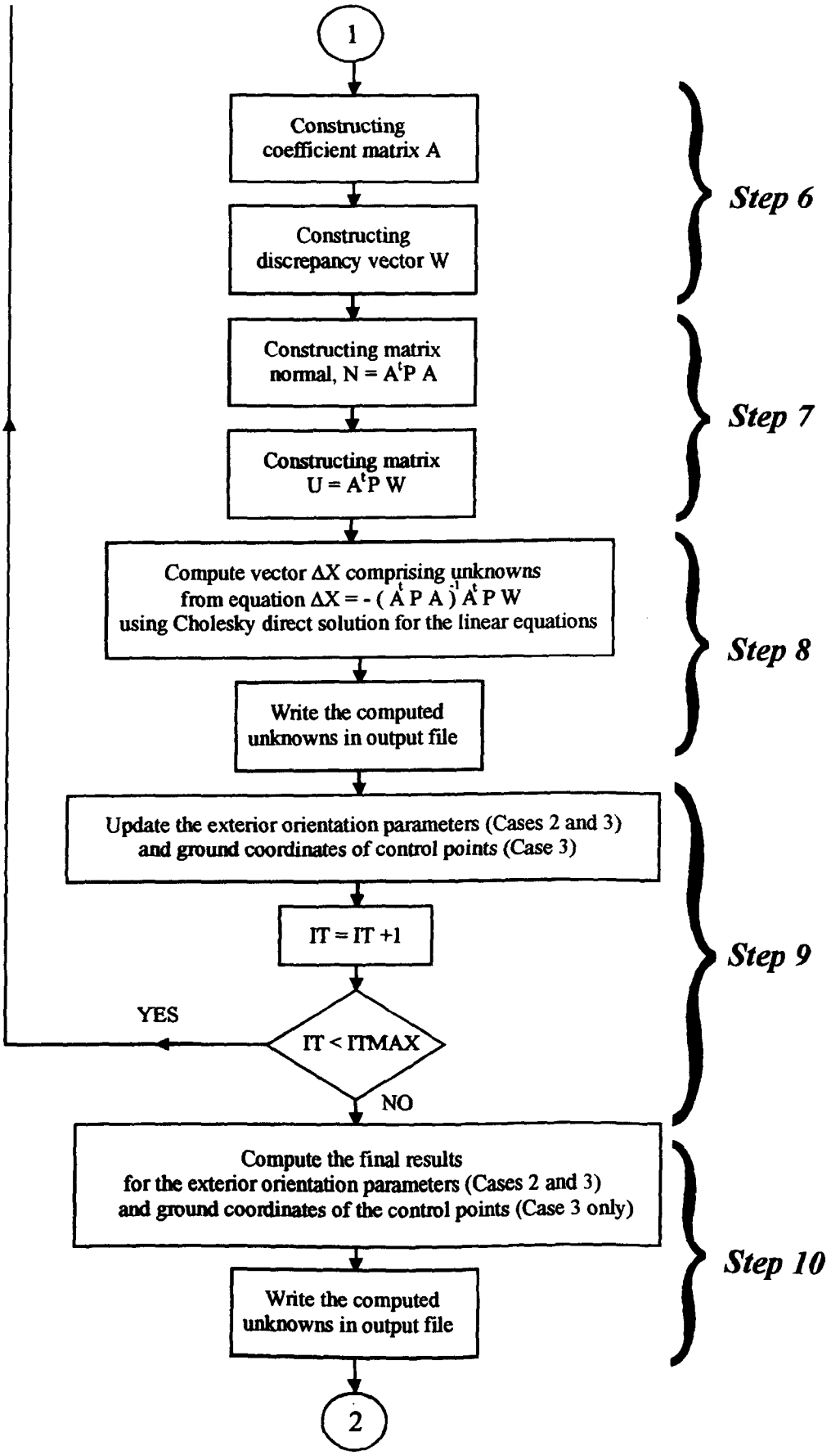
1
Constructing coefficient matrix A
Constructing discrepancy vector W
Step 6
Constructing matrix normal, N = A^t P A
Constructing matrix U = A^t P W
Step 7
Compute vector ΔX comprising unknowns from equation ΔX = - (A^t P A)^-1 A^t P W using Cholesky direct solution for the linear equations
Write the computed unknowns in output file
Step 8
Update the exterior orientation parameters (Cases 2 and 3) and ground coordinates of control points (Case 3)
IT = IT +1
YES
IT < ITMAX
NO
Step 9
Compute the final results for the exterior orientation parameters (Cases 2 and 3) and ground coordinates of the control points (Case 3 only)
Write the computed unknowns in output file
Step 10
2

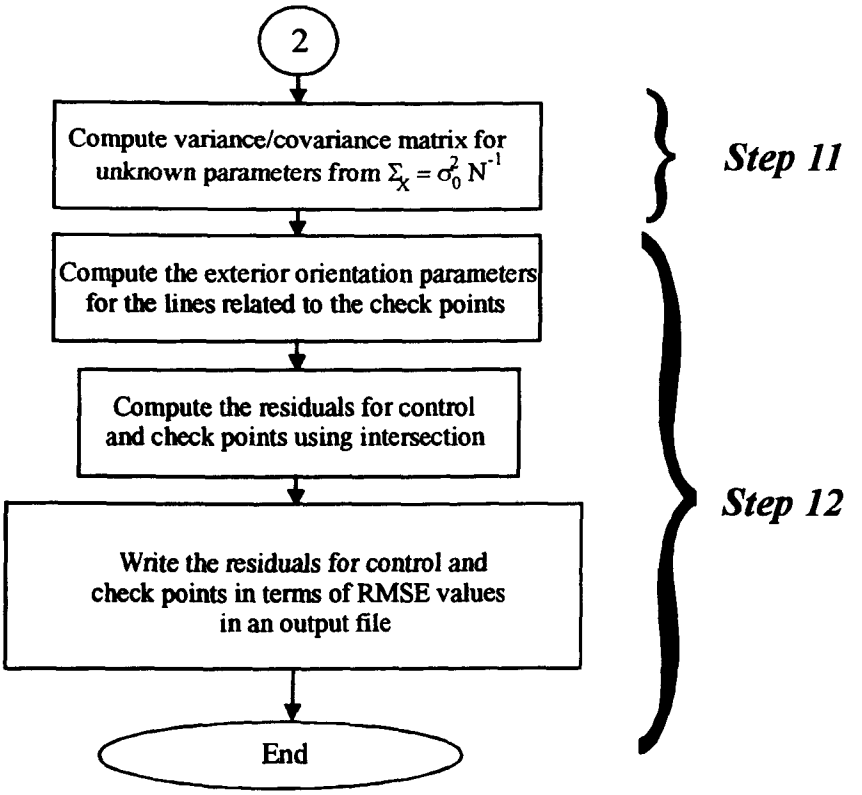

Figure 7.7 The flow diagram shows the steps that are executed in the case of the bundle adjustment program

Step 8: The program again calls the matrix manipulation sub-module for the computation of the corrections for the parameters in the least squares adjustment (i.e. for the exterior orientation parameters (Cases 2 and 3) and for the control points (Case 3 only).

Step 9: The values of the exterior orientation parameters (Cases 2 and 3) and control points (Case 3) are updated. Then the iteration procedure is repeated untill the maximum number of iterations has been reached.

Step 10: The program computes the final values for the exterior orientation parameters (Cases 2 and 3) and the ground coordinates of the control points and writes the computed values in an output file.

Step 11: The matrix of variances and covariances of the parameters is computed using the matrix manipulation sub-module.

Step 12: The intersection sub-module computes the ground coordinates of the control and check points using the computed exterior orientation parameters. Then the residuals for the control and check points (in ground and image space) in terms of their RMSE values, are computed and written in an output file.

The main adjustment program presented in this Chapter is listed and included as Appendix E. It has been tested with various satellite-based linear array systems and different types of ground control points derived both from maps and GPS measurements. The next two Chapters (8 and 9) outline these tests and discuss the results achieved using this program. They also attempt to evaluate the program itself as well as the use of satellite-based linear array imaging systems as seen from a photogrammetric point of view.

CHAPTER 8 : GEOMETRIC ACCURACY TESTS OF CROSS-TRACK LINEAR ARRAY IMAGES

In the case of cross-track linear array imagery, the geometric accuracy of a number of SPOT Level 1A and 1B images has been tested in two and three dimensions using the adjustment program outlined in Chapter 7. Two sets of SPOT imagery were available to be tested. The first set comprised five SPOT Level 1B stereo-images and one SPOT Level 1A stereo-image over an area in Jordan. The second set comprised one SPOT Level 1A stereo-pair and its corresponding SPOT level 1B stereo-pair over an area in Crete. Different tests have been carried out using these images. They include using different numbers of control points and unknown parameters in the adjustment program. In the first section of this Chapter, the tests carried out with SPOT images over the Jordanian test field are outlined; in the second section, the test conducted over Crete will be discussed.

8.1 Geometric Accuracies Achieved with SPOT Stereo Imagery over a Jordanian Test Field

Five SPOT Level lB stereo-pairs and one Level 1A stereo-pair covering the Badia project area in Jordan have been provided by my research colleague, Mr N. Al-Rousan, to be tested in the author's program. The Badia Project is a joint Jordanian and British project to undertake inter-disciplinary scientific research which will lead to development activities in (i) the field of environmental improvement; (ii) the delivery of better targetted government services; and (iii) beneficial economic change, for an area in North Eastern Jordan.

The Badia is a vast arid area covering some 72,000 km^2 in the Eastern part of Jordan. It receives on average between 50mm and 200mm of rainfall annually. It covers over four-fifths of the country yet contains only about one-twentieth of its population. The actual study area is located in the Northern part of the Badia and covers an area of 12,000 km^2 (see Figure 8.1). Much of this terrain is undulating, hilly land covered by basalt stones or chert making it very difficult to traverse by vehicle or even on foot. The variation in elevation over the Project area is from 500m to 1,200m. Most of the population and all of the villages are

located in the highest land, located at the north-west corner of the Project area, which is also the coolest part and receives most rainfall (up to 250mm per year). The main wadi, the Wadi Rajil, drains from the Syrian border in the north-east, southwards and then south-westwards to empty into the interior drainage basin of Azraq. A line of volcanic hills creates the eastern border of the study area. To the south, the land drains into the Wadi Sirhan, which carries occasional flood water into Saudi Arabia. In this area, the land is free of basalt, and, in part, is covered by sand.

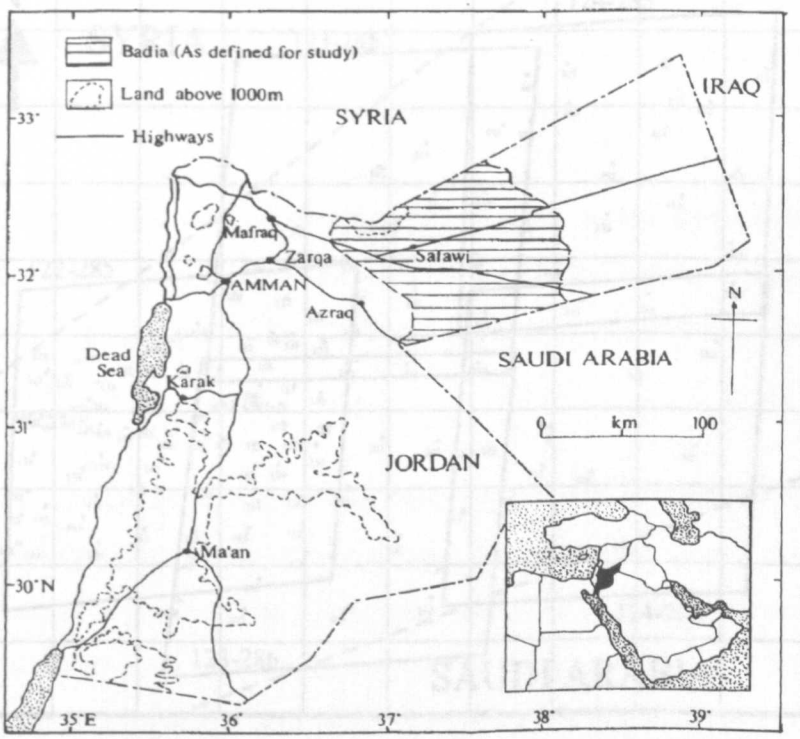

Figure 8.1 Jordanian test field area (Badia)

In the next Section, after describing the availability of control points in this test area, the geometric accuracy tests using SPOT images in both two and three dimensions will be discussed.

8.1.1 Ground Control Availability in the Jordanian Test Field Area

For this project, a total of 130 ground control points (GCPs) have been established (Figure 8.2) by surveyors from the Royal Jordanian Geographic Centre (RJGC) using differential GPS techniques based on the use of five Ashtech 12 dual frequency GPS sets. The accuracy

of these points is estimated to be of the order of 1 to 2 metres. 60 of these points are located in the most westerly scene (122/285) to enable it to be used as a special test model. The remaining 70 points are located across the other four scenes, so that each has between 15 and 20 points spread as evenly as possible over the area covered by the stereo-pair. Of course, parts of these scenes have no GCPs within them since they cover areas belonging to neighbouring countries (Syria and Saudi Arabia).

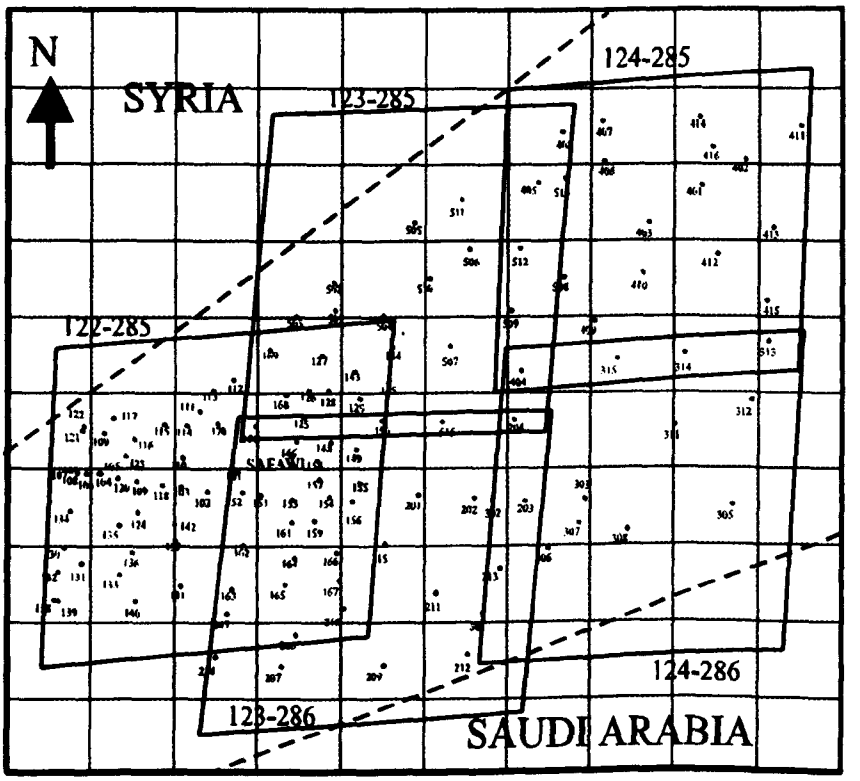

Figure 8.2 Location of the GCPs with respect to the individual SPOT scenes

The observed GPS data was processed by RJGC at its headquarters in Amman and the final X, Y, Z coordinates were output in four different forms: (i) WGS 84 geocentric coordinates; (ii) latitude, longitude and height values; (iii) UTM coordinates; and (iv) JTM (Jordan Transverse Mercator) coordinate values. For the last three coordinate systems, the heights of the GCPs have been produced as elevations above Mean Sea Level (MSL). However, for the work described in this research, both the UTM and the WGS84 geocentric coordinates have been used; the former for the 2D tests, the latter for the 3D tests of geometric accuracy.

8.1.2 Test Material and Measurements

The two overlapping images comprising the principal stereo-pair (Scene 122-285) used for the tests were available in both Level 1A and 1B forms. They were acquired in August and June 1987 respectively, with incidence angles of L28.2 and R23.7 degrees. This results in an excellent base-to-height ratio of 0.97. This particular pair was selected for the test since around 60 GCPs were available in the area and this gave the opportunity to have a good number of independent check points to check that the program worked correctly. The other four stereo pairs are in Level 1B form only and have nearly the same base-to-height ratio as the reference stereo pair.

All the images were of a very good radiometric quality, so the control points could be measured on the images quite easily without any enhancement. Figure 8.3 shows a hardcopy of the right scene of the SPOT Level 1B image of the main stereo pair used over the Jordanian test field.

The positions of the GCPs on each image were measured monoscopically using the PCI EASI/PACE package with the help of my colleague, Mr Al-Rousan, who knew the positions of these points on the ground. The points were measured with zoom factors of 2, 4, and even 8 to allow a sub-pixel accuracy in the pointing of up to 0.15 pixel. All of the points have been measured in an image coordinate system with its origin at the top left corner of the image, with its x axis in the direction of the motion of the satellite and its y axis in the direction of the lines. The image measurements were then presented and input to the adjustment program in pixel units.

In the case of the two dimensional accuracy test, only the right scene of the main stereo-pair (122/285) has been tested in both its Level 1A and 1B forms, while, in the three dimensional accuracy test, all of the five SPOT stereo-images have been used. In the next Section, the results achieved by the author with his 2D polynomial adjustment program are outlined. Then the results achieved using SPOT stereo-images in both their Level 1A and 1B forms over the Badia test field will be discussed in the Section after that.

Figure 8.3 Main SPOT Level 1B image (122-285) over Jordanian test field

8.1.3 Two-Dimensional Accuracy Test

The polynomial adjustment program described in Chapter 7 has been employed to carry out various tests on the right scene of the main stereo-pair (122/285). Although the terrain in the Jordanian test field area is not so flat as to work really well with a 2D polynomial transformation, nevertheless the execution of this test could reveal gross errors at the image mensuration stage and provide an overall view of the quality of the data being used in the test, including the ground control points accuracy as well as the image measurement accuracy.

Different 2D polynomial tests have been carried out. These include using different sets of control and independent check points with different configurations and detecting the effects of including successive additional terms in the polynomial transformation. Using these data, both the Level 1A and Level 1B forms of the SPOT image have been tested using the 2D polynomial adjustment program. The first part of the next Section outlines the results of these tests using the SPOT Level 1A image, while in the second part, the 2D geometric accuracy test of the SPOT Level 1B image will be discussed and the results analyzed.

8.1.3.1 Two-Dimensional Geometric Accuracy Test of the SPOT Level 1A Image

Five different sets of data have been considered. First, all of the 38 available ground control points (GCPs) have been used as control points. The other four sets comprise different combinations of control and check points in the image as follows: Set A with 15 control points and 23 check points; Set B with 10 control points and 28 check points; Set C with 8 control points and 30 check points; and Set D with 6 control points and 32 check points. Table 8.1 gives the results of the 2D test using the polynomial adjustment program for the first case in which all of the 38 ground control points are considered as control points. As can be seen from this Table, the RMSE values in the case of using just three terms (an affine transformation) and 4 terms of the polynomial transformation are very large and highly systematic in the Easting direction compared with the Northing direction. Since the affine transformation aims to remove the effects of scaling, rotation, and shearing of the image,

the large residual errors could be the result of image warping (Mather, 1987) or some other source of systematic errors on the image.

Table 8.1 Results (in metres) of the RMSE values achieved in the 2D (planimetric) accuracy tests of the Jordanian SPOT Level 1A image using all 38 control points

Polynomial Transformation	ΔE (m)	ΔN (m)	Δpl (m)
3 terms (affine)	±164.32	±29.43	±166.93
4 terms (xy)	±151.68	±26.22	±153.93
5 terms (x^2)	±27.80	±9.71	±29.45
6 terms (y^2)	±27.62	±8.97	±29.04
7 terms (x^2y)	±26.32	±8.93	±27.79
8 terms (xy^2)	±23.17	±8.89	±24.82
9 terms (x^2y^2)	±19.43	±8.78	±21.32
10 terms (x^3)	±11.52	±8.23	±14.16
11 terms (y^3)	±11.48	±7.46	±13.69
12 terms (xy^3)	±11.45	±7.29	±13.57
13 terms (x^3y)	±8.12	±7.02	±10.73
14 terms (x^2y^3)	±8.11	±6.98	±10.70
15 terms (x^3y^2)	±8.04	±6.96	±10.63
16 terms (x^3y^3)	±7.75	±6.87	±10.36
17 terms (x^4)	±7.65	±5.70	±9.54
18 terms (y^4)	±7.64	±5.65	±9.50
19 terms (x^4y)	±7.56	±5.57	±9.39
20 terms (xy^4)	±7.54	±5.06	±9.08
21 terms (x^4y^2)	±7.49	±3.72	±8.36
22 terms (x^2y^4)	±6.97	±3.68	±7.88
23 terms (x^4y^3)	±6.85	±3.56	±7.72
24 terms (x^3y^4)	±5.13	±3.18	±6.04
25 terms (x^4y^4)	±4.70	±2.94	±5.54

In the case of the affine transformation, Figure 8.4(a) is the plot of the planimetric errors as vectors at each control point and shows the extent and direction of the systematic errors which are still present on the image.

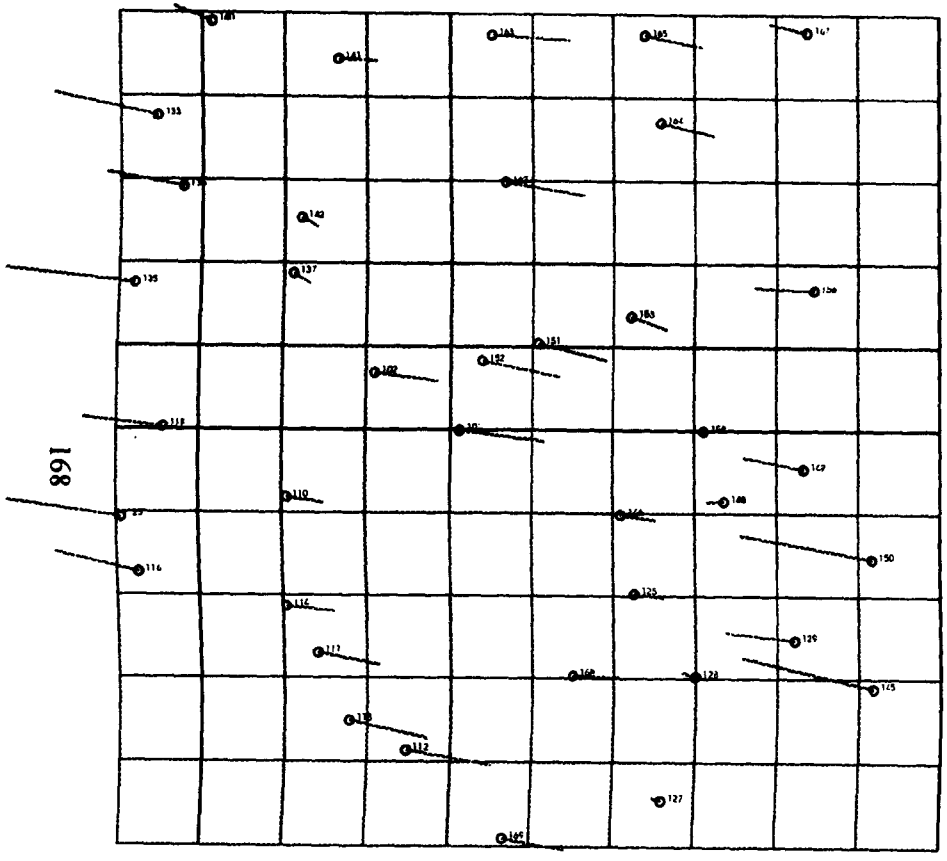

Figure 8.4(a) Vector plot of the planimetric errors at the control points for the Jordanian testfield using the SPOT Level 1A image, for the case in which 3 polynomial terms (affine transformation) have been used. (all 38 GCPs used as control points).

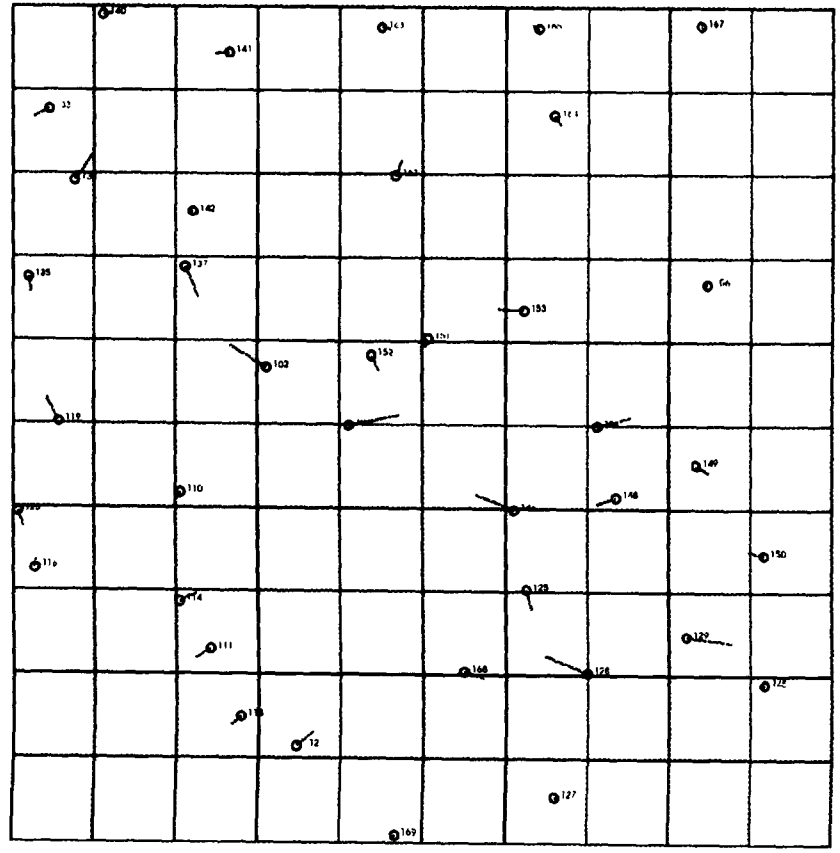

Figure 8.4(b) Vector plot of the planimetric errors using the full 25 terms of the polynomial transformation, for the Jordanian SPOT Level 1A image. (all 38 GCPs used as control points).

Regarding the projection and terrain coordinate system which, in this case is UTM, this seems most unlikely to be the source of such large systematic errors. Instead it seems much more likely that these large errors are the result of some other effects, such as Earth rotation, Earth curvature and the tilt of the image resulting from the use of the inclination mirror to give off-nadir viewing and cross-track coverage. The effect of Earth rotation on the image is like a shearing action, so it should be eliminated largely by the use of the affine transformation. This leaves the other two effects, Earth curvature and tilt as the likely sources of the large systematic errors. The effect of the Earth curvature on the image when the image is acquired with a vertical or nadir pointing can be computed using the following formula (Methley, 1986):

$$\Delta = \frac{Hr^3}{2Rf^2} \tag{8.1}$$

where

Δ : is the Earth curvature correction on the image;

H : is the altitude of the spacecraft;

r : is the distance of the point on the image from the central pixel; and

f : is the focal length of the imaging system.

Figure 8.5 is a cross-section through the SPOT image in the cross-track direction and shows the effect of the Earth curvature on the image line for its vertical case; where a and á are the uncorrected and corrected image positions of point A respectively. This displacement can only take place in the cross-track direction of the SPOT image. At the outer edge of a SPOT image, this correction amounts to about 4μm which is equal to around 3m on the ground.

However, the SPOT image which has been used in this test is not vertical and has an incidence angle of 23.7 degrees which results in a viewing angle of 20.8 degrees. Figure 8.6 shows the effect of Earth curvature in an oblique image. In this Figure, α is the viewing angle of the pointable mirror corrected to the map plane and θ is the angle at the perspective centre between the optical axis and the pixel in question at the outer edge of the SPOT image.

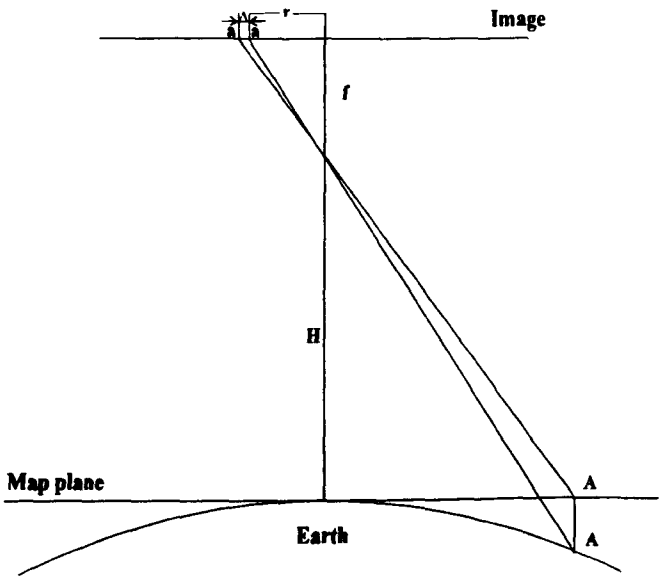

Figure 8.5 The effect of Earth curvature on a vertical image (Methley, 1986)

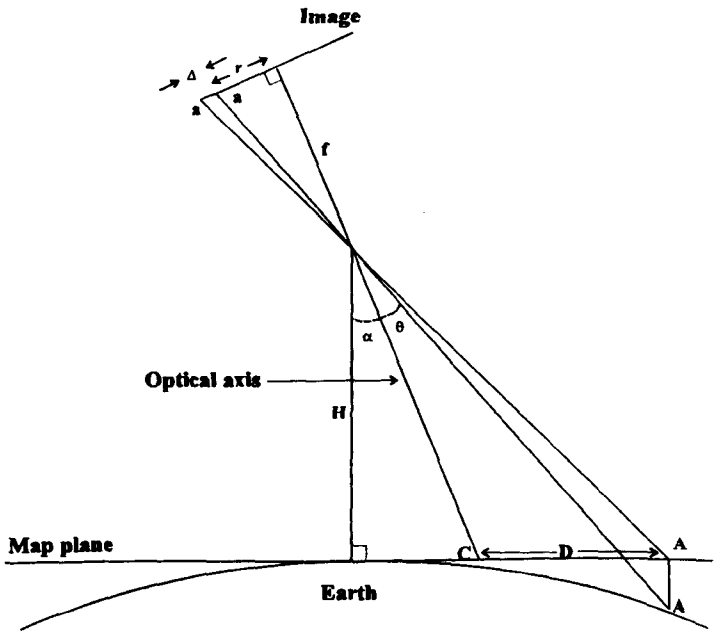

Figure 8.6 The effect of Earth curvature on an oblique image (Orun, 1990)

The remainder of the notation is as before in the case of vertical image, except that D is given by:

$$D = \frac{H \sin\theta}{\cos(\theta + \alpha)\cos\alpha} \tag{8.2}$$

The effect of Earth curvature at the edge of the image can then be calculated using the following formula (Orun, 1990):

$$\Delta = \frac{D^2 \sin(\theta + \alpha)\sqrt{(r^2 + f^2)}}{2R\sqrt{[H^2 + (D + H\tan\alpha)^2]}} \tag{8.3}$$

The maximum value of Δ is about 50μm, equal to about 40m on the ground, which is highly significant in the present context considering the source of the systematic errors revealed by the test of the Level 1A image.

Therefore it seems likely that the main source of the systematic errors in this Level 1A image could be a combination of the effects of Earth curvature and the oblique viewing angle of the SPOT image. The reason why this feature affects the Easting direction more than the Northing direction is that SPOT satellite moves in a near polar orbital plane. Thus the image lines are always imaged in the cross -track (approximately east-west) direction. As a result, this characteristic shows up as a large systematic error in the Easting coordinates. The other source which has to be mentioned are the relief displacements which result from the topography of Badia area and create their own particular pattern on the image, which has to be added to the Earth curvature and tilt displacements.

It is noticeable that the size of the errors is reduced significantly when the 5th term of the polynomial transformation (i.e. x^2) is used. This improves the RMSE value by nearly ±125m in the East direction and ±17m in the North direction. The other significant changes in the dimensions and direction of the errors in the Easting values occured when implementing the 8th (xy^2), 9th (x^2y^2), 10th (x^3), and 13th (x^3y) terms of the polynomial transformation with improvements of about ±3m, ±4m, ±8m and ±3m respectively. As can be seen from equations 8.1 and 8.3 describing the effects of Earth curvature and tilt, both of which contain quadratic and cubic terms, this is the likely reason why the second and third order terms of the polynomial work so effectively.

With regard to the other terms, there is a continuous improvement got by increasing the number of terms used in the polynomial adjustment. The vector plot of the planimetric errors after the application of the 25 terms of the polynomial (Figure 8.4(b)), shows that the errors at the control points are random in direction and amount, i.e. the residual errors that remain

after application of the polynomial adjustment are not affected any more by systematic errors.

Tables 8.2 to 8.5 give the results of the tests carried out with the other four sets of data and show the overall effects of each of the different terms used in the polynomial adjustment program. Note that the number of terms which could be used in the polynomial adjustment is limited by the number of control points.

Table 8.2 ΔE, ΔN RMSE values (in metres) of the residual errors achieved in terms of UTM coordinates for the Jordanian SPOT Level 1A image (Set A)

Polynomial Transformation	Control points (n=15)			Check points (n = 23)		
	ΔE (m)	ΔN (m)	Δpl (m)	ΔE (m)	ΔN (m)	Δpl (m)
3 terms (affine)	±167.52	±32.71	±170.68	±170.09	±29.88	±172.69
4 terms (xy)	±161.86	±31.16	±164.83	±154.53	±25.93	±156.17
5 terms (x^2)	±27.52	±13.23	±30.53	±30.54	±9.14	±31.88
6 terms (y^2)	±27.51	±12.19	±30.09	±30.58	±8.07	±31.63
7 terms (x^2y)	±27.24	±11.89	±29.72	±29.22	±8.62	±30.46
8 terms (xy^2)	±19.41	±11.70	±22.66	±31.43	±9.29	±32.77
9 terms (x^2y^2)	±18.93	±11.16	±21.97	±25.94	±11.90	±28.54
10 terms (x^3)	±11.97	±10.04	±15.62	±14.94	±10.51	±18.27
11 terms (y^3)	±11.97	±7.27	±14.00	±14.92	±12.65	±19.57
12 terms (xy^3)	±11.89	±6.89	±13.74	±16.53	±16.26	±23.18
13 terms (x^3y)	±7.81	±5.59	±9.60	±19.33	±18.25	±26.59
14 terms (x^2y^3)	±3.40	±2.32	±4.12	±73.72	±49.39	±88.74
15 terms (x^3y^2)	≈0.0	≈0.0	≈0.0	±39.84	±84.17	±93.12

Table 8.3 ΔE, ΔN RMSE values (in metres) of the residual errors achieved in terms of UTM coordinates for the Jordanian SPOT Level 1A image (Set B)

Polynomial Transformation	Control points (n=10)			Check points (n = 28)		
	ΔE (m)	ΔN (m)	Δpl (m)	ΔE (m)	ΔN (m)	Δpl (m)
3 terms (affine)	±177.97	±32.45	±180.90	±186.91	±32.76	±189.76
4 terms (xy)	±174.05	±31.67	±176.91	±180.10	±30.73	±182.60
5 terms (x^2)	±26.07	±12.80	±29.04	±35.98	±10.77	±37.56
6 terms (y^2)	±26.06	±11.58	±28.52	±36.20	±11.46	±37.97
7 terms (x^2y)	±20.16	±9.87	±22.45	±53.26	±15.24	±55.40
8 terms (xy^2)	±13.22	±9.65	±16.37	±44.28	±15.98	±47.08
9 terms (x^2y^2)	±6.23	±9.30	±11.19	±42.91	±11.94	±44.54
10 terms (x^3)	≈0.0	≈0.0	≈0.0	±36.46	±32.05	±48.54

Table 8.4 ΔE, ΔN RMSE values (in metres) of the residual errors achieved in terms of UTM coordinates for the Jordanian SPOT Level 1A image (Set C)

Polynomial Transformation	Control points (n=8)			Check points (n = 30)		
	ΔE (m)	ΔN (m)	Δpl (m)	ΔE (m)	ΔN (m)	Δpl (m)
3 terms (affine)	±191.62	±31.64	±194.21	±200.99	±36.48	±204.27
4 terms (xy)	±186.16	±27.58	±188.19	±193.12	±34.74	±196.22
5 terms (x^2)	±19.74	±8.75	±21.59	±42.96	±11.13	±44.38
6 terms (y^2)	±19.44	±7.29	±20.76	±44.22	±9.83	±45.30
7 terms (x^2y)	±4.76	±2.68	±5.46	±57.81	±18.86	±60.81
8 terms (xy^2)	≈0.0	≈0.0	≈0.0	±55.96	±19.17	±59.15

Table 8.5 ΔE, ΔN RMSE values (in metres) of the residual errors achieved in terms of UTM coordinates for the Jordanian SPOT Level 1A image (Set D)

Polynomial Transformation	Control points (n=6)			Check points (n = 32)		
	ΔE (m)	ΔN (m)	Δpl (m)	ΔE (m)	ΔN (m)	Δpl (m)
3 terms (affine)	±201.53	±35.23	±204.59	±178.31	±33.43	±181.42
4 terms (xy)	±200.71	±34.03	±203.56	±174.83	±31.93	±177.72
5 terms (x^2)	±2.15	±5.64	±6.04	±38.02	±11.22	±39.64
6 terms (y^2)	≈0.0	≈0.0	≈0.0	±38.34	±10.45	±39.74

As can be seen from these Tables, the significant improvements in all of them occur when the 5th term (i.e. x^2) of the polynomial transformation is applied. With a further increase in the number of terms used in the polynomial transformation, first of all, the residual errors at the check points improve, i.e. they grow smaller. After that, the residual errors show a nearly constant improvement before finally starting to become poor again. This is in fact the result of decreasing the degree of freedom in the adjustment due to the lack of redundancy in the number of control points used. Comparing the results of the 2D test with Set A (Table 8.2) and the other sets of data (Tables 8.3 to 8.5) shows that, with Sets B, C, and D, the terms 9 (x^2y^2) and 10 ($\hat{x}^3$) of the polynomial transformation could not be used with a sufficient degree of freedom, so further significant improvements never occured.

Graphical analysis of the residual errors occuring in the control and check points for Set A (see Figure 8.7) using the first 10 terms of the polynomial transformation, shows that the residual errors are random in extent and direction and the final results are not affected by systematic errors.

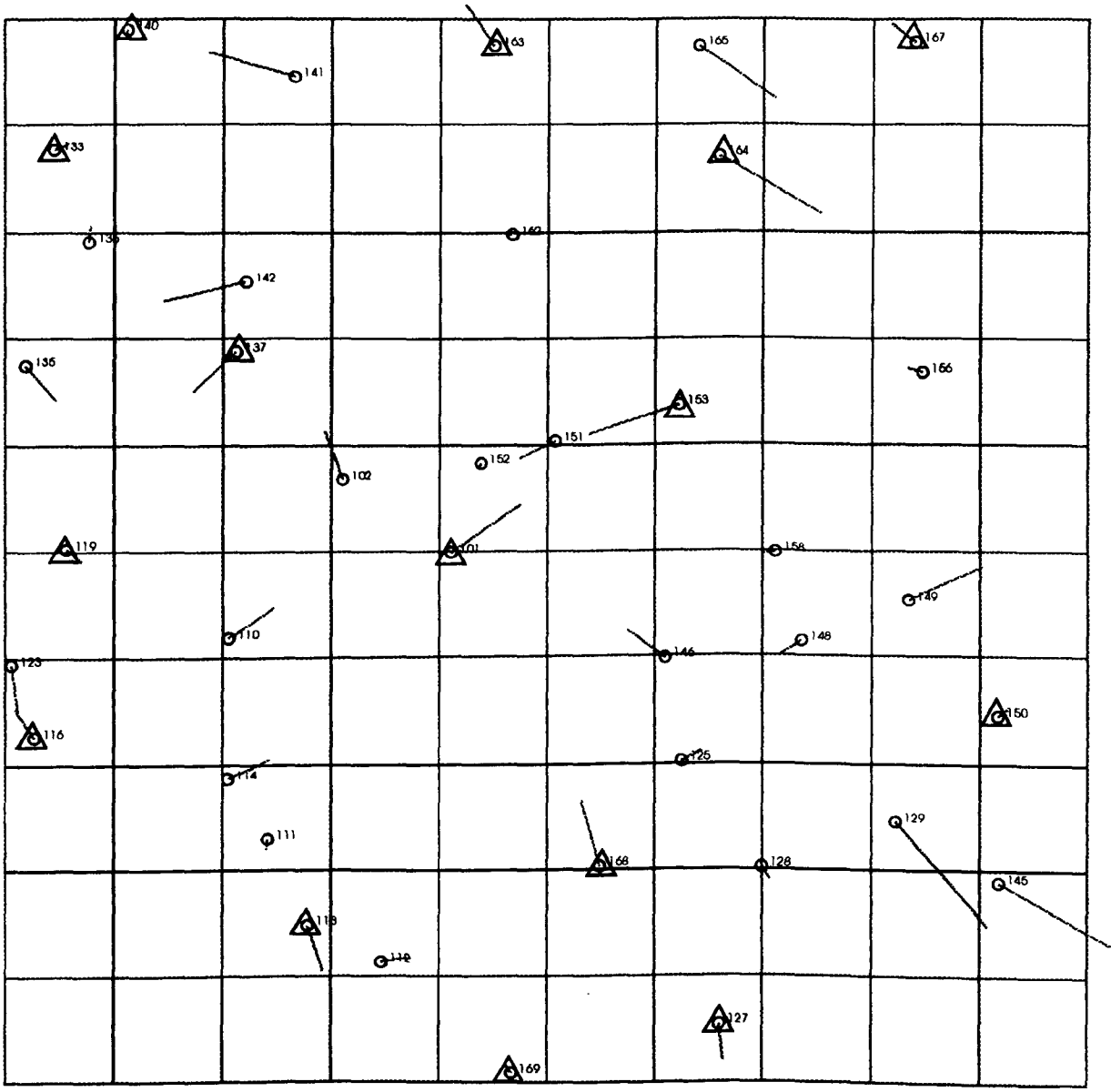

Figure 8.7 Vector plot of the planimetric errors at the control and check points for the Jordanian test field using the SPOT Level 1A image (Set A).
Δ = Control Point ; o = Check Point

8.1.3.2 Two-Dimensional Geometric Accuracy Test of the SPOT Level 1B Image

The polynomial adjustment program described in Chapter 7 has also been used to carry out various tests on the SPOT Level 1B image over the area of the Jordanian test field. Again, as in the case of the 2D test carried out on the corresponding SPOT Level 1A image, five different sets of data have been considered. Table 8.6 gives the results of the 2D test for the first case in which all of the 38 ground control points are considered as control points.

Table 8.6 Results (in metres) of the RMSE values achieved in the 2D (planimetric) accuracy tests of the Jordanian SPOT Level 1B image using all 38 control points

Polynomial Transformation	ΔE (m)	ΔN (m)	Δpl (m)
3 terms (affine)	±35.90	±12.36	±37.97
4 terms (xy)	±21.53	±8.32	±23.08
5 terms (x^2)	±21.40	±8.19	±22.91
6 terms (y^2)	±19.13	±7.48	±20.54
7 terms (x^2y)	±18.59	±7.35	±19.99
8 terms (xy^2)	±17.22	±7.34	±18.72
9 terms (x^2y^2)	±15.97	±7.27	±17.54
10 terms (x^3)	±9.98	±7.05	±12.19
11 terms (y^3)	±9.92	±6.83	±12.04
12 terms (xy^3)	±9.81	±6.40	±11.71
13 terms (x^3y)	±6.69	±5.98	±8.97
14 terms (x^2y^3)	±6.68	±5.95	±8.94
15 terms (x^3y^2)	±6.62	±5.51	±8.61
16 terms (x^3y^3)	±6.37	±5.48	±8.40
17 terms (x^4)	±6.27	±5.40	±8.27
18 terms (y^4)	±6.25	±5.40	±8.26
19 terms (x^4y)	±5.98	±5.28	±7.98
20 terms (xy^4)	±5.97	±4.94	±7.75
21 terms (x^4y^2)	±5.39	±4.42	±6.97
22 terms (x^2y^4)	±5.24	±4.30	±6.78
23 terms (x^4y^3)	±5.17	±4.28	±6.71
24 terms (x^3y^4)	±4.21	±3.81	±5.68
25 terms (x^4y^4)	±4.21	±3.81	±5.68

Comparing the results of employing the polynomial with its affine transformation given in Table 8.6 with the corresponding set given in Table 8.1 for the Level 1A image shows a significant improvement in the Level 1B image. The reason is that SPOT Image in its procedure for the production of Level 1B images uses a third order or fifth order polynomial transformation to correct for the geometric displacements that are inherent in the raw image. The control points that are used in their polynomial solution are taken from the available topographic maps, normally at 1:50,000 and 1:100,000 scale. Then the image is rectified and resampled in such a way as to have pixels in the direction of both the lines and the spacecraft motion with 10m size. As a result, the effects of Earth curvature and the tilting angle of the pointable mirror are largely corrected.

However, probably as a result of SPOT Image having to use poor control points in the production of the Level 1B image, there are still some residual systematic errors existing in the image. The vector plot of the planimetric errors in the case of affine transformation (Figure 8.8(a)) shows that some systematic errors still exist on the SPOT Level 1B image that has been tested. These errors are reduced significantly when the 4th term of the polynomial transformation (i.e. the xy term) is used. This improves the RMSE value by nearly ±6m in Easting and ±4m in the Northing direction. As in the case of the SPOT Level 1A image, the other significant changes occured in the Easting direction when implementing the 10th (x^3), and the 13th (x^3y) terms of the polynomial transformation with improvements of about ±6m and ±3m respectively.

Using other terms, there is a continuous improvement got by increasing the number of terms used in the polynomial adjustment. The vector plots (Figure 8.8(b)) show that the final errors at the control points after the use of the higher order terms are random in amount and direction and free from systematic errors.

The results of the tests on the SPOT Level 1B image using the other four sets of data are given in Tables 8.7 to 8.10, including the effect of each of the different terms used in the polynomial adjustment program. Note that the number of terms that could be used in the polynomial adjustment is limited by the number of control points.

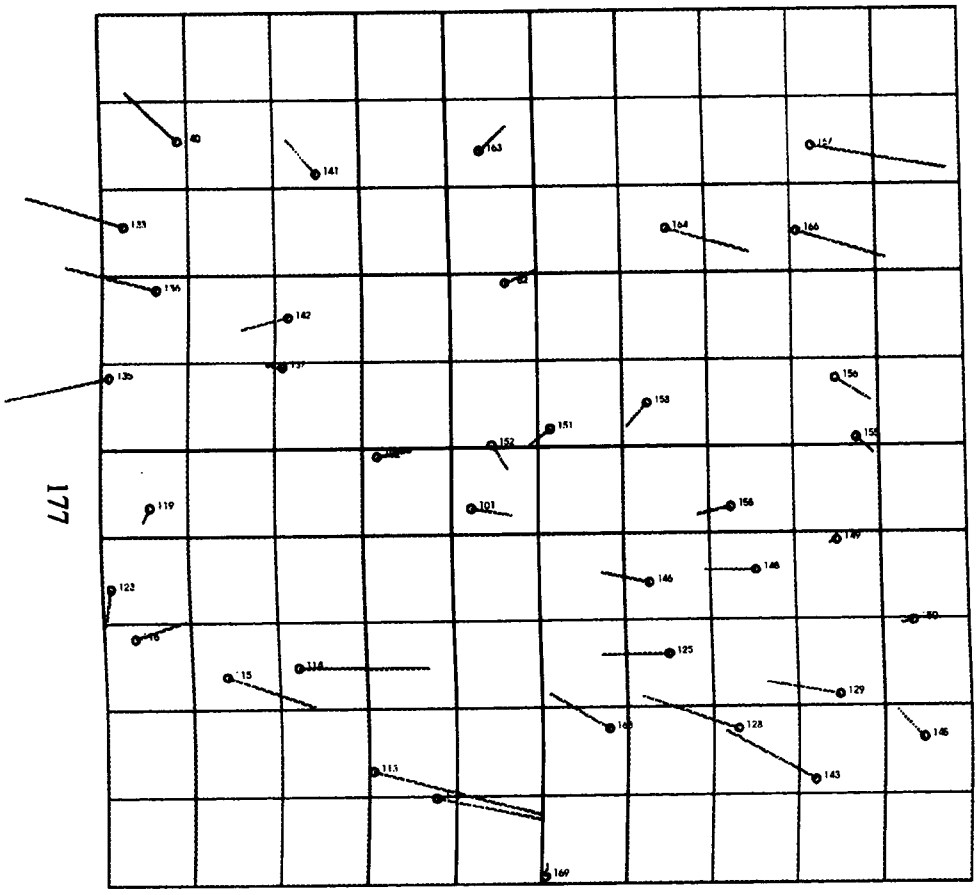

Figure 8.8(a) Vector plot of the planimetric errors at the control points for the Jordanian testfield using the SPOT Level 1B image, for the case in which 3 polynomial terms (affine transformation) have been used (all 38 GCPs used as control points).

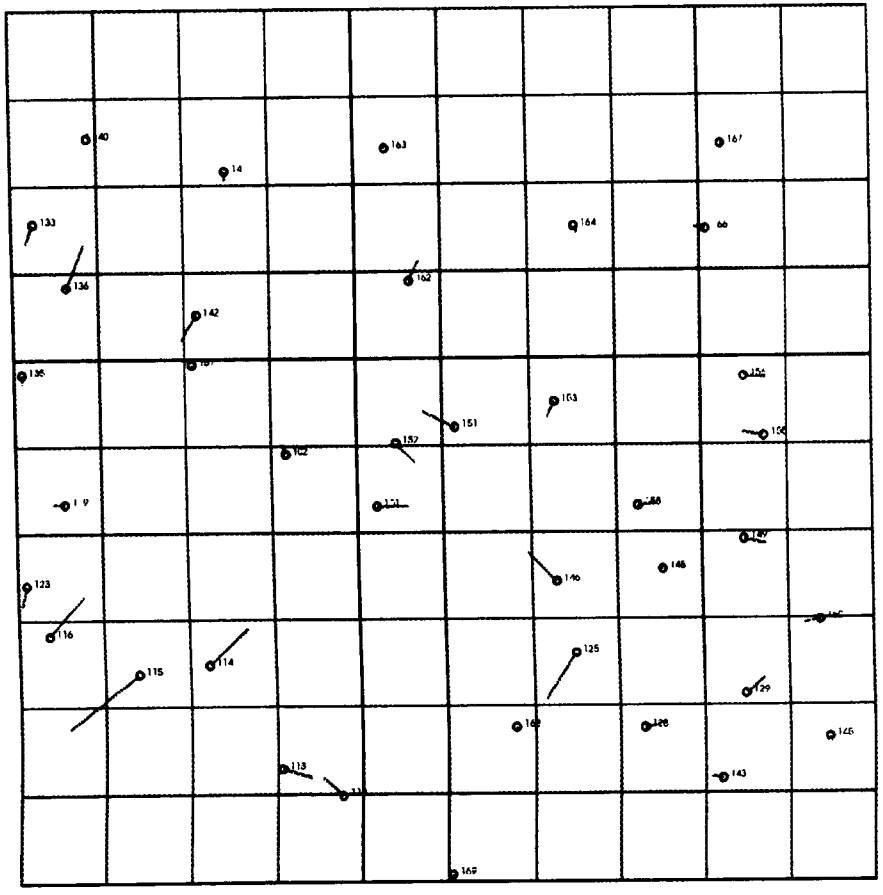

Figure 8.8(b) Vector plot of the planimetric errors using the full 25 terms of the polynomial transformation for the Jordanian SPOT Level 1B image (all 38 GCPs used as control points).

Table 8.7 ΔE, ΔN RMSE values (in metres) of the residual errors achieved in terms of UTM coordinates for the Jordanian SPOT Level 1B image (Set A)

Polynomial Transformation	Control points (n=15)			Check points (n = 23)		
	ΔE (m)	ΔN (m)	Δpl (m)	ΔE (m)	ΔN (m)	Δpl (m)
3 terms (affine)	±37.81	±13.64	±40.20	±37.81	±12.71	±39.89
4 terms (xy)	±19.96	±9.12	±21.94	±24.75	±8.48	±26.16
5 terms (x^2)	±19.33	±9.08	±21.36	±25.31	±8.80	±26.80
6 terms (y^2)	±18.11	±7.90	±19.76	±22.00	±8.90	±23.73
7 terms (x^2y)	±18.09	±6.69	±19.29	±22.36	±10.42	±24.67
8 terms (xy^2)	±15.88	±6.42	±17.13	±21.35	±10.79	±23.92
9 terms (x^2y^2)	±14.93	±6.33	±16.22	±20.26	±10.63	±22.28
10 terms (x^3)	±10.16	±6.02	±11.81	±12.10	±10.04	±15.72
11 terms (y^3)	±9.93	±6.01	±11.61	±15.73	±10.56	±18.95
12 terms (xy^3)	±9.40	±5.30	±10.79	±19.51	±12.72	±23.29
13 terms (x^3y)	±3.42	±2.68	±4.34	±20.54	±12.99	±24.30
14 terms (x^2y^3)	±2.68	±2.67	±3.78	±21.15	±12.96	±24.80
15 terms (x^3y^2)	≈0.0	≈0.0	≈0.0	±19.904	±15.36	±25.14

Table 8.8 ΔE, ΔN RMSE values (in metres) of the residual errors achieved in terms of UTM coordinates for the Jordanian SPOT Level 1B image (Set B)

Polynomial Transformation	Control points (n=10)			Check points (n = 28)		
	ΔE (m)	ΔN (m)	Δpl (m)	ΔE (m)	ΔN (m)	Δpl (m)
3 terms (affine)	±40.24	±14.40	±42.74	±40.94	±12.20	±42.72
4 terms (xy)	±24.74	±10.98	±27.07	±27.52	±8.27	±28.74
5 terms (x^2)	±22.61	±10.96	±25.13	±30.56	±8.20	±31.64
6 terms (y^2)	±21.90	±10.13	±24.13	±26.17	±7.79	±27.30
7 terms (x^2y)	±21.41	±8.43	±23.01	±25.17	±9.30	±26.83
8 terms (xy^2)	±19.38	±8.10	±21.00	±23.68	±9.92	±25.67
9 terms (x^2y^2)	±11.60	±8.07	±14.13	±27.19	±9.76	±28.89
10 terms (x^3)	≈0.0	≈0.0	≈0.0	±31.16	±31.98	±44.65

Table 8.9 ΔE, ΔN RMSE values (in metres) of the residual errors achieved in terms of UTM coordinates for the Jordanian SPOT Level 1B image (Set C)

Polynomial Transformation	Control points (n=8)			Check points (n = 30)		
	ΔE (m)	ΔN (m)	Δpl (m)	ΔE (m)	ΔN (m)	Δpl (m)
3 terms (affine)	±27.53	±14.84	±31.28	±43.27	±12.02	±44.91
4 terms (xy)	±15.57	±7.64	±17.34	±31.30	±9.43	±32.69
5 terms (x^2)	±12.14	±5.54	±13.34	±33.59	±10.41	±35.17
6 terms (y^2)	±11.42	±2.88	±11.78	±31.49	±9.26	±32.82
7 terms (x^2y)	±2.14	±2.22	±3.08	±37.01	±9.73	±38.27
8 terms (xy^2)	≈0.0	≈0.0	≈0.0	±36.45	±10.12	±37.83

Table 8.10 ΔE, ΔN RMSE values (in metres) of the residual errors achieved in terms of UTM coordinates for the Jordanian SPOT Level 1B image (Set D)

Polynomial Transformation	Control points (n=6)			Check points (n = 32)		
	ΔE (m)	ΔN (m)	Δpl (m)	ΔE (m)	ΔN (m)	Δpl (m)
3 terms (affine)	±26.65	±16.40	±31.29	±42.92	±12.03	±44.58
4 terms (xy)	±6.18	±5.78	±8.46	±32.91	±9.39	±34.22
5 terms (x^2)	±1.93	±4.16	±4.58	±33.97	±10.07	±35.43
6 terms (y^2)	≈0.0	≈0.0	≈0.0	±35.37	±8.62	±36.40

As can be seen from these Tables, significant improvements in all of them take place when using the 4th term (i.e. the xy term) of the polynomial transformation. Increasing further the number of terms used in the polynomial transformation causes the residual errors at the check points to be improved. The residual errors show a nearly constant improvement before finally starting to become poor as a result of decreasing the degree of freedom in the adjustment. The vector plot (see Figure 8.9) for Set A using 10 terms of the polynomial transformation shows that the residual errors in both the control points and check points are random in direction and extent and are not affected by systematic errors.

Comparing the results of the 2D tests with SPOT Level 1A and SPOT Level 1B images using the various sets of data, the residual errors at the check points show that the best results in the case of SPOT Level 1A are achieved when implementing 10 terms in Set A of the data with an RMSE in terms of the planimetric vector equal to ±18.27m. In the case of Level 1B, the best result is again achieved when using the same terms in Set A of the data but with an improvement of nearly 2.5m (to ±15.72m) in the planimetric vector error.

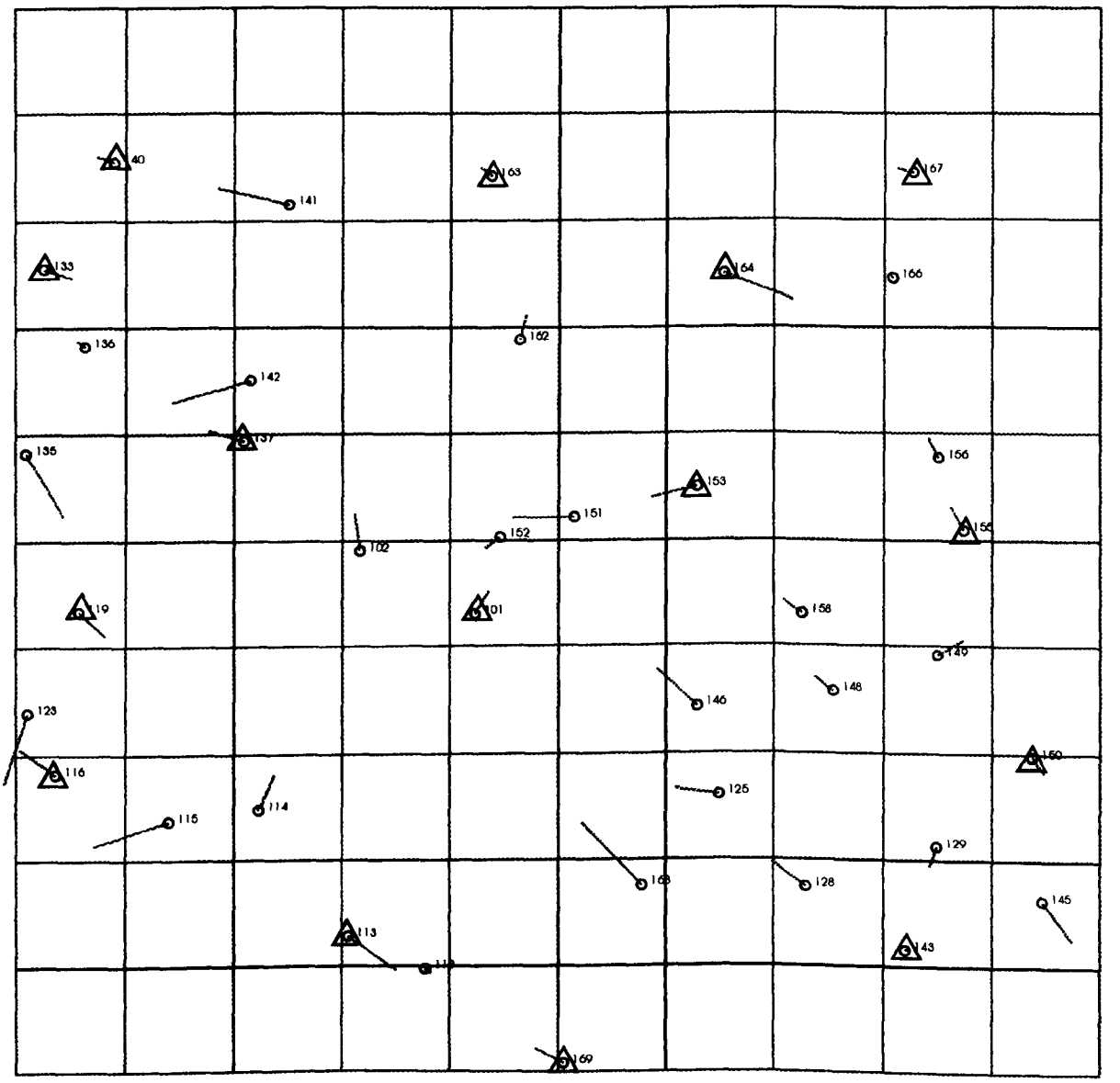

Figure 8.9 Vector plot of the planimetric errors at the control and check points for the Jordanian test field using the SPOT Level 1B image (Set A).
Δ = Control Point ; o = Check Point

However, although the result of ±15m RMSE in planimetry at the check points using the polynomial transformation with 15 control points is quite reasonable, having regard to the accuracy of the ground control points which have been measured by Differential GPS, more accurate results should have been achieved. Evidently the remaining errors in the image are the results of relief displacements which can only be removed using a more rigorous three-dimensional model. In the next Section, tests using the author's 3D modelling are described and discussed.

8.1.4 Three-Dimensional Accuracy Test

The bundle adjustment program outlined in Chapter 7 has been used to test the geometric accuracy of the SPOT Level 1A and 1B stereo-pairs in three dimensions. Again, the same four sets of control and check points (A, B, C, and D) have been used as were used in the two-dimensional accuracy test.

The bundle adjustment program is designed in such a way as to use different numbers of exterior orientation parameters. These parameters can be reduced from 15 to 9. In the case of 15 parameters, all of the exterior orientation parameters explained in Chapter 5 are used in the program. At a second stage, they can be reduced to 12, by removing the three quadratic terms of the polynomial which have been used to model the changes in the conventional rotation parameters (i.e. ω, φ and κ) with respect to time. At the third stage, the first order terms in the polynomials for ω, φ, and κ, which again describe the effects of the dynamic nature of linear array imagery in terms of these conventional rotation parameters, can be eliminated to result in 9 exterior orientation parameters. These other parameters are necessary in the bundle adjustment program and so no further reduction in the number of terms can be considered.

Based on this particular feature of the program, different tests have been carried out on the SPOT Level 1A stereo-pair, using different numbers of exterior orientation parameters. In the case of the Level 1B stereo-pair, all 15 parameters described in Chapter 5 are necessary and have to be utilised in the bundle adjustment program.

Since the stated accuracy of the ground control points measured by the Differential GPS survey is extremely high (less than 1 metre), the coordinates of the ground control points are considered to be fixed and so only Case 2 of the bundle adjustment program has been used in the tests.

8.1.4.1 Tests with the Level 1B Stereo-Pairs

The number of GCPs available on each of the four SPOT Level 1B stereo-pairs other than the main test model (122-285), is limited, therefore all of the GCPs in these stereo-images have been used as control points. The residuals errors (ΔX, ΔY, ΔZ) at the ground control points after the application of the bundle adjustment program for all five Level 1B stereo-pairs are given as RMSE values and are summarized in Table 8.11.

Table 8.11 ΔX, ΔY, ΔZ RMSE values of the residual errors in terms of the WGS 1984 coordinates for the five SPOT Level 1B stereo-pairs covering the Jordan Badia project area using all available GCPs

Scene ID	B/H ratio	No. of GCPs	RMSE ΔX (m)	RMSE ΔY (m)	RMSE ΔZ (m)
122-285/1B	0.975	38	±7.04	±6.50	±7.70
123-285/1B	0.858	18	±6.2	±5.7	±8.3
123-286/1B	0.858	20	±6.4	±7.4	±8.1
124-285/1B	0.975	13	±8.0	±8.6	±13.2
124-286/1B	0.975	13	±4.8	±9.0	±3.3

As can be seen from Table 8.11, good results have been achieved using these stereo-images. The graphical analyses of these results are given in Appendix D and show that the errors are random and free from systematic errors. Figure 8.10 illustrates the vector plot in X/Y and in Z for the case of the main SPOT Level 1B stereo-pair (122-285). The errors are random and no systematic error can be observed.

The four sets of data (A, B, C, and D), described previously in this chapter, have also been used to carry out a series of tests on the main SPOT Level 1B stereo-pair. The results from each of these tests using the full 15 exterior orientation parameters in terms of their RMSE values are given in Table 8.12.

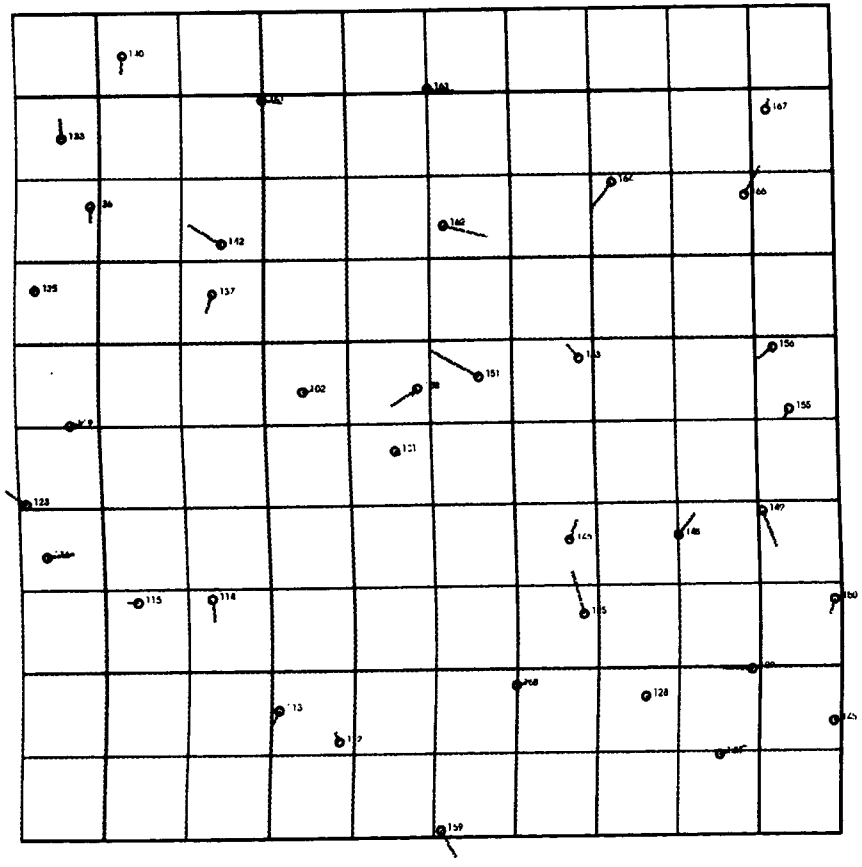

Figure 8.10 (a) Vector plot of the X/Y errors at the control points for the Jordanian test field with the main SPOT Level 1B stereo-pair.

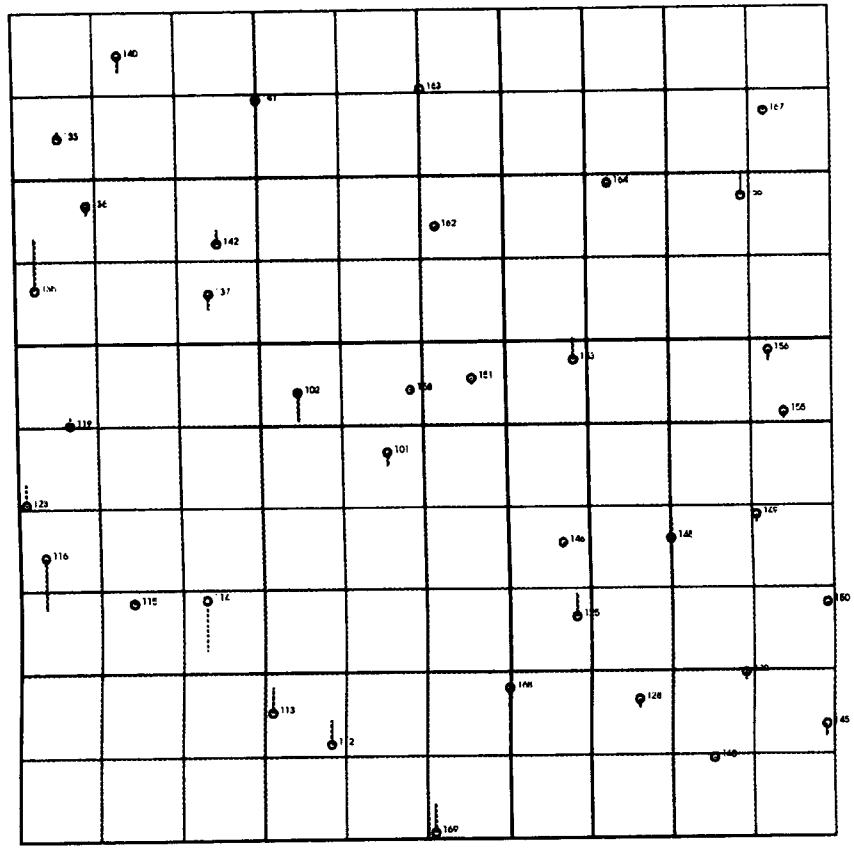

Figure 8.10 (b) Vector plot of the Z errors at the control points for the Jordanian test field with the main SPOT Level 1B stereo-pair.

Table 8.12 ΔX, ΔY, ΔZ RMSE values (in metres) of the residual errors in terms of the WGS 1984 coordinate system achieved in the 3D accuracy tests of the main Jordanian SPOT Level 1B image (122/285)

Name of the data set	No. of control points	RMSE at control points			No. of check points	RMSE at check points		
		ΔX (m)	ΔY (m)	ΔZ (m)		ΔX (m)	ΔY (m)	ΔZ (m)
A	15	±5.04	±5.12	±6.36	23	±8.86	±8.24	±9.99
B	10	±4.37	±3.14	±10.50	28	±8.80	±8.18	±7.04
C	8	±2.66	±3.24	±6.40	30	±8.50	±8.61	±9.73
D	6	±2.68	±3.05	±2.67	32	±9.36	±8.25	±11.50

As can be seen from the results given in Table 8.12, the RMSE values achieved with different sets and combinations of control and check points are nearly the same. The slightly poorer RMSE in the Z direction in Set D appears to be a result of the distribution and number of the control points on the images. Comparing the residual errors in terms of RMSE values for the main SPOT Level 1B stereo-pair (122-285) given in Table 8.11, with those for the check points in Table 8.12 does not show up significant discrepancies. In fact, this shows the effectiveness of the procedure developed in this research for the modelling of SPOT Level 1B stereo-pairs and confirms the powerful nature of the general bundle adjustment program. The vector diagrams constructed from the ΔX, ΔY and ΔZ values achieved with Set A for the Level 1B stereo-pairs of the reference model are included as Figures 8.11 (a,b). These diagrams show that the residual errors at the individual GCPs are completely random; no systematic component can be discovered in these vector plots. For the independent check points, the pattern is mostly random with small systematic components in specific areas.

8.1.4.2 Tests with the Level 1A Stereo-Pair

A further series of tests have been carried out on the main stereo-model (122-285) in its Level 1A form, using all 38 available GCPs on the image as control points. These tests have been carried out using different numbers of exterior orientation parameters. This makes it possible to evaluate the effects of the quadratic and linear terms of the polynomial modelling of the rotation parameters that have been used in the bundle adjustment program. The results of these tests in terms of the RMSE values are given in Table 8.13.

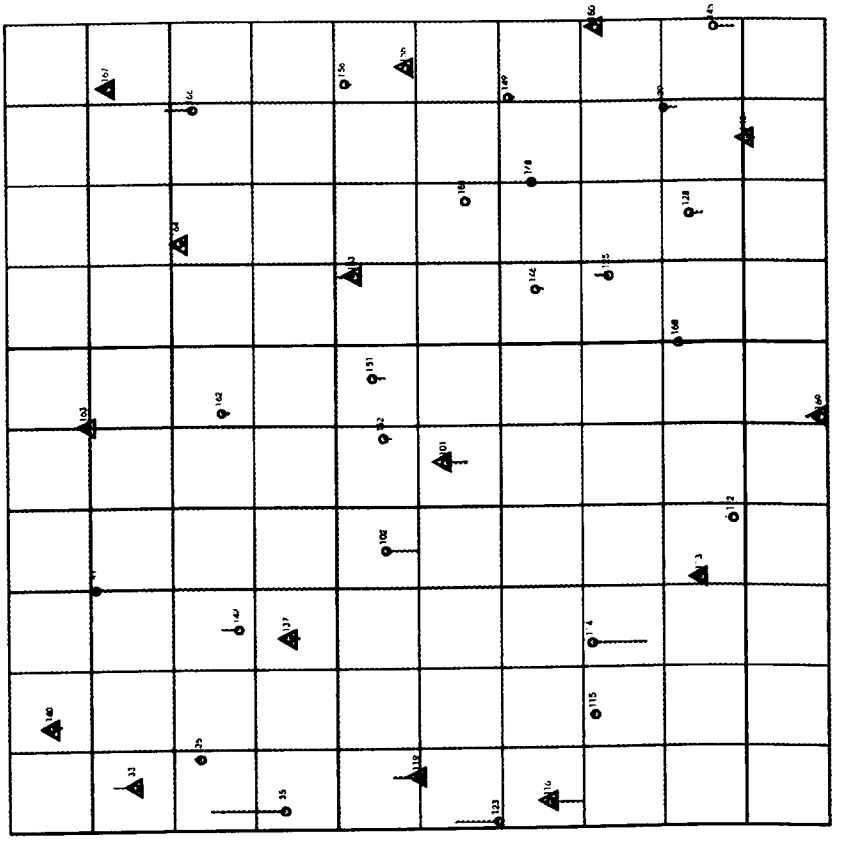

Figure 8.11 (b) Vector plot of the Z errors at the control and check points for the Jordanian test field with the main SPOT Level 1B stereo-pair (Set A).
Δ = Control Point ; o = Check Point

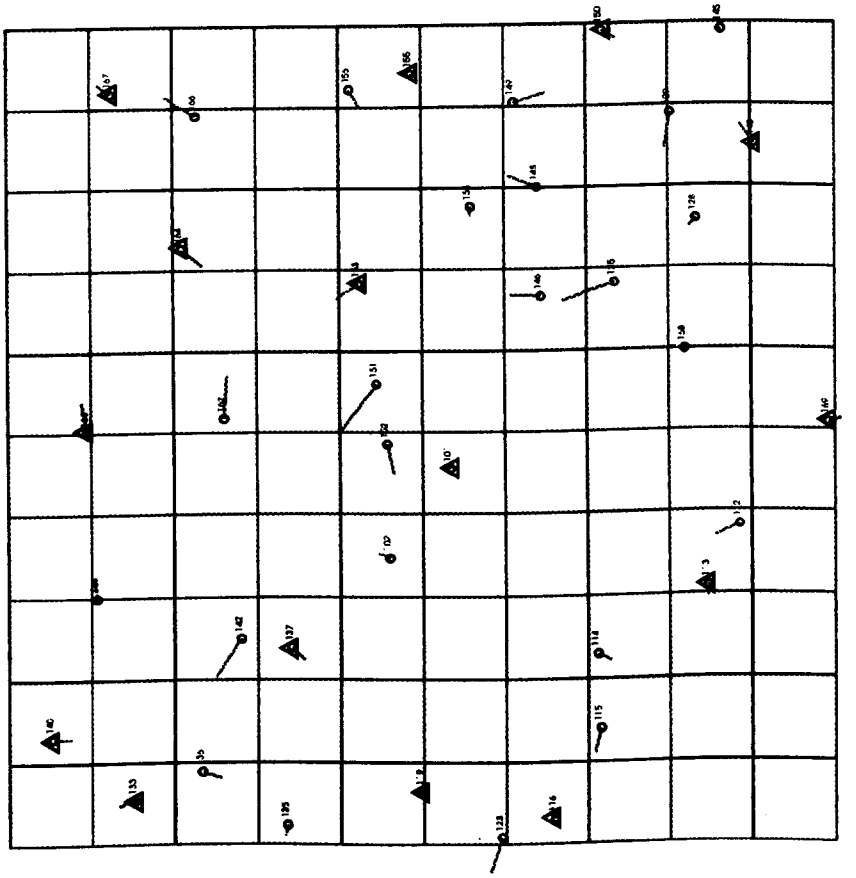

Figure 8.11 (a) Vector plot of the X/Y errors at the control and check points for the Jordanian test field with the main SPOT Level 1B stereo-pair (Set A).
Δ = Control Point ; o = Check Point

Table 8.13 ΔX, ΔY, ΔZ RMSE values of the residual errors in terms of the the WGS 1984 coordinate system achieved in the 3D accuracy tests of the Jordanian SPOT Level 1A stereo-pair using all 38 control points

No. Of exterior orientation parameters	RMSE values at control points		
	ΔX (m)	ΔY (m)	ΔZ (m)
15	±7.89	±7.16	±8.00
12	±8.38	±7.13	±8.60
9	±8.49	±7.23	±8.67

As can be seen from Table 8.13, the results of the bundle adjustment for the SPOT Level 1A stereo-pair using all of the GCPs as control points are good. In the case of using 15 exterior orientation parameters in the solution, the RMSE values for the vector errors in three dimensions are equal to ±13.32m which is quite good. The vector plots (Figure 8.12) in the X/Y and Z directions show that the errors are random and free from systematic errors.

Comparing the RMSE values for the case of main reference SPOT Level 1B stereo-pair, given in Table 8.11, with those from the corresponding SPOT Level 1A stereo-pair given in Table 8.13, shows nearly the same values. This shows in fact how well the mathematical procedure which has been developed by the present author for handling the SPOT Level 1B stereo-pairs (see Chapter 5, Section 5.8.3), works.

Using the four data sets A, B, C, and D, various tests have also been carried out on the SPOT Level 1A stereo pair. These comprise also the changes in the number of exterior orientation parameters. The results of these tests in terms of their RMSE values are given in Tables 8.14 to 8.17.

Table 8.14 ΔX, ΔY, ΔZ RMSE values of the residual errors in terms of the WGS 1984 coordinate system achieved in the 3D accuracy tests of the Jordanian SPOT Level 1A stereo-pair (Set A)

No. of parameters	No. of control points	RMSE at control points			No. of check points	RMSE at check points		
		ΔX (m)	ΔY (m)	ΔZ (m)		ΔX (m)	ΔY (m)	ΔZ (m)
15	15	±8.21	±7.18	±9.48	23	±8.58	±7.85	±7.80
12	15	±8.95	±7.21	±10.23	23	±8.98	±7.54	±8.77
9	15	±8.89	±7.44	±10.25	23	±8.93	±7.57	±8.84

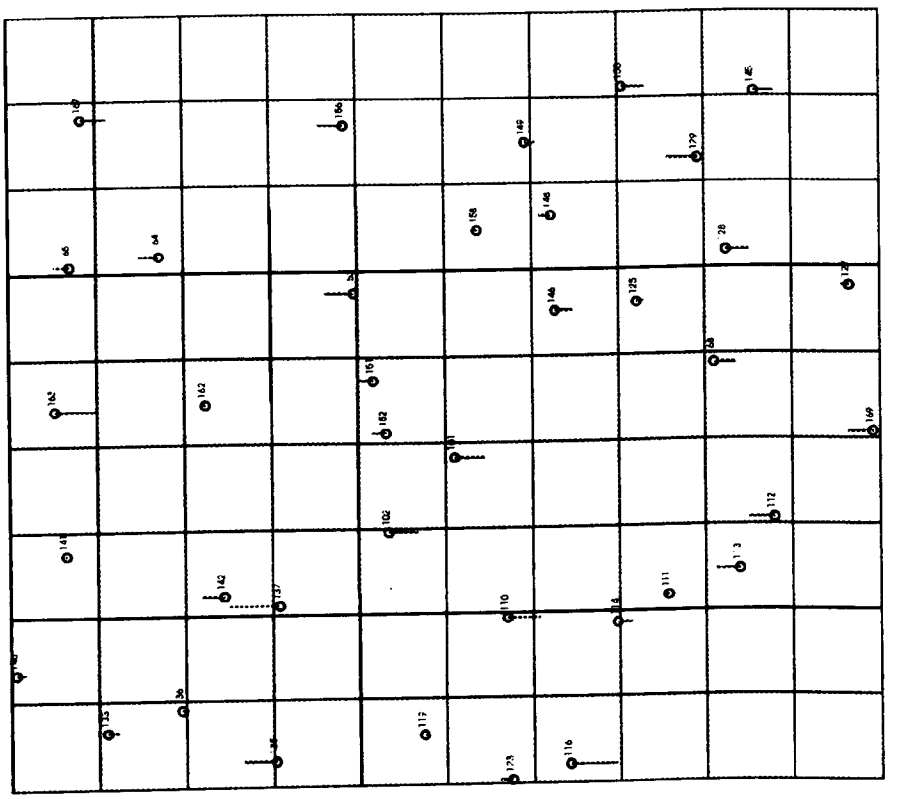

Figure 8.12 (b) Vector plot of the Z errors at the control points for the Jordanian test field with the SPOT Level 1A stereo-pair. (using all 38 GCPs as control points)

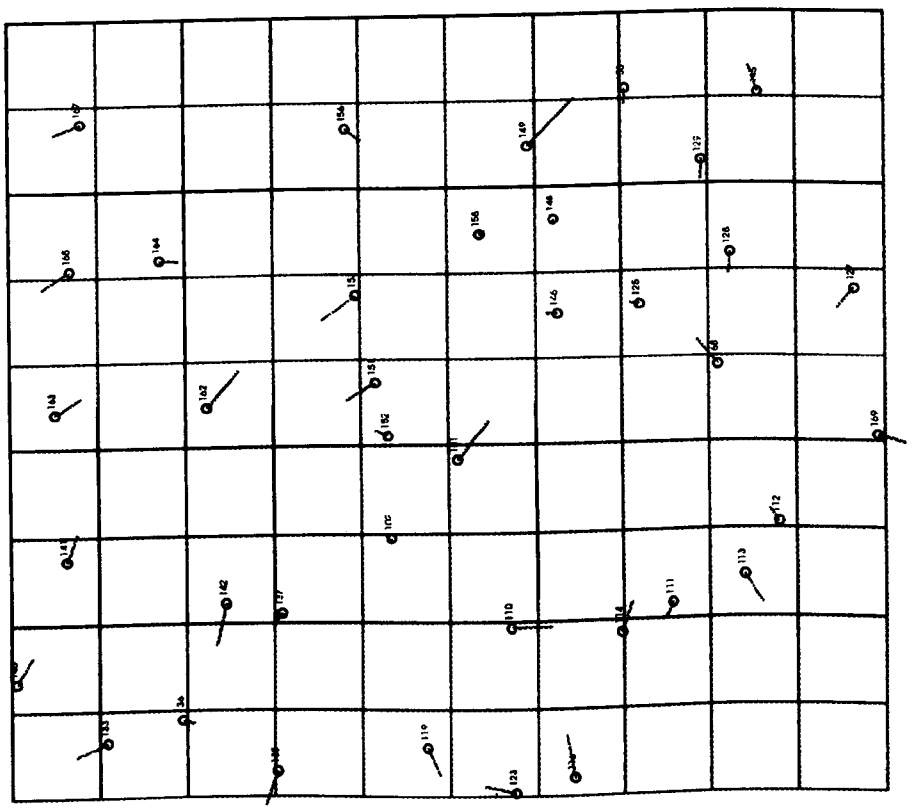

Figure 8.12 (a) Vector plot of the X/Y errors at the control points for the Jordanian test field with the SPOT Level 1A stereo-pair. (using all 38 GCPs as control points)

Table 8.15 ΔX, ΔY, ΔZ RMSE values of the residual errors in terms of the WGS 1984 coordinate system achieved in the 3D accuracy tests of the Jordanian SPOT Level 1A stereo-pair (Set B)

No. of parameters	No. of control points	RMSE at control points			No. of check points	RMSE at check points		
		ΔX (m)	ΔY (m)	ΔZ (m)		ΔX (m)	ΔY (m)	ΔZ (m)
15	10	±8.86	±5.37	±10.92	28	±8.37	±8.87	±7.43
12	10	±9.54	±5.18	±11.59	28	±8.83	±8.77	±7.90
9	10	±9.56	±6.22	±11.69	28	±9.01	±8.25	±7.97

Table 8.16 ΔX, ΔY, ΔZ RMSE values of the residual errors in terms of the WGS 1984 coordinate system achieved in the 3D accuracy tests of the Jordanian SPOT Level 1A stereo-pair (Set C)

No. of parameters	No. of control points	RMSE at control points			No. of check points	RMSE at check points		
		ΔX (m)	ΔY (m)	ΔZ (m)		ΔX (m)	ΔY (m)	ΔZ (m)
15	8	±7.84	±6.13	±5.86	30	±8.72	±8.30	±10.60
12	8	±8.61	±5.60	±7.16	30	±9.27	±8.26	±11.23
9	8	±10.50	±7.14	±9.07	30	±9.00	±7.66	±10.15

Table 8.17 ΔX, ΔY, ΔZ RMSE values of the residual errors in terms of the WGS 1984 coordinate system achieved in the 3D accuracy tests of the Jordanian SPOT Level 1A stereo-pair (Set D)

No. of parameters	No. of control points	RMSE at control points			No. of check points	RMSE at check points		
		ΔX (m)	ΔY (m)	ΔZ (m)		ΔX (m)	ΔY (m)	ΔZ (m)
15	6	±1.87	±2.54	±2.22	32	±9.95	±9.95	±11.36
12	6	±5.02	±4.81	±4.92	32	±10.56	±8.36	±11.72
9	6	±5.82	±7.97	±5.06	32	±10.47	±7.64	±11.87

Comparison of the residual errors in terms of the RMSE values given in Table 8.13 with those for the check points given in Tables 8.14 to 8.17 does not show up any significant discrepancies. In the first place, this shows that the observations are free of systematic errors and, secondly, it helps to confirm that the mathematical model developed by the present author works quite well and powerfully for cross-track stereo-images such as SPOT. The vector plots in X/Y and in the Z direction (Figure 8.13) for Set A in the case of using 15 exterior orientation parameters, show that the residual errors at both the control and check points are random in both direction and dimension. This means that the final results are not affected by systematic errors.

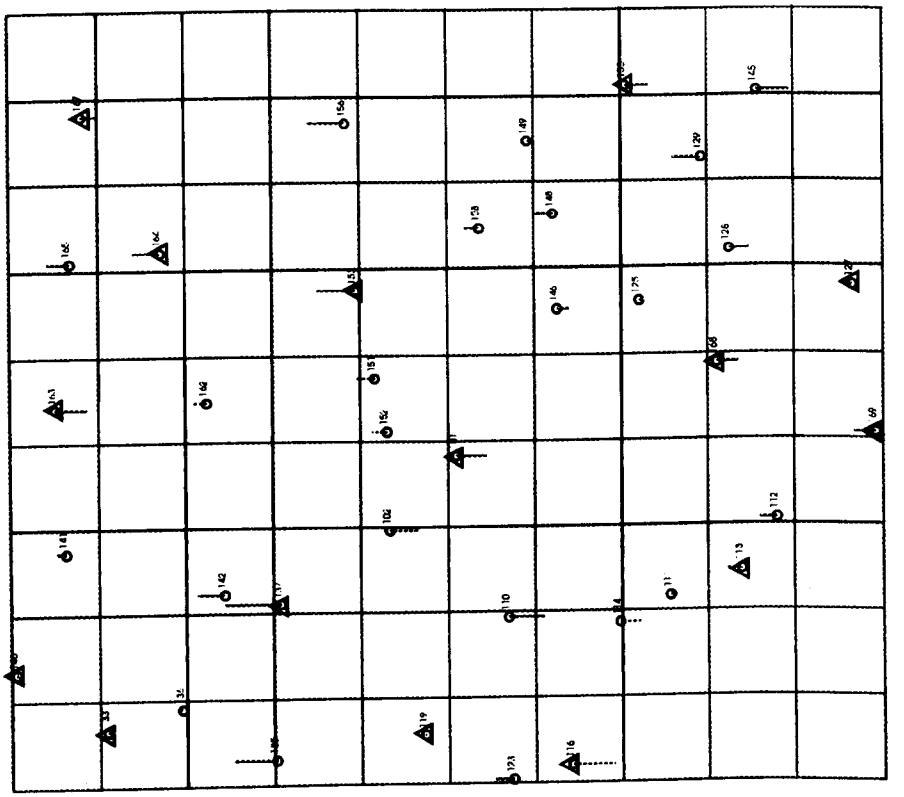

Figure 8.13 (b) Vector plot of the Z errors at the control and check points for the Jordanian test field with the SPOT Level 1A stereo-pair (Set A).
Δ = Control Point ; o = Check Point

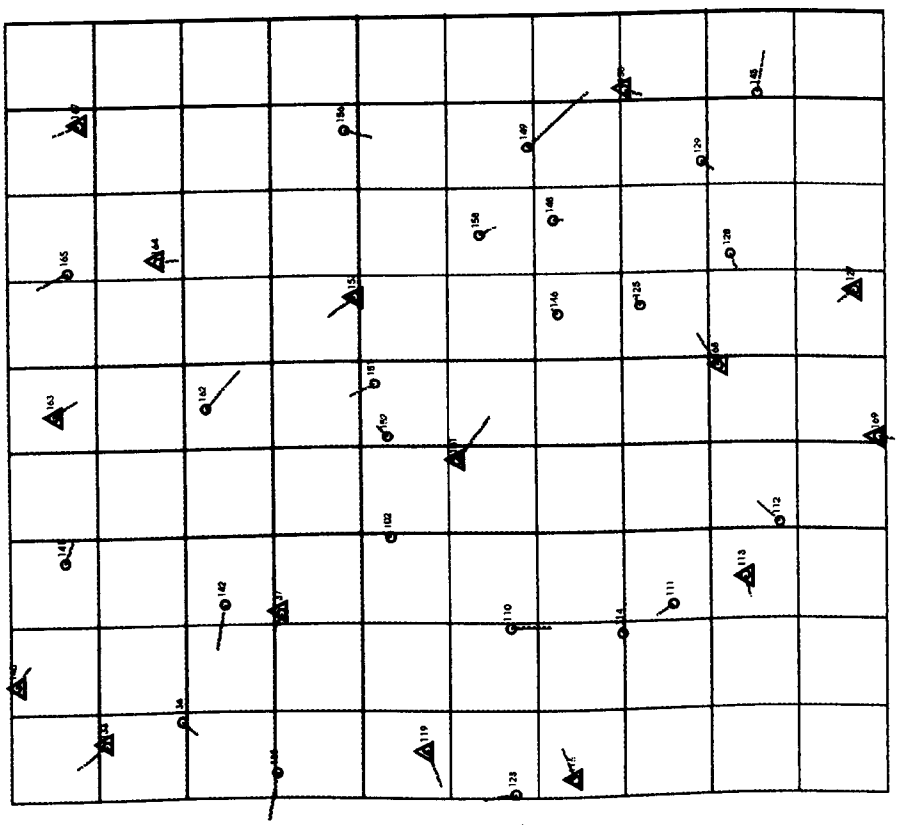

Figure 8.13 (a) Vector plot of the X/Y errors at the control and check points for the Jordanian test field with the SPOT Level 1A stereo-pair (Set A).
Δ = Control Point ; o = Check Point

As can be seen from the results given in Tables 8.13 to 8.17, the effects of including the quadratic terms and linear terms of the polynomial modelling of the rotation elements in the case of the SPOT Level 1A stereo-pair are very small and can be neglected. In fact, the results point also to the inherent stability of the platform and the sensor over the period of imaging a single scene. Furthermore the results show that the changes in the attitude of the imaging system as a result of the dynamic nature of the pushbroom system are well modelled by the first order polynomial equations used to describe the changes in the true anomaly (f) and the right ascension of the ascending node (Ω) with respect to time.

8.1.4.3 Tests with Combined SPOT Level 1A+1B Stereo-Pair

Another test has been carried out on the reference stereo-model (122-285) with 15 control points and 19 check points where the left image is in its Level 1B form and the right image is in its Level 1A form. The resulting RMSE values in terms of their X, Y, and Z coordinates are given in Table 8.18.

TABLE 8.18 ΔX, ΔY, ΔZ residuals in the WGS 1984 coordinates for the control and check points on the combined SPOT Level 1B and Level 1A stereo-pair for the main reference model (122/285) over the Jordan Badia project area

Level	No. of control points	RMSE in control points			No. of check points	RMSE in checkl points		
		ΔX (m)	ΔY (m)	ΔZ (m)		ΔX (m)	ΔY (m)	ΔZ (m)
1B + 1A	15	± 10.69	± 4.88	± 9.52	23	± 10.01	± 8.88	± 11.28

Again this test shows the power of the mathematical model developed by the present author for the modelling of SPOT Level 1A and 1B stereo-pairs in particular and cross-track stereo-images in general.

In the next Section, the different accuracy tests which have been carried out, in three dimensions only, on a SPOT Level 1A stereo-pair and its corresponding Level 1B equivalent over a test field in Crete are discussed. The data for these further tests were kindly provided by Dr Devereux and his research student, Mr. Amable, at the University of Cambridge.

8.2 Geometric Accuracy Achieved with SPOT Stereo Imagery over a Test Area in Crete

The area of the Crete test field has been covered by a single SPOT Level 1A stereo pair (with the reference number 96-279) and its corresponding Level 1B stereo-pair. The right and left images were acquired on 4th and 8th July 1993 respectively, with incidence angles of R18.9 and L21.6 degrees. This results in a good base-to-height ratio of 0.74 and about 60% overlap between the two images.

The area comprises a hilly terrain and is limited in its overall dimensions by the part of the Mediterranean Sea which occupies the southern part of the image. A GPS survey to provide the test field of ground control points (GCPs) has been carried out by staff from the University of Cambridge. Magnavox dual-frequency GPS sets, used in differential mode, have been used to measure around 30 ground control points with sub-metre accuracy. The points are well distributed across the images.

The positions of the ground control points were measured on both the SPOT Level 1A and the corresponding Level 1B stereo-pairs by Mr Amable using the PCI EASI/PACE package. They have been measured in terms of their pixel and line coordinate values with respect to the top left corner of the image. The GCPs provided by University of Cambridge group were presented to the author in the UTM coordinate system based on the WGS 1984 ellipsoid. Therefore the equations (5.22) to (5.25) described in Chapter 5, Section 5.7.2.1, have been used to transform these coordinates to the WGS 1984 geocentric coordinate system. Various tests in three dimensions using different data sets and different numbers of exterior orientation parameters have been carried out on these images. The results of these tests are presented in the next Section.

8.2.1 Three-Dimensional Accuracy Test

The various three-dimensional accuracy tests of the SPOT Level 1A and 1B stereo-pairs over the Crete test area have been carried out using the bundle adjustment program

developed by the present author and described in Chapter 7. These tests include changes in the number and distribution of the control and check points as well as changes in the number of exterior orientation parameters used in the case of the SPOT Level 1A stereo-pair. Regarding the various combinations of control and check points, three sets of data have been considered: Set A, having 13 control points and 18 check points; Set B with 8 control points and 23 check points; and Set C with 4 control points and 27 check points in the case of the Level 1A stereo-pair and 5 control points and 26 check points in the case of the Level 1B stereo-pair.

8.2.1.1 Test of Level 1A Stereo-pair

In order to obtain an overall view of the ground control points accuracy and to check on the possible occurrence of systematic errors in the measurements or in the control point data, first all of the 31 available GCPs have been used as control points in the bundle adjustment program in the case of the SPOT Level 1A stereo-pair. This test also includes changes in the number of exterior orientation parameters to evaluate the effects of the linear and quadratic terms of the polynomial modelling of these orientation parameters. Table 8.19 gives the results of these tests in the terms of their RMSE values.

Table 8.19 ΔX, ΔY, ΔZ RMSE values of the residual errors in terms of the WGS 1984 coordinate system achieved in the 3D accuracy tests of the SPOT Level 1A stereo-pair over the Crete test area using all 31 control points

No. Of exterior orientation parameters	RMSE values at control points		
	ΔX (m)	ΔY (m)	ΔZ (m)
15	±5.37	±3.63	±4.99
12	±5.39	±3.81	±4.98
9	±5.45	±3.82	±4.99

The really excellent results of the bundle adjustment program for the SPOT Level 1A stereo-pair using all of the GCPs as control points, as illustrated in Table 8.19, need some explanation and analysis. First of all, the distribution of the ground control points in the test area is very good. Secondly, the points on the image and on the ground have been measured by Mr. Amable with exceptional care and very good accuracy. And thirdly, in comparison with the Jordanian Badia test area, the area is much smaller because of the 60% overlap area

between right and left images (compared with 90% in the case of the main Badia reference model) and the fact that the sea occupies the southern part of the image. In the case of using all 15 exterior orientation parameters, the vector plots (Figure 8.14) for the residual errors in ΔX, ΔY and ΔZ. show that these errors are random in direction and size and free from systematic effects.

Using the three data sets A, B and C, described above in this Section, various tests have been carried out on the SPOT Level 1A stereo-pair, including the changes in the number of exterior orientation parameters. The results of these tests in terms of the RMSE values at the control and check points are given in Tables 8.20 to 8.22.

Table 8.20 ΔX, ΔY, ΔZ RMSE values (in metres) of the residual errors in terms of the WGS 1984 coordinate system achieved in the 3D accuracy tests of the Crete SPOT Level 1A stereo-pair (Set A)

No. of parameters	No. of control points	RMSE at control points			No. of check points	RMSE at check points		
		ΔX (m)	ΔY (m)	ΔZ (m)		ΔX (m)	ΔY (m)	ΔZ (m)
15	13	±3.63	±3.56	±5.07	18	±6.91	±5.30	±5.92
12	13	±3.93	±4.44	±5.47	18	±6.63	±4.50	±5.21
9	13	±4.12	±4.44	±5.58	18	±6.51	±4.50	±5.07

Table 8.21 ΔX, ΔY, ΔZ RMSE values (in metres) of the residual errors in terms of the WGS 1984 coordinate system achieved in the 3D accuracy tests of the Crete SPOT Level 1A stereo-pair (Set B)

No. of parameters	No. of control points	RMSE at control points			No. of check points	RMSE at check points		
		ΔX (m)	ΔY (m)	ΔZ (m)		ΔX (m)	ΔY (m)	ΔZ (m)
15	8	±4.24	±2.83	±4.59	23	±6.52	±5.69	±6.60
12	8	±4.88	±3.99	±4.58	23	±5.92	±4.78	±6.26
9	8	±5.28	±3.98	±4.67	23	±5.86	±4.77	±6.30

Table 8.22 ΔX, ΔY, ΔZ RMSE values (in metres) of the residual errors in terms of the WGS 1984 coordinate system achieved in the 3D accuracy tests of the Crete SPOT Level 1A stereo-pair (Set C)

No. of parameters	No. of control points	RMSE at control points			No. of check points	RMSE at check points		
		ΔX (m)	ΔY (m)	ΔZ (m)		ΔX (m)	ΔY (m)	ΔZ (m)
15	4	≈0.0	≈0.0	≈0.0	29	±6.12	±5.55	±9.57
12	4	±0.11	±0.22	±0.35	29	±5.91	±5.71	±8.80
9	4	±0.59	±1.76	±1.71	29	±6.30	±5.40	±7.32

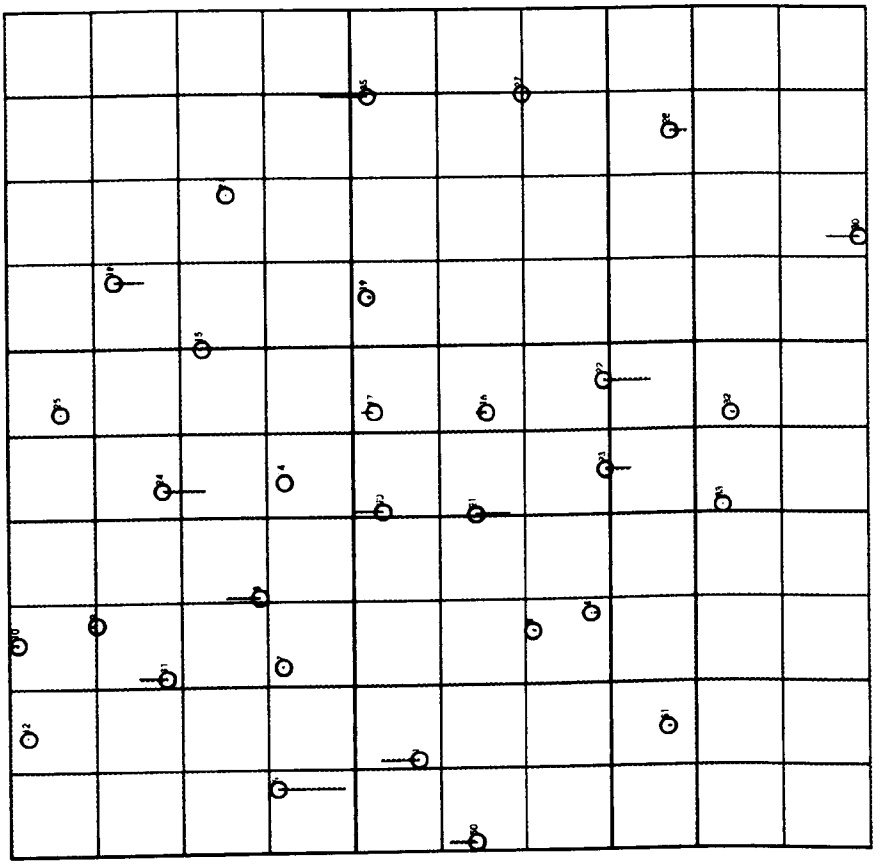

Figure 8.14 (a) Vector plot of the Z errors at the control points for the Crete test field with the SPOT Level 1A stereo-pair. (all GCPs used as control points)

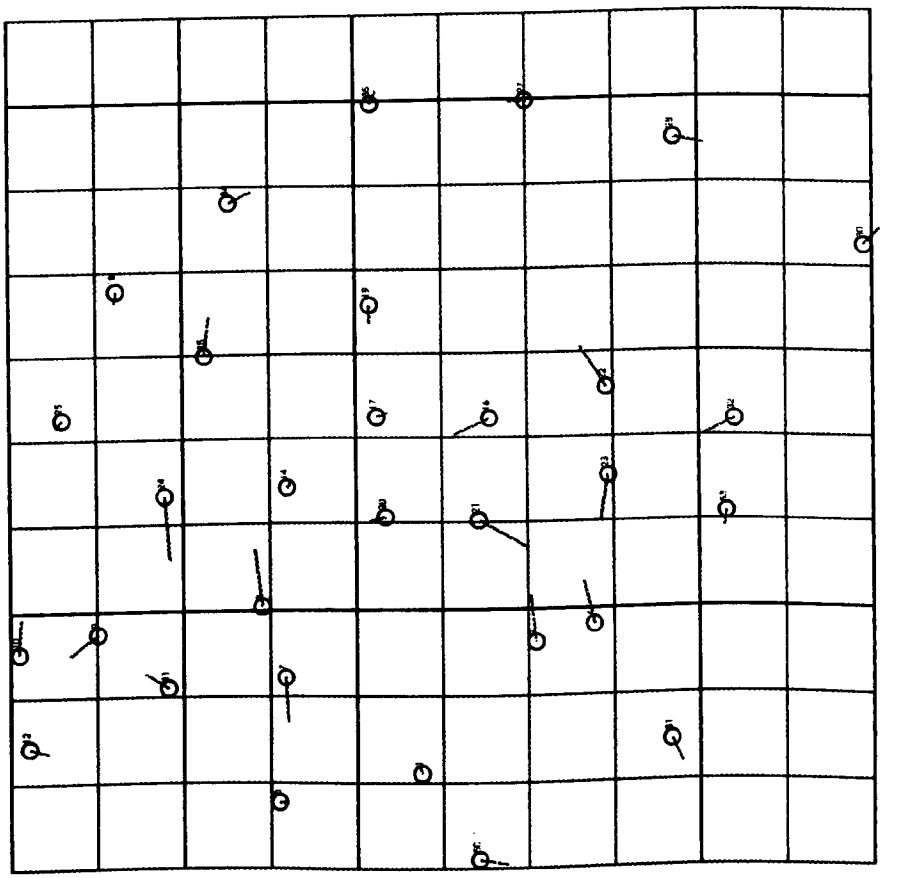

Figure 8.14 (a) Vector plot of the X/Y errors at the control points for the Crete test field with the SPOT Level 1A stereo-pair. (all GCPs used as control points)

A comparison of the residual errors in terms of the RMSE values given in Table 8.19 with those for the check points contained in Tables 8.20 to 8.22 does not show significant discrepancies between these sets of results. This confirms that the observations are good and free of systematic errors, and provides additional evidence that the mathematical model developed by the present author works quite well and in a powerful manner for cross-track stereo-images such as SPOT. The vector plots for the residual errors in ΔX, ΔY and ΔZ (Figure 8.15) for Set A, in the case of using all 15 exterior orientation parameters show that the residual errors at both the control points and check points are random in direction and amount and are not affected by systematic errors.

Comparing the results given in Tables 8.19 to 8.22, this shows that the effects of the quadratic and linear terms of the polynomial equations, used to model the changes in the rotation elements in the mathematical model, are very small and can be neglected easily in the case of SPOT Level 1A stereo-pairs. Again this points to the stability of the imaging system over the period of imaging a single scene. Furthermore it should be noted that, in the case of the SPOT Level 1B image stereo-pair, all of the exterior orientation parameters described in Chapter 5 have to be used in the bundle adjustment program.

8.2.1.2 Test of Level 1B Stereo-Pair

As in the case with the SPOT Level 1A stereo-pair, three sets of data (A, B, and C) have been used to test the corresponding SPOT Level 1B stereo-pair. The results of these tests, using the full 15 exterior orientation parameters for the processing of SPOT Level 1B stereo-pairs, are given in terms of the RMSE values of the residual errors at the control and check points in Table 8.23. Comparison between the results for the check points in terms of their RMSE values for the different sets given in this Table, shows that these values are nearly the same and that they are very good indeed. Comparing the residual errors in terms of their RMSE values in the case in which all of the GCPs are considered as control points with those for the check points only in Table 8.23 does not show any significant discrepancies. Again this shows that the observations are not affected by systematic errors. It also confirms the powerful nature of the general bundle adjustment program.

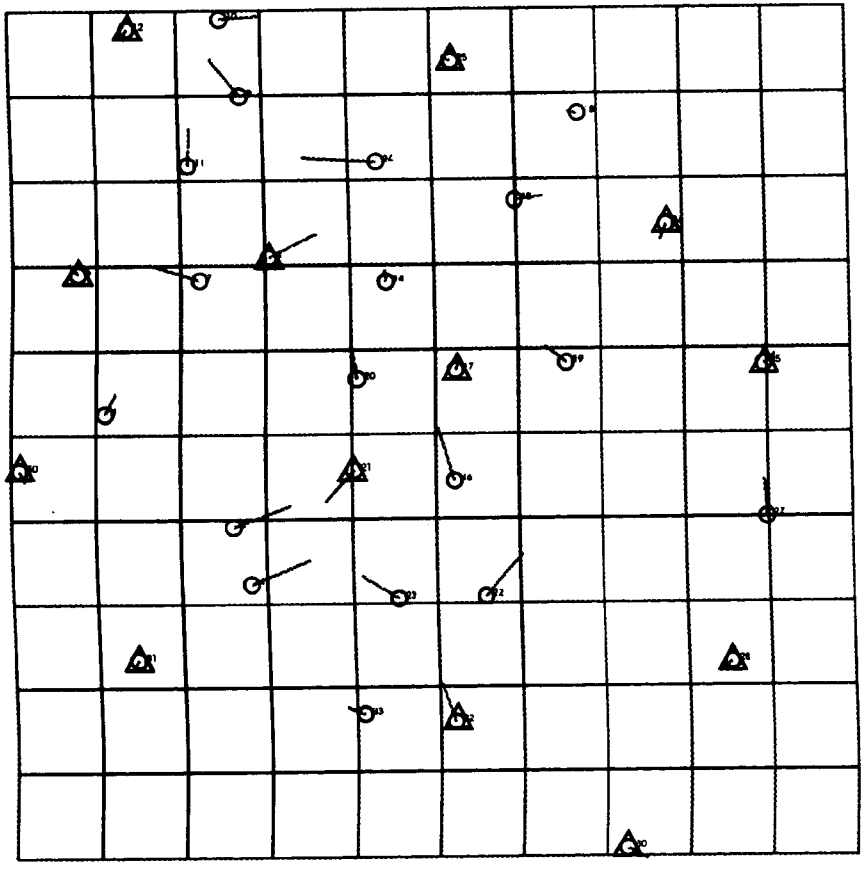

Figure 8.15 (a) Vector plot of the X/Y errors at the control and check points for the Crete test field with the SPOT Level 1A stereo-pair (Set A).
Δ = Control Point ; o = Check Point

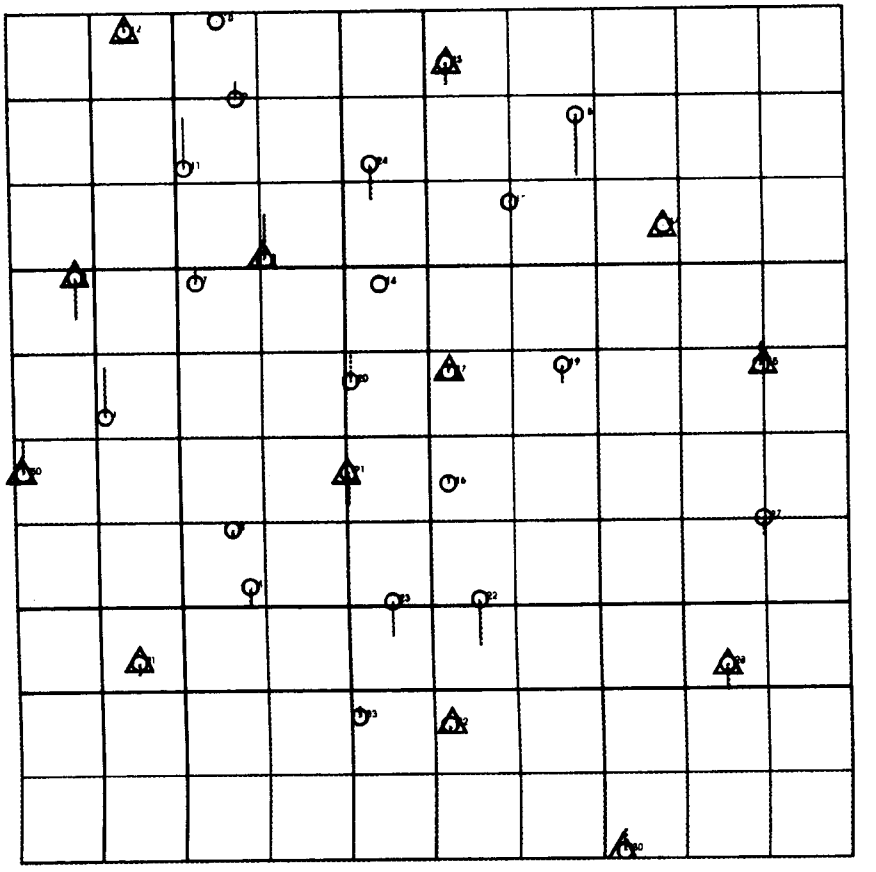

Figure 8.15 (a) Vector plot of the Z errors at the control and check points for the Crete test field with the SPOT Level 1A stereo-pair (Set A).
Δ = Control Point ; o = Check Point

Table 8.23 ΔX, ΔY, ΔZ RMSE values (in metres) of the residual errors in terms of the WGS 1984 coordinate system achieved in the 3D accuracy tests of the Crete SPOT Level 1B stereo-pair

Name of the data set	No. of control points	RMSE at control points			No. of check points	RMSE at check points		
		ΔX (m)	ΔY (m)	ΔZ (m)		ΔX (m)	ΔY (m)	ΔZ (m)
Full GCPs as control	31	±6.22	±4.66	±4.94	0	------	------	------
A	13	±5.98	±3.73	±2.28	18	±7.70	±6.49	±7.17
B	8	±6.94	±2.48	±2.53	23	±7.91	±7.13	±6.45
C	5	±0.62	±0.15	±0.46	26	±7.87	±7.51	±7.34

The vector diagrams constructed from the ΔX, ΔY and ΔZ values, in the case of using the full set of GCPs as control points and that for Set A for the Level 1B stereo-pairs, are included as Figures 8.16 and 8.17 respectively. As can be seen from these figures, the residual errors at the individual control and check points are once again random in direction and extent and no systematic component can be discovered in these vector plots.

Comparing the results obtained from various tests carried out on the SPOT Level 1A stereo-pair (Tables 8.19 to 8.22) with those from SPOT Level 1B stereo-pair, shows that these various values support one other quite well and the discrepancies between these values are not significant. Again, it shows in fact that the mathematical procedure to model SPOT Level 1B image, developed in this research, works properly and in a precise manner.

8.3 Conclusion

In summary, it can be said that the extensive series of tests carried out using SPOT Level 1A and 1B stereo-pairs over two quite different test fields gave excellent results and validate both the modelling and the programs developed by the present author. As will be discussed later in Chapter 10 of this dissertation, the overall results of the geometric accuracy tests are among the best that have been achieved and published, especially those for the Level 1B stereo-pairs.

In the next Chapter, the results from a series of comparable but different 2D and 3D tests which have been carried out on MOMS-02 along-track stereo-images using the adjustment program developed by the present author will be presented, discussed and analyzed.

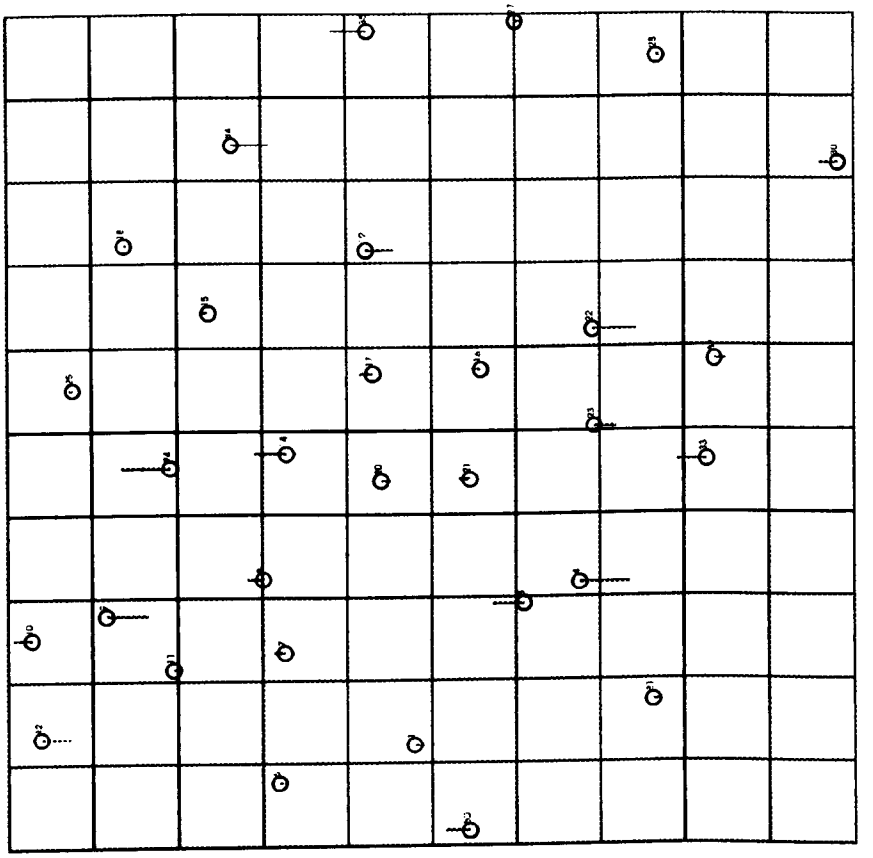

Figure 8.16 (b) Vector plot of the Z errors at the control points for the Crete test field with the SPOT Level 1B stereo-pair. (using all 31 GCPs as control points)

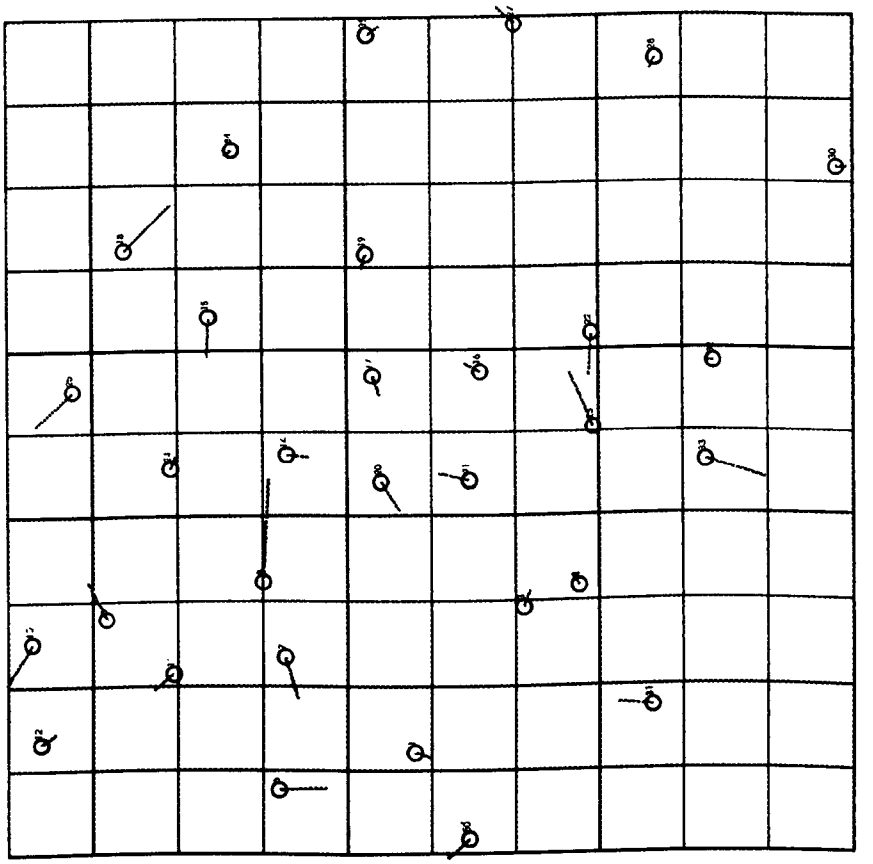

Figure 8.16 (a) Vector plot of the X/Y errors at the control points for the Crete test field with the SPOT Level 1B stereo-pair. (using all 31 GCPs as control points)

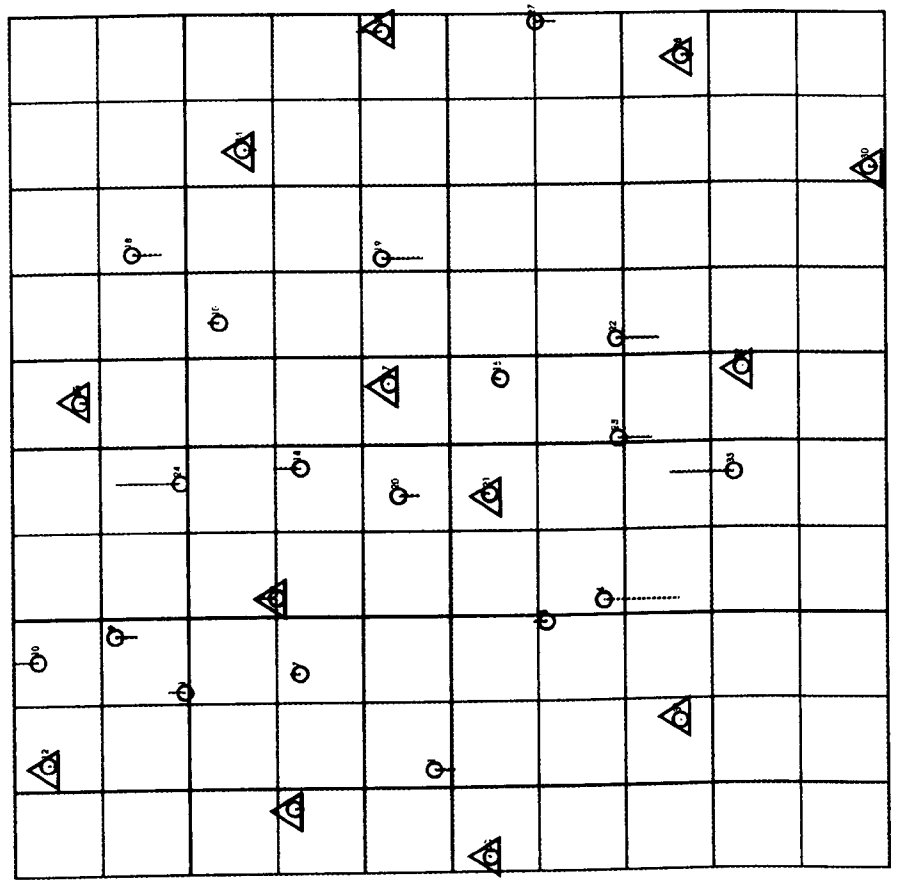

Figure 8.17 (b) Vector plot of the Z errors at the control and check points for the Crete test field with the SPOT Level 1B stereo-pair (Set A).
Δ = Control Point ; o = Check Point

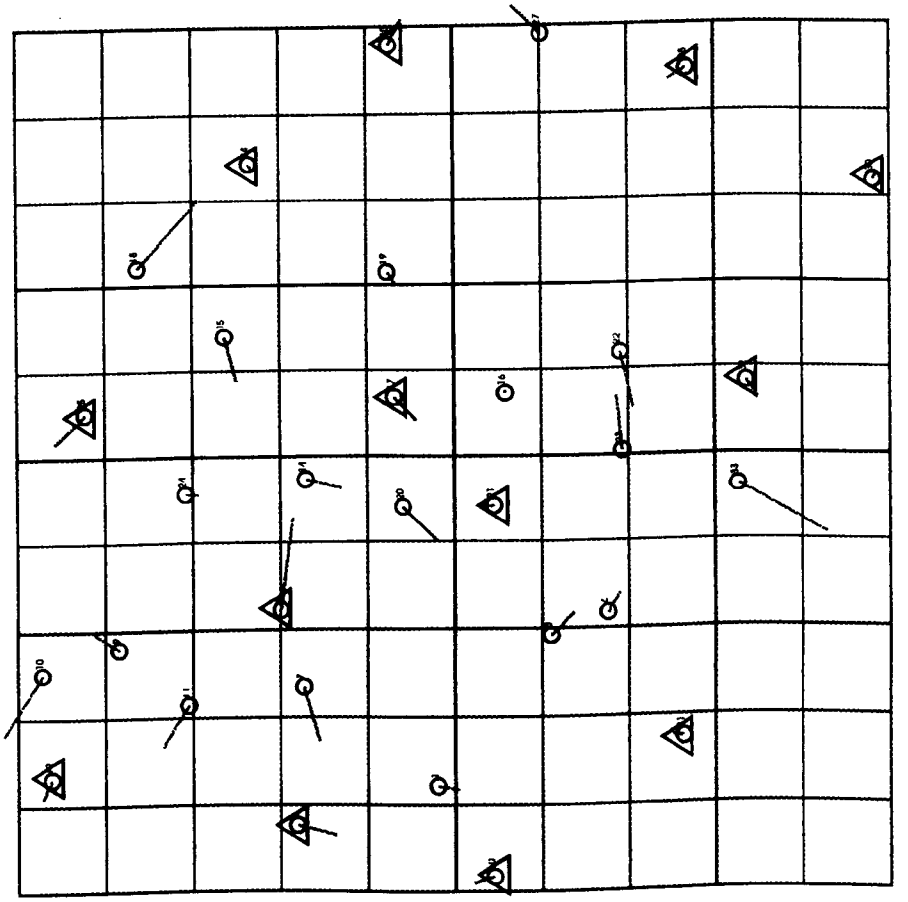

Figure 8.17 (a) Vector plot of the X/Y errors at the control and check points for the Crete test field with the SPOT Level 1B stereo-pair (Set A).
Δ = Control Point ; o = Check Point

CHAPTER 9 : GEOMETRIC ACCURACY TESTS OF ALONG-TRACK LINEAR ARRAY IMAGES

In the case of along-track linear array imagery, the geometric accuracy of MOMS-02 stereo-imagery has been tested using the adjustment program outlined in Chapter 7. It includes tests of a MOMS-02 mode 3 stereo-pair taken over an area in Sudan and a MOMS-02 mode 1 stereo-pair acquired over a test area in Australia. These tests comprise an assessment of the geometric accuracy of point determination in both two and three dimensions using different numbers of GCPs and different numbers of unknown parameters.

9.1 Geometric Accuracy Achieved with MOMS-02 Mode 3 Stereo Imagery over a Test Area in Sudan

During the ten days of the experimental mission of MOMS-02 carried out from the Space Shuttle in 1993, parts of Sudan have been imaged using mode 3 of the MOMS-02 sensor on two occasions from two different orbits. The first strip of MOMS-02 imagery covers an area beginning to the north east of Khartoum, crossing the River Atbara and finishing in the area of Kassala located on the border with Ethiopia (Strip A in Figure 10.1). From this strip, three scenes (numbers 34, 35, and 36) acquired during Orbit 14 were purchased from DLR in Germany.

Also a second strip, comprising six scenes (numbers 1, 2, 3, 4, 5, and 6) taken during Orbit 61 (Strip B in Figure 10.1) was purchased. This latter strip covers an area to the south of the first strip mainly over the Gezira and crossing first the White Nile and later the Blue Nile close to the Ethiopian border. The area is mostly flat and includes extensive cultivated areas in some parts. The quality of these scenes was somewhat variable, some having radiometric flaws that could not be removed. Further restrictions were caused through the lack of availability of control points in several scenes. This meant that just a single scene (number 5) was tested over Sudan. In this section, after first describing the status and accuracy of the control points comprising the Sudanese test field, the procedures that were followed and the results achieved in the tests of geometric accuracy in both two and three dimensions using

the MOMS-02 stereo-imagery are outlined.

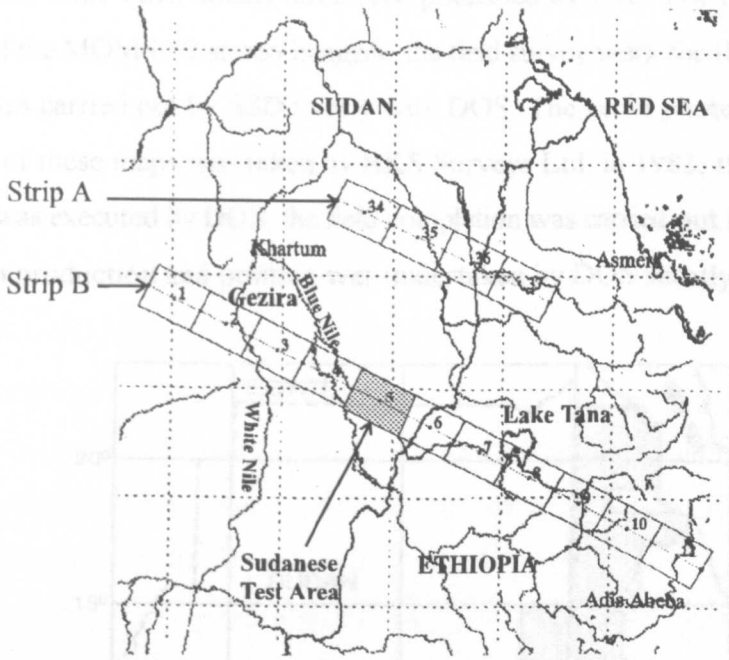

Figure 9.1 Strips A and B of MOMS-02 Imagery Over Sudan

9.1.1 Test Area and Its Map Coverage

Sudan is a country with a considerable land area and very poor topographic map cover. Until the mid 1970s, it was only covered by a purely planimetric 1:250,000 scale series originally compiled at the begining of the 20th Century. In the 1970s, it was decided that a new 1:100,000 scale series with contours should also be produced (Petrie and El Niweiri, 1992). Partly this was done by the Sudan Survey Department (SSD) through a UNDP-supported programme, but mostly it was undertaken through a joint survey and mapping programme with the British Directorate of Overseas Surveys (DOS). This produced more than 136 sheets at 1:100,000 scale during the late 1970s and early 1980s. These maps cover much of the Red Sea Hills and the area running southwards to the Ethiopian border, including the areas around the towns of Port Sudan, Suakin and Kassala. Also the area along the Ethiopian border west of Kassala was covered, including the areas around Wad Medani and Damazin along the Blue Nile and the huge Gezira irrigated area lying between the two Nile Rivers south of Khartoum (see Figure 9.2). The control points used in the production of these maps from aerial photography were established using Tellurometer traverses and

satellite Doppler translocation techniques based on the existing survey network in the area. Later, in 1989, some other sheets have been published by SSD. For the test area covered by Scene 5 of the MOMS-02 stereo-imagery, the field survey work for the relevant 1:50,000 scale maps was carried out by SSD jointly with DOS. The aerial photography used for the compilation of these maps was taken by BKS Surveys Ltd. in 1983, the photogrammetric compilation was executed by DOS, the field completion was carried out by SSD in 1987 and the final map production and printing was undertaken by DOS shortly afterwards.

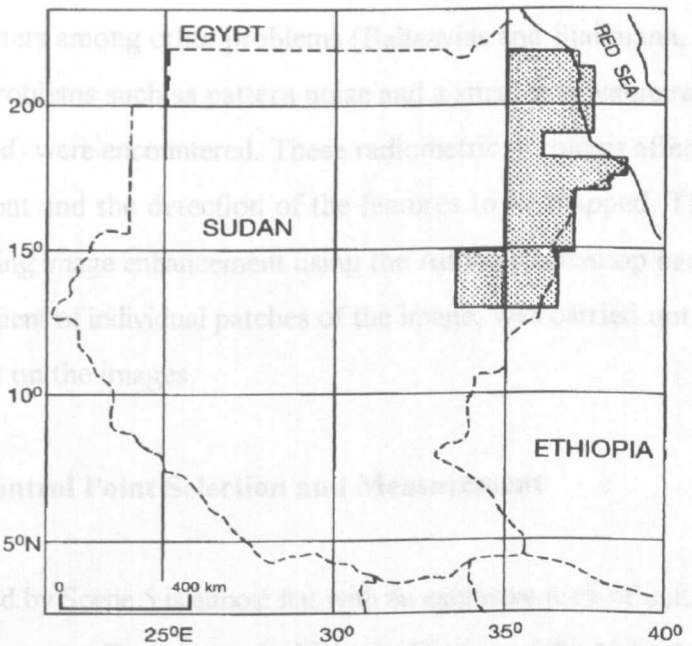

Figure 9.2 Map coverage at 1:100,000 scale resulting from the joint DOS/SDD mapping project (Petrie and El Niweiri, 1992)

The area imaged by Scene 5 of Orbit 61 has been covered totally by six of the DOS 1:100,000 scale maps comprising sheets numbers 513, 514, 543, 544, 545 and 573. The accuracy of the planimetric detail (m_{pl}) contained in these maps is estimated to be ±0.3mm (equivalent to ±30m), while the accuracy of the contours (m_h) where a 20m interval has been used is estimated to be ±4.25m. The coordinate system and projection used for these maps is UTM, based on the Clarke 1880 ellipsoid and the Adindan Datum. The UTM coordinate values in Easting and Northing could be used directly in the polynomial adjustment. However, for the bundle adjustment program, the ground coordinates need to be input to the program in geocentric (XYZ) coordinates (i.e. in the WGS 1984 system). Thus all of the

control points taken from these maps had to be converted to this system based on the equations (5.22) to (5.25) given in Chapter 5, Section 5.7.2.1.

9.1.2 Test Imagery Used

The images that were used for the test, i.e. stereo channels 6 and 7 of Scene 5, were of a quite poor radiometric quality when delivered in their raw state. The temperature on the Space Shuttle was too high and this resulted in the application of unsuitable sensor calibration parameters among other problems (Baltsavias and Stallmann, 1996). In the two stereo channels, problems such as pattern noise and a small grey value range (only 55 grey values were utilised) were encountered. These radiometric problems affect both the control point measurement and the detection of the features to be mapped. Thus, a strong pre-processing, including image enhancement using the Adobe Photoshop package, comprising the separate treatment of individual patches of the image, was carried out before measuring the control points on the images.

9.1.3 Ground Control Point Selection and Measurement

The terrain covered by Scene 5 is almost flat with an extensive area of cultivation occupying the right part of the scene. Two rivers, the Nahr Ad Dindir and the Nahr Ar Rahad, run from the top to the middle and from the top to the bottom of Scene 5 respectively. The area appears to be lightly populated with scattered small villages and townships (see Figure 9.3). A variety of well-defined detail is present in this area. The well-defined field corners and the junctions between the cultivated fields appearing on the image could be considered as good ground control points (GCPs) but most of them could not be found or recognized in the maps. The intersection of the tracks and streams could also be considered as control points. But in the case of the tracks marked on the maps, it is very difficult to find them on the image. In the case of the streams, although they can be recognized on the image, in some cases, their planimetric positions appear to have changed a lot, which reduces the accuracy of the ground control points using such features.

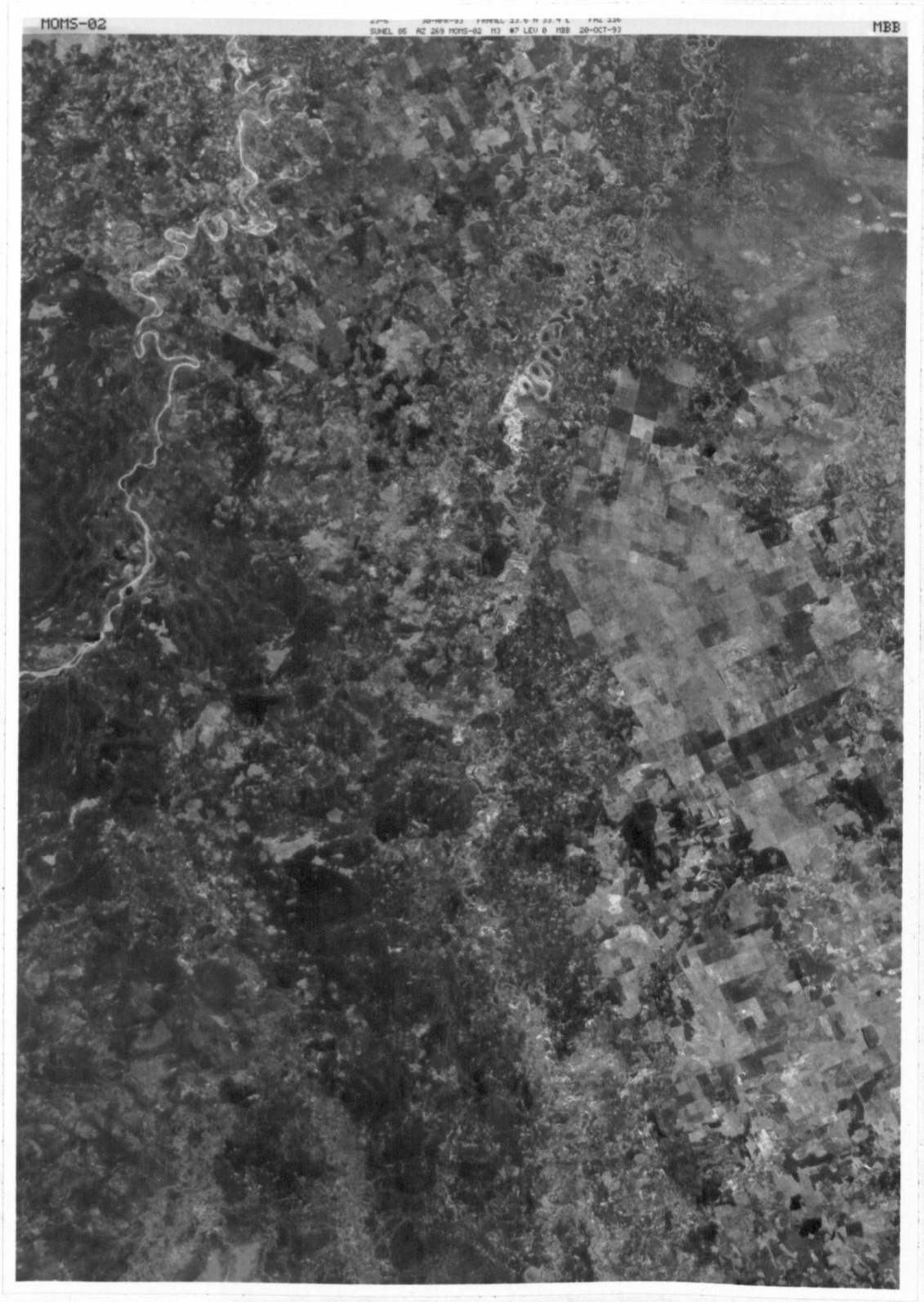

Figure 9.3 MOMS-02 imagery, Channel 7, Scene 5, over Sudanese test field area

However, a big effort has been made to find suitable GCPs, although, in the end, they are not distributed evenly over the image. Unfortunately, in some parts of the image, especially in the middle of the scene, no suitable features could be recognized that could be measured on the map. This central part of the image is rather featureless with only a few small rivers passing through it. However, nearly 50 GCPs have been selected and measured on the map sheets using a precision scale with an accuracy of 0.1mm. Later they have been measured monoscopically on each image to produce pixel and line coordinate values with respect to the top left corner of the scene using the PCI EASI/PACE package running on a PC. In order to reduce the systematic errors, especially in terms of the measured x parallaxes, two image windows were opened at the same time on the EASI/PACE display system so that the ground control points were measured on the corresponding forward and backward images at the same time. The ground control points were measured using a zoom factor of 2 to 4 on the screen to allow a sub-pixel accuracy in the pointing, estimated to be 0.5 to 0.25 pixel. After measuring the control points, the image (pixel and line) coordinates and the corresponding terrain coordinates have been entered into the adjustment program outlined in Chapter 7. In the bundle adjustment program, the image coordinates based on pixels and lines were transformed later into the image coordinates defined in Chapter 5. In the following Sections, the results of a series of tests of the geometric accuracy of the MOMS-02 stereo-pair over the Sudanese test area in both two and three dimensions will be given.

9.1.4 Two-Dimensional (Planimetric) Accuracy Test

Since the test area was so flat, this provided an excellent opportunity to test the planimetric accuracy of an individual (non-stereo) MOMS-02 image. Using the polynomial adjustment program described in Chapter 7, various tests have been carried out on the Channel 6 (forward) image of MOMS-02, Scene 5. In the first instance, all of the 49 ground control points measured on the image have been used as control points in order to derive the transformation parameters of the specific polynomial used. Then the resulting transformed values of the measured image coordinates were compared with the given terrain coordinate values of these control points. The results of this test and the effects of adding successively

the different individual terms in the polynomial are given in Table 9.1.

Table 9.1 Results (in metres) of the RMSE values achieved in the 2D (planimetric) accuracy tests of the Sudanese MOMS-02 image using all 49 control points

Polynomial Transformation	ΔE (m)	ΔN (m)	Δpl (m)
3 terms (affine)	± 18.97	± 22.28	± 29.26
4 terms (xy)	± 18.97	± 21.84	± 28.93
5 terms (x^2)	± 18.12	± 17.98	± 25.53
6 terms (y^2)	± 18.11	± 16.09	± 24.23
7 terms (x^2y)	± 17.35	± 16.09	± 23.66
8 terms (xy^2)	± 16.97	± 15.87	± 23.23
9 terms (x^2y^2)	± 16.86	± 15.49	± 22.90
10 terms (x^3)	± 16.81	± 15.47	± 22.84
11 terms (y^3)	± 16.64	± 15.47	± 22.72
12 terms (xy^3)	± 16.58	± 15.47	± 22.68
13 terms (x^3y)	± 16.08	± 15.46	± 22.31
14 terms (x^2y^3)	± 15.29	± 15.43	± 21.72
15 terms (x^3y^2)	± 15.22	± 14.91	± 21.30
16 terms (x^3y^3)	± 15.15	± 14.91	± 21.26
17 terms (x^4)	± 15.15	± 14.66	± 21.08
18 terms (y^4)	± 14.26	± 14.65	± 20.44
19 terms (x^4y)	± 13.68	± 14.64	± 20.04
20 terms (xy^4)	± 13.68	± 14.58	± 19.99
21 terms (x^4y^2)	± 13.31	± 14.08	± 19.38
22 terms (x^2y^4)	± 12.17	± 14.06	± 18.60
23 terms (x^4y^3)	± 12.04	± 14.04	± 18.50
24 terms (x^3y^4)	± 12.04	± 13.64	± 18.19
25 terms (x^4y^4)	± 9.75	± 13.01	± 16.26

As can be seen from Table 9.1, the significant improvements in fit occured in Northing with the use of the 5th term (x^2) and in Easting with the 25th term (x^4y^4) of the polynomial transformation, with improvements of 3.8 m and 2.3m respectively. Comparing the results of this test in the case of affine transformation with those from SPOT Level 1A imagery given in Table 8.1, Chapter 8, shows a significant discrepancy between these two sets of data. The reason could be that, in the case of MOMS-02 imagery, since there is no tilt in the cross track direction, so the maximum effect of Earth curvature on the image, using

equation 8.1 is 10μm, which is approximately equal to 13.5m on the ground. On the other hand, since the orbital inclination of the Space Shuttle which was carrying the MOMS-02 imaging system was 28.5 degrees, then the effect of Earth curvature will be divided between the Easting and Northing directions rather than being concentrated in the Easting direction as happens with SPOT.

The vector plots (Figure 9.4(a)) show that the residual errors, when using the full 25 terms of the polynomial transformation, are random both in extent and direction. This shows that the final results are not affected by systematic errors.

Other 2D accuracy tests have been carried out using four sets of measurements comprising different numbers and combinations of control points and independent check points. In Set A, 19 of the measured image points have been used as control points with the other 30 points used as check points. In Sets B, C, and D, the number of control points has been reduced to 14, 10 and 8 respectively, while the corresponding number of check points has been increased to 35, 39, and 41 respectively. Tables 9.2 to 9.5 give the results of these tests, including the effect of including successive additional terms. Note that the number of terms that could be used in the polynomial adjustment is limited by the number of control points. As can be seen from these Tables, increasing the number of correction terms from the polynomial improves (i.e. makes smaller) the residual errors occuring at the independent check points. There is generally a significant improvement when implementing the second order terms x^2 and y^2. Then the results remain nearly constant when additional terms are employed. Finally the values begin to increase. The reason for this is of course the decrease in the degrees of freedom of the adjustment and the lack of redundancy in the control points.

Graphical analysis of the residuals in the control points for Set A (see Figure 9.4b), shows that the residual errors at the individual control points are completely random; no systematic component can be discovered in the vector plots. For the independent check points, the pattern is mostly random with small systematic components in specific areas which could be a result of not having a good distribution of the GCPs.

Table 9.2 ΔE, ΔN RMSE values (in metres) of the residual errors achieved in terms of UTM coordinates for the Sudanese MOMS-02 image (Set A)

Polynomial Transformation	Control points (n=19)			Check points (n = 30)		
	ΔE (m)	ΔN (m)	Δpl (m)	ΔE (m)	ΔN (m)	Δpl (m)
3 terms (affine)	± 17.14	± 21.51	± 27.50	± 21.05	± 24.69	± 32.44
4 terms (xy)	± 17.12	± 21.43	± 27.43	± 21.10	± 24.31	± 32.19
5 terms (x^2)	± 16.23	± 15.67	± 22.56	±20.83	± 20.59	± 29.29
6 terms (y^2)	± 14.94	± 13.70	± 20.27	± 22.54	± 18.58	± 29.21
7 terms (x^2y)	± 14.08	± 13.69	± 19.64	± 21.58	± 18.59	± 28.48
8 terms (xy^2)	± 13.28	± 13.69	± 19.07	± 21.33	± 18.58	± 28.29
9 terms (x^2y^2)	± 12.48	± 13.68	± 18.52	± 21.99	± 18.74	± 28.89
10 terms (x^3)	± 11.60	± 13.09	± 17.49	± 22.32	± 19.87	± 29.88
11 terms (y^3)	± 9.02	± 13.09	± 15.90	± 24.03	± 19.92	± 31.20
12 terms (xy^3)	± 8.36	± 11.33	± 14.08	± 25.58	± 24.82	± 35.64
13 terms (x^3y)	± 6.93	± 10.50	± 12.58	± 25.06	± 25.84	± 36.00
14 terms (x^2y^3)	± 4.95	± 10.44	± 11.55	± 24.27	± 26.00	± 35.57
15 terms (x^3y^2)	± 4.64	± 10.12	± 11.13	± 24.01	± 25.99	± 35.38
16 terms (x^3y^3)	± 4.35	± 10.11	± 11.01	± 24.62	± 25.90	± 35.73
17 terms (x^4)	± 4.22	± 9.42	± 10.32	± 25.66	± 30.33	± 39.73
18 terms (y^4)	± 4.15	± 4.48	± 6.11	± 24.58	±110.24	±112.95
19 terms (x^4y)	≈0.0	≈0.0	≈0.0	± 55.41	± 72.95	± 91.61

Table 9.3 ΔE, ΔN RMSE values (in metres) of the residual errors achieved in terms of UTM coordinates for the Sudanese MOMS-02 image (Set B)

Polynomial Transformation	Control points (n=14)			Check points (n = 35)		
	ΔE (m)	ΔN (m)	Δpl (m)	ΔE (m)	ΔN (m)	Δpl (m)
3 terms (affine)	± 15.58	± 23.90	± 28.53	± 25.07	± 24.90	± 35.33
4 terms (xy)	± 14.76	± 23.72	± 27.94	± 26.45	± 24.41	± 35.99
5 terms (x^2)	± 14.36	± 21.73	± 26.05	± 26.10	± 20.18	± 32.99
6 terms (y^2)	± 14.18	± 14.66	± 20.40	± 26.69	± 22.27	± 34.76
7 terms (x^2y)	± 9.20	± 14.41	± 17.10	± 28.40	± 22.12	± 36.00
8 terms (xy^2)	± 5.67	± 12.45	± 13.68	± 27.93	± 23.14	± 36.27
9 terms (x^2y^2)	± 2.77	± 8.48	± 8.64	± 27.64	± 25.53	± 37.63
10 terms (x^3)	± 2.70	± 8.16	± 8.60	± 27.74	± 25.75	± 37.85
11 terms (y^3)	± 2.66	± 6.78	± 7.28	± 28.19	± 31.15	± 42.01
12 terms (xy^3)	± 2.49	± 5.75	± 6.26	± 29.80	± 68.15	± 74.38
13 terms (x^3y)	± 1.70	± 4.64	± 4.94	± 41.16	± 96.66	±105.05
14 terms (x^2y^3)	≈ 0.0	≈ 0.0	≈ 0.0	± 51.48	±283.01	±287.65

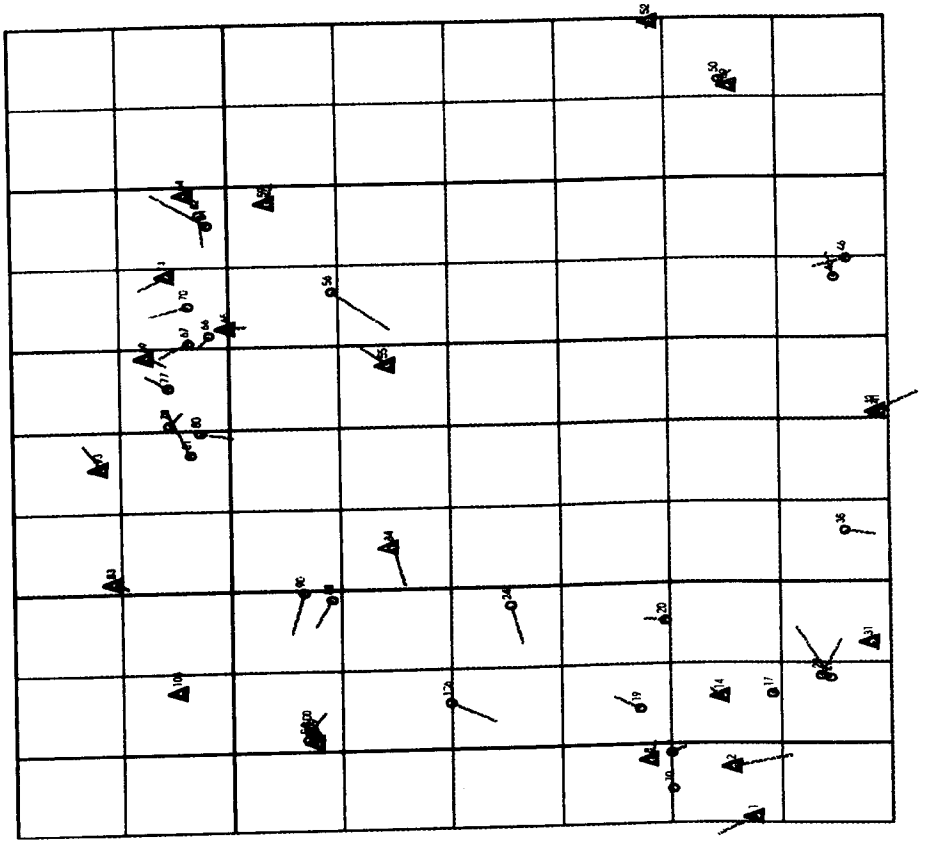

Figure 9.4(b) Vector plot of the planimetric errors at control points and check points for the Sudanese testfield (Set A)
Δ = Control Point ; o = Check Point

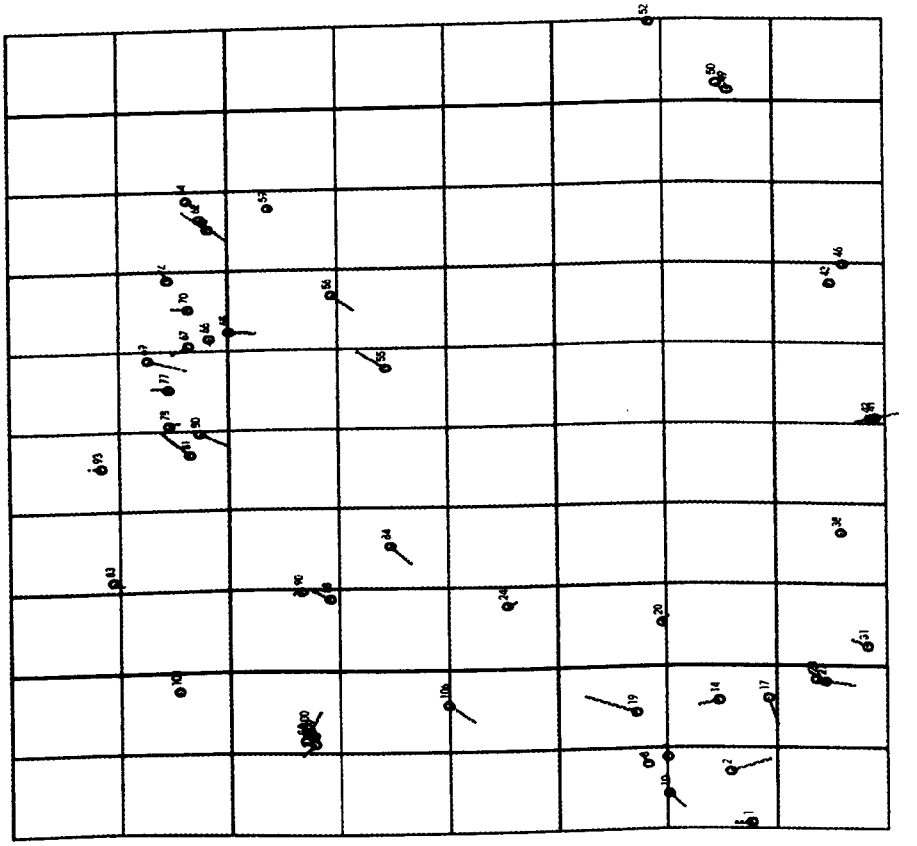

Figure 9.4(a) Vector plot of the planimetric errors at control points for the Sudanese testfield (All 49 GCPs used as control points)

Table 9.4 ΔE, ΔN RMSE values (in metres) of the residual errors achieved in terms of UTM coordinates for the Sudanese MOMS-02 image (Set C)

Polynomial Transformation	Control points (n=10)			Check points (n = 39)		
	ΔE (m)	ΔN (m)	Δpl (m)	ΔE (m)	ΔN (m)	Δpl (m)
3 terms (affine)	± 13.71	± 16.94	± 21.79	± 27.57	± 23.81	± 36.43
4 terms (xy)	± 11.98	± 16.58	± 20.46	± 26.95	± 24.08	± 36.14
5 terms (x^2)	± 7.86	± 16.57	± 18.34	± 23.58	± 24.02	± 33.66
6 terms (y^2)	± 7.62	± 16.22	± 17.92	± 22.76	± 23.55	± 32.75
7 terms (x^2y)	± 6.57	± 12.16	± 13.82	± 22.49	± 23.04	± 32.20
8 terms (xy^2)	± 5.11	± 11.79	± 12.85	± 24.05	± 22.11	± 32.67
9 terms (x^2y^2)	± 4.97	± 10.63	± 11.73	± 27.71	± 34.09	± 43.93
10 terms (x^3)	≈0.0	≈0.0	≈0.0	± 24.61	± 30.40	± 39.11

Table 9.5 ΔE, ΔN RMSE values (in metres) of the residual errors achieved in terms of UTM coordinates for the Sudanese MOMS-02 image (Set D)

Polynomial Transformation	Control points (n=8)			Check points (n = 41)		
	ΔE (m)	ΔN (m)	Δpl (m)	ΔE (m)	ΔN (m)	Δpl (m)
3 terms (affine)	± 14.35	± 22.98	± 27.09	± 22.91	± 25.75	± 34.47
4 terms (xy)	± 13.86	± 22.73	± 26.62	± 23.40	± 25.33	± 34.48
5 terms (x^2)	± 13.78	± 13.88	± 19.56	± 23.30	± 22.78	± 32.59
6 terms (y^2)	± 13.60	± 8.55	± 16.06	± 23.54	± 20.82	± 31.43
7 terms (x^2y)	± 12.16	± 7.50	± 14.29	± 22.54	± 20.86	± 30.71
8 terms (xy^2)	0.0	0.0	0.0	± 59.70	± 39.39	± 71.52

However, in general terms, the results of these tests are reasonably good, especially having regard to the use of control points which have been extracted from a 1:100,000 scale map. This arises from this fact that, in the first place, the spacecraft movements during the image data acquisition appear to have been quite small. Secondly the effects of relief displacement on the measured image points are also very small as a result of having a nearly flat test area.

A comparison can be made between the 2D tests on MOMS-02 imagery over Sudan which have been described in this Section, with those which had been carried out previously in this Department by El-Niweiri (1988) on MOMS-01 imagery over a different test area in Sudan. Table 9.6 summarizes the results of his 2D test using a polynomial transformation program, when using 20 check points and 31 check points, which is a configuration close to that of Set A in the present tests.

Table 9.6 ΔE, ΔN RMSE values (in metres) of the residual errors achieved in terms of UTM coordinates for the Sudanese MOMS-01 image (El-Niweiri, 1988)

Polynomial Transformation	Control points (n=20)			Check points (n=31)		
	ΔE (m)	ΔN (m)	Δpl (m)	ΔE (m)	ΔN (m)	Δpl (m)
3 terms (affine)	±22.11	±20.23	±29.97	±18.31	±21.23	±28.03
4 terms (xy)	±22.68	±19.83	±30.13	±18.47	±21.61	±28.42
5 terms (x^2)	±23.34	±20.21	±30.87	±19.24	±22.84	±29.87
6 terms (y^2)	±23.76	±20.87	±31.62	±19.32	±22.85	±29.92
7 terms (x^2y)	±23.15	±21.44	±31.55	±19.63	±22.57	±29.91
8 terms (xy^2)	±24.08	±22.31	±32.83	±19.53	±22.57	±29.85
9 terms (x^2y^2)	±25.05	±21.41	±32.95	±19.03	±23.67	±30.38
10 terms (x^3)	±23.75	±22.09	±32.44	±19.26	±23.56	±30.43

Comparing these RMSE values with those given in Table 9.2 (Set A), shows nearly the same results in both cases. The best results for the check points and the control points in the case of El-Niweiri's test have been obtained with just 3 terms (i.e. an affine transformation). Thereafter the results did not improve even when additional higher order terms were used in his solution. In the case of author's test for the check points, the best results are obtained when using 8 terms and the results for the control points become better with an increase in the number of terms until the limiting number of terms was reached by the number of control points used in the polynomial transformation. Since the ground pixel size of MOMS-01 was 20m compared with the 13.5m pixel size of MOMS-02 and the area which has been tested by El-Niweiri had more relief than the area that has been tested by the author, then obtaining nearly the same results in both tests could be the result of certain characteristics common to the two tests. Indeed, it may well be that the limiting factor is simply the planimetric accuracy (±0.2mm to ±0.3mm equivalent to ±20m to ±30m) with which the control points can be extracted from the 1:100,000 scale maps.

In the next Section, the procedure used and the results achieved in the three-dimensional accuracy testing of the same MOMS-02 scene over the same test field in Sudan are discussed.

9.1.5 Three-Dimensional Accuracy Test

The bundle adjustment program outlined in Chapter 7 has been used to test the geometric accuracy of the MOMS-02 stereo-pair in three dimensions. Again, the same four sets of control and check points (A, B, C, and D) have been used as were used in the two-dimensional accuracy test.

The bundle adjustment program is very flexible and the number of exterior orientation parameters can be reduced from 15 to 9. Based on this particular characteristic, different tests have been carried out using different numbers of exterior orientation parameters. As a first test, all 15 exterior orientation parameters (see Chapter 6) have been utilised in the bundle adjustment program. Then the quadratic terms of the polynomials which model the change of the conventional rotation parameters (i.e. ω, φ, and κ) with respect to time have been removed, which results in only 12 exterior orientation parameters being used. Finally the first order terms in the polynomials which again describe the effects of the dynamic nature of linear array imagery in terms of conventional rotation parameters (ω, φ, and κ), have also been eliminated to result in 9 exterior orientation parameters. The other parameters are necessary in the bundle adjustment program and so no further reduction in the number of terms can be considered. The results of these tests when using all of the GCPs as control points and for the four other combinations of control points and check points (Sets A, B, C, and D) are given in Tables 9.7 to 9.11.

First the bundle adjustment program in its Case 2 configuration (resection with quasi-observations) has been used. This means that all of the ground control points (GCPs) are considered to have fixed coordinate values. The results of the bundle adjustment using all of the GCPs as control points (Table 9.7) show a reasonably good accuracy having regard to the limitations of the control points selected from 1:100,000 scale maps. In the case of using all 15 exterior orientation parameters in the solution, the vector of the errors in all three dimensions is equal to 28.06m which is quite good. The results also show that the relative positioning of the ground control points is good enough for this case. In other words, the points on the images have been measured and identified with a reasonable

accuracy.

Table 9.7 ΔX, ΔY, ΔZ RMSE values (in metres) of the residual errors in terms of the WGS 1984 coordinate system achieved in the 3D accuracy tests of the Sudanese MOMS-02 image using all 49 control points

No. of parameters	RMSE values at control points		
	ΔX (m)	ΔY (m)	ΔZ (m)
15	± 13.01	± 19.48	± 15.45
12	± 16.35	± 20.05	± 15.82
9	± 14.81	± 23.81	± 16.20

The vector plots (Figure 9.5) show that the errors are mostly random with small systematic components in specific areas which could be a result of the test area not having a good distribution of the GCPs.

Table 9.8 ΔX, ΔY, ΔZ RMSE values (in metres) of the residual errors in terms of the WGS 1984 coordinate system achieved in the 3D accuracy tests of the Sudanese MOMS-02 image (Set A)

No. of parameters	No. of control points	RMSE at control points			No. of check points	RMSE at check points		
		ΔX (m)	ΔY (m)	ΔZ (m)		ΔX (m)	ΔY (m)	ΔZ (m)
15	19	± 13.28	± 22.28	± 17.36	30	± 15.56	± 21.58	± 17.35
12	19	± 14.77	± 26.33	± 17.52	30	± 16.67	± 24.00	± 18.31
9	19	± 14.73	± 26.93	± 17.49	30	± 16.62	± 24.73	± 18.39

Table 9.9 ΔX, ΔY, ΔZ RMSE values (in metres) of the residual errors in terms of the WGS 1984 coordinate system achieved in the 3D accuracy tests of the Sudanese MOMS-02 image (Set B)

No. of parameters	No. of control points	RMSE at control points			No. of check points	RMSE at check points		
		ΔX (m)	ΔY (m)	ΔZ (m)		ΔX (m)	ΔY (m)	ΔZ (m)
15	14	± 10.02	± 15.48	± 12.06	35	± 16.57	± 29.13	± 21.86
12	14	± 14.75	± 20.06	± 13.93	35	± 16.20	± 29.17	± 19.52
9	14	± 17.08	± 23.65	± 14.24	35	± 15.57	± 28.57	± 20.27

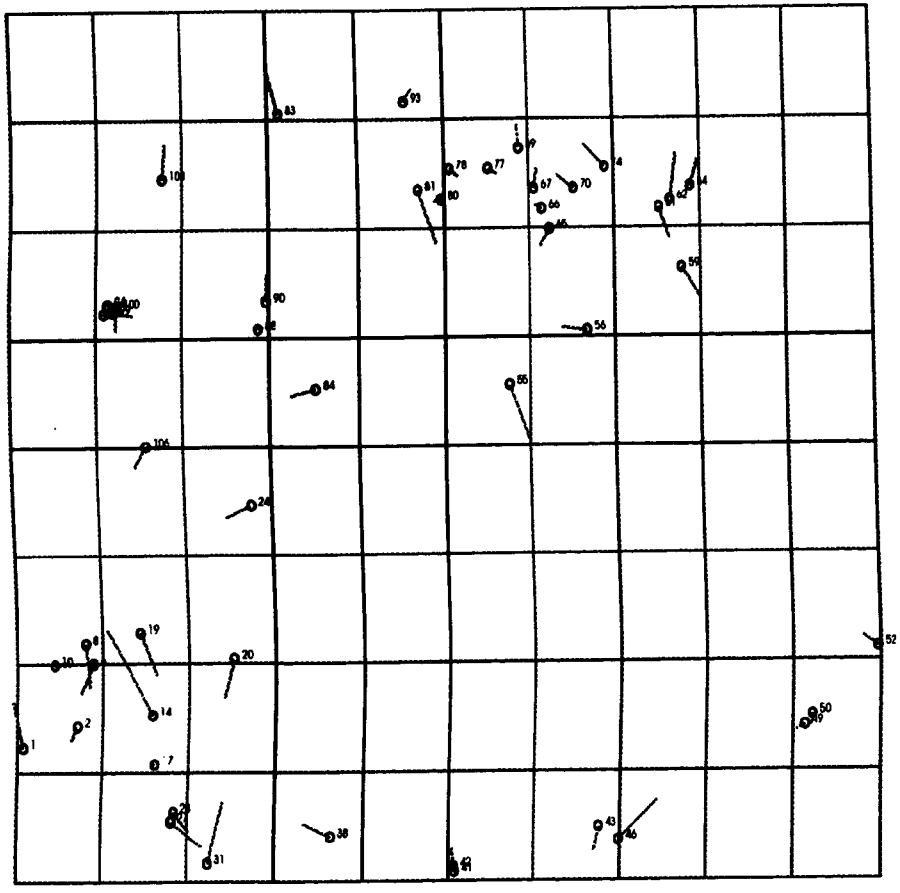

Figure 9.5(a) Vector plot of the X/Y errors at the control points for the Sudanese test field with the MOMS-02 stereo-imagery. (all 49 GCPs considered as control points)

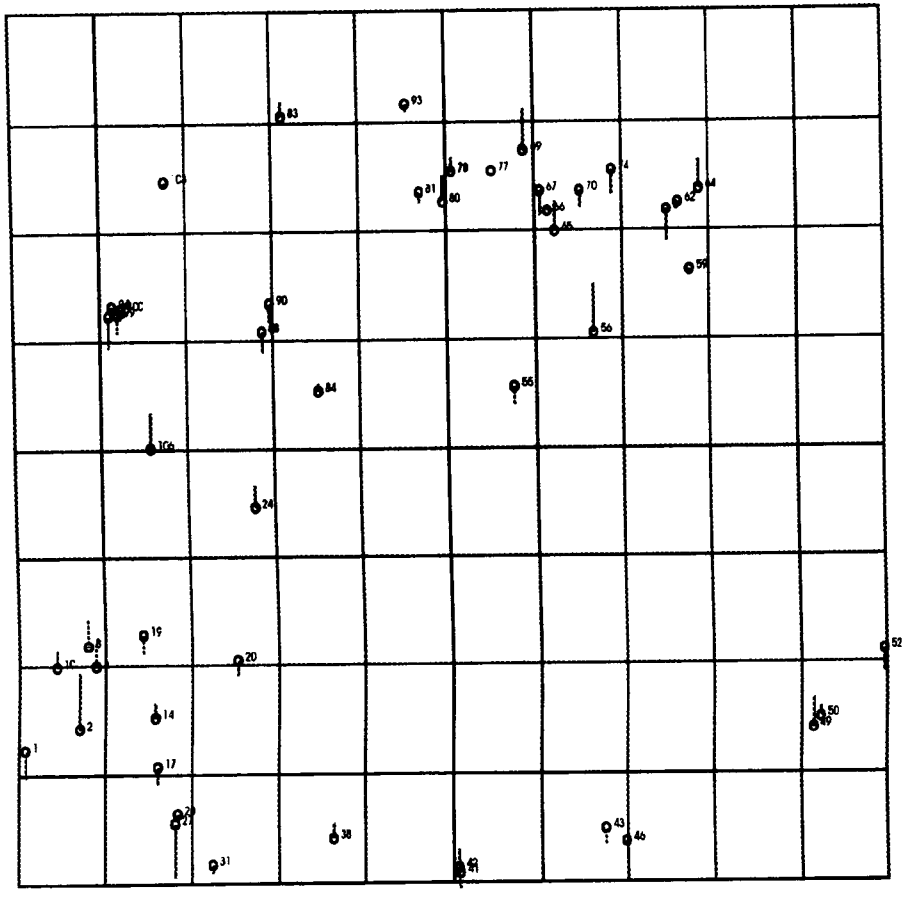

Figure 9.5(b) Vector plot of the Z errors at the control points for the Sudanese test field with MOMS-02 stereo-imagery. (all 49 GCPs considered as control points)

Table 9.10 ΔX, ΔY, ΔZ RMSE values (in metres) of the residual errors in terms of the WGS 1984 coordinate system achieved in the 3D accuracy tests of the Sudanese MOMS-02 image (Set C)

No. of parameters	No. of control points	RMSE at control points			No. of check points	RMSE at check points		
		ΔX (m)	ΔY (m)	ΔZ (m)		ΔX (m)	ΔY (m)	ΔZ (m)
15	10	± 9.24	± 16.94	± 5.75	39	± 15.98	± 24.76	± 23.78
12	10	± 13.25	± 18.73	± 6.44	39	± 16.25	± 26.86	± 23.94
9	10	± 14.72	± 23.02	± 5.76	39	± 15.80	± 27.36	± 24.56

Table 9.11 ΔX, ΔY, ΔZ RMSE values (in metres) of the residual errors in terms of the WGS 1984 coordinate system achieved in the 3D accuracy tests of the Sudanese MOMS-02 image (Set D)

No. of parameters	No. of control points	RMSE at control points			No. of check points	RMSE at check points		
		ΔX (m)	ΔY (m)	ΔZ (m)		ΔX (m)	ΔY (m)	ΔZ (m)
15	8	± 11.22	± 14.52	± 7.13	41	± 14.61	± 26.04	± 21.90
12	8	± 13.86	± 17.42	± 8.07	41	± 15.99	± 24.78	± 21.86
9	8	± 14.61	± 21.98	± 11.27	41	± 16.08	± 26.17	± 21.36

Comparisons of the RMSE values in Table 9.7 with those for the check points in Tables 9.8 to 9.11 do not show up significant discrepancies. Firstly this confirms again that the observations are free of systematic errors, and secondly, it shows the power of the mathematical model used in this type of geometric accuracy test. The vector plots for Set A (Figure 9.6) show that the residual errors at the control points are completely random. For the check points, the residual errors are mostly random with small systematic components in specific areas which again could be the result of not having a good distribution of the GCPs.

As can be seen from these tests, the effect of including the quadratic terms and linear terms of the polynomial transformation used to model the changes in the rotation elements is not very high. In fact, the results point to the inherent stability of the platform and sensor over the period of imaging a single scene. The results also show that the changes in the attitude of the imaging system as a result of the dynamic nature of the pushbroom system are well modelled by the first order polynomial equations used to describe the change of the true anomaly (f) and the right ascension of the ascending node (Ω) with respect to the time period over which the image was acquired. However, it is evident that, in the case of the user requiring maximum accuracy, the full set of exterior orientation parameters (15) have to be used.

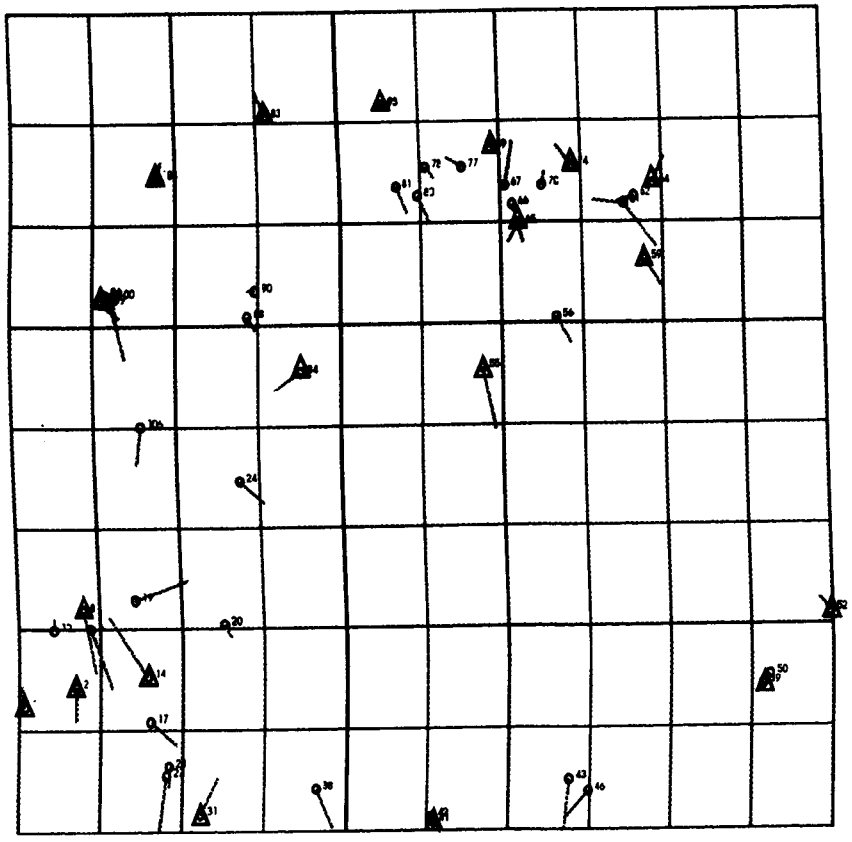

Figure 9.6(a) Vector plot of the X/Y errors at the control and check points for the Sudanese test field with the MOMS-02 stereo-imagery (Set A).
Δ = Control Point ; o = Check Point

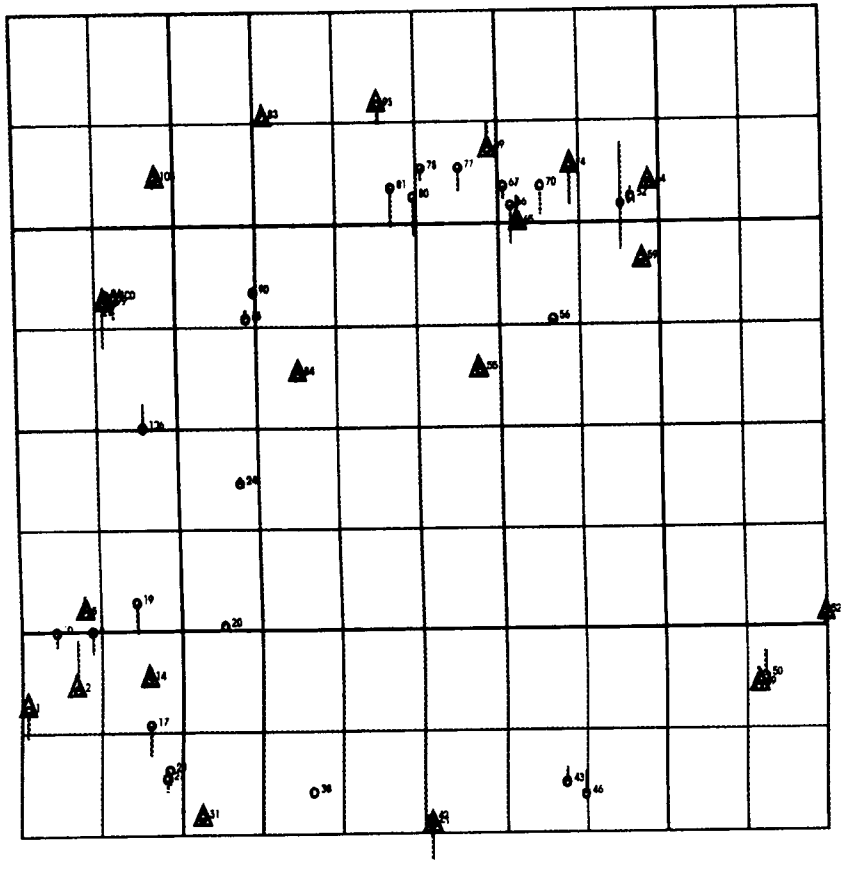

Figure 9.6(b) Vector plot of the Z errors at the control and check points for the Sudanese test field with the MOMS-02 stereo-imagery (Set A).
Δ = Control Point ; o = Check Point

Since the ground control points have been extracted from the 1:100,000 scale maps, the bundle adjustment program in its Case 3 form (resection and intersection) has been implemented with a standard deviation of ± 10m in X, Y, and Z. Since the bundle adjustment program in its Case 3 form is limited by the number of control points used in the test (see Chapter 7), so this Case has only been implemented for Sets B, C, and D. Table 9.12 gives the RMSE values in the X, Y, and Z directions which resulted from using this Case.

Table 9.12 ΔX, ΔY, ΔZ residuals in the WGS 1984 coordinate system for the MOMS-02 imager over Sudan (Case 3 of bundle adjustment program)

Name of the set	No. of control points	RMSE at control points			No. of check points	RMSE at check points		
		ΔX (m)	ΔY (m)	ΔZ (m)		ΔX (m)	ΔY (m)	ΔZ (m)
B	14	± 10.67	± 12.55	± 8.92	35	± 15.63	± 26.48	± 20.66
C	10	± 6.86	± 13.15	± 2.98	39	± 16.72	± 24.24	± 23.57
D	8	± 8.09	± 11.24	± 6.11	41	± 16.45	± 22.86	± 21.31

As can be seen from the results contained in Tables 9.9, 9.10, 9.11 and 9.12, the RMSE values for the three sets of data used in Cases 2 and 3 are approximately the same. Thus although the adjustment lets the points move over a range of ±10m, still the residuals remain the same. Again this shows that the relative positional accuracies of the measured image points are good.

Comparing the results achieved in the case of the 2D and 3D solutions shows only relatively small differences in their respective planimetric accuracy values. The reason for this unusual result is that the area covered by the scene is flat (with only 70m elevation change over a distance of 110km). Thus the effects of relief displacement are very small and can simply be neglected. It shows also how, in such circumstances, a rigorous mathematical model such as the orbital parameter model employed in the bundle adjustment program can be replaced successfully by a simple mathematical model such as that employed in the polynomial adjustment when only planimetry needs to be considered and accuracy requirements are not overly demanding.

While the results of the geometric accuracy tests carried out over the test area in Sudan

were quite acceptable, it was obvious that their main limitations lay in the quality of the ground control points (GCPs) which had been extracted from the 1:100,000 scale topographic maps of the area. In order to test out fully the geometric accuracy of the MOMS-02 imagery and the author's modelling and programs, a test field with more accurate points similar to that available for the Badia area was required. In fact, a similar test field had been set up in Australia and access to the data was kindly provided by Dr C. Fraser of the University of Melbourne. This allowed a further series of tests of the MOMS-02 imagery to be carried out using the author's programs.

9.2 Geometric Accuracy Achieved with MOMS-02 Mode 1 Stereo Imagery over a Test Area in Australia

Using its two stereo modes (modes 1 and 3), the MOMS-02 sensor was able to image parts of Australia twice on two different orbits during its mission. During Orbit 75b, an image strip comprising 9 scenes (numbers 10 to 18) covered a swath of approximately 500km×40km over the Northern Territory and Queensland in the area south west of Mount Isa (see Strip A in Figure 9.7). This strip had been taken in stereo mode 1. The second strip consisted of 9 scenes (numbers 1 to 9) taken in stereo mode 3 and covered a swath of approximately 500km × 80km to the east of Mount Isa (see Strip B in Figure 9.7).

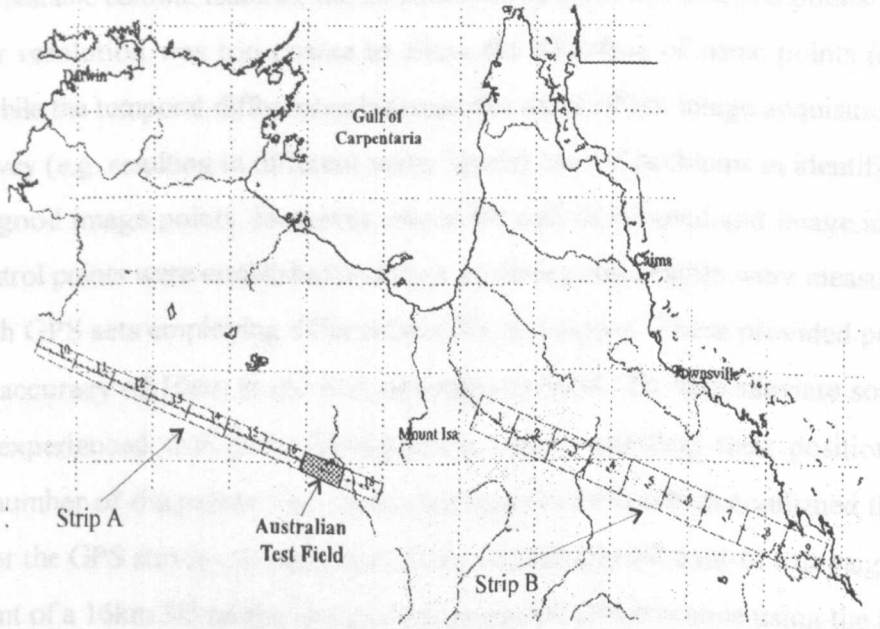

Figure 9.7 Strips A and B of the MOMS-02 coverage over Australia

Through a collaborative arrangement between the Department of Geomatics at the University of Melbourne and the MOMS-02 photogrammetric research teams in Germany, part of the first area covering Scene 17 of Strip A was chosen as an "accuracy testbed" for exterior orientation determination and ground point triangulation (Fraser and Shao, 1996b). This Scene has been also tested for geometric accuracy in both two and three dimensions by the present author using the adjustment programs outlined in Chapter 7. In the next sections, after a review of the ground control point availability for this test area, the results of these tests are described and a comparison is made between the results of the author's tests and those achieved in the tests carried out in Switzerland and Australia.

9.2.1 Ground Control Point Availability in the Australian Test Field area

The Australian test field area covered by Scene 17 of the MOMS-02 imagery comprises a deserted and flat region in the Lake Nash/Georgina River area located in the south east part of the Northern Territory. It has very little vegetation cover and almost no cultural features apart from a few dams, tracks and fences. A GPS survey to provide the test field of ground control points (GCPs) has been carried out by staff from the University of Melbourne in two campaigns in 1994 and 1995. Fraser et al. (1996) reported that considerable problems arose concerning the identification of the ground control points in the images. Due to lack of any other more suitable cultural features, the definition of many of the selected points was poor. The sensor resolution was too coarse to allow the detection of some points (e.g. fence corners), while the temporal differences between the dates of the image acquisition and the ground survey (e.g. resulting in different water levels) caused problems in identifying some otherwise good image points. However, about 80 well distributed and image identifiable ground control points were established and their positions and heights were measured using five Ashtech GPS sets employing differential GPS techniques. These provided points with a nominal accuracy of 10cm in the first campaign in 1994. To help alleviate some of the problems experienced with point identification when measuring their positions on the images, a number of the points were measured again in 1995 which confirmed the quality estimates for the GPS survey. A final phase of the second ground control campaign was the measurement of a 16km 3D profile along an image identifiable fenceline using the kinematic

GPS technique. This heighting profile was established to provide an evaluation of the precision of DTM extraction from the MOMS-02 stereo-pair. Further details of the test field and the GPS control point survey are given in the paper by Fraser et al (1996).

9.2.2 Test Measurements

Two independent sets of image coordinate measurements have been used by the author for the accuracy tests using his polynomial and bundle adjustment programs. One is the set of observations which were obtained by Dr Fraser and his collaborators at the University of Melbourne through purely manual image measurement on an Intergraph Image Station. The second set had been measured quite independently by Dr Baltsavias at ETH Zurich employing stereo-matching with the aid of a much more refined image enhancement and filtering technique and an iterative quality evaluation which discarded the more dubious points.

9.2.2.1 Image Coordinate Measurements at the University of Melbourne

According to Fraser and Shao (1996a), only a limited image enhancement was carried out on the component images and the image coordinates were measured monoscopically, using an Intergraph ImageStation digital photogrammetric workstation. A subset of 60 of the available 80 points were measured with an accuracy of 1 pixel or better. From these points, 40 were estimated to have an accuracy of less than half a pixel. As mentioned before, the main problem encountered was in trying to achieve a satisfactory correspondence between the imagery and the actual conditions present on the ground because of the elapse of more than one year between the image capture and the GPS survey.

The image ccordinate system used at the University of Melbourne is quite different to that which has been used in the author's adjustment program (i.e. image coordinates defined as pixels and lines with respect to the top left corner of the image scene). Therefore a transformation was necessary before using these coordinate values in the program. The image coordinate system used at the University of Melbourne is a common coordinate

system for all three (i.e. forward, nadir, and backward) channels of MOMS-02 image mode 1 with its x coordinate in the direction of the motion of the spacecraft and its y axis in the direction of the lines of the linear arrays. The origin of this system is placed at a point with pixel coordinates in x of line = -624.34 and in y at pixel = 1,713.5 with respect to the top left corner of the forward scene (see Figure 9.8).

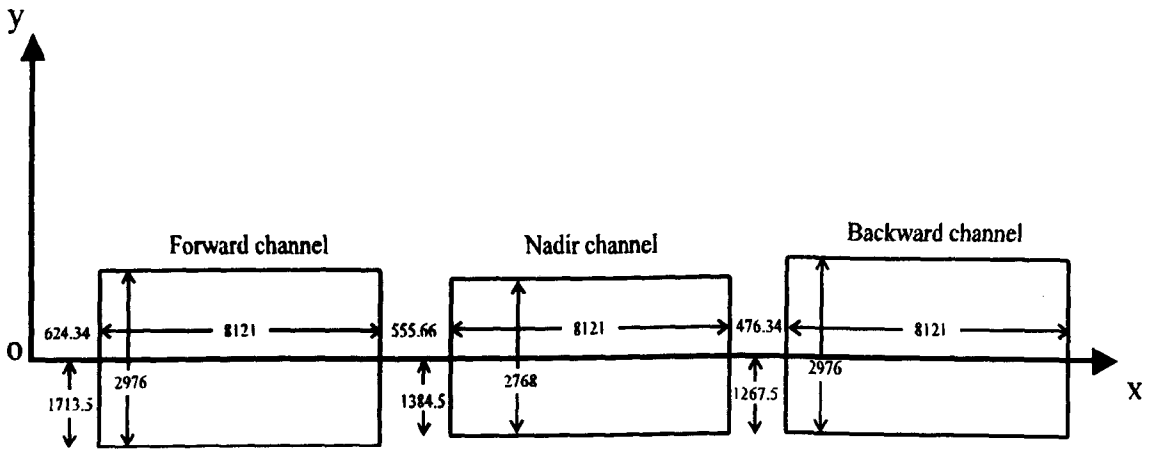

Figure 9.8 University of Melbourne image coordinate system

(N.B. the numerical values are given in pixels)

Regarding the line counts given in the line header information, there is an offset between Channels 6 (forward) and 5 (nadir) and also between Channels 5 (nadir) and 7 (backward) which results in two gaps of 555.66 and 476.34 pixels respectively between these channel images. It should be noted that, in this coordinate system, regarding the position of the active window within the CCD linear array, the x axis passes through pixel numbers 1,713.5 in the forward scene; 1,384.5 in the nadir scene and 1,267.5 in the backward scene.

By contrast, the image coordinate system that has been used by the present author for input of the image data into his adjustment program, is considered independently for the image produced by each channel. In each case, its origin lies in the top left corner of the image, its x axis in the direction of the motion of the spacecraft, and its y axis in the direction of the individual lines. To transform the image coordinates supplied by the University of Melbourne to the author's image coordinate system, the following formulae have been used:

(i) In the case of the forward channel:

$$x_{Glasgow} = x_{Melbourne} - 624,34$$

$$y_{Glasgow} = y_{Melbourne} + 1,713.5$$

(ii) In the case of the nadir channel:

$$x_{Glasgow} = x_{Melbourne} - 9301$$

$$y_{Glasgow} = y_{Melbourne} + 1,384.5$$

(iii) In the case of the backward channel:

$$x_{Glasgow} = x_{Melbourne} - 17,898.34$$

$$y_{Glasgow} = y_{Melbourne} + 1,267.5$$

9.2.2.2 Image Coordinate Measurements at ETH Zurich

Baltsavias and Stallmann (1996) reported the same difficulties as those reported by Fraser regarding the identification of the points on the images. In this case, the image coordinates were refined by making several preliminary runs of Kratky's program, which had been modified for use in the bundle adjustment, and by removing or correcting some of the control points through analysis of the residual errors produced by the program. Also use was made of the Wallis filter which helps in the identification of the points on the image. This procedure was performed for both the forward and backward channel images. In addition, the manual measurements made on the forward image were used as reference points and transferred to the backward image by least squares image matching. Altogether the ETH group spent a great deal of time refining the data that was used in their test. However, since the image coordinate system used by the ETH group was the same as that used in author's program, these data could be used directly without need for a preliminary transformation in the adjustment program.

In the first part of the next Section, the results achieved by the author with the MOMS-02 image data for the Australian test field are discussed using the ETH image coordinate measurements only in conjunction with the 2D polynomial adjustment program. Then, in the second part, the results of the geometric accuracy test using the 3D bundle adjustment program with both the Melbourne and the ETH image coordinate measurements will be given and analysed.

9.2.3 Two-Dimensional (Planimetric) Accuracy Test

The polynomial adjustment program described in Chapter 7 has been used to carry out various tests on the ETH data set. Again, as in the case of the 2D test carried out on the MOMS-02 image of the Sudanese test field, five different sets of data have been considered. First all 51 measured image points of the ETH data set have been used as control points. The results of this test and the effects of each of the successive terms in the polynomial are given in Table 9.13.

Table 9.13 Results (in metres) of the RMSE values achieved in the 2D (planimetric) accuracy tests of the Australian MOMS-02 image using all 51 ground control points of the ETH data set

Polynomial Transformation	ΔE (m)	ΔN (m)	Δpl (m)
3 terms (affine)	± 17.45	± 12.69	± 21.58
4 terms (xy)	± 16.58	± 12.11	± 20.53
5 terms (x^2)	± 11.93	± 11.64	± 16.67
6 terms (y^2)	± 10.70	± 9.36	± 14.22
7 terms (x^2y)	± 9.13	± 9.27	± 13.01
8 terms (xy^2)	± 9.13	± 8.75	± 12.64
9 terms (x^2y^2)	± 9.12	± 8.55	± 12.50
10 terms (x^3)	± 8.91	± 8.27	± 12.16
11 terms (y^3)	± 8.90	± 8.20	± 12.10
12 terms (xy^3)	± 8.89	± 8.20	± 12.09
13 terms (x^3y)	± 8.84	± 8.20	± 12.06
14 terms (x^2y^3)	± 8.82	± 8.17	± 12.02
15 terms (x^3y^2)	± 8.36	± 8.14	± 11.67
16 terms (x^3y^3)	± 8.36	± 8.00	± 11.57
17 terms (x^4)	± 8.36	± 7.76	± 11.41
18 terms (y^4)	± 8.35	± 7.71	± 11.36
19 terms (x^4y)	± 8.31	± 7.60	± 11.26
20 terms (xy^4)	± 8.31	± 7.53	± 11.21
21 terms (x^4y^2)	± 8.03	± 7.31	± 10.86
22 terms (x^2y^4)	± 7.80	± 7.30	± 10.68
23 terms (x^4y^3)	± 7.46	± 7.14	± 10.33
24 terms (x^3y^4)	± 6.57	± 6.93	± 9.55
25 terms (x^4y^4)	± 6.30	± 6.82	± 9.28

As can be seen from this Table, the significant improvements in fit occured with the use of the 5th term (i.e. x^2) of the polynomial transformation, with improvements of nearly 4m in the vector (Δpl) error value, mainly resulting from the improvement in the ΔE error value. With the other terms, there is a continuous improvement got by simply increasing the number of terms used in the polynomial adjustment. The vector plots (Figure 9.9(a)) show that the errors at the control points are random, i.e. the final results are not affected by systematic errors.

The other four 2D tests have been carried out using different combinations of control and check points in the images as follows: Set A with 18 control points and 33 check points; Set B with 12 control points and 39 check points; Set C with 9 control points and 42 check points; and Set D with 8 control points and 43 check points. Tables 9.14 to 9.17 give the results of these tests as well as the effects of each of the different terms used in the polynomial adjustment program. Note that the number of terms which could be used in polynomial adjustment is limited by the number of control points.

Table 9.14 ΔE, ΔN RMSE values (in metres) of the residual errors achieved in the 2D (planimetric) accuracy tests in terms of UTM coordinates for the ETH data (Set A)

Polynomial Transformation	Control points (n=18)			Check points (n = 33)		
	ΔE (m)	ΔN (m)	Δpl (m)	ΔE (m)	ΔN (m)	Δpl (m)
3 terms (affine)	± 17.78	± 11.98	± 21.44	± 20.00	± 14.67	± 24.80
4 terms (xy)	± 17.04	± 10.94	± 20.25	± 19.17	± 14.24	± 23.88
5 terms (x^2)	± 11.28	± 10.64	± 15.51	± 13.45	± 13.79	± 19.26
6 terms (y^2)	± 8.84	± 5.63	± 10.48	± 12.47	± 11.88	± 17.22
7 terms (x^2y)	± 6.63	± 5.63	± 8.70	± 10.91	± 11.88	± 16.13
8 terms (xy^2)	± 6.31	± 3.58	± 7.25	± 11.30	± 11.72	± 16.28
9 terms (x^2y^2)	± 6.30	± 2.40	± 6.74	± 11.31	± 11.85	± 16.38
10 terms (x^3)	± 5.37	± 2.37	± 5.87	± 11.60	± 12.01	± 16.70
11 terms (y^3)	± 4.90	± 2.36	± 5.44	± 11.49	± 12.11	± 16.69
12 terms (xy^3)	± 4.73	± 2.29	± 5.26	± 11.99	± 11.94	± 16.92
13 terms (x^3y)	± 4.62	± 2.29	± 5.16	± 12.48	± 11.93	± 17.26
14 terms (x^2y^3)	± 4.56	± 1.60	± 4.83	± 12.71	± 11.63	± 17.22
15 terms (x^3y^2)	± 3.53	± 0.90	± 3.64	± 15.42	± 12.30	± 19.72
16 terms (x^3y^3)	± 3.47	± 0.15	± 3.47	± 15.80	± 12.34	± 20.05
17 terms (x^4)	± 2.02	± 0.15	± 2.02	± 18.41	± 12.34	± 22.16
18 terms (y^4)	≈0.0	≈0.0	≈0.0	± 85.88	± 14.83	± 87.15

Figure 9.9(a) Vector plot of the planimetric errors at control points for Australian test field with ETH data. (all 51 GCPs used as control points)

Figure 9.9(b) Vector plot of the planimetric errors at control points and check points for Australian test field with ETH data set (Set A). Δ = Control point ; o = Check point

Table 9.15 ΔE, ΔN RMSE values (in metres) of the residual errors achieved in terms of the UTM coordinates for the ETH data (Set B)

Polynomial Transformation	Control points (n=12)			Check points (n = 39)		
	ΔE (m)	ΔN (m)	Δpl (m)	ΔE (m)	ΔN (m)	Δpl (m)
3 terms (affine)	± 18.78	± 12.34	± 22.47	± 22.86	± 14.09	± 26.85
4 terms (xy)	± 18.12	± 11.89	± 21.67	± 21.88	± 13.81	± 25.87
5 terms (x^2)	± 9.26	± 11.65	± 14.88	± 14.58	± 13.16	± 19.64
6 terms (y^2)	± 8.06	± 5.06	± 9.52	± 12.83	± 11.75	± 17.40
7 terms (x^2y)	± 6.94	± 5.01	± 8.56	± 10.84	± 11.64	± 15.90
8 terms (xy^2)	± 6.42	± 2.04	± 6.74	± 11.27	± 11.36	± 16.00
9 terms (x^2y^2)	± 5.87	± 1.40	± 6.03	± 11.58	± 11.29	± 16.17
10 terms (x^3)	± 5.16	± 0.46	± 5.18	± 11.40	± 11.85	± 16.25
11 terms (y^3)	± 2.22	± 0.46	± 2.27	± 21.19	± 11.82	± 24.26
12 terms (xy^3)	≈0.0	≈0.0	≈0.0	± 25.56	± 12.23	± 28.34

Table 9.16 ΔE, ΔN RMSE values (in metres) of the residual errors achieved in terms of the UTM coordinates for the ETH data (Set C)

Polynomial Transformation	Control points (n=9)			Check points (n = 42)		
	ΔE (m)	ΔN (m)	Δpl (m)	ΔE (m)	ΔN (m)	Δpl (m)
3 terms (affine)	± 14.04	± 13.56	± 19.52	± 29.03	± 13.74	± 32.12
4 terms (xy)	± 13.29	± 13.27	± 18.78	± 28.42	± 13.27	± 31.36
5 terms (x^2)	± 6.91	± 13.24	± 14.93	± 17.43	± 13.19	± 21.86
6 terms (y^2)	± 4.90	± 4.80	± 6.86	± 15.17	± 12.42	± 19.60
7 terms (x^2y)	± 4.39	± 4.11	± 6.01	± 18.22	± 13.23	± 22.52
8 terms (xy^2)	± 1.71	± 0.30	± 1.74	± 18.43	± 11.16	± 21.54
9 terms (x^2y^2)	≈0.0	≈0.0	≈0.0	± 21.24	± 11.35	± 24.08

Table 9.17 ΔE, ΔN RMSE values (in metres) of the residual errors achieved in terms of the UTM coordinates for the ETH data (Set D)

Polynomial Transformation	Control points (n=8)			Check points (n = 43)		
	ΔE (m)	ΔN (m)	Δpl (m)	ΔE (m)	ΔN (m)	Δpl (m)
3 terms (affine)	± 14.08	± 14.48	± 20.20	± 27.92	± 13.52	± 31.02
4 terms (xy)	± 13.58	± 14.19	± 19.64	± 27.39	± 13.42	± 30.50
5 terms (x^2)	± 6.78	± 14.16	± 15.70	± 16.71	± 13.06	± 21.21
6 terms (y^2)	± 2.26	± 3.34	± 4.03	± 13.89	± 12.96	± 19.00
7 terms (x^2y)	± 2.26	± 3.24	± 3.95	± 13.87	± 12.77	± 18.85
8 terms (xy^2)	≈0.0	≈0.0	≈0.0	± 15.57	± 10.97	± 19.05

As can be seen from these Tables, with an increase in the number of terms used in the polynomial transformation, first of all, the residual errors in the check points improve (i.e. they grow smaller). There is generally a significant improvement when implementing the second order terms x^2 and y^2, as was the case with the MOMS-02 image tested over the Sudanese test field. After that, the residual errors show a nearly constant improvement before finally starting to become large. As mentioned before in this Chapter, the reason for this is the decrease in the degrees of freedom and the lack of enough redundancy in the control points. Graphical analysis of the individual residual errors in the control points and check points for Set A (see Figure 9.9(b)) shows that these residual errors are random and the final results are not burdened or affected by systematic errors.

It is interesting to note the improvement in the results achieved in this 2D accuracy test of the MOMS-02 image over the Australian test field with those achieved in the MOMS-02 image tested over the Sudanese testfield. For example, taking the roughly comparable Set A in each case, the Δpl values at the check points are between 8 and 10m better in the Australian case. The most obvious source for this marked improvement would appear to be the much better ground control point values provided through the use of GPS.

9.2.4 Three-Dimensional Accuracy Test

The bundle adjustment program outlined in Chapter 7 has also been employed to test the geometric accuracy of the MOMS-02 stereo-imagery over the Australian test field using both the image coordinate set measured at the University of Melbourne as well as that measured at ETH. For the ETH data, the same four sets of control and check points (Sets A, B, C, and D) have been used in the test as were used with the polynomial adjustment. In the case of the Melbourne data, different sets of data have been considered and various tests have been carried out decreasing the number of exterior orientation parameters from 15 to 9, as was done in the 3D test with the MOMS-02 data over the Sudanese test field.

In the next Section, first the results of the bundle adjustment program using the Melbourne image data set are presented and then, in the second part, the results using ETH's image

data set are given and discussed.

9.2.4.1 3D Accuracy Test Using the University of Melbourne Data Set

For the three-dimensional accuracy test of MOMS-02 imagery over the Australian test field, only the forward and backward channels have been used. Five sets of data were run in the adjustment program. First the whole set of GCPs were used as control points to give an overview of the existence of systematic errors in the data. Then four other sets, each with a different distribution and number of control points and check points, were used. From the 49 ground control points which were available and could be used in the program, Set A comprises 18 control points and 31 check points; Set B has 14 control points and 35 check points; Set C comprises 12 control points and 37 check points; and finally Set D has 10 control points and 39 check points.

Since the stated accuracy of the ground control points measured by the GPS survey is extremely high (10cm), the coordinates of the ground control points have been considered as fixed, so only Case 2 of the bundle adjustment program has been used. The results of the adjustment program for the various situations when, first of all, the whole set of GCPs were used as control points and then, later, the other four sets of GCPs (A, B, C, and D) with different numbers of control and check points and exterior orientation parameters are given in Tables 9.18 to 9.22.

Table 9.18 ΔX, ΔY, ΔZ RMSE values (in metres) of the residual errors in terms of WGS 1984 coordinate system achieved in the 3D accuracy tests of the Melbourne data set using all 49 ground control points

No. of parameters	RMSE at control points		
	ΔX (m)	ΔY (m)	ΔZ (m)
15	± 8.47	± 9.18	± 9.55
12	± 8.84	± 9.75	± 10.00
9	± 17.37	± 11.43	± 11.67

The results of the bundle adjustment using all of the GCPs as control points (Table 9.18) show a reasonable accuracy having regard to the source and the quality of the control point

coordinates derived from Differential GPS measurements and the difficulties which have been reported in identifying and measuring the control points on the images.

The vector diagrams constructed from the ΔX, ΔY and ΔZ values are included as Figures 9.10 (a,b). These diagrams show that the residual errors at the individual control points and independent check points are random and no systematic component can be discovered in the vector plots.

Table 9.19 ΔX, ΔY, ΔZ RMSE values (in metres) of residual errors in terms of the WGS 1984 coordinate system achieved in the 3D accuracy tests of the Melbourne data set (Set A)

No. of parameters	No. of control points	RMSE at control points			No. of check points	RMSE at check points		
		ΔX (m)	ΔY (m)	ΔZ (m)		ΔX (m)	ΔY (m)	ΔZ (m)
15	18	± 11.41	± 10.61	± 11.65	31	± 8.00	± 10.57	± 9.66
12	18	± 11.93	± 11.19	± 12.50	31	± 8.41	± 11.13	± 9.91
9	18	± 23.10	± 15.89	± 14.54	31	± 15.45	± 8.89	± 10.98

Table 9.20 ΔX, ΔY, ΔZ RMSE values (in metres) of residual errors in terms of the WGS 1984 coordinate system achieved in the 3D accuracy tests of the Melbourne data set (Set B)

No. of parameters	No. of control points	RMSE at control points			No. of check points	RMSE at check points		
		ΔX (m)	ΔY (m)	ΔZ (m)		ΔX (m)	ΔY (m)	ΔZ (m)
15	14	± 12.36	± 10.03	± 11.57	35	± 8.33	± 12.44	± 10.68
12	14	± 12.92	± 10.70	± 12.15	35	± 9.47	± 13.01	± 10.82
9	14	± 22.62	± 14.08	± 16.10	35	± 20.01	± 12.91	± 11.19

Table 9.21 ΔX, ΔY, ΔZ RMSE values (in metres) of residual errors in terms of the WGS 1984 coordinate system achieved in the 3D accuracy tests of the Melbourne data set (Set C)

No. of parameters	No. of control points	RMSE at control points			No. of check points	RMSE at check points		
		ΔX (m)	ΔY (m)	ΔZ (m)		ΔX (m)	ΔY (m)	ΔZ (m)
15	12	± 13.28	± 10.54	± 12.17	37	± 8.18	± 11.82	± 10.46
12	12	± 13.69	± 11.55	± 13.04	37	± 9.00	± 12.86	± 10.45
9	12	± 23.46	± 15.03	± 16.96	37	± 20.29	± 12.23	± 11.19

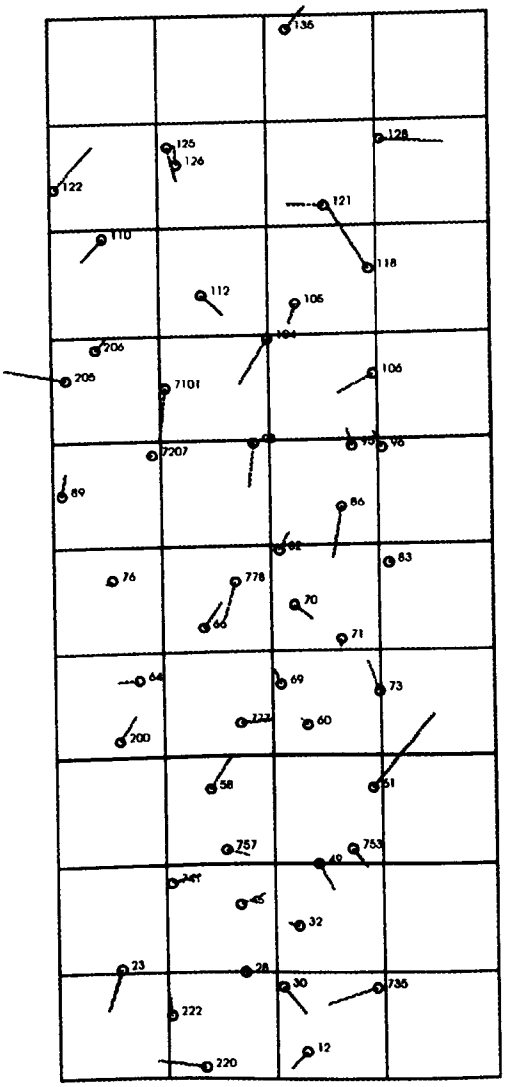

Figure 9.10 (a) Vector plot of the X/Y errors at the control points using the Melbourne data set. (all 49 GCPs considered as control points)

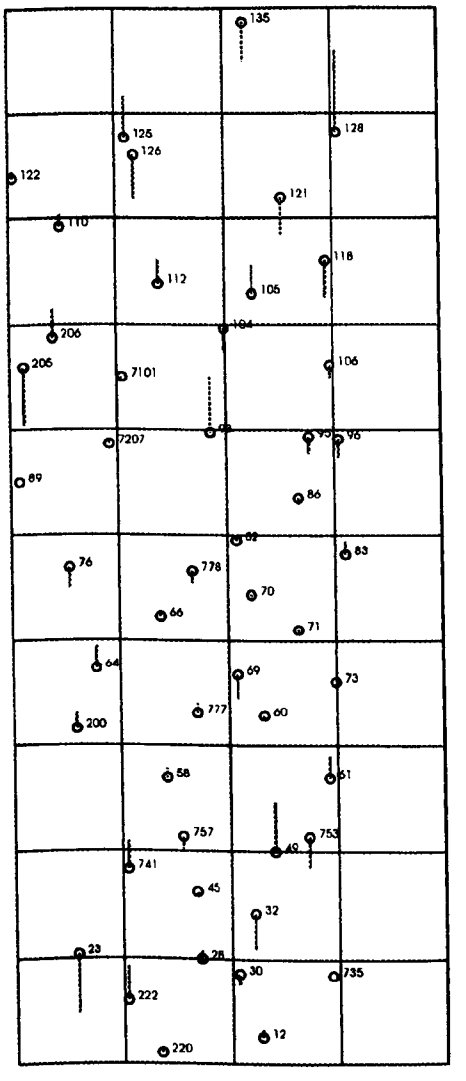

Figure 9.10 (b) Vector plot of the Z errors at the control points using the Melbourne data set. (all 49 GCPs considered as control points)

Table 9.22 ΔX, ΔY, ΔZ RMSE values (in metres) of residual errors in terms of the WGS 1984 coordinate system achieved in the 3D accuracy tests of the Melbourne data set (Set D)

No. of parameters	No. of control points	RMSE at control points			No. of check points	RMSE at check points		
		ΔX (m)	ΔY (m)	ΔZ (m)		ΔX (m)	ΔY (m)	ΔZ (m)
15	10	± 10.90	± 8.96	± 13.20	39	± 12.81	± 10.99	± 10.40
12	10	± 11.83	± 11.00	± 14.40	39	± 11.67	± 12.22	± 9.94
9	10	± 25.49	± 12.50	± 18.55	39	± 20.14	± 12.64	± 11.51

A comparison of the RMSE values for the control points only that are given in Table 9.18 with those for the check points given in Tables 9.19 to 9.22 does not show significant discrepancies. This shows that the observations are free from systematic errors, and that the accuracy of the mathematical model used to represent the MOMS-02 stereo-imagery in this research is quite sound.

The vector plots for Set A (Figure 9.11) show that the residual errors at both the control points and the independent check points are quite random which means that the final results are not affected by systematic errors.

As can be seen from these tests, the effect of employing the quadratic terms of the polynomial is small compared to that of the linear terms of the polynomial which is high. A reason could be the existence of some poorer points compared to the others. In which case, more exterior orientation parameters are needed to fit these poorer points with respect to the other points.

The results of the experimental tests carried out at the University of Melbourne when implementing three-fold stereo imagery (Channels 5, 6, and 7) are given in Table 9.23. As mentioned before, the mathematical modelling that has been used by the University of Melbourne group to evaluate the MOMS-02 stereo-imagery is based on that given by Ebner et al. (1992) [see also Fraser and Shao (1996b)].

In Table 9.23, the term OI means the number of orientation image lines which have been used in the Lagrange polynomial and implemented in the Melbourne bundle adjustment program (see Chapter 6).

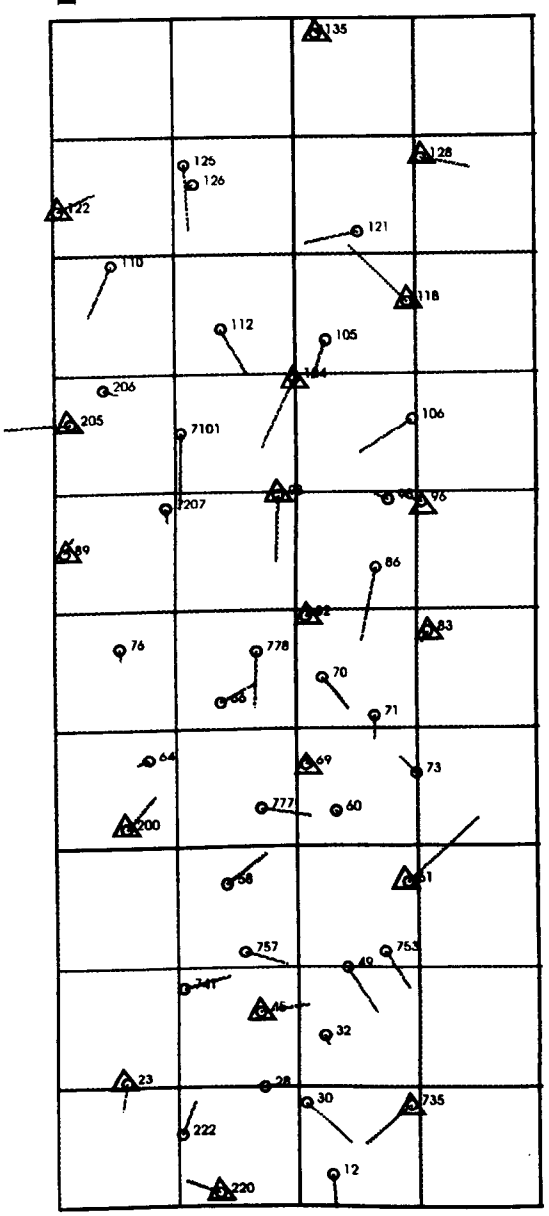

Figure 9.11(a) Vector plot of the X/Y errors at the control and check points using Melbourne data set (Set A). Δ = Control point ; o = Check point

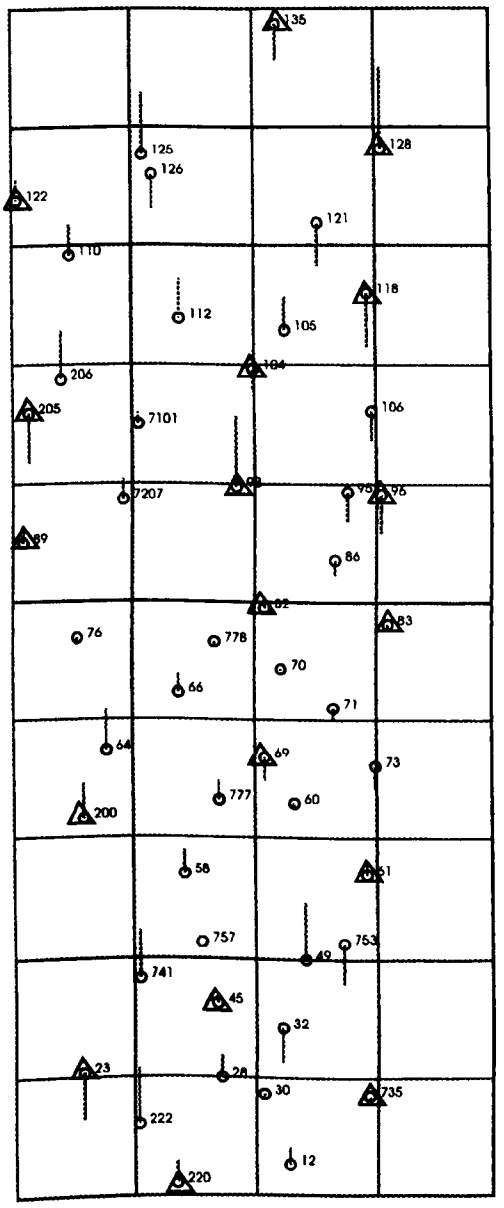

Figure 9.11(b) Vector plot of the Z errors at the control and check points using Melbourne data set (Set A). Δ = Control Point ; o = Check Point

Table 9.23 ΔX, ΔY, ΔZ RMSE values (in metres) of the residual errors at the check points achieved in the 3D accuracy tests of the Melbourne data using the University of Melbourne bundle adjustment program (Fraser and Shao, 1996a)

OI No.	Control point configuration (No. of control / check points)																	
	Set 1 (4/52)			Set 2 (12/44)			Set 3 (12/44)			Set 4 (20/36)			Set 5 (20/36)			free-net (56/0)		
	ΔX	ΔY	ΔZ	ΔX	ΔY	ΔZ	ΔX	ΔY	ΔZ	ΔX	ΔY	ΔZ	ΔX	ΔY	ΔZ	ΔX	ΔY	ΔZ
8	±10.9	±10.1	± 8.4	±10.7	±10.4	±7.7	± 9.4	± 9.7	± 9.8	± 9.8	± 9.4	± 9.1	± 8.3	± 8.6	±10.8	± 4.7	± 4.6	± 1.1
6	±12.9	±13.7	±10.6	±12.1	±12.5	± 9.7	±10.3	±11.1	±13.0	±10.7	±10.4	± 9.9	± 9.6	± 8.9	±13.7	± 5.6	± 5.7	± 1.5
4	±11.3	±10.1	± 9.5	±11.7	± 9.2	± 8.8	±10.4	± 9.7	± 9.4	±10.5	± 9.3	± 9.5	± 9.5	± 8.2	± 9.1	± 5.5	± 4.9	± 1.2

As can be seen from Tables 9.19 and 9.22, the RMSE values are nearly the same when 15 exterior orientation parameters and 18 control points have been used in the author's bundle adjustment program and when 8 OIs and 20 control points were used in the case of the Melbourne bundle adjustment program. The slightly better results achieved with the Melbourne bundle adjustment program could be a result of using the high resolution nadir channel 5 (4.5m pixel size) in the solution.

One thing which should be noted in Table 9.23 is that large discrepancies exist between the free-net case in which all GCPs used as control and the other five sets of data. Fraser and Shao, (1996a) give two reasons for this occurance: firstly, they are most probably due to errors in identification; and secondly, a slight degree of overparameterization or weakness in the fidelity of the mathematical model could be a reason for this problem.

Since the results of the bundle adjustment program used in this present research in the case of using all of the GCPs as control points (Table 9.18) and when using using the other four sets of data (Tables 9.19 to 9.22) do not show this type of discrepancy, some comment is required. In the opinion of the present author, the problem in the University of Melbourne bundle adjustment program may well arise from a weakness in the mathematical model used to describe the geometry of along-track linear array images such as those produced by MOMS-02.

9.2.4.2 3D Accuracy Test Using the ETH Data

The whole set of GCPs used as control points and the same four ETH data sets which had been used in the 2D test have been used again here. As was the case with the University of Melbourne data set, given the quality of the GPS coordinates, only Case 2 of the bundle adjustment program has been used for the test. The results of the adjustment program for the case in which all 51 GCPs are used as control points and the other four sets (A, B, C, and D) of GCPs with different numbers of exterior orientation parameters are given in Tables 9.24 to 9.28.

Table 9.24 ΔX, ΔY, ΔZ RMSE values of the residual errors in terms of the WGS 1984 coordinate system achieved in the 3D accuracy tests of the ETH data using all 51 ground control points

No. of parameters	RMSE at control points		
	ΔX (m)	ΔY (m)	ΔZ (m)
15	± 5.03	± 5.51	± 6.47
12	± 6.94	± 6.97	± 6.63
9	± 14.09	± 8.31	± 9.84

Table 9.24 shows that the results from the bundle adjustment program using all of the GCPs as control points are very good. The output of the bundle adjustment program showed an accuracy of 0.3 pixel in the x and y values of the image coordinates for both the left and right images. This shows that the images of the control points have been measured with a very high accuracy. The vector plots (Figure 9.12) show that the residual errors in the control points are random and free of systematic errors both in extent and direction.

Table 9.25 ΔX, ΔY, ΔZ RMSE values (in metres) of the residual errors in terms of the WGS 1984 coordinate system achieved in the 3D accuracy tests of the ETH data set (Set A)

No. of parameters	No. of control points	RMSE at control points			No. of check points	RMSE at check points		
		ΔX (m)	ΔY (m)	ΔZ (m)		ΔX (m)	ΔY (m)	ΔZ (m)
15	18	± 5.18	± 5.21	± 6.35	33	± 5.51	± 5.84	± 7.01
12	18	± 8.07	± 7.91	± 5.94	33	± 8.24	± 6.68	± 7.79
9	18	± 16.45	± 10.14	± 9.73	33	± 14.77	± 7.46	± 10.39

Figure 9.12(a) Vector plot of X/Y errors at the control points using ETH data set. (all 51 GCPs considered as control)

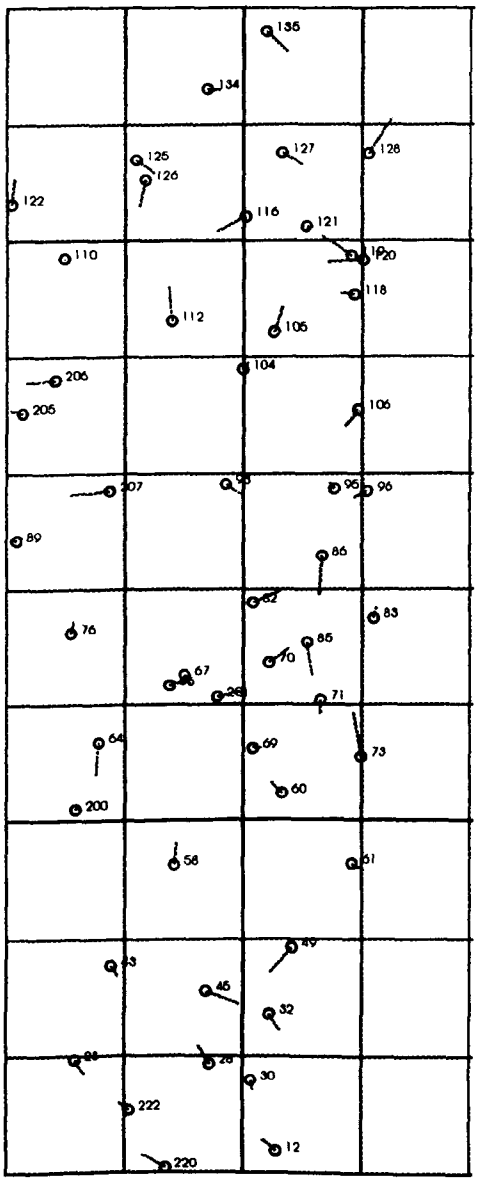

Figure 9.12(b) Vector plot of Z errors at the control points using ETH data set. (all 51 GCPs considered as control)

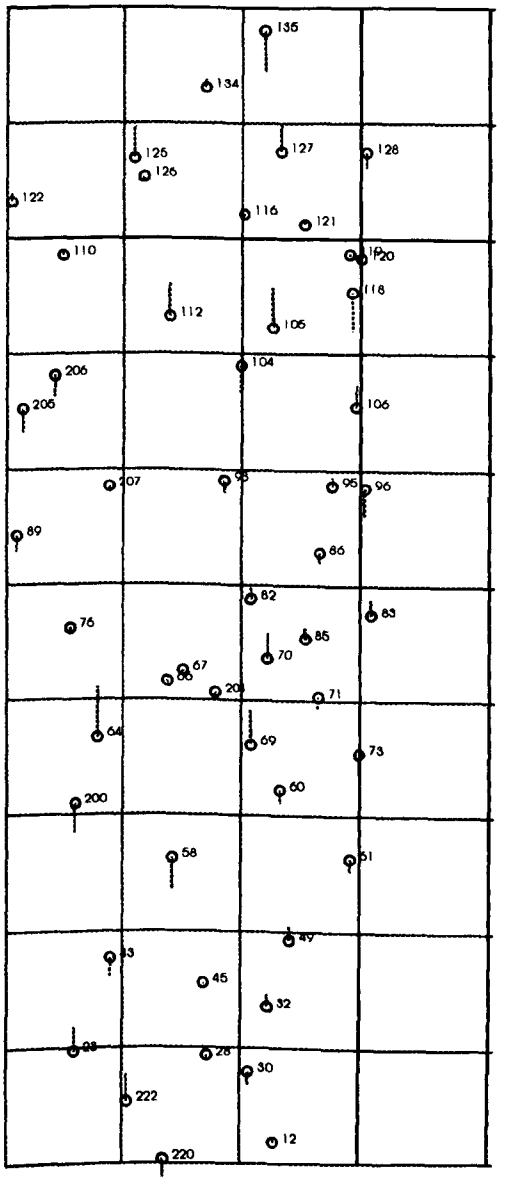

Table 9.26 ΔX, ΔY, ΔZ RMSE values (in metres) of the residual errors in terms of the WGS 1984 coordinate system achieved in the 3D accuracy tests of the ETH data set (Set B)

No. of parameters	No. of control points	RMSE at control points			No. of check points	RMSE at check points		
		ΔX (m)	ΔY (m)	ΔZ (m)		ΔX (m)	ΔY (m)	ΔZ (m)
15	12	± 5.00	± 5.67	± 5.16	39	± 5.92	± 6.27	± 8.36
12	12	± 8.53	± 7.47	± 5.94	39	± 9.99	± 8.10	± 8.57
9	12	± 16.83	± 8.78	± 8.62	39	± 17.90	± 9.04	± 11.31

Table 9.27 ΔX, ΔY, ΔZ RMSE values (in metres) of the residual errors in terms of the WGS 1984 coordinate system achieved in the 3D accuracy tests of the ETH data set (Set C)

No. of parameters	No. of control points	RMSE at control points			No. of check points	RMSE at check points		
		ΔX (m)	ΔY (m)	ΔZ (m)		ΔX (m)	ΔY (m)	ΔZ (m)
15	9	± 2.78	± 5.96	± 4.59	42	± 8.24	± 6.89	± 7.52
12	9	± 6.87	± 6.78	± 6.47	42	± 14.08	± 9.82	± 8.46
9	9	± 14.62	± 8.19	± 8.94	42	± 22.77	± 10.48	± 11.11

Table 9.28 ΔX, ΔY, ΔZ RMSE values (in metres) of the residual errors in terms of the WGS 1984 coordinate system achieved in the 3D accuracy tests of the ETH data set (Set D)

No. of parameters	No. of control points	RMSE at control points			No. of check points	RMSE at check points		
		ΔX (m)	ΔY (m)	ΔZ (m)		ΔX (m)	ΔY (m)	ΔZ (m)
15	8	± 1.38	± 6.14	± 4.56	43	± 7.06	± 7.58	± 7.73
12	8	± 6.93	± 6.34	± 6.87	43	± 13.63	± 10.98	± 8.54
9	8	± 14.79	± 7.42	± 9.21	43	± 22.28	± 12.15	± 11.40

A comparison of the RMSE values in Table 9.24 with those for the check points in Tables 9.25 to 9.28 shows only very small differences in all three dimensions. This confirms again the power of the mathematical model used in this research for the modelling of the MOMS-02 imagery. It shows also that the observations are free from systematic errors.

The vector plots for Set A (Figure 9.13) show that the residual errors at both the control points and the check points are random which means the final results are not affected by systematic errors.

Figure 9.13(a) Vector plot of the X/Y errors at the control points and check points using ETH data set (Set A). Δ = Control Point ; o = Check Point

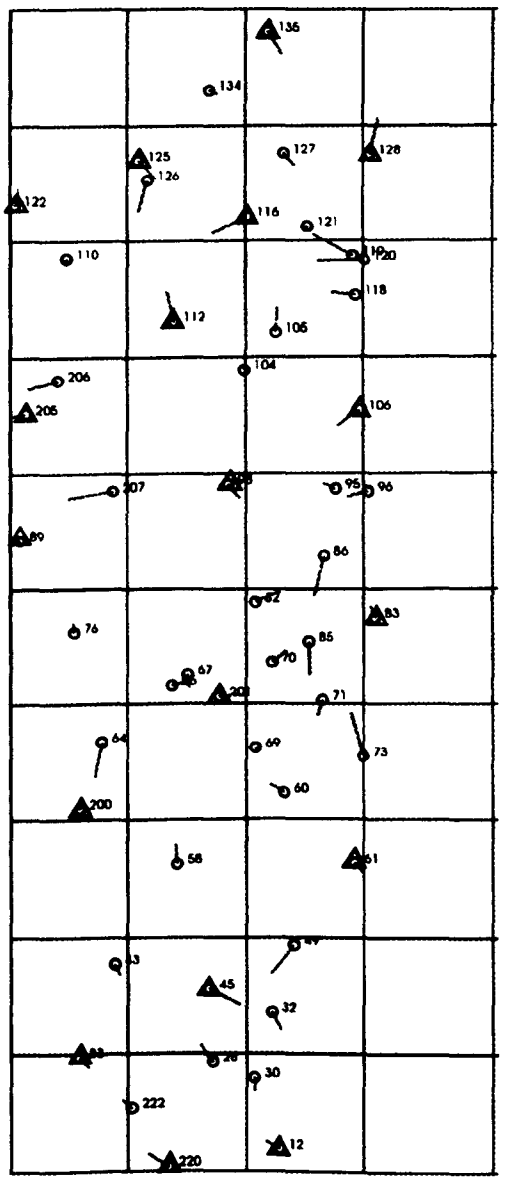

Figure 9.13(b) Vector plot of the Z errors at the control points and check points using ETH data set (Set A). Δ = Control Point ; o = Check Point

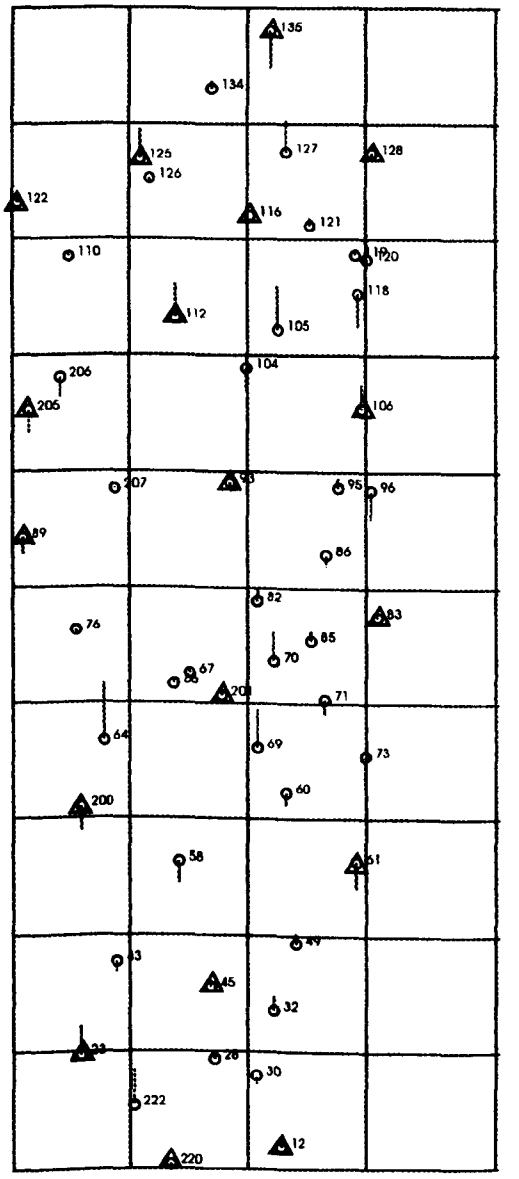

As can be seen from these tests, the effect of the quadratic terms of the polynomial is about 3 to 6 metres and that of the linear terms varies from 6 to 9 metres, and depends on the number of control points used in the adjustment. What is also quite sriking from an inspection of Tables 9.25 to 9.28 is that the elimination of the linear terms leads to a doubling of the RMSE values in the X direction for both the control and the check points. It is difficult for someone who is not in the Melbourne and ETH groups to offer an explanation for such an unusual event. Thus to get a good geometric accuracy in this case, it is necessary to use all 15 exterior orientation parameters. In the opinion of the present author, the differences between the effect of quadratic and linear terms in the case of the MOMS-02 stereo-pair tested over the Australian test field compared with that over the Sudanese test field lie in the different nature of the measured image coordinates in the two cases. In the Australian case, since the positions of some of the control points were not well known and could not be identified with enough certainty, so at both Universities (ETH and Melbourne) attempts have been made to refine the image coordinates of some of the control points but not others. This becomes quite evident when one compares the image coordinates measured at ETH with those measured in Melbourne. For some control points, a difference of 3 pixels (equal to 40 metres) can be observed. This points to the need to employ some type of differential weighting between these refined points and the other points used in the bundle adjustment program. However, notwithstanding these differences in the image coordinate values, the author's bundle adjustment program tries to fit the set of coordinates together and treats all of them with the same weight. As a result, the errors present in some points have been modelled with the additional exterior orientation parameters. In the opinion of the present author, that is why the effects of the quadratic and linear terms are so pronounced and, in this respect, are a little unusual.

Considering the above Tables, the RMSE values in X, Y, and Z in the case of the ETH measured coordinates are noticeably better than those achieved with the Melbourne data. One of the reasons could be the stereoscopic measurements of the image coordinates carried out by the ETH group as compared with the monoscopic measurements made in Melbourne. This probably helped in the identification of the control points. It is also apparent that the powerful image enhancement carried out at ETH helped a lot in the identification of the

control points on the image.

Implementing the ETH measured data in the University of Melbourne bundle adjustment program resulted in much better RMSE values as given in Table 9.29.

Table 9.29 ΔX, ΔY, ΔZ RMSE values (in metres) of residual errors at the check points achieved in the 3D accuracy tests of the ETH data using University of Melbourne bundle adjustment program (Fraser and Shao, 1996a)

OI No.	Control point configuration (No. of control / check points)																	
	Set 1 (4/44)			Set 2 (9/39)			Set 3 (9/39)			Set 4 (20/28)			Set 5 (20/28)			free-net (48/0)		
	ΔX	ΔY	ΔZ	ΔX	ΔY	ΔZ	ΔX	ΔY	ΔZ	ΔX	ΔY	ΔZ	ΔX	ΔY	ΔZ	ΔX	ΔY	ΔZ
8	± 8.2	± 9.6	± 4.6	± 8.9	± 7.7	± 4.8	± 6.8	± 7.2	± 7.2	± 6.0	± 5.9	± 7.0	± 9.0	± 6.7	± 6.9	± 2.3	± 2.7	± 0.8
6	±10.9	± 7.5	± 4.9	±11.7	± 7.3	± 5.1	± 7.1	± 7.0	± 7.8	± 6.7	± 6.2	± 5.9	±10.0	± 6.2	± 8.1	± 2.7	± 2.7	± 0.9
4	± 9.8	±13.8	± 5.2	±13.1	± 7.8	± 5.1	± 9.7	± 7.0	± 5.2	± 9.9	± 6.0	± 5.6	±13.8	± 6.6	± 5.0	± 3.6	± 2.8	± 0.7

In ETH, Baltsavias and Stallmann (1996) used Kratky's bundle adjustment program for the evaluation of the MOMS-02 imagery over the Australian test field. The results of their test in terms of RMSE values in metres when using the forward and backward channels only are given in Table 9.30.

Table 9.30 ΔX, ΔY, ΔZ RMSE values (in metres) of residual errors at the check points achieved in the 3D accuracy tests of the ETH data using Kratky's bundle adjustment program in ETH (Baltsavias and Stallmann, 1996)

Model	Control points	Check points	ΔX	ΔY	ΔZ
Linear	20	45	± 9.9	± 7.4	± 9.4
Linear	10	55	± 9.0	± 8.7	± 10.1
Linear	6	59	± 10.9	± 8.1	± 12.2
Quadratic	20	45	± 6.2	± 6.4	± 6.7
Quadratic	10	55	± 6.7	± 5.9	± 7.4
Quadratic	6	59	± 7.4	± 10.7	± 7.9

The terms "Linear" and "Quadratic" in the above Table (9.30) refer to the polynomial terms which have been used in Kratky's model to describe the changes in the rotation angles (ω, φ, and κ) resulting from the dynamic nature of the imaging system. As can be seen, the

results achieved when using "Quadratic" terms are much better than those using just the "Linear" terms.

As can be seen from Table 9.29, the problem of the discrepancies which exist between the set in which all of the GCPs have been used as control points and the other five sets still exists. This could be another pointer which shows the slight weakness in the mathematical modelling of the MOMS-02 imagery that has been used at the University of Melbourne.

Comparing the results of the ETH test when using quadratic terms and 20 control points and 45 check points with those of the University of Melbourne test when using 20 control points and 36 check points and 8 orientation image lines in the Lagrange polynomial, it can be seen that the results are nearly the same. Comparing these results with the test using the present author's approach using 18 control points and 33 check points with 15 exterior orientation parameters (Table, 9.25) again these show nearly the same RMSE values for the X, Y, and Z coordinates. The slight differences could simply be the result of the different distribution and number of control points, but it could also result from the different mathematical models that have been used.

In the next Chapter, the geometric potential of SPOT, as a case of cross-track linear array imagery, and MOMS-02, as a case of along-track linear array imagery, for topgraphic mapping at medium scales are discussed and evaluated.

CHAPTER 10 : COMPARATIVE STUDY AND ANALYSIS OF THE GEOMETRIC POTENTIAL OF LINEAR ARRAY IMAGES FOR TOPOGRAPHIC MAPPING

10.1 Introduction

In Chapters 8 and 9, various 2D and 3D geometric accuracy tests have been carried out on SPOT images (as a case of cross-track linear array imagery) and MOMS-02 images (as a case of along-track linear array imagery). This Chapter presents a further discussion of the results reported in these chapters and analyzes them specifically regarding their geometric potential to produce medium scale topographic maps. It also attempts to take a much more general view and compares the results obtained in the author's research with those obtained by other investigators in this field of activity over quite different areas and test fields to those utilized by the present author.

The first part of this chapter investigates the geometric potential of SPOT imagery for the production of medium scale topographic maps. In the part after that, the geometric potential of MOMS-02 imagery for producing medium scale topographic maps will be discussed.

10.2 The Potential Geometric Accuracy of SPOT Imagery for Mapping Purposes as a Case of Cross-Track Stereo Images

(1) 2D Geometric Accuracy Tests

Several two-dimensional tests carried out on SPOT Level 1A and 1B images over a very accurate test field located in Jordan (Chapter 8, Section 8.1.3) have shown that well-defined topographic details with a planimetric accuracy of ±18m and ±16m can be extracted from Level 1A and 1B images respectively. Regarding the American standards for topographic mapping which are in widespread use world-wide, planimetric accuracies of ±15m and ±30m are needed for mapping at the scales 1:50,000 and 1:100,000 respectively. Consequently for areas like the Jordanian test field where substantial relief is present and control points with

sub-metre accuracy are available, the use of a 2D polynomial transformation with SPOT Level 1A and Level 1B images can be accepted for 1:50,000 scale maps but only just. However, in conjunction with the use of a 2D polynomial transformation program, SPOT images in both their Level 1A and 1B forms can easily provide the planimetric accuracies needed for 1:100,000 scale maps based on the American standards when using very accurate (sub-metre) GCPs.

(2) 3D Geometric Accuracy Tests

In Chapter 8, Section 8.1.4, the results of the 3D geometric accuracy tests using several SPOT Level 1A and Level 1B stereo-pairs over the Jordanian test field and a test area in Crete have been given and discussed. Theoretically, the ability to extract positional and elevation data from photogrammetric stereo models is given by the following standard formulas:

$$\sigma_P = \frac{H}{f}\,\sigma_{xy} \tag{10.1}$$

$$\sigma_E = \frac{H}{B}\cdot\frac{H}{f}\,\sigma_p \tag{10.2}$$

where,

σ_P : is the planimetric RMSE,

σ_E : is the vertical RMSE,

σ_{xy} : is the RMSE in x/y in pixel coordinates,

σ_p : is the RMSE for x-parallaxes,

H : is the flying altitude,

B : is the base length, and

f : is the focal length.

Regarding the above equations, and assuming an accuracy of 1 pixel (13μm) for both image coordinate measurements and the x-parallax measurements and taking account of the 830km altitude of the SPOT satellite, then, in the case of main Jordanian SPOT stereo-pair (122/285) with a base-to-height ratio of 0.975, the expected RMSE values in planimetry and

elevation are roughly equal to ±10m. In the case of the Crete SPOT stereo-pair, with a base-to-height ratio of 0.74, the expected values are equal to ±10m for planimetric accuracy and ±13.5m for altimetric accuracy.

Table 10.1 summarizes the actual results of the 3D accuracy tests of SPOT Level 1A and 1B stereo-pairs carried out over the Jordanian and Crete test fields. From the various tests discussed in Chapter 8, only the results from data Set A from each group have been selected and included in the Table. To have more relevance to topographic mapping and to be able to compare these values with the standard theoretical values, the equivalent RMSE values (ΔE, ΔN, ΔH) in terms of the UTM coordinate system are given as well as those expressed in the geocentric coordinate system as ΔX, ΔY and ΔZ values in Chapter 8.

Table 10.1 RMSE values of the residual errors in the independent check points in terms of both the WGS 1984 geocentric coordinate system and the UTM coordinate system achieved in the 3D accuracy tests of the Jordanian and Crete SPOT Level 1A and 1B stereo-pairs (Set A)

Test Area	Image Level	No. of control pts.	No. of check pts.	RMSE ΔX (m)	RMSE ΔY (m)	RMSE ΔZ (m)	RMSE ΔE (m)	RMSE ΔN (m)	RMSE ΔP (m)	RMSE ΔH (m)
Jordan	1A	15	23	±8.58	±7.85	±7.80	±9.89	±8.16	±12.82	±5.62
Jordan	1B	15	23	±8.86	±8.24	±9.99	±9.74	±9.13	±13.35	±8.24
Crete	1A	13	18	±6.91	±5.30	±5.92	±5.66	±6.02	±8.26	±6.52
Crete	1B	13	18	±7.70	±6.49	±7.17	±6.60	±8.54	±10.80	±6.02

As can be seen from Table 10.1, all of the SPOT images in both their Level 1A and 1B forms give a better accuracy in elevation than that which has been computed based on the standard formula (10.2). In the case of planimetric accuracy, the Jordanian results show a little weakness comparing them with the standard values computed from the formula (10.1). Maybe this is a result of some difficulties which were experienced in the identification of some control points on the image. In the opinion of the present author, the reason why the elevation data gives a better accuracy than the planimetry is that, although the positions of some points could not be identified with enough accuracy, the selected points in the left and right images have been pointed to (i.e. measured) in the same position with sub-pixel accuracy. This means that the x-parallax accuracy is high; consequently the elevations derived from these parallaxes are in good sympathy with the measurements conducted on

the ground by the RJGC surveyors.

Regarding the American standards for topographic mapping, in the case of planimetric accuracy (i.e. map scale = σ_P / 0.3mm), the accuracies achieved with the Jordanian SPOT Level 1A and 1B stereo-pairs correspond to the requirements of topographic maps at 1:43,000 and 1:44,500 scales respectively. In the case of the Crete SPOT Level 1A and Level 1B stereo-pairs, they correspond to the accuracy requirements of 1:27,500 and 1:36,000 scale topographic maps respectively. In general terms, with the use of stereo-pairs and a full 3D photogrammetric solution, it is clear that SPOT images can satisfy the planimetric accuracy for topographic maps of 1:50,000 scale and smaller.

Considering the American standards for elevation accuracy in a topographic map (contour = σ_E / 0.3), the corresponding contour intervals for the Jordanian SPOT Level 1A and 1B stereo-pair are 18.7m and 27.5m respectively which, according to Doyle (1984), correspond to the requirements of topographic maps at 1:100,000 and 1:250,000 scales respectively - although, as noted previously, the actual contour interval used at these scales will also depend on the elevation range and the characteristics of the relief and the land forms in the area being mapped. In the case of the Crete SPOT Level 1A and 1B stereo-pairs, the RMSE values in elevation result in contour intervals of 21.7 and 20 metres respectively. Again, according to Doyle (1984), these values correspond to the specification for standard 1:100,000 scale topographic maps. However, since, depending on the area, larger or smaller contour intervals can be used, a given contour interval is not necessarily associated with a fixed scale.

In summary, the results from these tests show that SPOT stereo images can, in general, satisfy the 3D geometrical (i.e. planimetric and altimetric) accuracy requirements of topographic maps at scales of 1:50,000 and smaller.

10.2.1 Tests of SPOT Level 1B Stereo-Pairs

It is possible to make a comparison between the tests carried out on SPOT imagery in this

research with some other tests carried out by other researchers concerned with SPOT stereo images. However, in the case of the 3D geometric accuracy tests carried out on SPOT Level 1B images, the present author has found only a single test carried out by Gugan and Dowman (1988). Table 10.2 gives the residual errors in terms of RMSE values for their test carried out on a SPOT Level 1A stereo-pair and the corresponding Level 1B stereo-pair over a test area in south west Cyprus.

Table 10.2 Accuracy results for SPOT Level 1A and 1B stereo images over a test area in south west Cyprus in terms of the residual errors at the independent check points (Gugan and Dowman, 1988)

Level 1A		Level 1B	
RMSE ΔP (m)	RMSE ΔH (m)	RMSE ΔP (m)	RMSE ΔH (m)
±28.2	±11.1	±35.8	±15.9

For these tests, 10 points were used as ground control points (GCPs); the results given in Table 10.2 are those obtained at 15 check points. Almost certainly, the poorer RMSE values achieved by Gugan and Dowman compared with those resulting from the tests carried out over the Jordanian and Crete test areas in the course of the present research arise from the source and nature of the ground control points. In the case of Gugan and Dowman's tests, all of the control and check points were taken from an existing 1:50,000 scale map. However, as can be seen from Table 10.2, the relative accuracies in planimetry and elevation between the two Levels are 7:9 and 11:16 respectively. Regarding the RMSE values given in Table 10.1, it can be seen that not only are the absolute accuracy values very much improved as shown in the author's tests, especially with the Level 1B stereo images, but the relative accuracies in planimetry and elevation between the two Levels, in the case of Jordanian test area are 1:1 and 3:4 and in the case of Crete test area, 0.8 and 1.1 respectively. Compared to Gugan and Dowman's tests, these values show the substantial improvement in the residual values resulting from SPOT Level 1B images with respect to those from Level 1A images. This also shows how well the mathematical solution developed by the present author for the geometric correction of SPOT Level 1B images works in practice.

The results achieved with the Level 1B stereo-pairs have a certain importance since Level

1B images are in widespread use by the geoscience, geoexploration and geophysical communities because of their near orthographic qualities after removal of the displacements due to the viewing angle. At the same time, these Level 1B images still retain the displacements due to topographic relief. The results of the tests over the Jordanian and Crete test fields show that quite comparable accuracies can be obtained from Level 1B data - in fact, the results are almost as good as those achieved with the Level 1A images that are favoured by the photogrammetric community.

10.2.2 Tests of SPOT Level 1A Stereo-Pairs

In the case of the geometric accuracy tests that have been executed with SPOT Level 1A stereo images, it is possible to compare the results obtained in the present research with those achieved by different investigators using different mathematical models in the course of the OEEPE (European Organisation for Experimental Photogrammetric Research) experimental test on SPOT stereo images, carried out over a test area located in the area between Marseilles and Grenoble (France) (Dowman et al., 1991). The control points for this test have been extracted from four different sources with reasonable accuracies as given in Table 10.3.

Table 10.3 Accuracy and type of the control point data provided for the OEEPE test

Type of GCPs	Accuracy in metres	
	Planimetry	Height
1:25,000 scale topographic maps	5	2
1:30,000 scale aerial stereo-pairs	5	2
1:60,000 scale aerial stereo-pairs	4	2
computed by field stereo-preparation	3	2

A comparison of the geometric accuracy tests using the same 10 control points over the same OEEPE test field which have been achieved by different contributors to the test is given in Table 10.4. As can be seen from this Table, the results obtained by these researchers are quite good and fairly consistent. Comparing these results with the results obtained

during the present research (summarized in Table 10.1) shows more or less the same accuracy for both the planimetry and the height. Regarding the lower accuracy of the GCPs used for the OEEPE test (Table 10.3), the results achieved in these OEEPE tests show slightly better RMSE values (especially the IGN test results) compared with those obtained in the present research using GCPs having sub-metre accuracy. This is probably because of the very good identification and distribution of the GCPs in the case of OEEPE test carried out over an area with well defined points in a highly developed country as compared with those available in a test field located in a desert area.

Table 10.4 RMSE values in metres at the check points obtained from the OEEPE geometric accuracy tests of a common SPOT scene using different mathematical models (Dowman et al, 1991)

Research centres and their mathematical models used for OEEPE test	RMSE values in metres	
	ΔP	ΔH
Hannover (additional parameter model developed by Konecny et al., 1987)	13.5	6.4
IGN (unknown)	7.6	4.9
Milan (orbital parameter model developed by De Haan, 1991)	16.5	11.5
Queensland (orbital parameter model developed by Priebbenow, 1991)	13.3	6.8
CCM (multiple projection centre model developed by Kratky, 1988)	21.1	6.7
UCL (orbital parameter model developed by Gugan, 1987)	16.1	7.3

In general terms, as has been shown by different investigators and confirmed by this research, SPOT stereo images in both their Level 1A and 1B forms can provide easily the planimetric accuracy requirements for 1:50,000 scale topographic maps and smaller, although the elevation accuracies are more marginal. However, as will be discussed later in Chapter 11, the main shortfall when using SPOT imagery for topographic mapping and map revision lies in the limitations in the information content that can be extracted from the present SPOT imagery arising from its comparatively large pixel size and poor ground resolution.

10.3 The Potential Geometric Accuracy of MOMS-02 Image for Mapping Purposes as a Case of Along-Track Stereo Images

(1) 2D Geometric Accuracy Tests

Various two-dimensional accuracy tests, using different terms within the 2D polynomial equation, have been carried out on a MOMS-02 mode 3 image over an Sudanese test area as well as a MOMS-02 mode 1 image over an Australian test field (Chapter 9, Sections 9.1.4 and 9.2.3). These tests have shown that, using a suitable 2D polynomial transformation, topographic details with planimetric accuracies of ±28m and ±16m respectively can be obtained from the Sudanese and Australian MOMS-02 images. Indeed the differences between these RMSE values arise solely from the different quality (in terms of the accuracy) of the ground control points which have been used in the tests. The achievement of such good results with a simple mathematical model such as the polynomial transformation used in these tests arises from the purely fortuitous situation of having a flat test area in both Sudan and Australia. In the case of the Sudanese MOMS-02 image, the GCPs have been collected from the 1:100,000 scale topographic maps with an accuracy of 20 to 30 metres in planimetry and about 5m in height. For the Australian MOMS-02 images, the positions and heights of the GCPs have been obtained using differential GPS field survey techniques with sub-metre accuracy; i.e. they are comparable in quality to the GCPs used in the geometric accuracy tests of the SPOT stereo-pairs conducted over Jordan and Crete. However, relating these results to the American standards for topographic mapping, the resulting planimetric accuracies correspond to those specified for 1:100,000 scale topographic maps and smaller in the case of the Sudanese image, and 1:50,000 scale topographic maps and smaller in the case of the Australian MOMS-02 image.

(2) 3D Geometric Accuracy Tests

The detailed results of the 3D geometric accuracy tests using the MOMS-02 mode 3 image over the Sudanese test field are given in Chapter 9, Section 9.1.5. The 3D geometric accuracy test results using MOMS-02 mode 1 images over the Australian test area are given

in Chapter 9, Section 9.2.4.1 (for the University of Melbourne image coordinate data set) and in Section 9.2.4.2 (for the ETH image coordinate data set). These need not be repeated here. Instead a more general discussion is presented which looks more widely at the results that are now becoming available for other test areas than the Sudanese and Australian test fields used by the present author.

Based on equations (10.1) and (10.2), and assuming an accuracy of 1 pixel (10μm) for image coordinate measurements as well as the x-parallax measurements and adopting 295km as the height of the Space Shuttle carrying the MOMS-02 imaging system, then, in the case of MOMS-02 images acquired when using stereo Channels 6 and 7 with a 13.5m ground pixel size and with a base-to-height ratio of 0.8, the theoretical values for the planimetric and altimetric RMSE are equal to ±13.4m and ±16.7m respectively. In the case of MOMS-02 mode 1 data when combining HR Channel 5 with an inclined Channel 6 or 7, the base-to-height ratio decreases by a factor 2, but, at the same time, the pointing accuracy is improved theoretically by a factor of 3 due to the use of the HR Channel 5 and its higher resolution. Then, based on equations (10.1) and (10.2), the theoretical accuracy values for the resulting planimetric and altimetric measurements amount to ±4.5m and ±11.2m respectively. Table 10.5 gives the actual results of the 3D accuracy tests carried out by the author with the Sudanese and Australian MOMS-02 stereo-pairs in the case of their Set A configuration of GCPs. To be able to compare these results with their theoretical values, the equivalent RMSE values in terms of the UTM coordinate system have been computed and are given in this Table.

Table 10.5 RMSE values of the residual errors in the check points in terms of both the WGS 1984 geocentric (X,Y,Z) coordinate system and the UTM (E,N,H) coordinate system achieved in the 3D accuracy tests of the Sudanese and Australian MOMS-02 stereo-pairs (Set A)

Test Area	No. of control pts.	No. of check pts.	RMSE ΔX(m)	RMSE ΔY(m)	RMSE ΔZ(m)	RMSE ΔE(m)	RMSE ΔN(m)	RMSE ΔP(m)	RMSE ΔH(m)
Sudan	19	30	±15.56	±21.58	±17.35	±21.92	±18.45	±28.65	±13.71
Australia (Melb.)	18	31	±8.00	±10.57	±9.66	±9.55	±8.27	±12.64	±10.46
Australia (ETH)	18	33	±5.51	±5.84	±7.01	±5.81	±6.44	±8.68	±6.2

Once again, the weakness of the Sudanese planimetric accuracy figures lies in the limitations in the geometric accuracy of the GCPs extracted from the 1:100,000 scale maps. The 4m higher accuracy in planimetry and altimetry achieved in the case of the ETH data set compared with those achieved with the Melbourne data set appears to be the consequence of the difficulties that the Melbourne research team had in the identification of the GCPs on the images. By contrast, as mentioned in Chapter 9, Section 9.2.2.2, the ETH research group performed a comprehensive enhancement and refinement operation to find the most suitable position of each of the GCPs on the image. As can be seen from Table 10.5, all of the MOMS-02 images, even those from the Sudanese test, show a better accuracy in elevation than the theoretical value based on the standard formula (10.2). In the case of the planimetric accuracy, the results obtained with the MOMS-02 stereo-pairs over the Australian test field with both the ETH and the Melbourne data sets correspond with the expected accuracy values which have been computed based on the standard formula (10.1) in the case of neglecting HR channel 5. The reason for having better results could be the sub-pixel accuracy in the image coordinate measurements which are a consequence of using the HR channel 5 to help in the identification of the GCPs on the image. Comparing the RMSE values in planimetry and altimetry for the Australian test field using the ETH and Melbourne data sets with the theoretical values when considering HR channel in the solution, shows a difference of 8m and 4m in planimetry for the Melbourne and the ETH data sets respectively. The heights still show better accuracy than that computed theoretically. The weakness in planimetry arises probably from firstly the poor radiometric quality of the images and secondly the fact that stereo channels 6 and 7 were only available with a 13.5m pixel size instead of 4.5m.

However, regarding the American standards for the planimetric accuracy needed to compile a topographic map in a given scale (i.e. map scale = σ_P / 0.3mm), the results from the Sudanese MOMS-02 stereo-pair correspond to the requirements of topographic maps at 1:95,500 and smaller. In the case of the Australian MOMS-02 stereo-pair employing the Melbourne data set, this corresponds to a 1:42,100 topographic map scale and, with ETH data set, it corresponds to 1:28,900 scale topographic maps and smaller. In general terms, it is evident that, if the GCPs could be measured with good accuracy, then MOMS-02 stereo

image easily satisfy the planimetric accuracy requirements for topographic maps of 1:50,000 scale and smaller.

Considering the American standards for altimetric accuracy in a topographic map (contour interval = σ_H / 0.3), the corresponding contour interval for the Sudanese MOMS-02 stereo-pair is 45.7m. According to Doyle (1984), this value corresponds only to the topographic maps of 1:500,000 scale. Since the Sudanese test area is flat, the required contour interval will be very small, e.g. 10m. In the case of the Australian MOMS-02 stereo-pair and the Melbourne and ETH data sets, the RMSE values in elevation result in contour intervals of 35m and 21m respectively. Again, based on Doyle (1984), these values correspond to 1:250,000 scale topographic maps in the case of the Melbourne data set and 1:100,000 scale topographic maps in the case of the ETH data set. Again, because of having flat land in the Australian test field, the contour interval required to show the relief features that are present on the ground will be quite small, e.g. 5 to 10m, so the MOMS-02 stereo-imagery falls a long way short of satisfying such a demanding requirement.

In the case of the 3D geometric accuracy test carried out on the Sudanese MOMS-02 image in its mode 3, a comparison can be made with a similar 3D test which has been carried out by Lehner and Kornus (1995) on MOMS-02 mode 3 data over two test areas in Mexico and Ethiopia. For the Ethiopian test area, three sources of GCPs were available: (I) 46 GPS control and check points which were already available in the area and could be measured on the images; (ii) hard copies of 58 aerial frame camera images taken at 1:50,000 scale; and (iii) topographic maps at 1:50,000 scale. The control and check points were estimated to have ±5m accuracy in planimetry and ±6m in altimetry. For the Mexican test area, the GCPs were all extracted from 1:100,000 scale topographic maps. The results of these tests carried out at the Technical University of Munich using the adjustment program CLIC (outlined in Chapter 6, Section 6.3) are given in Table 10.6. As can be seen from this Table, the results of the 3D geometric accuracy test conducted over the test field in Mexico - which, in terms of the accuracy of its GCPs, were (like the Sudanese data) collected from 1:100,000 scale topographic maps - correspond to those achieved in the Sudanese test carried out in this research, but show a deficit of 8m in planimetry and 18m in altimetry.

Table 10.6 RMSE values of the residual errors at the check points achieved in the 3D accuracy tests of the Mexican and Ethiopian MOMS-02 mode 3 stereo-pairs using the CLIC block adjustment program (Lehner and Kornus, 1995)

Test area	No. of check points	RMSE ΔX (m)	RMSE ΔX (m)	RMSE ΔP (m)	RMSE ΔZ (m)
Mexico	52	±24	±28	±37	±32
Ethiopia	34	±23	±19	±30	±13

In the case of the Ethiopian test area, since the ground control points have been fixed using GPS techniques, the results would be expected to have more accurate RMSE values, but in fact they exhibit similar values to those achieved in the Sudanese 3D test which has been carried out during the present research. According to Lehner and Kornus (1995), the principal reason for these poor results was the difficulties that they had in identifying the control points measured by GPS on the image. If so, then some of these points were located, identified and measured with poor accuracy. Since the adjustment program used by Lehner and Kornus for these tests was in its original form before its recent modification by Ebner et al. (1996a) - which implemented orbital constraints in the program - then, in the opinion of the present author, a further potential explanation for these poor RMSE values could be a weakness which was present in the program at that time.

In Chapter 9, Section 9.2.4.2, a comparison was made between the results of the various 3D geometric accuracy tests carried out on the Australian MOMS-02 mode 1 data which have been made in this research and those which have been achieved by the University of Melbourne research team (Fraser and Shao, 1996a) and by the ETH Zurich research group (Baltsavias and Stallmann, 1996). Table 10.7 summarizes the results which have been obtained:

(1) using University of Melbourne adjustment program with the ETH data set where 8 orientation image lines are used in the Lagrange polynomial;

(2) using Kratky's bundle adjustment program in ETH with the ETH data set where quadratic polynomial terms have been used; and

(3) using the present author's adjustment program with ETH data set where 15 exterior orientation parameters have been used.

In each case, the same data set from ETH and similar numbers of control and check points have been used.

Table 10.7 RMSE values (in metres) of the residual errors in the check points achieved in the 3D accuracy tests of the Australian MOMS-02 mode 1 data obtained at the University of Melbourne, ETH Zurich and the University of Glasgow using the ETH data set

University	No. of control points	No. of check points	RMSE ΔE (m)	RMSE ΔN (m)	RMSE ΔP (m)	RMSE ΔH (m)
Melbourne	20	28	±6.0	±5.9	±8.4	±7.0
ETH	20	45	±6.2	±6.4	±8.9	±6.7
Glasgow	18	33	±5.8	±6.4	±8.7	±6.2

As can be seen from Table 10.7, the results in terms of RMSE values for the residual errors at the check points obtained in the three different tests are more or less the same. The slightly different results could be a result of the different number and different distribution of the control points used. It could also be a result of the different mathematical models used by the researchers.

A further comparison can be made with the results from another recently published 3D test, which has been carried out by Schiewe (1996) at the University of Hannover, on a sub-scene of a MOMS-02 mode 1 stereo-pair covering a small 10km by 10km large area within Dubai City. The control points have been extracted from 1:10,000 scale orthophotomaps of Dubai City. The test has been carried out using the BLASPO adjustment program available at the University of Hannover, which implements the additional parameter mathematical model (see Chapter 5, Section 5.4). The results of this test when combining HR channel 5 with the oblique channel 6 and measuring the image coordinates of the control points monoscopically and stereoscopically are given in Table 10.8. This Table shows a significant increase in accuracy, especially in height, when the image coordinates of the GCPs are measured in stereoscopic rather than in monoscopic mode, apparently because the pointing accuracy is improved. Comparing the results of this test with those achieved in the present research, University of Melbourne and ETH, there is indeed an improvement. This could be the result of using a smaller test site, and very well defined ground control points (since the area is a city).

Table 10.8 RMSE values (in metres) of the residual errors at the check points achieved in the 3D accuracy tests of the Dubai City MOMS-02 mode 1 stereo-pair obtained at the University of Hannover (Schiewe, 1996)

Image coordinate measurement	No. of control points	No. of check points	RMSE ΔX (m)	RMSE ΔY (m)	RMSE ΔP (m)	RMSE ΔZ (m)
Mono	25	30	±4.6	±4.4	±6.4	±10.9
Stereo	25	30	±4.2	±3.6	±5.5	±4.5

The use of a much smaller test site and therefore only a part of a MOMS-02 scene may reduce the effects of the changes in the attitude and the position of the MOMS-02 imaging system arising from its dynamic geometry over a short distance and therefore results in a better accuracy in the point determination.

10.4 Comparison Between the Results Achieved with the SPOT and MOMS-02 Stereo-pairs

Based on the tests which have been carried out regarding the geometric potential of linear array imaging systems, a further comparison can be made between SPOT as a cross-track stereo imaging system and MOMS-02 as an along-track stereo imaging system. Table 10.9 shows the best results which have been obtained in this research for SPOT data (when using the Crete SPOT Level 1A stereo-pair) and MOMS-02 data (when using the ETH data set obtained with the Australian MOMS-02 mode 1 stereo-pair).

Table 10.9 RMSE values (in metres) of the residual errors in the check points achieved in the 3D accuracy tests of the Crete SPOT Level 1A stereo-pair and the Australian MOMS-02 mode 1 stereo-pair with ETH data set

Image data	No. of control points	No. of check points	RMSE ΔX (m)	RMSE ΔY (m)	RMSE ΔP (m)	RMSE ΔZ (m)
Crete SPOT 1A	13	18	±5.66	±6.02	±8.26	±6.52
Australian MOMS-02 mode 1	18	33	±5.81	±6.44	±8.68	±6.20

As can be seen from Table 10.9, the results of these tests are nearly the same for both planimetry and altimetry - although it might at first appear that, because of the lower altitude

of the Shuttle spacecraft, the results from MOMS-02 should be better. The main reason for the similarity in the two sets of results lies in the combination of the different parameters given in equations (10.1) and (10.2). Thus the base-to-height ratio in both the Crete SPOT stereo imagery (0.74) and the MOMS-02 stereo imagery (0.8) is nearly the same. Although the spacecraft's altitude (295km) in the case of MOMS-02 is only 0.36 of that used with SPOT (830km), on the other hand, the focal length (237mm) of MOMS-02 is only 0.22 of that used with SPOT (1,084mm). In which case, the ratio of H/f in the case of MOMS-02 is 1.5 times that used with SPOT. It should also be considered that the pixel size of the SPOT image (13μm) in the image space is 1.3 times that of MOMS-02 (10μm). As a result, SPOT would be expected to have near 1.1 times better planimetric and altimetric accuracy than that expected from MOMS-02. Since in both cases, the GCPs used for both sets of tests had similar accuracies got from GPS dual frequency measurements, then the slightly better results obtained in the case of MOMS-02 (especially in the altimetry) are probably the result of using HR channel 5 (4.5m pixel size and 660mm focal length) for the identification of GCPs on the stereo Channels 6 and 7 as well as measuring the points in stereo using matching techniques, as reported by Baltsavias and Stallmann (1996).

In general terms, the results of the various recent tests carried out on the SPOT and MOMS-02 stereo imagery by the present author and by other investigators show that, from the point of view of planimetric and altimetric accuracy, both types of data can be used successfully for the production of topographic maps at 1:50,000 scale and smaller. However, although the SPOT and MOMS-02 stereo-pairs can be accepted from the standpoint of their geometric accuracy for use in topographic mapping at these scales, quite another set of criteria have to be tested with this type of imagery before it can actually be used for such mapping. This is its potential to provide the required information content and the features that have to be included in topographic maps at 1:50,000 or 1:100,000 scale. This matter, which is usually described as image interpretation and feature extraction, is discussed in the next Chapter.

CHAPTER 11 : PHOTOGRAMMETRIC INTERPRETATION OF SATELLITE LINEAR ARRAY IMAGES FOR MEDIUM SCALE TOPOGRAPHIC MAPS

11.1 Introduction

After the determination of the positional and height accuracy of satellite linear array images for map compilation, they have to be tested for their potential to provide the information content and features which have to be extracted with respect to the scale of the topographic map. The suitability of satellite linear array images for topographic mapping at certain map scales with respect to their information content depends on two main factors (Konecny et al., 1994):

(i) ground-side factors, such as the relief and the contrast and texture of the landscape features, and of

(ii) scanner-side factors, such as the spatial and spectral resolution of the sensor and the provision of stereoscopic imagery which will offer an improved interpretation of the landscape.

According to Konecny et al. (1982), for the detection and the identification of topographic features for vector line mapping at a scale of 1:50,000, a ground pixel size of 3 metres for monoscopic imaging or 6 metres for stereoscopic viewing is necessary for a single building - this being one of the most critical objects in the identification process. For the interpretation of areal features such as forest, cultivated areas or vegetation or large linear features such as streets or rivers, larger pixel sizes can be accepted.

For a good perception of the detail present in an orthoimage, Doyle (1984) recommends a maximum scale which is achieved by multiplying the ground pixel size by the factor 10,000 (see Chapter 2, Section 2.3.3). In which case, even from the theoretical point of view, neither SPOT as a cross-track linear array imager nor MOMS-02 in its mode 3 as an along-track linear array imager can fulfill the information requirements for line mapping at

1:50,000 scale or even 1:100,000 scale (in the case of MOMS-02 image, mode 3). Furthermore, even if the HR channel of MOMS-02 (with its 4.5m pixel size) is being used, then, on Doyle's basis, it would only seem to be acceptable for mapping at scales 1:45,000 and smaller. Using the same criteria, SPOT could be used successfully for the production of image maps at 1:100,000 scale and smaller and MOMS-02 in its mode 3 (i.e. using the 13.5m pixel size of the forward and backward channels) could only be used for the production of an image map at 1:135,000 scale and smaller.

In this Chapter, first of all, some significant examples of the topographic mapping carried out by certain national mapping organizations using SPOT stereo images and some previous tests carried out at the University of Glasgow are reviewed from the point of view of their interpretational qualities. In the second part of the Chapter, the results of an experimental test of feature extraction and photogrammetric image interpretation using MOMS-02 mode 3 stereo imagery over the Sudanese test area against a 1:100,000 scale topographic map are outlined and discussed. The third part of this Chapter outlines a simple terrain analysis of the test area which reveals the advantages of generating image maps rather than line maps for the representation of this type of area.

11.2 Suitability of SPOT Stereo Images for Topographic Mapping with Respect to Their Information Content

Various tests and investigations have been already carried out on this matter. Also, quite a lot of production experience has been gained through the use of SPOT imagery for topographic mapping in the Red Sea region. For example, the Ordnance Survey (OS) has used 18 SPOT stereo images for 1:50,000 and 1:100,000 scale map compilation in North Yemen using Kern DSR analytical plotters (Hartley, 1988; Murray and Farrow, 1988; Murray and Newby, 1990). This project required a thorough field completion to pick up the quite substantial number of missing features. Similarly the French Institut Geographique National (IGN) used 16 SPOT stereo images for map compilation at 1:50,000 and 1:200,000 scales for Djibouti (Veillet, 1990, 1992). This project also utilised analytical plotters (from Matra) for the map compilation, which again needed a very substantial field

completion for missing features. The Ethiopian Mapping Agency (EMA) has also been using SPOT hardcopy stereo images processed to Level 1A for orthoimage and DTM generation using a Wild BC-2 analytical plotter (Jobre, 1993; Medhin, 1993). Specific difficulties which have been reported from these projects have included those arising from the individual SPOT images comprising a stereo-pair being taken three months apart at the beginning and the end of the rainy seasons, resulting in the very different appearance of vegetation and water features in the two images. This caused very serious difficulties with feature extraction, besides its impact on stereo viewing and measurement. Jacobsen (1993) has also commented in similar terms on his experiences in trying to measure SPOT stereo images in Germany where the individual SPOT images had been taken at different points in the growing season.

In the University of Glasgow, Petrie and El Niweiri (1992) tested six types of satellite images - Landsat MSS; RBV and TM; MOMS-01; the ESA Metric Camera (MC) and NASA's Large Format Camera (LFC) - for topographic mapping at 1:100,000 scale over a semi-arid area in Sudan comparing the results with the corresponding DOS maps of the same area produced from aerial photography. Based on their tests, all of these images showed substantial shortcomings in the extraction of communications and settlement features. Indeed their best results in terms of information content for the 1:100,000 scale maps were achieved with the MC and LFC photography, though a thorough field completion would still be required.

Since this work, a further series of interpretational tests has been carried out in Glasgow for a number of countries (Kenya, Tanzania, Zambia and Botswana) in Eastern, Central and Southern Africa, with an emphasis on the use of SPOT Pan and XS imagery. Petrie and Liwa (1995) reported that SPOT Pan and XS imagery can only supply the data for a preliminary or provisional edition of a 1:50,000 scale topographic map or for the rapid but incomplete revision of an existing map at that scale. They also mentioned that the present SPOT data is still substantially deficient in providing the details required for the production of a full or final edition of a new 1:50,000 scale map or for the comprehensive revision of an existing published map at that scale. These deficiencies are particularly apparent with

regard to both the communication features and many of the smaller man-made cultural features which are present in the landscapes of the region. In order to overcome these deficiencies, which can amount to 30% of the total map content, an additional comprehensive field completion is necessary - which will be both time consuming and expensive. Moreover, without this extensive additional work on the ground, there is a danger that a product will be made available that is substantially incomplete and may not then be acceptable to users (Petrie and Liwa, 1995).

In the next Section, the capability of the MOMS-02 imagery to provide the information needed to complete a 1:100,000 scale topographic map is tested and discussed. This test has been carried out over the Sudanese test field. In view of the relative novelty of MOMS-02 imagery, this represents one of the first assessments from the purely interpretational point of view regarding its suitability for topographic map compilation.

11.3 Photogrammetric Interpretation of and Feature Extraction from MOMS-02 Imagery over the Sudanese Test Field for 1:100,000 Scale Topographic Mapping

This test has been carried out on the MOMS-02 Channel 7 image of Scene 5. A part of this monoscopic panchromatic image covering nearly the whole of a 1:100,000 scale topographic map (sheet number 544), and which included as many different types of feature as possible, was selected. A hard copy image on photographic paper at approximately 1:100,000 scale has been produced in the Department from the digital image data to be used in this test. To be able to carry out the detection and identification of the features on the image as accurately as possible, the two nadir multispectral images generated by Channels 3 (with wavelength 645-677nm) and 4 (with wavelength 772-815nm) of the MOMS-02 imager when operated in its mode 3 have also been used for the purpose. Since this image covers a flat area and has not too many features which would normally be included and shown in a line map, so a part of Scene 3, which is covered by part of Sheet 449 and includes some additional line features such as water channels and light railways, was also used in this test. Since the author's knowledge of the area is limited to his familiarity with the topographic map at 1:100,000 scale, so his feature identification and extraction

depended on his own general interpretative abilities and, to a certain extent, on the ground resolution of the image and on the spectral and tonal differences between individual features and their background reflectances.

As noted above, the area covered by Scene 5 is a nearly flat area and, in terms of man-made features and cultural detail, it is lacking features. The Nahr-ar-Rahad river passes through the area from east to the north western part of the enlarged hard copy image. Along the raised banks (or levees) of this river, a number of small settlements or villages can be recognized on the image. In the northern part of the test area, the image comprises a large expanse of cultivated terrain in which the borders of the fields can be recognized easily on the image. In the north western part of the image, two small hills - Jabal-Ab-Sabika and Jabal Haffar - are visible and easily recognised. In the southern part of the image, the Nahr-Ad-Dindir river and its branches, Khor Qlaque and Khour Um Masawik, can be identified.

Based on the different types of features, i.e. the line features (such as roads, railways, rivers and streams, etc.), the point features (such as buildings, bridges, water tanks, microwave towers, etc.), and the areal features (such as towns, villages, fields, forests, etc.), which need to be included in a 1:100,000 scale topographic map, a detailed interpretation of and feature extraction from the MOMS-02 imagery has been carried out visually by the author using both the enlarged hard copy using a simple magnifier and the images displayed on the monitor screen. The results of this work are discussed below under the following classes:

(i) Lines of communication;
(ii) Cultural features;
(iii) Hydrology; and
(iv) Vegetation and forests.

11.3.1 Lines of Communication

This group includes linear features such as roads, tracks, telephone lines, power lines and railway lines and bridges.

11.3.1.1 Hard Surfaced and Unsurfaced Roads, Major and Minor Tracks

Not a single tarred surfaced road exists in the test area. However, the so-called loose surfaced or improved surfaced roads, although they occur only rarely in the area, were easily detected and identified. Comparing the plot of the interpreted detail with the existing 1:100,000 scale map, overall 100% of these features were correctly detected, interpreted and identified.

Within the area, there are a lot of minor and major tracks which obviously form the main communication network of the area. In the northern part of the image, there are quite a number of tracks which also act as boundaries between the different cultivated areas. These could be easily detected and identified. This was possible because of the high contrast existing between different cultivated areas. In the other parts of the image, according to the DOS map, there are major or minor tracks which traverse the dry stream beds and connect the scattered small villages. It is very difficult to detect these tracks on the MOMS-02 image because they lie in the highly reflective sandy beds of the wadis and khors. Therefore the contrast between these tracks and the background is negligible and indeed the vast majority of these features cannot be found, even with the help of the collateral information provided by the existing DOS map of the area.

It is worth mentioning that, although there are no tarred surfaced roads in the area, regarding the possibility of detecting these improved roads, it can be concluded that these features could be detected and identified easily too.

11.3.1.2 Railway Lines and Railway Stations

While there was no railway or railway station existing in Scene 5 of MOMS-02 imagery, the existing map shows that a light railway, which is running parallel to a main irrigation channel, does exist in Scene 3. It could be detected with difficulties through the help of the map using the neighbouring irrigation channel as a guide. However, without the knowledge given by map, it would be quite impossible to identify this feature. Since the unsurfaced

roads could be identified on the image, it is expected that maybe the railway with its station could be recognised on the image, although the narrow guage of the single line track must be a drawback in this respect.

11.3.1.3 Bridges and Roundabouts

It was very difficult to identify any bridges in the test area. No roundabout was present in the test areas.

11.3.2 Cultural Features

This group of features includes power lines, telephone lines, triangulation pillars, microwave towers, water tanks, built-up areas and quarries. The power and telephone lines are linear features of a small dimension; similarly the triangulation pillars and microwave towers are very small point features. The individual built-up areas and quarries cover only a quite small area of the image.

11.3.2.1 Power Lines and Telephone Lines

The 1:100,000 scale topographic map covering Scene 3 of the MOMS-02 imagery shows a power transmission line running parallel to a main irrigation channel, but it could not be identified on the image. Telephone lines do not exist on the test areas or at least none are shown on the map. Certainly none appear on the MOMS-02 images.

11.3.2.2 Triangulation Pillars, Microwave Towers and Water Tanks

These features are normally presented symbolically as point features on the 1:100,000 scale map. Given their small dimensions, none of these could be expected to be detected and identified on the image and indeed none were found.

11.3.2.3 Built-up Areas

The settlements or built-up areas in the test field covered by the MOMS-02 image comprise small villages, nomadic camps and refugee camps. The more densely built-up areas could be detected on the image, more especially when using the digital image on the screen. This is more because of the different reflectance of these features with respect to the background. It must be said however that having their positions marked on the existing map helped greatly in their location and identification. Some camps scattered around the image can also be recognized for the same reasons given above. However none of the individual buildings which are required to be shown on the 1:100,000 scale map, including schools, mosques, churches, and factories, could be identified.

11.3.3 Hydrology

The hydrological features which are required for inclusion in the 1:100,000 scale map comprise rivers, irrigation channels, water pipelines, dams and reservoirs and water bodies.

11.3.3.1 Rivers, Irrigation Channels and Water Pipelines

The Nahr Ar Rahad river passing through the middle of the test area could be identified and detected easily. In the southern and south western parts of the image, the Nahr Ad Dindir river is running across the area and could also be identified clearly. There are several seasonal streams in the area which also could be detected and identified on the image, although with some difficulties in a number of cases. Irrigation channels and water pipelines do exist in the Scene 3 of MOMS-02 image. All of them could be detected easily but their identification needs the map to be certain of their identity.

11.3.3.2 Dams, Reservoirs and Water Bodies

No large water bodies were present in the test areas, not even dams - which is quite remarkable in what appears to be a semi-arid area with a large extent of irrigated agricultural

land. But some seasonal lakes or ponds associated with the Nahr Ar Rahad river could clearly be identified. This suggests that, if other water bodies were available in the area, they could be identified quite easily.

11.3.4 Vegetation, Forest and Cultivated Land

No specific or coherent areas of vegetation or forest of any significant size is shown on the 1:100,000 scale maps of the test areas. Instead a general representation of the scattered trees and bushes is shown. On the MOMS-02 images, no distinctive areas of vegetation or woodland such as planted forest could be identified. However, obviously from the detailed inspection of the images, there is a ground cover of vegetation, but it is not defineable by lines. In absence of any ground inspection, it must be presumed that this cover consists of extensive areas of scattered thorn scrub and bushes typical of semi-arid areas in the region. Once again, field completion is needed to identify the nature of this ground cover to establish whether it could be represented in some way either by using symbols or colours on a classical type of line map.

In the test areas, there are many small tracts of cultivated land and several large agricultural schemes with regularly-shaped fields which are quite distinctive and easy to recognize. Most of them could be identified as a result of the high (light/dark) contrast between adjacent cultivated areas and fields. Besides these large geometrical shaped fields, there are also scattered smaller fields, often of an irregular shape, which presumably are the expression of an older and more traditional type of agriculture.

The results of the identification and feature extraction test of the MOMS-02 image over the Sudanese test field are summarized in Table 11.1.

Testing the same area with the images from the multispectral Channels 3 and 4 did not show a significant change in the interpretation or in the results. This could be the result of there being no vegetation with a distinctive signature and comprising areas of significant size present in the area.

Table 11.1 Results of the photogrammetric interpretation and feature extraction for the construction of a vector line map from MOMS-02 imagery over the Sudanese test field

Main Class of Features	Features	Percentage of Extraction
Communication Lines	Surfaced roads	100
	Unsurfaced roads	100
	Major and minor tracks	50
	Bridges	0
	Railway lines	0
Cultural Features	Towns	100
	Villages	70
	Isolated buildings	0
	Power and telephone lines	0
Vegetation / Land Cover	Cultivated land	90
	Forests	80
	Scattered trees	0
Hydrology	Rivers	100
	Streams	90
	Pipelines	100
	Irrigation channels	100
	Water bodies	100

11.4 Improved Cartographic Representation of the Test Area Through the Production of an Image Map

Although, based on the standards which are applied to the compilation of conventional topographic line mapping, nearly 60% of the area of the Sudanese test field would be characterised as featureless, there are indeed features present on the land surface of the area. However, the weakness of its representation by vector line maps means that they do not

show these features. Thus the use of the MOMS-02 imagery to form the basis of an image map for this type of area would appear to be promising. With this in mind, and to try and interpret and extract more information from the image, a simple broad brush terrain analysis has been carried out which will be discussed in the next section.

11.4.1 Terrain Analysis of the Sudanese Test Field Using MOMS-02 Imagery

In general terms, the whole area covered by Scene 5 can be classified into seven different and distinct regions (see Figure 11.1).

Region A in the north western part of the image is rather amorphous in character and lacking in contrast. There are a few isolated rocky hills standing prominently above the mainly flat terrain. There appear to be numerous small fields separated by uncultivated areas which show up in a fairly uniform dull grey appearance. There are also quite a number of distinctive larger circular or oblong shaped areas which show up as whitish (high reflectance) areas against the grey background. Without a ground inspection, these cannot be identified in a positive manner. However, inspection of the 1:100,000 scale map suggests that they are the sites of villages, some being clustered around the bases of the isolated hills. It must be pointed out too, that the map indicates that a number of the larger settlements are refugee camps which were set up to accomodate the large numbers of people fleeing from the civil war in Eritrea and Tigre and the severe famine which affected Northern Ethiopia in the mid-1980s at the time these maps were being prepared. Only ground inspection can ascertain whether or not those were operational at the time of the acquisition of the MOMS image. Figure 11.2 shows a representative part of this area.

Region B comprises the area of cultivated land with its large square or rectangular - shaped fields laid out in a very regular and distinctive pattern. The individual fields are up to 2km×2km = 4km^2 in size and fairly uniform in tone and texture, suggesting some type of monoculture using mechanised farming techniques. There are more than 120 of these fields set in a series of regular patterns adjacent to one another; almost certainly, collectively they form part of a large development project.

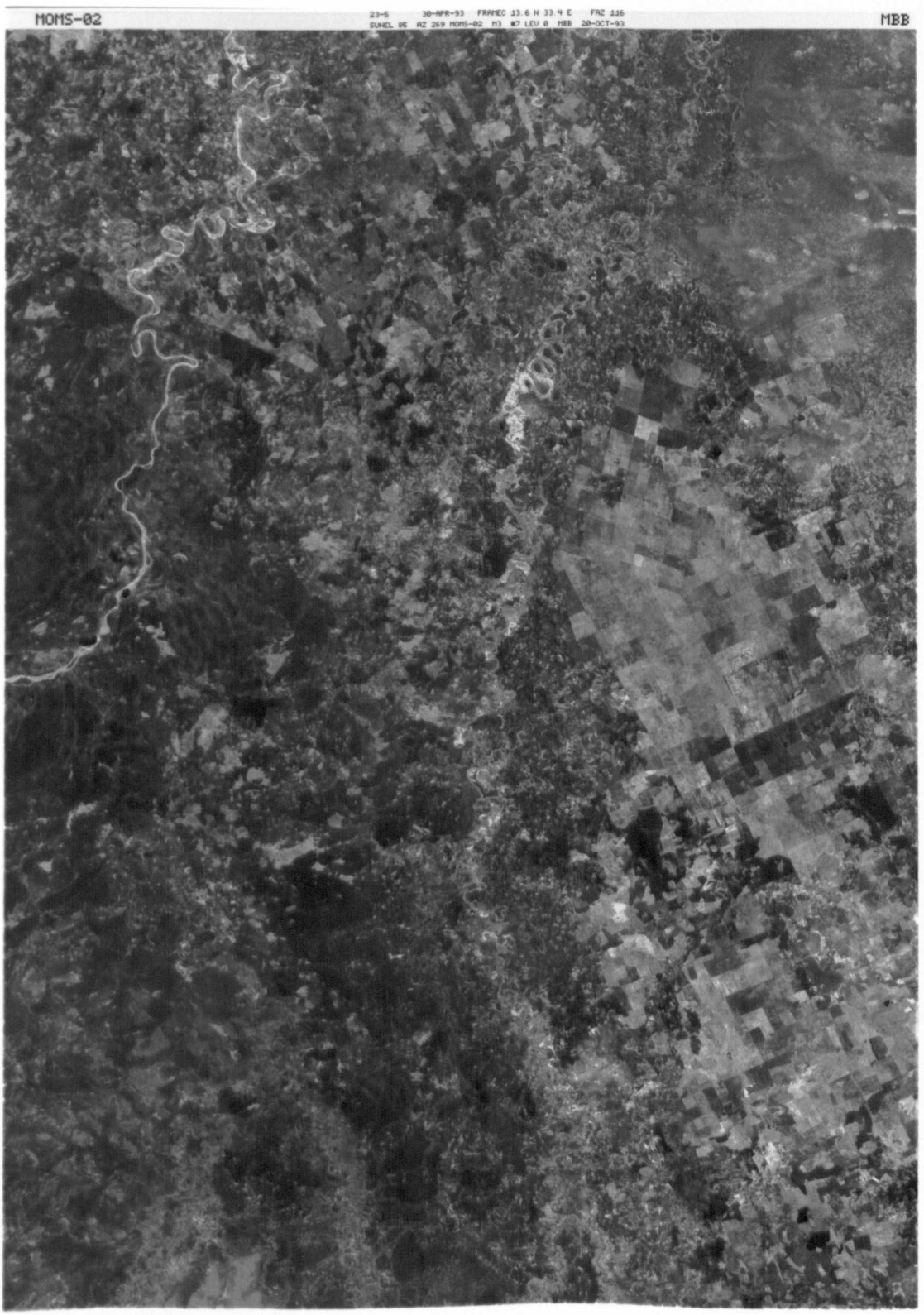

Figure 11.1 MOMS-02 Scene 5, Channel 7, image of the Sudanese test area with an overlay of the Regions defined in Section 11.4

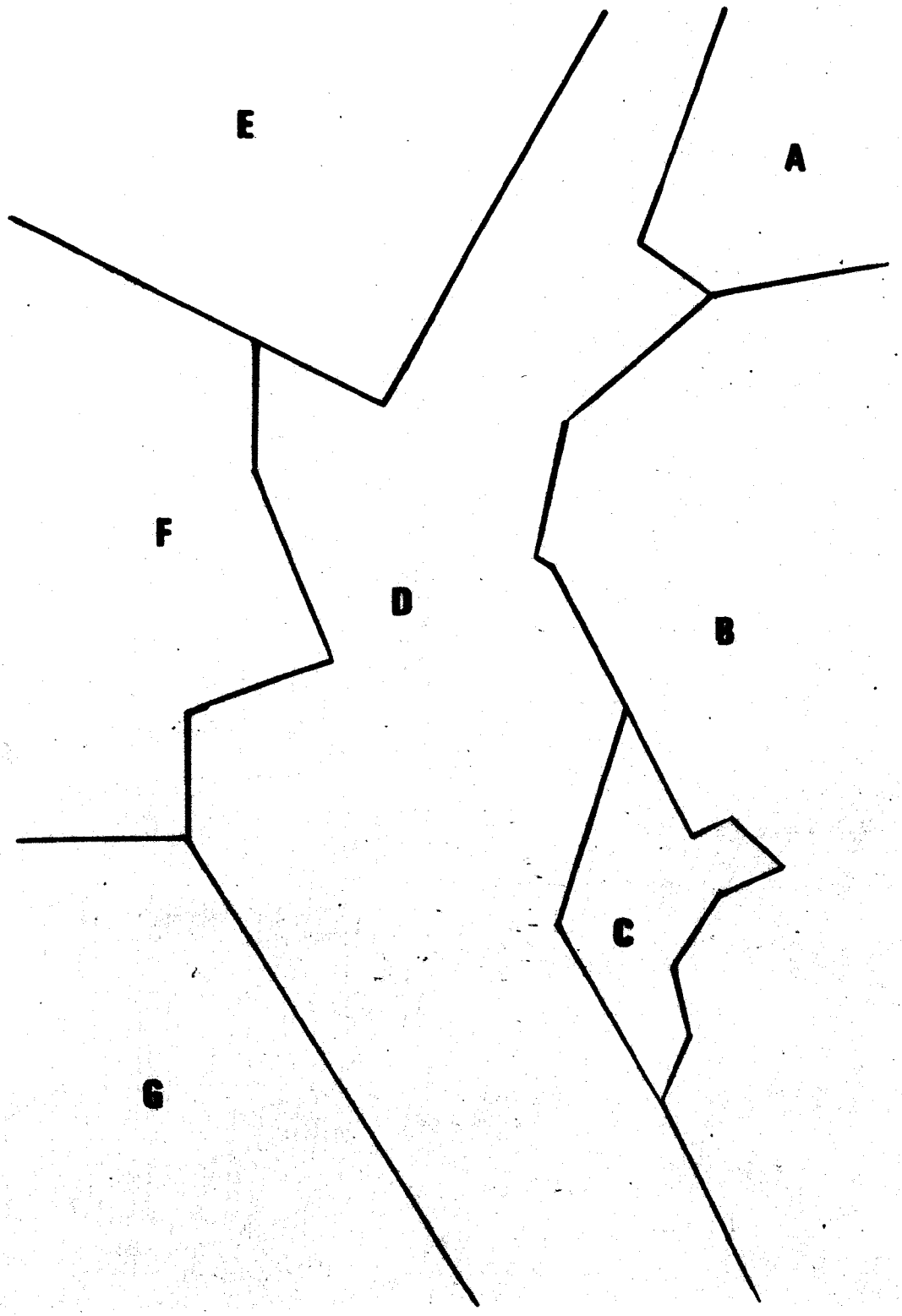
E
A
F
D
B
C
G

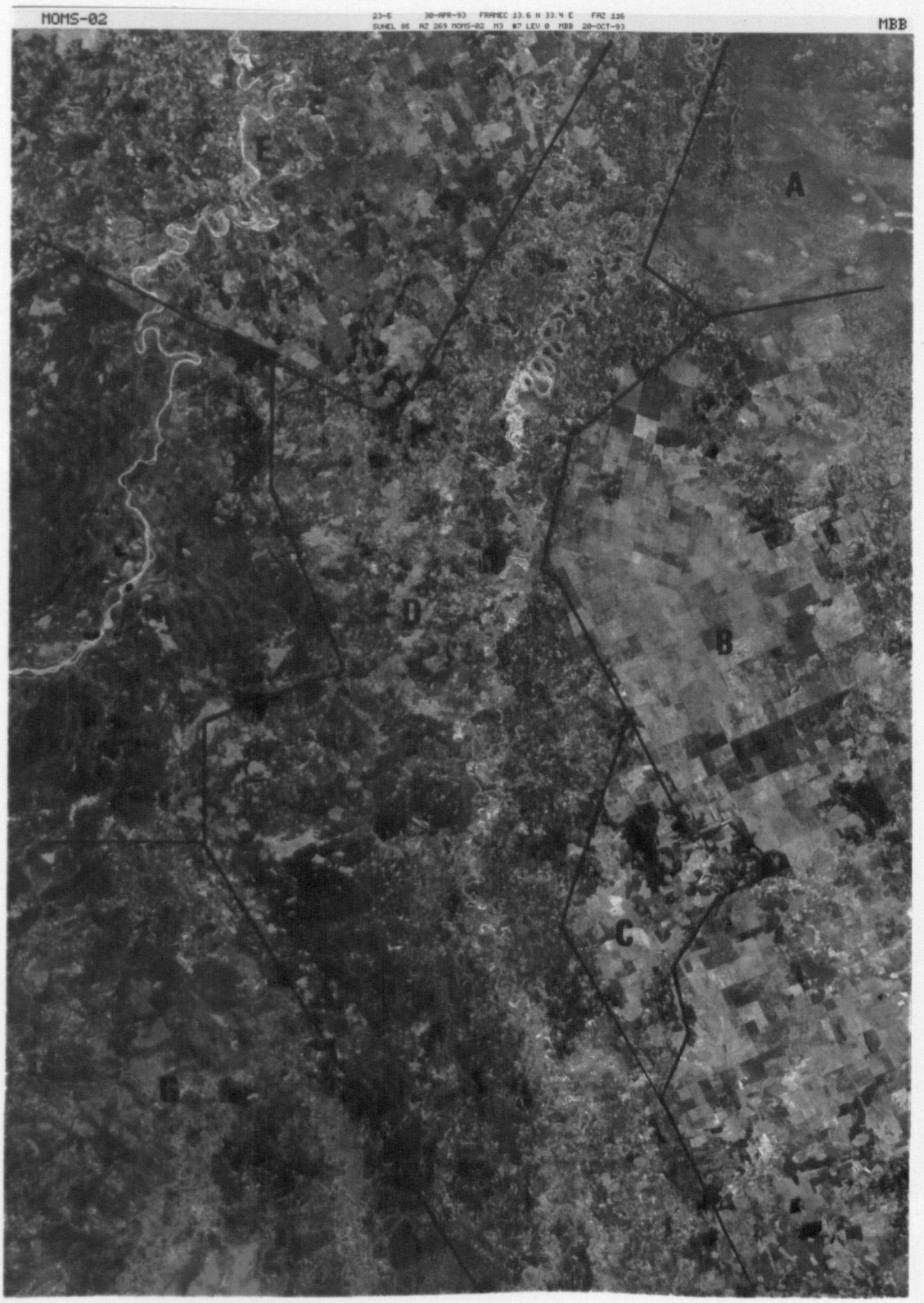

Figure 11.1 MOMS-02 Scene 5, Channel 7, image of the Sudanese test area with an overlay of the Regions defined in Section 11.4

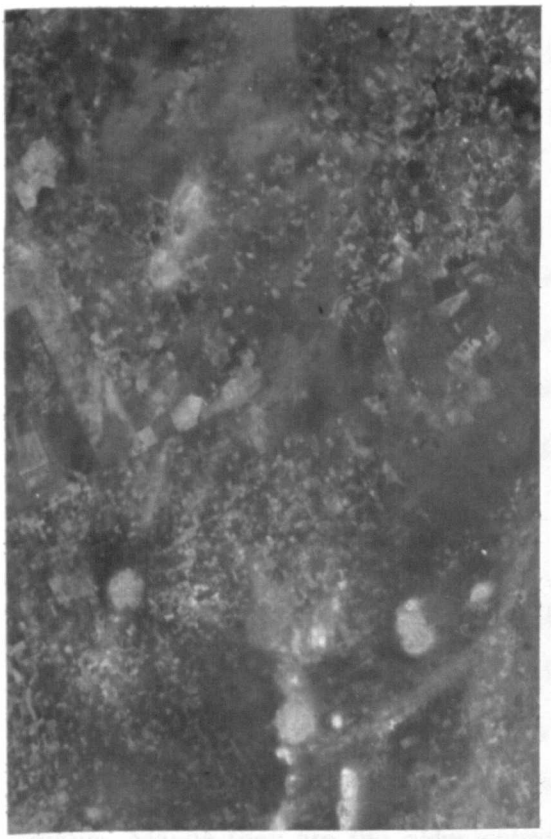

Figure 11.2 Region A

Figure 11.4 Region C

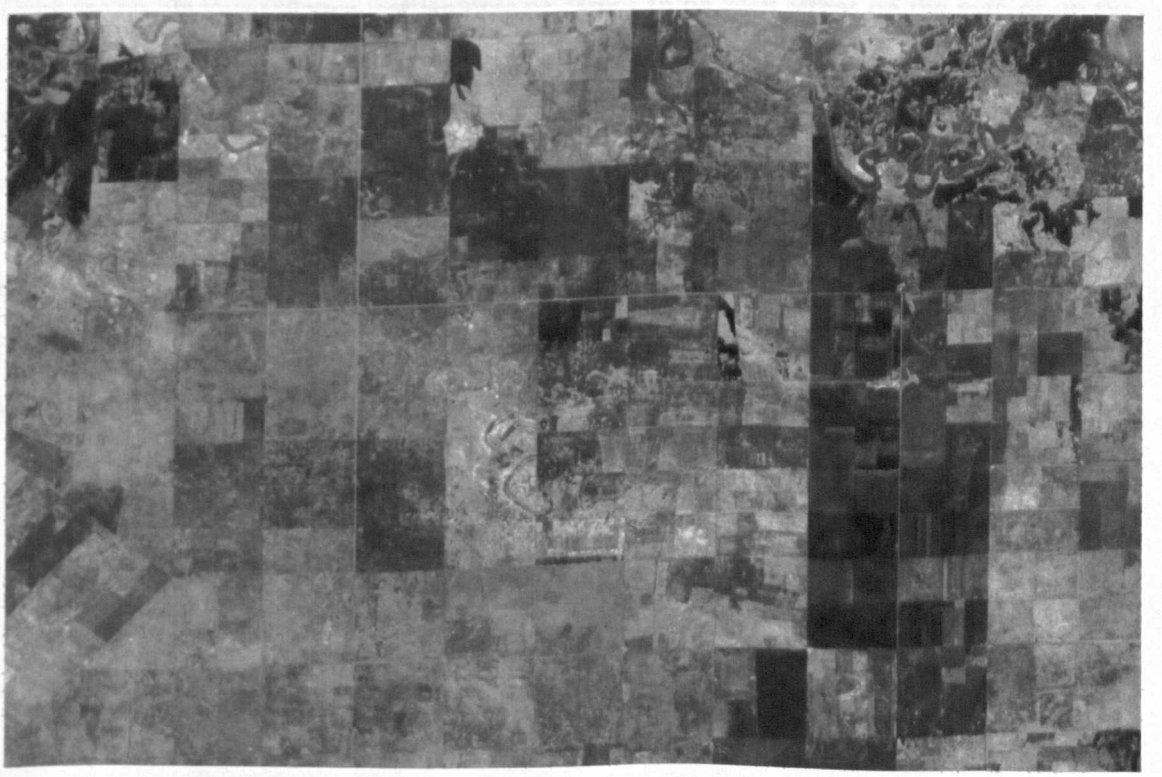

Figure 11.3 Region B

The actual fields show up in a chequerboard pattern with quite different reflectances which are probably the result either of growing different crops or of the ground cover being at different stages (e.g. cultivated/fallow) of a crop rotation cycle. These differences make it possible for the borders of these fields to be identified quite easily. In different parts of Region B, some small areal features which seem to be settlements could be recognised. Again, on the basis of the collateral information given by the existing 1:100,000 scale map, these are probably the camps or settlements used to house the people working in the area. In the northern and eastern parts of this region, some low hills can be detected quite clearly. Figure 11.3 shows a part of this area.

Region C lies immediately to the south of Region B. Again it comprises some cultivated land but it is much smaller in total area and the individual fields are also smaller and more irregular in shape compared with those occuring in Region B. These quite different characteristics can be observed clearly when comparing this region with the adjacent regions. Maybe they are the older cultivated lands which already existed prior to the establishment of the large development scheme covered by Region B (see Figure 11.4). There are no obvious villages, settlements or camps to be seen either on the map or on the MOMS-02 image. The map indicates the presence of scattered individual buildings, but these cannot be detected on the MOMS-02 image. In fact, the area lies within the boundary of the Dinder National Park, which may well mean that, within this area, the mechanised farming development of the adjacent Region B will not be permitted and only traditional farming practices will be allowed. But, once again, the image interpretation needs to be followed up by a field inspection of the area by topographers completing the map on the ground.

Region D extends from the east to the west of the test area and comprises the meandering river Nahr-ar-Rahad and its shallow valley with many oxbow lakes or cutoffs which can all be identified and detected quite easily on the image. At intervals along the river, small areas having similar patterns to one another can be recognized. At first, it was difficult to recognise these, but, using the 1:100,000 scale map, they could be identified as villages.

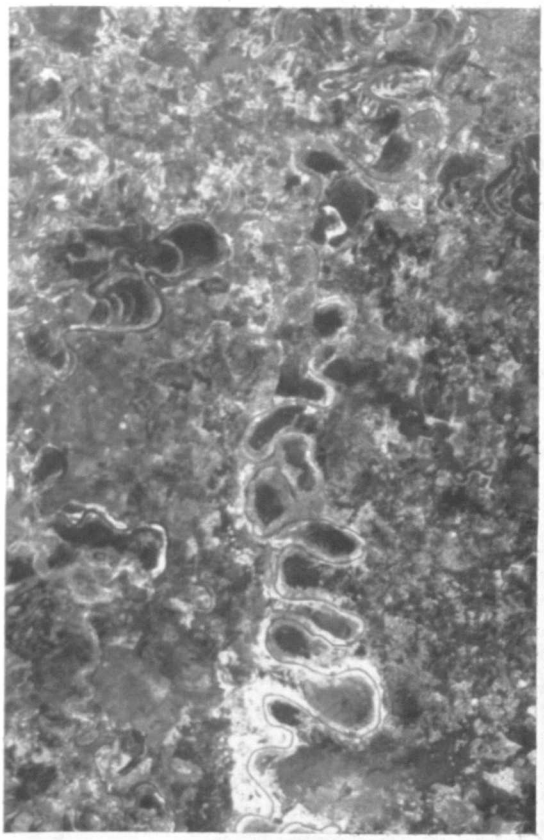

Figure 11.5 Region D

Figure 11.6 Region E

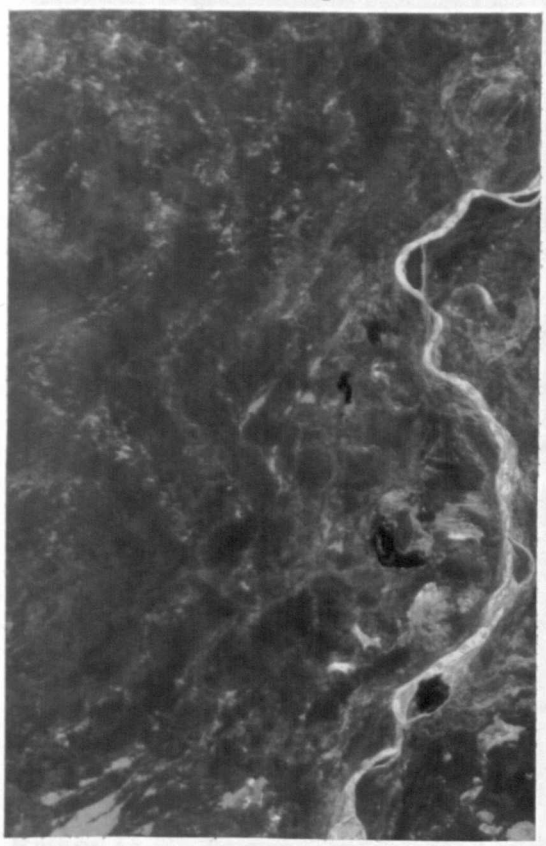

Figure 11.7 Region F

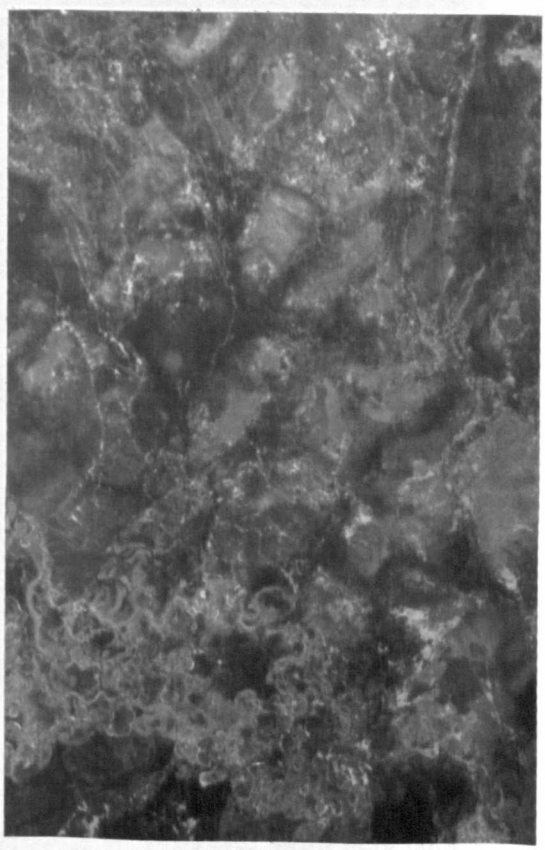

Figure 11.8 Region G

In fact, once one or two had been identified from this collateral information, the others could be easily detected and identified in the image. It appears that these villages have all been established at intervals along the banks or levees of the river. The characteristics of this area show that probably the landscape adjacent to the meandering river is a ill-drained flood plain area with extensive swamps and marshy regions. Figure 11.5 illustrates a part of this region.

Region E comprises the lower part of another meandering river (the Nahr-ad-Dindir) again with distinctive oxbow lakes occupying part of the river valley. It is noticeable that the amplitude of the meanders and the cut-offs and oxbow lakes is much greater than with those visible and associated with the other river crossing Region D. In the northern part of the river valley, several areas of cultivated land can be observed with quite different characteristics to those of Region B. To the south of this river, a series of smaller cultivated fields can be identified. Figure 11.6 shows a small part of this area.

Region F is a large area which extends from the east to the south of the image and comprises a large variety of different features including low hills, river and streams. In general, it lacks any obvious settlement or cultivation pattern. Moreover the overall reflectance pattern is much darker than those of the other parts of the image and exhibits, in many places, a series of long curved features mostly several kilometres in length which are very dark in tone and which lie parallel to one another separated by a narrow strip of land which is lighter in tone. This distinctive pattern, which in total covers a large area could comprise a series of parallel low ridges and shallow valleys but, once again, this can really only be confirmed by inspection on the ground. The upper part of the Nahr-ad-Dindir river flows through the area, but noticeably it does not exhibit the obvious meanders and oxbow lakes shown by the lower part of the same river in Region E. Instead it has a more direct course with braided channels separated by small islands. Figure 11.7 illustrates a part of this region. Once again, it will be apparent that this type of terrain is better depicted via an ortho-image map than by a conventional type of symbolised line map such as the existing DOS map of the area.

Region G, in the south western part of the area appears to be a slightly more hilly land,

including several large low hills and ridges with vegetation cover which could be identified easily on the image. There are also some small streams, apparently seasonal, crossing Regions F and G in a very meandering pattern which eventually feed into the two main rivers (Nahr-ar-Rahad and Nahr-ad-Dindir). In general, the area lacks a distinct settlement or a cultivation pattern though some cultivated fields can be discerned (see Figure 11.8).

11.5 A Brief Discussion and Summary

From the test, it seems that certain groups of features can be detected well using the MOMS-02 image. These include nearly 90% of hydrological features, 50% of cultural features, and 40% of communication lines. Although areas of distinctive vegetation or land cover could be identified, they do not lend themselves to delineation and to representation on the traditional type of line map. In general terms, it could be said that, in the areas with quite distinct types of features, the total amount of information which could be extracted from the MOMS-02 images might be expected to reach about 60% of the total information which is required to be shown on the conventional 1:100,000 scale topographic maps. However, in order to complete the remaining 40% of the information required for the total map content, an additional comprehensive field completion operation would be necessary to meet the specifications for content of this map series. The shortfall would be still greater if a 1:50,000 scale topographic map had to be compiled for this type of area. Needless to say, this adds greatly to the time and expense required for the mapping of the area.

In this context, It is also worth mentioning some other aspects of the data collection required for the production of 1:50,000 and 1:100,000 scale topographic maps. The overall cost of acquiring aerial photographs to cover an area is normally estimated to be twice as much as the cost of satellite linear array imagery collected by operational systems such as SPOT or MOMS-2P. However this situation is always changing. The resolution of aerial cameras and photographic film has improved enormously over the last few years which means that the same ground resolution can be obtained from much smaller scale aerial photography. Thus fewer photographs and ground control points are required to carry out the topographic mapping at a given scale. Thus it is likely that the economic advantages of

satellite imagery will no longer be favourable, while its ground resolution is definitly much poorer. Moreover the cost of acquisition of the image data is only a small fraction of the costs involved in converting it into map form using photogrammetric, cartographic and field completion techniques. The stereo-compilation of maps from satellite linear array imagery such as SPOT, MOMS-02 or MOMS-2P requires the availability of an analytical plotter or digital photogrammtric system and appropriate software, but should take substantially less time than that required for the aerial photography. But of course, the aerial photography is a whole order of magnitude better in terms of ground resolution (1.5m versus 15m), providing much more complete and detailed information content and requiring far less field completion and expense. On the other hand, the aerial photography usually needs substantially more GCPs than satellite linear array imagery if original mapping has to be carried out, but not if map revision is the main task. However, with the advent of airborne in-flight GPS navigation data that can be used for ground control purposes, this situation is also changing. So the matter is quite complex and not at all clear cut.

However, although the MOMS-02 mode 3 image with 13.5m ground pixel size shows deficiencies in not providing at least 40% of features which need to be shown in a topographic line map, maybe mode 1 of this type of image with its 4.5m ground pixel size could overcome these deficiencies to a considerable extent. After a photogrammetric evaluation and interpretation of MOMS-02 mode 1 image against existing 1:25,000 scale topographic maps over a test area in Dubai City, Schiewe (1996) reported that, in typical contrast conditions, road and water networks could be extracted nearly completely. However, in urban areas, it was found that the detection of building blocks or single houses smaller than 20m was either quite difficult or impossible. Again he reported that to be able to extract this class of feature, a pixel size of 2m leading to a ground resolution of 4m would be necessary. This brings into the discussion frame the forthcoming American Commercial Earth observation satellites equipped with linear array sensors with their 1m to 3m pixel size which are expected to become operational during 1997 and 1998. However, at the time of writing this Chapter, no information is available regarding the costs of this type of imagery to the user.

As can be seen from the discussion conducted in Section 11.4 above, there are a lot of land cover features present in the image which, because of the limitations of vector line maps, could not be shown on these maps. The big advantage of orthoimages produced from satellite imagery such as SPOT or MOMS-02 compared with the corresponding line maps is that, in areas such as that of the Sudanese test field, they do indeed retain and show these features on the image maps and allow them to be interpreted and utilised by map users.

CHAPTER 12 : CONCLUSIONS AND RECOMMENDATIONS

12.1 Introduction

Nowadays, pushbroom scanners operated from spaceborne platforms are being considered seriously by photogrammetrists as a source of data for topographic mapping at medium and small scales. This arises from the various favourable characteristics of this type of sensor such as their digital nature, their good geometry and resolution, and their cost and performance. Regarding the capability of these imaging systems to acquire stereo images, they can be classified into three groups: (i) cross-track stereo imagers; (ii) along-track stereo imagers and (iii) flexible systems in which the pointing can take place in any direction and therefore combines both cross-track and along-track capabilities to generate the overlapping stereo images.

In this research, the suitability of these systems for topographic mapping at medium scales has been investigated in terms of the information (i.e. position, elevation, and information content), which should be contained in a map. For this purpose, first a mathematical model has been developed in such a way as to describe the geometry of cross-track and along-track linear array stereo images. Then, in order to evaluate the geometric potential of these systems in terms of both planimetry and altimetry, a general adjustment program has been written, based on the analytical photogrammetric solutions developed from this mathematical model. In the case of 3D point determination, a bundle adjustment program has been developed in such a way to implement both cross-track and along-track stereo imagery as well as to accommodate the forthcoming flexible pointing systems. This program has been validated via an extensive series of geometric accuracy tests carried out on both cross-track and along-track images over high quality test fields. As the final test for topographic mapping, the suitability of one of these systems for the provision of the information content for such mapping has been tested and evaluated.

This Chapter presents the general conclusions that can be drawn from this research project and also gives some recommendations for future research into this area of topographic

mapping using satellite linear array images, very much from the point of view of a photogrammetrist.

12.2 Summary

Four main objectives have been set out in the introduction (Chapter 1) for the photogrammetric evaluation of satellite linear array images. These comprise the following:

(1) The 2D and 3D mathematical modelling of satellite linear array images in such a way as to cope readily with the geometry of both cross-track and along-track stereo systems.
(2) The development of an adjustment program which implements analytical photogrammetric solutions to these mathematical models.
(3) The testing of the geometric accuracy of representative satellite linear array images to be carried out in both 2D and 3D over suitable test fields.
(4) The evaluation of the capability of linear array images to provide the information content required for medium and small scale topographic mapping.

In the case of 2D mathematical models, a polynomial transformation (Chapter 4) has been adopted and implemented as a general solution within the adjustment program (Chapter 7).

Whereas 2D polynomial equations can be implemented for all types of linear array images taken from Earth-orbiting satellites, in the case of the 3D mathematical modelling of linear array images, the possible geometric arrangements (i.e. whether cross-track or along-track) that can be adopted to ensure an appropriate overlap and a stereo-viewing capability have had to be considered in the model. In Chapters 5 and 6, different types of 3D mathematical models of the satellite orbital path have been described and discussed. The orbital parameter model has been chosen for implementation because of the following reasons:

(i) Mathematically a full and absolute relationship between the image space and object space can be constructed using the Keplerian elements.

(ii) The ephemeris data available from the sensors on-board the spacecraft define the orbit with a good approximation. This has the effect of reducing the number of GCPs required to solve the parameters in the bundle adjustment program;

(iii) The orbital parameter model can be modified in a simple manner to be used with different types of space imaging systems.

(iv) Since a geocentric coordinate system is used as the object coordinate system, the effects of Earth curvature are eliminated and, since the position of the projection centre of the sensor becomes a function of the orbital elements, then inherently the solution does not need to include Earth rotation.

The 3D mathematical models for both cross-track and along-track linear array stereo-images described in Chapters 5 and 6 respectively, have been implemented in a bundle adjustment program and set out as a part of the general adjustment program (Chapter 7) to give the ground position and elevation of all points appearing on the images.

Using the general adjustment program, a comprehensive series of geometric accuracy tests have been carried out on SPOT (as a case of cross-track) images and MOMS-02 (as a case of along-track) images. The results have been reported and analysed in Chapters 8, 9 and 10. These have allowed the validation of the bundle adjustment program and established the geometric accuracies that can be obtained using stereo-imagery taken with both the SPOT and MOMS-02 linear array scanners. In particular, the results obtained with the SPOT Level 1B solution are far superior to any others using Level 1B stereo-imagery that have been obtained till now. The results obtained with the MOMS-02 imager are also excellent and represent a real contribution to the research efforts which are currently under way to make use of this new type of space imagery. Then the potential of these MOMS-02 images to satisfy the information content requirements of a topographic map has been investigated and the results discussed in Chapter 11.

12.3 Conclusions

Following conclusions regarding these tests can be set out.

(1) 2D Geometric Accuracy Tests of SPOT as a Case of Cross-Track Linear Array Imagery:

Various tests using a 2D polynomial transformation have been carried out on SPOT Level 1A and Level 1B images (Chapter 8, Section 8.1.3 and Chapter 10, Section 10.2). These show that, for semi-arid areas like that of the Jordanian test field, SPOT Level 1A and 1B images can fulfill the planimetric accuracy requirements for 1:50,000 and 1:100,000 scale maps based on the American national mapping standards when using very accurate (sub-metre) GCPs.

(2) 3D Geometric Accuracy Tests of SPOT as a Case of Cross-Track Linear Array Imagery:

In general terms, as has been shown by different investigators and confirmed by this research (Chapter 8, Section 8.1.4 and Chapter 10, Section 10.2), SPOT stereo images in both their Level 1A and 1B forms can easily provide the planimetric accuracy requirements for 1:50,000 scale topographic maps and smaller, although the elevation accuracies are more marginal. As noted in Chapter 11, the main shortfall when using SPOT imagery for topographic mapping and map revision lies in the limitation in the information content that can be extracted from the present SPOT imagery arising from its comparatively large pixel size and poor ground resolution.

(3) 2D Geometric Accuracy Tests of MOMS-02 Image as a Case of Along-Track Stereo Images:

Various two-dimensional accuracy tests have been carried out on a MOMS-02 mode 3 image over a Sudanese test area as well as a MOMS-02 mode 1 image over an Australian test field (Chapter 9, Sections 9.1.4 and 9.2.3). These tests show that, in terms of satisfying the American standards for topographic mapping, in flat areas such as those used as the Sudanese and Australian test fields, MOMS-02 can fulfill the planimetric accuracy requirements for 1:50,000 scale topographic maps and smaller when the control points have been fixed by an accurate GPS field survey (such as that carried out for the Australian test).

(4) 3D Geometric Accuracy Tests of MOMS-02 Image as a Case of Along-Track Stereo Images:

In Chapter 9, Sections 9.1.5., 9.2.4.1 and 9.2.4.2, the procedures used and the results achieved in the different tests that have been carried out with MOMS-02 stereo images over test fields in Sudan and Australia have been outlined and discussed. These results have been further investigated in more detail and compared with the results obtained by other researchers in Chapter 10, Section 10.3. In general, from the results of these tests, it can be concluded that, in terms of geometric accuracy, MOMS-02 stereo imagery can be used successfully for the production of topographic maps at 1:50,000 scale and smaller.

(5) Potential of SPOT Images to Provide the Information Content of Topographic Maps:

The various tests on the interpretation of SPOT images which have already been carried out at the University of Glasgow and by other organizations, show that SPOT images can only supply the data for a preliminary or provisional edition of a 1:50,000 scale topographic map or for the rapid but incomplete revision of an existing map at that scale. Regarding these tests, the present SPOT data is still substantially deficient in providing the details required for the production of a full or final edition of a new 1:50,000 scale map or for the comprehensive revision of an existing published map at that scale. These deficiencies are particularly apparent with regard to both the communications features and many of the smaller man-made cultural features. In order to overcome these deficiencies, which can amount to 30% of the total map content, an additional comprehensive field completion is necessary - which will be both time consuming and expensive. Moreover, without this extensive additional work on the ground, there is a danger that a product will be made available that is substantially incomplete and may not then be acceptable to users.

(6) Potential of MOMS-02 Images to Provide the Information Content of Topographic Maps:

In Chapter 11, Section 11.3, the results of an interpretation test of a MOMS-02 mode 3

image carried out over the Sudanese test area to see if it could supply the information content specified for the conventional 1:100,000 scale topographic maps of that country, have been discussed and analysed. The results of this interpretational test led to the conclusion that 60% of the topographic information required to be shown on the topographic maps at this scale can be extracted from these images. However many man-made features and cultural features, although they are required to be shown on the 1:100,000 scale maps, could not be detected and identified. Therefore, a substantial supplementary field survey completion will be required to include these features and this has quite severe implications for the logistical and economic aspects of mapping in developing countries such as Sudan. The use of MOMS-02 mode 1 images taken with its HR Channel 5 (4.5 ground pixel size) could largely overcome the deficiencies encountered with MOMS-02 mode 3. However, due to the poor radiometric quality of the images provided by this channel so far, this remains unproven. Even then, the detection of areal features smaller than 20m in length such as individual buildings in urban areas which normally should be presented in 1:50,000 and 1:100,000 scale maps does not appear to be possible.

Another matter which should be considered and evaluated concerns the character of the features which a topographic line map can illustrate. As mentioned in Chapter 11, Section 11.4, in an arid or semi-arid area such as the Sudanese test field, there are many features that can be seen on the image, including flood plains, large swampy areas, scrub and savanna areas, stony and sandy deserts and other landscape types and features which a conventional 1:100,000 scale topographic map does not show or cannot represent in a satisfactory manner. This points to a big advantage of image maps over topographic line maps in the representation of such features. Of course, such image maps can be produced from aerial photographs as well as satellite imagery.

It should be noted that the extent of the resources made available for mapping and the quality and pricing of the final map product which is acceptable to users will be the decisive factors in deciding if satellite linear array images will be adopted for 1:50,000 or 1:100,000 scale topographic mapping. While the current SPOT and MOMS-02 imagery represents the current state-of-the-art in terms of production space imagery, it will be most interesting to

see if the forthcoming scanners such as the American linear array imaging systems with a pixel size of 1 to 2 metres, will be able to compete with the high resolution small scale aerial photography which has been used so successfully up till now for 1:50,000 and 1:100,000 scale topographic mapping.

(7) Evaluation of the Orbital Parameter Model and the Bundle Adjustment Program Developed and Used in the Present Research:

The various tests carried out on SPOT stereo images (as a case of cross-track linear array scanners) and MOMS-02 stereo images (as a case of along-track scanners) in the present research validate the orbital parameter model that has been used to define and to describe the geometry of linear array images. They have shown how well this model can reconstruct the terrain model through the stereo images acquired by either cross-track or along-track linear array imagers. The different exterior orientation parameters implemented in the mathematical model and the flexibility of the model will also allow the forthcoming commercial linear array imaging systems to be modelled easily using this mathematical solution.

The results of these tests and their comparison with those achieved by other researchers shows that the bundle adjustment program implementing this mathematical model which was developed during this research, works quite well and accurately in both its Case 2 and Case 3 forms (see Chapter 7, Section 7.3.2). The bundle adjustment program itself is quite flexible and if required, the exterior orientation parameters used in the solution can be reduced from 15 to 9 without serious deficiencies in terms of the final results. The results from various tests carried out using different numbers of exterior orientation parameters and different number of GCPs and reported in Chapters 8 and 9, show the powerful performance of the mathematical model and the bundle adjustment program developed in the present research.

The mathematical model developed in the present research for the 3D geometric correction of SPOT Level 1B images has been tested quite successfully using 5 SPOT Level 1B stereo-pairs. The excellent results achieved by the bundle adjustment program show how well this

solution can reconstruct the terrain model through these images. This gives the potential to use Level 1B images for map compilation, DEM data acquisition and ortho-image generation in a way that has not been done before - the previous assumption being that only Level 1A images could be used for these purposes.

(8) Limitations and the Problems Encountered with Borland C++ Compiler:

As mentioned in Chapter 7, the general adjustment program has been written entirely by the author in the Borland C++ language, version 3.1 for Windows 3.1. It has been run on a PC 486/DX2/66 equipped with 32 MB RAM and 500 MB of hard disk. During the execution of the program, the author faced a lot of problems because of the limitations of this particular compiler for working with the large dimensions of the numbers involved in the computational solution. This originates from the limitations in the computational precision of the Borland C++ compiler. The occurrence of these problems resulted in the author having to spend a lot of time investigating their origin. All of the derivations were reviewed and the mathematical solution was investigated several times without errors being found. Finally the program was tested line by line, until at last, it was understood that, in fact, the problem arises from the limitations of this compiler in terms of its internal precision. The first clue came when the author tested the multiplication of a matrix and its transpose. When the differences between the symmetric elements in the output matrix were calculated, the result was not equal to zero and sometimes it was very large (1e+7)! To overcome this difficulty, first an attempt was made to change the weight matrix using the change in the first factor variance in such a way as to decrease this problem. Then secondly, instead of transposing a matrix first and then multiplying within the matrix itself, the transpose and multiplication operations have been combined in a single multiplication subroutine to simplify the operation.

However it was then discovered that the same problem arises during the inversion of the matrix using the Cholesky method. The initial solution that was attempted was to cut the large matrices into smaller ones. However it would still be necessary to have a routine for the inverse of the matrix, in which case, the same problems as those encountered before,

would arise again at the stage of matrix inversion. Consequently as an alternative, the direct solution of Cholesky to solve the equations was implemented and, in this way, fortunately this problem with the inversion of matrices has been solved. But the discovery of the problems and their subsequent solution consumed nearly one month of the author's research period.

12.4 Recommendations for Future Research

The mathematical modelling of linear array images and the bundle adjustment program developed during this research has already provided an analytical solution for the geometric correction of the images, the reconstruction of the terrain model, and the point position and elevation determination task which can be implemented either in an analytical photogrammetric instrument or a comparable digital system. With respect to photogrammetrically based map production in general and the situation regarding the use of satellite linear array images for topographic mapping in particular, based on the experience gained in the present project, a number of specific points and suggestions may be made regarding the research work which could be undertaken in the future.

12.4.1 Geometric Evaluation of the MOMS-2P Imagery and Comparison of Its Capability for Topographic Mapping with Other Space Linear Array Imagery

The MOMS-2P system has already been placed on board the Russian Mir space station and is expected to be made operational in the near future. Since its orbital inclination is 51 degrees (see Figure 12.1), it will cover most of the populated area on the Earth (though not Glasgow!). Also, because of its higher altitude, its ground pixel size will be degraded to 18m in Channels 6 and 7 and will be decreased to 6m in the case of the HR Channel 5. In the research work carried out in the present project, because of the limitations of MOMS-02 in terms of its Earth coverage (due to its orbital inclination of 28.5 degrees), MOMS-02 stereo image data could not be acquired for the Jordanian test area for which a very good test field of GPS ground control points has been established and digitized topographic maps and high precision elevation profiles (measured using kinematic GPS techniques) are available for DEM validation.

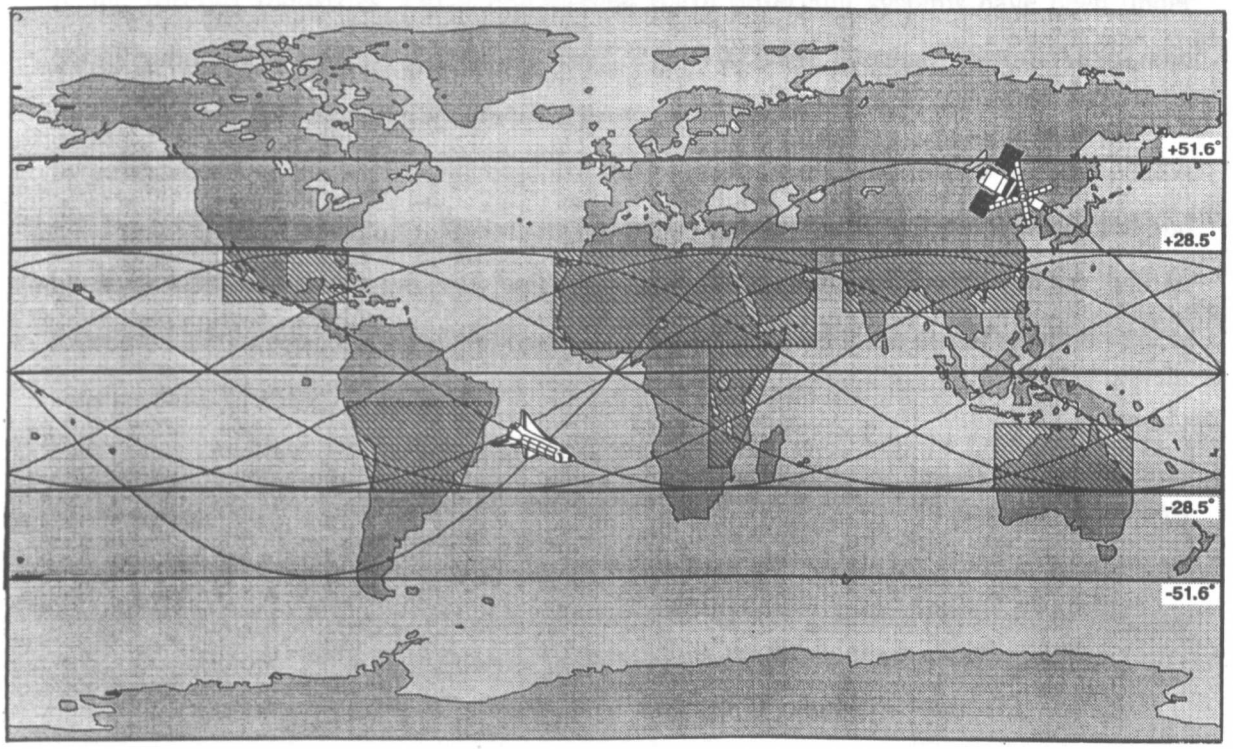

Figure 12.1 MOMS-02 and MOMS-2P Earth Coverage

But hopefully MOMS-2P is going to be able to image the same area, in which case, tests of a hilly area could be executed. Furthermore the Department has just acquired JERS-1 OPS stereo images of the same area, so obviously the material is now becoming available to provide an interesting research topic which will follow on from the present work and produce a more definitive comparative study of geometric potential of all of these linear array stereo-images.

12.4.2 The Potential of New Commercial Earth Observation Satellites to Provide Geometric Accuracy and Information Content Required in a Topographic Map

As mentioned in Chapter 3, Section 3.9, new commercial Earth observation satellite systems are being constructed to take high resolution images of the Earth surface from 1997 onwards. They comprise six American systems, including (i) QuickBird and EarlyBird from EarthWatch Inc.; (ii) CRSS from Space Imaging Inc.; (iii) OrbView-1 from the Orbital Science Corporation; (iv) the GDE imaging system; (v) the Resource 21 imaging system; and (vi) GEROS from the GER Corporation; and one Israeli system called EROS from

Israeli Aircraft Industries. Other commercial Earth observing systems have been under consideration for some time in several countries such as India, Germany, South Africa, and Russia. However, except for the Greensat program of South Africa, most are being funded by governments rather than private organizations in the manner being carried out in the USA and Israel (Fritz, 1996 a, b, c). Obviously not all of these projects will be implemented and be successful and some will not be viable and will disappear. However some will be successful and undoubtedly this will lead to a large expansion in the use of satellite remote sensing data for mapping purposes.

From the geometric point of view, the imaging systems that will be used in these new satellites can be classified into three groups based on the way in which they acquire stereo images: (1) Areal arrays; (2) Pushbroom along-track images; and (3) Flexible pointing systems.

(i) Areal or Staring Array Imaging Systems

Among the new imaging systems, only that installed in EarlyBird from the EarthWatch Company falls into this category. EarlyBird has two-dimensional CCD areal array cameras which are unique and both the panchromatic and multispectral digital images generated by these devices will have the same geometry as conventional frame cameras generating film images. It has been announced that this imaging system will be able to acquire along-track stereo images of the Earth surface. In which case, its stereo acquisition geometry will be the same as that of the convergent aerial photographs used for mapping in Europe and North America in the 1950s and 1960s and should be comparatively simple to solve. Its high resolution capability (3m ground pixel size) in its panchromatic mode should provide a very good geometric accuracy for topographic mapping. According to Fritz (1996c), if high quality, well identified control points are available, this system should be capable of providing an accuracy of ±6m in planimetry and ±4m in height. Based on the American standards for topographic mapping, the planimetric accuracy of this system corresponds to 1:20,000 scale topographic maps and the altimetric accuracy should result in a 12m contour interval which corresponds to that useable in 1:50,000 scale topographic maps. However,

since the contour interval is not associated with a fixed scale, then it may well be the case that the EarlyBird imagery can satisfy the accuracy requirements of a 1:25,000 topographic map, based on the American standards. Based on the criteria set out by Doyle (1984), it appears that this system can fulfill the information requirements for image maps at 1:30,000 scale and smaller.

(ii) Pushbroom Along-Track Stereo Imaging Systems

Both QuickBird and EROS belong to this category. The geometry and the mathematical modelling of this type of system have already been discussed in Chapter 6. Figure 12.2 shows the geometry of the along-track linear array systems with fixed off-nadir angles in the direction of the flight. The bundle adjustment program described in Chapter 7 can be used successfully for the geometric correction of these images in three-dimensions. Fritz (1996c) reports that the expected geometric accuracy of QuickBird will be ±2m in planimetry and ±3m in altimetry. If this can indeed be achieved, then based on the American standards for topographic mapping and Doyle's (1984) criteria, the planimetric and altimetric accuracies of QuickBird images correspond to the requirements of 1:7,000 and 1:50,000 scale topographic maps respectively. So once again, it can be concluded that, depending on the type of the terrain being mapped, this type of imagery can probably be used for the compilation and production of topographic maps at 1:25,000 scale and smaller.

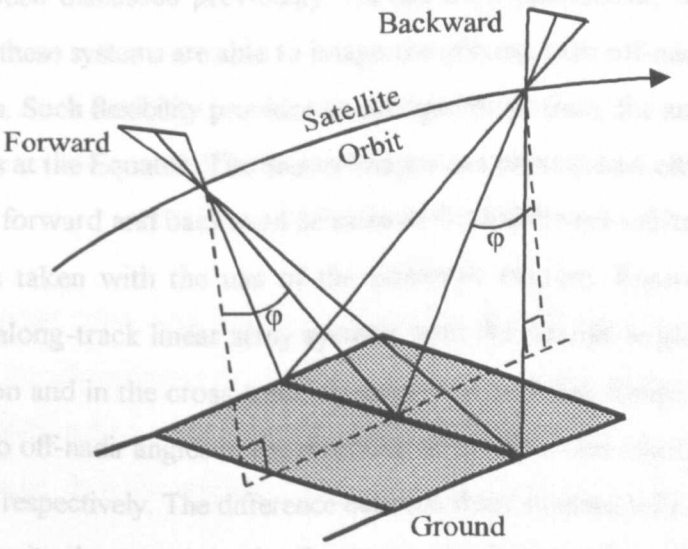

Figure 12.2 Geometry of along-track linear array stereo imagery

In the case of the EROS-A and EROS-B systems, the planimetric accuracies of the images produced by their sensors are reported to be ±6m and ±2m respectively; while the altimetric accuracies of these images are reported to be ±4m and ±3m respectively. As can be seen, EROS-B has the same geometric accuracy as QuickBird and consequently should provide the accuracy requirements for 1:25,000 scale topographic maps and smaller. The EROS-A imaging system is predicted to have the same geometric accuracy as EarlyBird, in which case, depending on the type of topography of the area to be mapped, it may also provide the accuracy requirements for maps at 1:1:25,000 scale and smaller.

Regarding their potential to provide information content for a topographic map, based on the criteria set out by Doyle (1984), the QuickBird and EROS-B imagery should be capable of being used successfully for the production of maps at 1:25,000 scale or smaller. They might even be used for production of orthoimages in 1:10,000 scale and smaller. Based on the same standards, EROS-A imagery can be used for 1:13,000 scale image map production and 1:25,000 scale topographic line map compilation.

(iii) Pushbroom Flexible Pointing Stereo Imaging Systems

Most of the new imaging systems such as OrbView-1, CRSS, GDE, Resource 21 and GEROS belong to this category. The geometry of these systems is somewhat different to those that have been discussed previously. As has been announced, through the use of pointable mirrors, these systems are able to image the ground with off-nadir angles of up to 45° in all directions. Such flexibility provides an average revisit time, for an area of repetitive interest of 1.8 days at the Equator. The stereo images can be acquired either from the same orbital path by the forward and backward sensors or from different orbital paths by the left and right images taken with the use of the pointable mirrors. Figure 12.3 shows the geometry of the along-track linear array systems with the flexible angles ($\omega$and φ) in the direction of motion and in the cross-track direction respectively. These systems employ a combination of two off-nadir angles in the direction of ω (the cross-track angle) and φ (the along-track angle) respectively. The difference between these systems with MOMS-02 mode 1/30, which, besides its along-track angles for stereo viewing, can also utilize a fixed cross-

track angle of 30 degrees, is that these angles are not fixed and can be changed from one scene to another. But since, during the acquisition of a single scene, these angles are fixed, then once again the mathematical modelling presented in this research (Chapter 6, Section 6.5) can be easily used to handle this type of image too. The off-nadir angles have to be entered into the bundle adjustment program as initial values for the ω and φ rotations. Then the additional angular displacements produced when imaging the ground will be computed by the program and added to these initial values and are given in the output once the bundle adjustment program has completed its computational task.

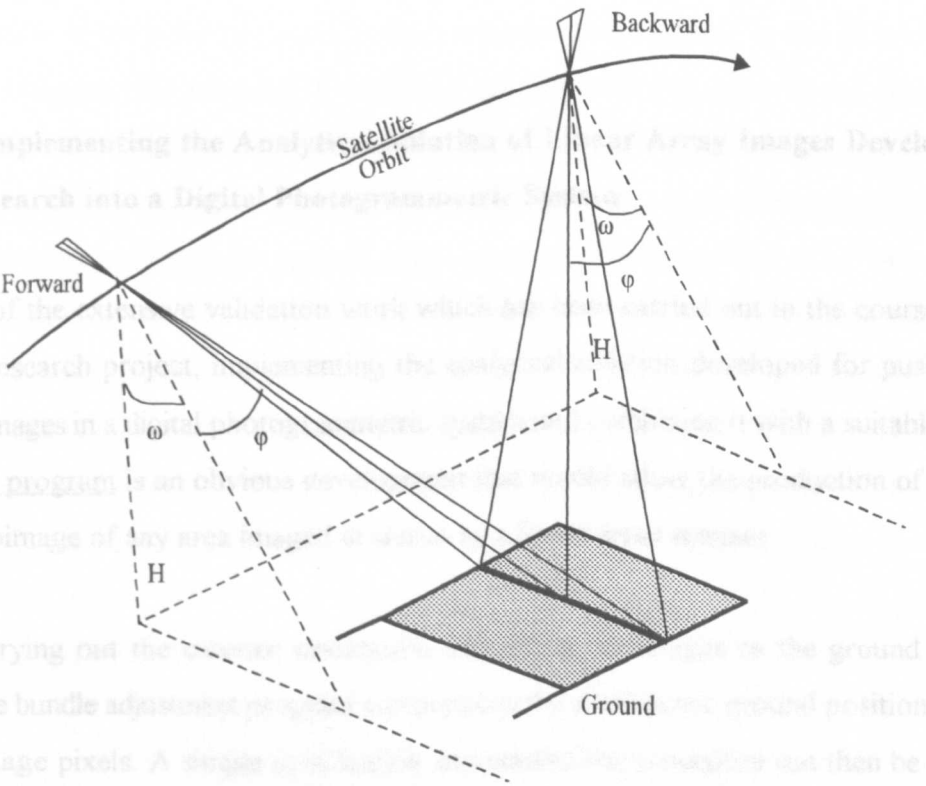

Figure 12.3 Geometry of flexibly pointed linear array stereo imagery acquired from a single orbit using forward and backward sensors

In the case of acquiring cross-track stereo images from two different orbits, the images can be handled in the bundle adjustment program in the sane way as stereo SPOT images. If there exists any additional rotation angle in the direction of the orbital path (φ) at the time of acquiring the image, then this angle can be input to the program as a part of the angle φ.

As reported by Fritz (1996c), most of these systems are designed to provide a planimetric

accuracy of ±2m and altimetric accuracy of ±3m. Therefore, at least theoretically, these imaging systems should be able to provide the planimetric, altimetric and information content requirements of topographic maps at scales of 1:25,000 and smaller and image maps at 1:10,000 scale and smaller. When they do become operational, it will be very interesting to test these images for their potential to produce topographic line and image maps at these scales and, in fact, it can be said that the research work carried out for the present project reported in this dissertation goes a very long way towards preparing for such tests and satisfying such an objective. In particular, the modelling and the programs that have been developed for this project are such that they can readily be employed in carrying out such tests.

12.4.3 Implementing the Analytical Solution of Linear Array Images Developed in This Research into a Digital Photogrammetric System

In view of the extensive validation work which has been carried out in the course of the present research project, implementing the analytical solution developed for pushbroom scanner images in a digital photogrammetric system and combining it with a suitable image matching program is an obvious development that would allow the production of a DEM and orthoimage of any area imaged in stereo by a linear array scanner.

After carrying out the exterior orientation and fitting the images to the ground control points, the bundle adjustment program can produce the planimetric ground positions for all of the image pixels. A simple rectification and resampling procedure can then be used to produce the rectified left and right satellite images. A stereo viewing program can show these images stereoscopically on the screen. Adding the floating marks to this system and using again the bundle adjustment program will provide the 3D measurement capability. Adding a matching program to this system will provide the capability of measuring a large number of conjugate points automatically which, in conjunction with the bundle adjustment program, can generate the digital elevation model (DEM). Combining this DEM with the rectified and resampled image will result in the production of an orthoimage using a differential rectification procedure.

This would be another interesting development for the future. In this respect, the linking of the analytical geometric solution with the image matching routines developed by the Turing Institute of this University would lead to the rapid development of those possibilities. Indeed such a development is already in discussion.

12.5 Final Remarks

This research has given the opportunity for the author to learn to program using the C, C++ and Windows API programming languages and to use them to implement a comprehensive mathematical solution for the satellite linear array imaging systems. It has also helped the author to extend his previous knowledge and research capability from close range photogrammetry to space photogrammetry. Furthermore, the various experimental tests carried out in this research have greatly reinforced the knowledge of the author in the field of topographic mapping in general and taught him how to deal with the detailed interpretation of a satellite image. Finally it has greatly increased his ability to analyse the results, to derive conclusions from these results and to look at and produce solutions to the many problems which arose during the research work from various angles of view. Hopefully too the results of this project will be viewed as having contributed substantially to promoting the use of satellite linear array imagery in topographic mapping.

REFERENCES

Abdel-Aziz, Y. I., H. M. Karara, 1971. Direct Linear Transformation from Comparator Coordinates into Object Space Coordinates in Close-Range Photogrammetry. Proceedings of ASP Symposium on Close-Range Photogrammetry: 420-475

Baltsavias, E. P., D. Stallmann, 1996. Geometric Potential of MOMS-02/D2 Data for Point Positioning, DTM and Orthoimage Generation. International Archives of Photogrammetry and Remote Sensing, 31(B4): 110-116.

Baudoin, A., C. Fratter, C. Latry, M. Pausader, 1993. Continué et Amélioration de la Fliliere SPOT au delà l'an 2000: SPOT 5-6. Actes du Symposium International "Des Images Satellites pour la Cartographie et les Systemes d'Information Géographique", Comité Francais de la Cartographie (CFC), Bulletin 142-143: 149-156.

Bodechtel, J., V. V. Salomonson, J. Zilger, 1986. Comparative Analysis of Different Sensor Data (Landsat-TM and MOMS) for Earth Observation of Future Sensor Development. Proceedings International Society for Optical Engineering (SPIE), Vol. 660: 152-158.

Case, J. B., 1967. The Analytical Reduction of Panoramic and Strip Photography. Photogrammetria, 22(4): 127-141.

Colvocoresses, A., 1979. Proposed Parameters for Mapsat. Photogrammetric Engineering and Remote Sensing, 35(4): 501-509.

Colwell, R. N., (Editor), 1983. Manual of Remote Sensing (2nd Edition). American Society of Photogrammetry, Falls Church, Virginia, USA, Two Volumes, 2440pp.

Deekshatulu, B. L., 1993. Indian Remote Sensing Programme and National Information Needs. Proceedings, Workshop and Conference on "International Mapping from Space", ISPRS Working Group IV/2, Hannover: 81-88.

De Haan, A., 1991. Contribution of the Politecnico di Milano to the OEEPE Test on Triangulation with SPOT Data. OEEPE Test of Triangulation of SPOT Data, OEEPE Publication, (26): 93-107.

De Haan, A., 1992. An Analysis of the Precision of a DEM Obtained from SPOT Data. International Archives of Photogrammetry and Remote Sensing, 29(B4): 440-447.

Deren, L., C. Jiayu, 1988. Bundle Adjustment of SPOT Imagery. International Archives of Photogrammetry and Remote Sensing, 27(B4): 449-455.

Derenyi, E. E., 1973. Orientation of Continuous Strip Imagery. Photogrammetric Engineering, 39(12): 1329-1335.

Dowman, I. J., F. Neto, I. Veillet, 1991. Description of Test and Summary of Results. OEEPE Test of Triangulation of SPOT Data, OEEPE Official Publication, (26): 19-41.

Doyle 1984, F. J., 1984. Surveying and Mapping with Space Data. ITC Publication, Series A, (4): 314-321.

Ebner, H., F. Muller, 1986. Processing of Digital Three Line Imagery Using a Generalized Model for Combined Point Determination. International Archives of Photogrammetry and Remote Sensing, 26(B3/1): 212-222.

Ebner, H., F. Muller, 1987. Combined Point Determination Using Digital Data of Three Line Opto-Electronic Cameras. Technical Papers, ASPRS-ACSM, Annual Convention, Volume 2: 293-302.

Ebner, H., O. Hofmann, W. Kornus, F. Muller, G. Strunz, 1990. A Simulation Study on Point Determination Using MOMS-02/D2 Imagery. International Archives of Photogrammetry and Remote Sensing, 28(B1): 21-29.

Ebner, H., W. Kornus, T. Ohlhof, 1992. A Simulation Study on Point Determination for the MOMS-02/D2 Space Project Using an Extended Functional Model. International Archives of Photogrammetry and Remote Sensing, 29(B4): 458-464.

Ebner, H., T. Ohlhof, E. Putz, 1996. Orientation of MOMS-02/D2 and MOMS-2P Imagery. International Archives of Photogrammetry and Remote Sensing, 31(B3): 158-164.

Ehlers, M., 1987. Integrative Verarbeitung von Digitalen Bilddaten der *Satellitenphotogrammetrie und* - Fernerkundung im Rahmen von Geographischen Informationssystemen. Wissenschaftliche Arbeiten der Fachirchtung Vermessungswesen der Universitat Hannover, No. 149: 137pp.

Ehlers, M., 1990. Remote Sensing and Geographic Information Systems: Towards Integrated Spatial Information Processing. IEEE Transactions on Geoscience and Remote Sensing, 28(4): 763-766.

Ehlers, M., 1993. Mapping Requirements for GIS Applications. Proceedings, Workshop and Conference on "International Mapping from Space", ISPRS Working Group IV/2, Hannover: 245-253.

Ehlers, M., 1996. Rectification and Registration. in Star J. L. and J. E. Estes (Eds.), Integration of Geographic Information Systems and Remote Sensing. Cambridge University Press, (in press).

El-Manadili, Y., K. Novak, 1996. Precision Rectification of SPOT Imagery Using the Direct Linear Transformation Model. Photogrammetric Engineering & Remote Sensing, 62(1): 67-72.

Elms, D. G., 1962. Mapping with a Strip Camera. Photogrammetric Engineering, 28(4): 638-653.

El-Niwieri, A. E. H., 1988. Geometric Accuracy Testing, Evaluation and Applicability of Space Imagery to the Small Scale Topographic Mapping of Sudan. PhD Dissertation, University of Glasgow, (2 Vols): 380pp.

Fraser, C. S., J. Shao, 1996(a). On the Triangulation Accuracy of MOMS-02 Three-Line Imagery. Geomatics Research Australia, No. 64: 47-64.

Fraser, C. S., J. Shao, 1996(b). Exterior Orientation Determination of MOMS-02 Three-Line Imagery: Experiment with the Australian Testfield Data. International Archives of Photogrammetry and Remote Sensing, 31(B3): 207-214.

Fraser, C. S., D. Fritsch, P. A. Collier, J. Shao 1996. Ground Point Determination of Using MOMS-02 Earth Observation Imagery. Presented Paper, 37th Australian Surveyors Conference, Perth: 13pp.

Fritz, L. W., 1996(a). The Era of Commercial Earth Observation Satellites. Photogrammetric Engineering and Remote Sensing, 62(1): 39-45.

Fritz, L. W., 1996(b). Commercial Earth Observation Satellites. International Archives of Photogrammetry and Remote Sensing, 31(B4): 273-282.

Fritz, L. W., 1996(c). Commercial Earth Observation Satellites. Paper Presented to 9th UN Regional Cartographic Conference for Africa, Addis Ababa: 14pp.

Ganguly, P. K., 1991. Mathematical Modelling for Mapping from SPOT. MSc Thesis, ITC, Netherlands: 89pp.

Ghosh, S. K., 1987. Photo-Scale, Map-Scale and Contour Interval in Topographic Mapping. Photogrammetria, 42(2): 34-50.

Goddard, G. W., 1951. New Developments for Aerial Reconnaissance. Photogrammetric Engineering, 28(4): 638-653.

Gopfert, W., 1982. Methodology for Thematic Image Processing Using Thematic and Topographic Data Bases and Base-Integrated Multi-Sensor Imagery. Proceedings ISPRS, Com. VII Symposium, Toulouse, France, Vol. 1:13-19.

Gugan, D. J., 1987. Topographic Mapping from SPOT Imagery. PhD Thesis, University College London: 253pp.

Gugan, D. J., I. J. Dowman, 1988. Topographic Mapping from SPOT Imagery. Photogrammetric Engineering & Remote Sensing, 54(10): 1409-1414.

Guichard, H., 1983. Etude Théorique de la Précision dans l'Exploitation Cartographique d'une Satellite à Défilement: Application à SPOT. Bulletin de la Société Française de Photogrammétrie et de Télédétection, 90: 15-26.

Hardy, R. L., 1971. Multiquadric Equations of Topography and Other Irregular Surfaces. Journal of Geophysical Research, 76(8): 1905-1915.

Hardy, R. L., 1990. Theory and Applications of the Multiquadric-Biharmonic Method. Computers and Mathematics with Applications, 19(8/9): 163-208.

Hartley, W. S., 1988. SPOT 1 Image Utilization, Assessment and Results. Photogrammetric Record, 12(71): 673-677.

Heipke, C., W. Kornus, A. Pfannenstein, 1994. The Evaluation of MEOSS Airborne 3-line Scanner Imagery - Processing Chain and Results. International Archives of Photogrammetry and Remote Sensing, 30(4): 239-250.

Hofmann, O., P. Nave, H. Ebner, 1982. DPS - A Digital Photogrammetric System for Producing Digital Elevation Models (DEM) and Orthophotos by Means of Linear Array Scanner Imagery. ISPRS Inter-Congress Symposium, Commission 3, Helsinki: 216-227.

Hofmann, O., F. Muller, 1988. Combined Point Determination Using Digital Data of Three Line Scanner Systems, International Archives of Photogrammetry and Remote Sensing, 27(B11): III/567-III/577.

Honda, Y., 1993. Japanese Earth Observation Satellite. Proceedings, Workshop and Conference on "International Mapping from Space", ISPRS Working Group IV/2, Hannover: 57-59.

Jacobsen, K., 1993. Comparative Analysis of the Potential of Satellite Images for Mapping. Proceedings, Workshop and Conference on "International Mapping from Space", ISPRS Working Group IV/2, Hannover: 107-114.

Jobre, N., 1993. EMA's Experience with the Production of 1:50,000 Photomaps Using SPOT Images and GPS Survey. Presented Paper, 8th UN Regional Cartographic Conference for Africa, Addis Ababa: 5pp.

Katz, A. H., 1951. A Problem in Inch'on. Photogrammetric Engineering, 17(1): 78-99.

Katz, A. H., 1952. Height Measurements with the Stereoscopic Continuous Strip Camera. Photogrammetric Engineering, 18(1): 53-62.

Kennie, T. J. M., G. Petrie, 1990. Engineering Surveying Technology. Blackie. London/Glasgow, 485pp.

Konecny, G., 1971. Metric Problems in Remote Sensing. Proceedings of the International Society for Photogrammetry, Com. IV Symposium, ITC Publication, Series A, (50): 152-177.

Konecny, G., 1972. Geometric Aspects of Remote Sensing. International Archives of Photogrammetry, 19(4): 47pp.

Konecny, G., 1976. Mathematical Models and Procedures for the Geometric Restitution of Remote Sensing. International Archives of Photogrammetry, 21(3): 11pp.

Konecny, G., 1987. Geometric Evaluation of SPOT Imagery. Seminar on Photogrammetric Mapping From SPOT Imagery, Hannover: 20-53.

Konecny, G., 1995. Current Status and Future Possibilities for Topographic Mapping from Space. EARSeL Advences in Remote Sensing 4(2): 1-18.

Konecny, G., W. Schuhr, J. Wu, 1982. Investigations of Interpretability of Images by Different Sensors and Platform for Small Scale Mapping. Proceedings ISPRS Commission IV Symposium, Crystal City: 373-387.

Konecny, G., P. Lohmann, H. Engel, E. Kruck, 1987. Evaluation of SPOT Imagery on Analytical Photogrammetric Instruments. Photogrammetric Engineering & Remote Sensing, 53(9): 1223-1230.

Konecny, G., J. Schiewe, E. Siebe, 1994. First Examination on the Cartographic Potential of MOMS-02/D2 Data. International Archives of Photogrammetry and Remote Sensing, 30(B4): 196-202.

Kornus, W., H. Ebner, C. Heipke, 1995. Photogrammetric Point Determination Using MOMS-02 Imagery. Proceedings of the MOMS Symposium, Cologne: 67-77.

Kratky, V., 1987. Rigorous Stereophotogrammetric Treatment of SPOT Images. SPOT 1 - Utilisation des Images, Bilan, Resultats, CNES, Paris: 1195-1204.

Kratky, V., 1988(a). Universal Photogrammetric Approach to Geometric Processing of SPOT Images. International Archives of Photogrammetry and Remote Sensing, 27(B3): 180-189.

Kratky, V., 1988(b). Rigorous Photogrammetric Processing of SPOT Image at CCM Canada. Proceedings of the International Symposium on Topographic Applications of SPOT Data, Canada: 35-49.

Kratky, V., 1989. Rigorous Photogrammetric Processing of SPOT Images at CCM Canada. ISPRS Journal of Photogrammetry and Remote Sensing, 44: 53-71.

Kruck, E., 1987. Bingo Bundle Adjustment Program for SPOT Data. Seminar on Photogrammetric Mapping From SPOT Imagery, Hannover: 18 pp.

Leatherdale, J. D., 1978. The Practical Contribution of Space Imagery to Topographic Mapping. International Archives of Photogrammetry, 22(4): 425-444.

Leberl, F. W., 1975. Photogrammetric Interpolation. Photogrammetric Engneering and Remote Sensing, 41(5): 603-611.

Leberl, F. W., 1990. Radargrammetric Image Processing. Artech House, Norwood: 595pp.

Lehner, M., W. Kornus, 1995. The Photogrammetric Evaluation of MOMS-02 Mode 3 Data (Mexico, Ethiopia). Proceedings of International Workshop on International Mapping from Space, Madras, India: 51-68.

Light, D. L., 1986(a). Mass Storage Estimates for the Digital Mapping Era. Photogrammetric Engineering and Remote Sensing, 52(3): 419-425.

Light, D. L., 1986(b). Planning for Optical Disk Technology with Digital Cartography. Photogrammetric Engineering and Remote Sensing, 52(4): 551-557.

Light, D. L., 1989. Remote Sensors for Mapping: What are the Essential Characteristics? Technical Papers, ASPRS/ACSM Annual Convention, Baltimore, Volume 3: 50-75.

Light, D. L., D. Brown, A. P. Colvocoresses, F. J. Doyle, M. Davies, A. El Assal, J. L. Junkins, J. R. Manent, A. McKenney, R. Undrejka, G. Wood, 1980. Satellite Photogrammetry. Chapter 17 in Manual of Photogrammetry, Fourth Edition, Edited by C. C. Slama, American Society of Photogrammetry: 883-977.

Marsden, L. E., 1960. How the National Map Accuracy Standards Were Developed. Surveying and Mapping, 20(4): 427-439.

Masry, S. E., 1969. Analytical Treatment of Stereo Strip Photos, Photogrammetric Engineering, 35(12): 1255-1262.

Mather, P. M., 1987. Computer Processing of Remotely-Sensed Images - An Introduction. John Wiley and Sons, Chichester, 352pp.

Medhin, H. G., 1993. Mapping in Ethiopia. SPOT Magazine, 20: 18-19.

Methley, B. D. F., 1986. Computational Models in Surveying and Photogrammetry. Blackie and Son Ltd, Glasgow, London, 346pp.

Muller, F., D. Hofmann, A. Kahenecker, 1994. Digital Photogrammetric Assembly (DPA) Point Determination Using Airborne Three-line Camera Imagery - Practical Results. International Archives of Photogrammetry and Remote Sensing, 30(3/2): 592-598.

Murray, K. J., J. E. Farrow, 1988. Experiences Producing Small Scale Line Mapping from SPOT Imagery. International Archives of Photogrammetry and Remote Sensing, 27(B11): IV 407-421.

Murray, K. J., P. R. T. Newby, 1990. Mapping from SPOT Imagery at the Ordnance Survey. International Archives of Photogrammetry and Remote Sensing, 28(B4): 430-438.

Naithani, K. K., 1990. Can Satellite Images Replace Aerial Photographs? A Photogrammetrist's View. ITC Journal, 1990(1): 29-31.

Novak, K., 1992. Rectification of Digital Imagery. Photogrammetric Engineering and Remote Sensing, 58(3): 339-344.

Ockert, D. L., 1960. Satellite Photography with Strip and Frame Cameras. Photogrammetric Engineering, 26(4): 592-596.

Orun, A. B., 1990. SPOT Satellite Imagery for Topographic Mapping. M.Phil. Thesis, Oxford Polythechnic in collaboration with University College London, 141pp.

Petrie, G., 1970. Some Considerations Regarding Mapping from Earth Satellites. Photogrammetric Record, 6(36): 590-624.

Petrie, G., 1985. Remote Sensing and Topographic Mapping. Chapter 6 in Kennie and Matthews: Remote Sensing in Civil Engineering. Surrey University Press, London: 119-161.

Petrie, G., 1994. Needs for Topographic Mapping in Developing Countries - Can Space Imagery Deliver Solutions? Presented Paper, 14th EARSEL Symposium on Sensors and Environmental Applications: 9pp.

Petrie, G., 1995. Photogrammetry and Remote Sensing. AGI Source Book 1995: 73-85.

Petrie, G., 1996. Topographic Mapping From Satellite Imagery in Africa. Invited Paper given to ISPRS Congress, Vienna: 21pp [to be Published]

Petrie, G., A. E. H. El Niweiri, 1992. The Applicability of Space Imagery to the Small Scale Topographic Mapping of Developing Countries: A Case Study - the Sudan. ISPRS Journal of Photogrammetry and Remote Sensing, 47(1): 1-42.

Petrie, G., A. E. H. El Niweiri, 1994. Comparative Testing of Space Images for Small Scale Topographic Mapping of Sudan. ITC Journal, 1994-2: 96-112.

Petrie, G., E. J. Liwa, 1995. Comparative Tests of Small Scale Aerial Photographs and SPOT Satellite Images for Topographic Mapping amd Map Revision in Eastern, Central and Southern Africa. ITC Journal, 1995-1: 43-55.

Priebbenow, R. J., 1991. Triangulation of SPOT Imagery at the Department of Lands, Queensland. OEEPE Publication, OEEPE Test of Triangulation of SPOT Data, (26): 109-128.

Radhadevi, P. V., R. Ramachandran, 1994. Orbital Attitude Modelling of SPOT Imagery with a Single Ground Control Point. Photogrammetric Record, 14(84): 973-982.

Rosenholm, D., 1987. Multi-Point Matching Using the Least Squares Technique for Evaluation of Three-Dimensional Models. Photogrammetric Engineering and Remote Sensing, 53(6): 621-626.

Salamonowicz, P. H., 1986. Satellite Orientation and Position for Geometric Correction of Scanner Imagery. Photogrammetric Engineering and Remote Sensing, 52(4): 491-499.

Schiewe, J., 1996. Mapping Using High-Resolution and Stereoscopic Space Imagery of MOMS-02. International Archives of Photogrammetry and Remote Sensing, 31(B4): 742-747.

Searle, P. R. E., 1984. An Analytical Approach to Map Revision. Photogrammetric Record, 11(64): 441-445.

Seige, P., 1993. Status of the MOMS-02 Experiment on the Spacelab Mission D2. Proceedings, Workshop and Conference on " International Mapping from Space", ISPRS Working Group IV/2, Hannover: 39-50.

Shibasaki, R., S. Murai, T. Okuda, 1988. SPOT Imagery Orientation with Auxiliary Satellite Position and Attitude Data. International Archives of Photogrammetry and Remote Sensing, 27(B9): III 125-132.

Tham, P., 1968. Aerial Map Accuracy in Photogrammetry - European Standard Error V. American C-Factor. Svensk Landmateritidskrift, (2): 12pp.

Toutin, T., 1985. Analyse Mathématique pour les Possibilités Cartographiques du Système SPOT. XYZ Revue de l'Association Français de Topographie, 25: 53-66.

Toutin, T., 1986. Etude Mathématique pour la Rectification d'Images SPOT. 18e Congres de la Federation Internationale des Geometres, Canada: 379-395.

Toutin, T., Y. Carbonneau, 1990. Multi-Sterescopy for the Correction of SPOT-HRV Images. International Archives of Photogrammetry and Remote Sensing, 28(B4): 298-313.

Vanicek , P., Krakiwsky, E., 1986. Geodesy the Concepts. Second Edition, Elsevier Science Publishers B.V.: 691pp.

Veillet, I., 1990. Block Adjustment of SPOT Images for Large Area Topographic Mapping. Presented Paper, ISPRS Commission IV Symposium, Japan: 10pp.

Veillet, I., 1992. Accuracy of SPOT Triangulation with Very Few or No Ground Control Points. International Archives of Photogrammetry and Remote Sensing, 29(B4): 448-450.

Welch, R., W. Marko, 1981. Cartographic Potential of a Spacecraft Line-Array Camera System: Stereosat. Photogrammetric Engineering and Remote Sensing, 47(8): 1173-1185.

Westin, T., 1990. Precision Rectification of SPOT Imagery. Photogrammetric Engineering and Remote Sensing, 56(2): 247-253.

Westin, T., 1991. Pass Processing and Extrapolation of SPOT Image Geometry. Photogrammetric Record, 13(78): 923-929.

Westin, T., 1996. Photogrammetric Potential of JERS-1 OPS, International Archives of Photogrammetry and Remote Sensing, 31(B4): 937-942.

Wong, K. W., 1975. Geometric and Cartographic Accuracy of ERTS-1 Imagery. Photogrammetric Engineering and Remote Sensing, 41(51): 621-635.

Wong, K. W., 1980. Basic Mathematics of Photogrammetry. Manual of Photogrammetry, Fourth Edition, Edited by C. C. Slama, American Society of Photogrammetry: 63-64.